Semiconductors, Vol. 34, No. 5, 2000, pp. 495–501. Translated from Fizika i Tekhnika Poluprovodnikov, Vol. 34, No. 5, 2000, pp. 513–518.

ATOMIC STRUCTURE AND NONELECTRONIC PROPERTIES OF SEMICONDUCTORS

Interaction between Copper and Antimony in a Solid Solution Based on Germanium with the Formation of a Charged Complex

V. M. Glazov and A. Ya. Potemkin

Moscow State Institute of Electronic Engineering (Technical University), Zelenograd, Moscow oblast, 103498 Russia

Submitted July 7, 1999; accepted for publication October 22, 1999

Abstract—A scheme of interaction between certain doping elements in solid solutions based on semiconductors is suggested; the scheme involves a reaction of formation of a charged complex on the introduction of double-charged donors or acceptors into the solution. Analytical expressions for the dependence of the solubility of donors on the acceptor concentration and vice versa were derived using the formulas for the mass action law for reactions of ionization of doping additives and interactions between them and taking into account the electron–hole interaction and the conditions for the electroneutrality of the semiconductor. The obtained relationships were tested for a Ge–Cu–Sb system. It is shown that the values of solubility calculated by the suggested theory and those obtained experimentally agree well with each other. © *2000 MAIK "Nauka/Interperiodica".*

Previously [1–4], we developed a theory of charged-complex formation as a result of interaction between doping elements in a silicon-based solid solution. In this work, we analyze the interaction between copper and antimony in a germanium-based solid solution with the formation of a charged complex.

Experimental data reported in [1, 5, 6] suggest that charged and neutral associations can be formed as a result of the following reactions between opposite-charged particles:

$$[Cu^{2-}]_s + [Cu^+]_i \rightleftharpoons [Cu_2]^-,$$

$$[Cu^{2-}]_s + [Sb^+] \rightleftharpoons [CuSb]^-,$$

$$[Cu_2^-] + [Sb^+] \rightleftharpoons [Cu_2Sb]^0,$$

$$[CuSb]^- + [Cu^+] \rightleftharpoons [Cu_2Sb]^0.$$

Here, $[Cu^{2-}]_s$ and $[Cu^+]_i$ are copper atoms in the lattice sites and interstices, respectively.

It is noteworthy that the processes of formation of neutral complexes $[Cu_2Sb]^0$ and charged centers $[Cu_2]^-$ are attributed to the presence of interstitial copper whose concentration, according to [5], is nearly an order of magnitude lower than the concentration of substitutional copper. Therefore, the governing process in the donor–acceptor interaction in the case of combined doping of germanium with copper and antimony is the process of formation of $[CuSb]^-$ charged complexes. Obviously, the products of other reactions may be ignored.

In connection with the above, it is expedient to use the well-justified model of copper–antimony interaction in germanium to consider generally the influence of the formation of charged donor–acceptor complexes on the cosolubility of donors and acceptors in semiconductors. In solving the problem, we use the general approach justified and developed by Reiss and coworkers [7–9] and by us [10–13]. Accordingly, we represent the processes of ionization and interaction between charged particles in the form of the following two systems of reactions corresponding to the cases of doping of a semiconductor with double-charged acceptors (A) and double-charged donors (B):

$$\begin{array}{ccccc}
(N_A)_{\text{ext}} & \rightleftharpoons & (N_A)_{\text{sol}} & \overset{(1)}{\rightleftharpoons} & N_{A^{2-}} + e^+ + e^+ \\
 & & & & + \quad\quad + \\
(N_D)_{\text{ext}} & \rightleftharpoons & (N_D)_{\text{sol}} & \overset{(2)}{\rightleftharpoons} & N_{D^+} \quad + \quad e^- \\
 & & & & + \quad\quad \updownarrow (3) \\
 & & & & \square \quad\quad (e^-e^+) \\
 & & & & (4)\updownarrow \\
 & & & & (DA)^-
\end{array} \qquad \text{(A)}$$

$$\begin{array}{ccccc}
(N_D)_{\text{ext}} & \rightleftharpoons & (N_D)_{\text{sol}} & \overset{(1)}{\rightleftharpoons} & N_{D^{2+}} + e^- \\
 & & & & + \quad\quad + \\
(N_A)_{\text{ext}} & \rightleftharpoons & (N_A)_{\text{sol}} & \overset{(2)}{\rightleftharpoons} & N_{A^-} + e^+ \\
 & & & & + \quad\quad \updownarrow (3) \\
 & & & & \square \quad\quad (e^-e^+) \\
 & & & & (4)\updownarrow \\
 & & & & (DA)^+
\end{array} \qquad \text{(B)}$$

Here, $(N_A)_{ext}$ and $(N_D)_{ext}$ are the concentrations of acceptors and donors, respectively, in an external phase (for example, a liquid phase), and $(N_A)_{sol}$ and $(N_D)_{sol}$ are the concentrations of acceptors and donors, respectively, in a solid semiconductor solution.

The adequacy of the above schemes (A) and (B) is verified experimentally; in fact, in the case of the combined doping of Ge (Si) semiconductors, the predominance of hole conduction is observed simultaneously with the formation of $(DA)^-$ complexes, whereas electron conduction is predominant if the $(DA)^+$ complexes are present. We now define more specifically the above equilibrium reactions (A) and (B) accompanied by the formation of charged complexes, as applied to a particular Ge–Cu–Sb system. Obviously, in accordance with the quantitative data on the solubility of interstitial and substitutional copper in germanium, we deal with a system of dissolution and ionization reactions involving donors and acceptors and resulting in the formation of charged $(CuSb)^-$ complexes; i.e., we deal with the following reaction of type (A):

$$
\begin{array}{ccccc}
(N_{Cu})_{ext} & \rightleftharpoons & (N_{Cu})_{sol} & \overset{(1)}{\rightleftharpoons} & N_{Cu^{2-}} + 2e^+ \\
 & & & & + \quad\quad + \\
(N_{Sb})_{ext} & \rightleftharpoons & (N_{Sb})_{sol} & \overset{(2)}{\rightleftharpoons} & N_{Sb^+} + e^- \\
 & & & & + \quad\quad \Updownarrow (3) \\
 & & & & \square \quad (e^+e^-) \\
 & & & & \Updownarrow (4) \quad\quad + \\
 & & & & (CuSb)^- \quad e^+
\end{array}
\qquad \text{(C)}
$$

Analyzing a system of equilibriums (1)–(4) in the chains of reactions in scheme (C), we may conclude that the formation of hard-to-dissociate electron–hole pairs according to reaction (3) and charged donor–acceptor complexes according to reaction (4) is bound to induce a shift of equilibriums (1) and (2) to the right; this, in turn, means that the solubility of acceptors in the presence of donors is bound to increase and the solubility of donors in the presence of acceptors is also bound to increase. In order to consider quantitatively the effect consisting in the double doping of a semiconductor and accompanying the formation of charged complexes, we used the mass action law and the conditions for conservation of the total number of particles of doping elements and for the electroneutrality of a semiconductor, which made it possible to describe each system of reactions by a relevant set of equations corresponding to systems of equilibriums (A) and (B), respectively.

Henceforth, in formulating the equilibriums and the corresponding equations, we use the following notation accepted for concentrations of defects in solid solutions: n and p refer to electrons and holes; $\square$, to vacancies; $N_{D^{2+}}$ and $N_{A^{2-}}$, to double-charged ions (donors and acceptors); N_{D^+} and N_{A^-}, to single-charged ions (donors and acceptors); and $N_{(DA)^-}$ and $N_{(DA)^+}$, to negatively and positively charged complexes. In addition, we denote the constants in the corresponding equations in using the mass action law by K_0, K_D^*, K_A^*, and K_{DA}^*.

In what follows, we perform various transformations only for the totality of equations obtained on the basis of scheme (A) corresponding to the formation of negatively charged complexes $(DA)^-$; all the required transformations for reaction system (B) are similar to those for system (A). We separate the system of equations (A) into two groups. The first group (I) includes all equations corresponding to the processes related to a variation in the solubility of an acceptor element N_A in germanium as the concentration of donor element N_D increases; the second group (II) involves all equations related to the processes of variation in the solubility of donor element N_D under the influence of the addition of acceptor element N_A.

As a result, we found that systems I and II differ from one another only in the first equations and the parameters K_{DA}^A and K_{DA}^D. We represent the equations of both groups in parametric form taking the hole concentration p as the main variable in equations I and the electron concentration n as the main variable in equations II; thus, we have

$$
\text{(I)}\quad
\begin{cases}
N_{A^{2-}} = K_A^*/p^2, & (1)\\
n = K_0/p, & (2)\\
N_{(DA)^-} = \dfrac{2K_A^*p^{-2} + K_0p^{-1} - 2p}{K_{DA}^A(K_A^*)^{-1}p^2 - 1}, & (3)\\
N_{D^+} = \dfrac{K_{DA}^A}{K_A^*}p^2\dfrac{2K_A^*p^{-2} + K_0p^{-1} - 2p}{K_{DA}^A(K_A^*)^{-1}p^2 - 1}, & (4)\\
N_A = \dfrac{K_A^*p^{-2} + K_0p^{-1} - 2p + K_{DA}^A}{K_{DA}^A(K_A^*)^{-1}p^{-2} - 1}, & (5)\\
N_D = \left(1 + \dfrac{K_{DA}^A}{K_A^*}p^2\right)\dfrac{2K_A^*p^{-2} + K_0p^{-1} - 2p}{K_{DA}^A(K_A^*)^{-1}p^2 - 1}. & (6)
\end{cases}
$$

(II)
$$\begin{cases} N_{D^+} = K_D^*/n, & (7)\\ p = K_0/n, & (8)\\ N_{(DA)^-} = \dfrac{(K_D^* + 2K_0)n^{-1} - n}{1 + 2K_{DA}^D (K_A^*)n}, & (9)\\ N_{A^{2-}} = \dfrac{K_{DA}^D}{K_D^*} n \dfrac{(K_D^* + 2K_0)n^{-1} - n}{1 + 2K_{DA}^D (K_D^*)^{-1} n}, & (10)\\ N_D = \dfrac{2(K_0 + K_D^*)n^{-1} - n + 2K_{DA}^D}{1 + 2K_{DA}^D (K_D^*)^{-1} n}, & (11)\\ N_A = \left(1 + \dfrac{K_{DA}^D}{K_D^*} n\right) \dfrac{(K_D^* + 2K_0)n^{-1} - n}{1 + 2K_{DA}^D (K_D^*)^{-1} n}. & (12) \end{cases}$$

Equations (5) and (6) of system I make it possible to relate the concentration of donors N_D, acceptors N_A, and holes p by the equality

$$N_D = 2N_A + \frac{K_0}{p} - 2p \tag{13}$$

and by the equation of the third degree in $1/p$

$$\left(\frac{1}{p}\right)^4 + \frac{K_0}{K_A^*}\left(\frac{1}{p}\right)^3 + \frac{N_A + K_{DA}^A}{K_A^*}\left(\frac{1}{p}\right)^2 - \frac{2}{K_A^*}\left(\frac{1}{p}\right) - \frac{K_{DA}^A N_A}{(K_A^*)^2} = 0. \tag{14}$$

The largest real positive root, whose existence can be established from the distribution of signs between the real coefficients of equation (14), is determined by the Ferrari method [14] with the formula

$$\frac{1}{p} = \frac{1}{2}\left\{\sqrt{\frac{K_0^2}{4(K_A^*)^2} + 2y - \frac{N_A + K_{DA}^A}{K_A^*}} - \frac{K_0}{2K_A^*} + \left[\left(\sqrt{\frac{K_0^2}{4(K_A^*)^2} + 2y - \frac{N_A + K_{DA}^A}{K_A^*}} - \frac{K_0}{2K_A^*}\right)^2 + 4\sqrt{y^2 + \frac{N_A K_{DA}^A}{(K_A^*)^2} - y}\right]^{1/2}\right\}. \tag{15}$$

Introducing (15) into (13), we obtain the following analytical expression for the isotherm $N_D = f(N_A)$ in the case of the predominance of acceptors ($N_D \le N_A$):

$$N_D = 2N_A + \frac{K_0}{2}\left\{\sqrt{\frac{K_0^2}{4(K_A^*)^2} + 2y - \frac{N_A + K_{DA}^A}{K_A^*}} - \frac{K_0}{2K_A^*} + \left[\left(\sqrt{\frac{K_0^2}{4(K_A^*)^2} + 2y - \frac{N_A + K_{DA}^A}{K_A^*}} - \frac{K_0}{2K_A^*}\right)^2 + 4\sqrt{y^2 + \frac{N_A K_{DA}^A}{(K_A^*)^2} - y}\right]^{1/2}\right\} - 4\left\{\sqrt{\frac{K_0^2}{4(K_A^*)^2} + 2y - \frac{N_A + K_{DA}^A}{K_A^*}} - \frac{K_0}{2K_A^*} + \left[\left(\sqrt{\frac{K_0^2}{4(K_A^*)^2} + 2y - \frac{N_A + K_{DA}^A}{K_A^*}} - \frac{K_0}{2K_A^*}\right)^2 + 4\sqrt{y^2 + \frac{N_A K_{DA}^A}{(K_A^*)^2} - y}\right]^{1/2}\right\}^{-1}. \tag{16}$$

In equality (15) and isothermal equation (16), we use a real root of resolvent of equation (14); this root is determined by the Ferro–Tartaglia–Cardano method [15] with the formula

$$y = \frac{N_A + K_{DA}^A}{6K_A^*} + \frac{1}{2K_A^*}x,$$

$$x = \left\{-\frac{a}{2} + \sqrt{\frac{a^2}{4} + \left[\frac{2}{3}(2N_A K_{DA}^A - K_0) - \frac{1}{9}(N_A + K_{DA}^A)^2\right]^3}\right\}^{1/3} - \left\{\frac{a}{2} + \sqrt{\frac{a^2}{4} + \left[\frac{2}{3}(2N_A K_{DA}^A - K_0) - \frac{1}{9}(N_A + K_{DA}^A)^2\right]^3}\right\}^{1/3}, \tag{17}$$

where

$$a = \left\{\frac{K_0^2 K_{DA}^A N_A}{K_A^*} - 4[K_A^* + N_A K_{DA}^A (N_A + K_{DA}^A)]\right.$$

$$-\frac{2}{27}(N_A + K_{DA}^A)^3 + \frac{2}{3}(N_A + K_{DA}^A)(2N_A K_{DA}^A - K_0)\Bigg\}.$$

Equations (11) and (12) of system II make it possible to relate the concentrations of donors N_D, acceptors N_A, and electrons n by the equality

$$N_A = \frac{1}{2}N_D + \frac{K_0}{n} - \frac{1}{2}n \tag{18}$$

and by the quadratic equation in $1/n$

$$2(K_0 + K_D^*)\left(\frac{1}{n}\right)^2 - (N_D - 2K_{DA}^D)\left(\frac{1}{n}\right) - \left(1 + 2\frac{K_{DA}^A}{K_D^*}N_D\right) = 0. \tag{19}$$

Substituting the positive root of equation (19) into expression (18), we obtain the following analytical equation for the isotherm $N_A = f(N_D)$ for the case of the predominance of donors ($N_A \le N_D$):

$$N_A = \frac{1}{2}N_D + \frac{K_0}{4(K_0 + K_D^*)} \times \left[N_D + \sqrt{(N_D - 2K_{DA}^*)^2 + 8(K_0 + K_D^*)\left(1 + \frac{K_{DA}^D}{K_D^*}N_D\right)} - 2K_{DA}^D\right] - 2(K_0 + K_D^*) \tag{20}$$

$$\times \left[N_D + \sqrt{(N_D - 2K_{DA}^D)^2 + 8(K_0 + K_D^*)\left(1 + \frac{K_{DA}^D}{K_D^*}N_D\right)} - 2K_{DA}^D\right]^{-1}.$$

In order to be able to use the functional relations $N_D = f(N_A)$ and $N_A = f(N_D)$ obtained on the basis of the model for the formation of negatively charged complexes in calculations of the ultimate values of the cosolubility of donor and acceptor elements in the case of the combined doping of germanium, we have to know the values of the constants K_0, K_A^*, K_{DA}^A, K_D^*, and K_{DA}^D for any temperature encountered in the experiment. Using the double systems Ge–*A* and Ge–*D* with the concentrations $N_D = N_D^0$ and $N_A = N_A^0$ and an equiatomic crosscut [*D*] : [*A*] = 1 : 1 with concentrations $N_D = N_A$, we can use the analytical equations $N_D = f(N_A)$ and $N_A = f(N_D)$ and systems I and II to derive the formulas for the above constants; it is these formulas that make it possible to calculate the parameters of the isotherms in terms of experimental values of solubilities for N_A^0, N_A, N_D^0, and N_D and the coefficient K_0. The latter can be expressed as a function of temperature T as

$$K_0 = 32\left(\frac{\pi m_0 k}{h^2}\right)^3\left(\sqrt{m_n^* m_p^*}\right)^3 T^3 \exp\left(-\frac{\Delta E}{kT}\right), \tag{21}$$

where m_0 is the rest mass of an electron, k is the Boltzmann constant, h is the Planck constant, m_n^* and m_p^* are the effective masses of electrons and holes, and ΔE is the bandgap of the semiconductor at the given temperature and for the specified positions of impurity levels.

The above-developed theoretical concepts were used to analyze the behavior of copper and antimony in the case of combined doping of germanium with these elements. For the Ge–Cu–Sb ternary system, it was experimentally established [6, 16] that a negatively charged $(DA)^-$ complex was formed as a result of interaction of a double-charged acceptor (copper) with a single-charged donor (antimony).

Previous microstructure studies of solid solutions belonging to the above Ge-based system made it possible to tentatively determine the boundaries of the homogeneity domains at 500 and 600°C [17]. In order to obtain more precise values of the cosolubility of copper and antimony in germanium in order to use them in calculations, we resorted here to the measurements of microhardness, which proved to be quite useful in solving the above problems. The microhardness H_μ was studied in solid solutions arranged in composition within the ray sections, with the ratios between the atomic concentrations of antimony and copper being equal to 1 : 1, 1 : 2, and 1 : 3. The solid solutions were subjected to long-term homogenization at 500 and 600°C and were quenched in water. Measurements were performed at a load of 50 g in a PMT-3 system with the automated application of load [18]. The data obtained were processed statistically by plotting the frequency curves. It was found that these curves follow the normal Laplace–Gauss distribution. The peaks in the frequency curves correspond to the mean values of actual microhardness.

Analysis of the arrangement of frequency curves in relation to the values of microhardness for solid solutions with different compositions showed that this arrangement is quite regular. Within the ranges of homogeneity, the peaks shift to higher values of microhardness of the solid-solution crystals as the concentration of solutes increases and virtually do not change their positions in relation to composition of solid solutions within the two-phase domains. Using the values of microhardness corresponding to the peaks in the frequency curves, we plotted the concentration dependences of microhardness of crystals of solid solution of copper and antimony in germanium in relation to the

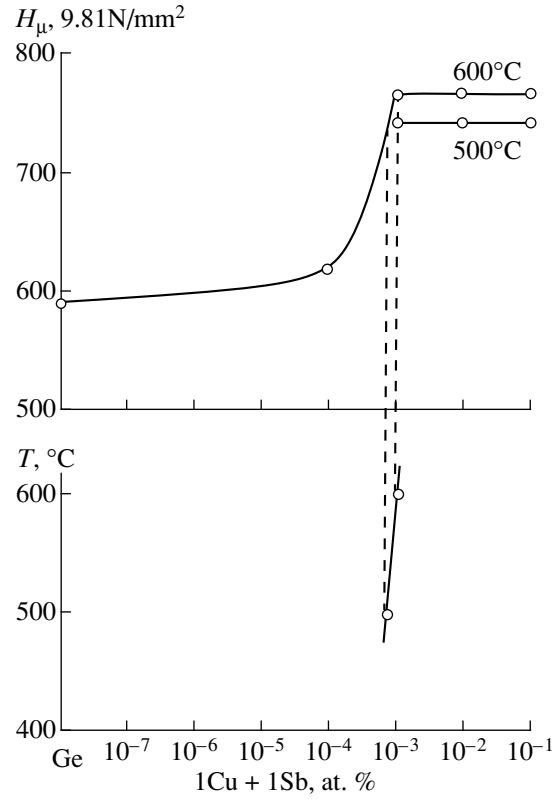

Fig. 1. Dependence of the microhardness of solid-solution crystals H_μ on the solid-solution composition and a segment of the solubility curve for the 1 : 1 crosscut in a Ge–Cu–Sb system.

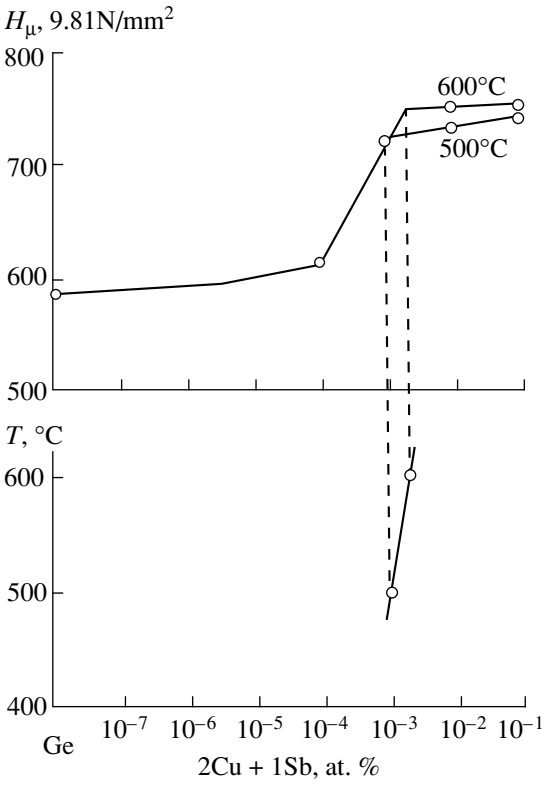

Fig. 2. Dependence of microhardness of solid-solution hardness H_μ on the solid-solution composition and a segment of solubility curve for the 2 : 1 crosscut in a Ge–Cu–Sb system.

solid-solution composition; these dependences are shown in Figs. 1–3. Kinks in the curves correspond to the boundary of saturation of solid solution at the given temperature. The values of solubilities of copper and antimony in germanium along the above ray crosscuts as obtained from the analysis of Figs. 1–3 were plotted on the Gibbs concentration triangle; as a result, we plotted the isotherms of solubility at 500 and 600°C shown in Fig. 4. It follows from Fig. 4 that the solubility of copper increases drastically in the presence of antimony, which, according to the data reported in [7–14], is indicative of donor–acceptor interaction. Numerical values of cosolubility of copper and antimony in germanium at temperatures of 500 and 600°C are listed in Table 1.

Using the values of individual solubilities of copper and antimony taken from [1], the data obtained in this work on the combined solubility of these elements for the crosscut $N_{Cu} : N_{Sb} = 1 : 1$ at 500 and 600°C (see Table 1), and the values of K_0 for these temperatures, we calculated the constants K_A^*, K_D^*, K_{AD}^D, and K_{AD}^A. The values of K_0 were calculated on the basis of equation (21); this equation, if the numerical values of the constants h, k, and m_0 are introduced, can be written as

$$K_0 \approx 2.32 \times 10^{31}\left(\sqrt{m_n^* m_p^*}\right)^3 T^3 \exp\left(-\frac{\Delta E}{kT}\right). \qquad (22)$$

Table 1. Ultimate solubilities of copper and antimony in the cases of simple and complex doping of germanium

Temperature, °C	Solubility of the elements, at. %				
	Separate		Combined $N_{Cu} + N_{Sb}$		
	N_{Sb}^0	N_{Cu}^0	3 + 1	2 + 1	1 + 1
500	6.6×10^{-3}	8.85×10^{-8}	1×10^{-5}	2×10^{-4}	1×10^{-3}
600	1.1×10^{-2}	6.63×10^{-7}	2×10^{-4}	1×10^{-3}	2×10^{-3}

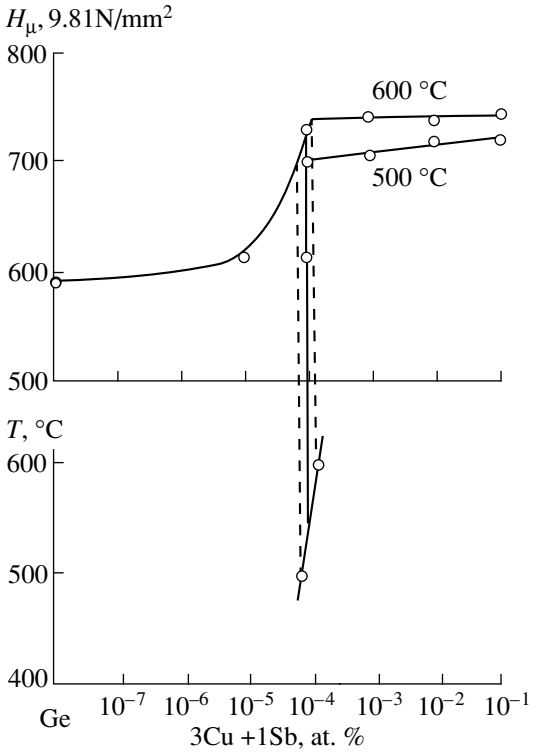

Fig. 3. Microhardness H_μ of solid-solution crystals as a function of the solid-solution composition and a segment of the solubility curve for the 3 : 1 crosscut in a Ge–Cu–Sb system.

In calculations, we took into account the dependences of the germanium bandgap on temperature and concentration and also the values of effective masses m_n^* and m_p^* [19, 20]. The values of all calculated parameters are listed in Table 2. Further calculations were performed with the use of formula (16) for the isotherm $N_D = f(N_A)$. In this case, we used the numerical values of the acceptor concentration N_A for the sections 3 : 1 and 2 : 1 and determined the donor-element concentration N_D. In performing the calculations, we found that, in the case of a Ge–Cu–Sb system, a negative number was obtained under the radical sign in formula (17); i.e.,

Table 2. The values of parameters in the isothermal equations for solubilities of copper and antimony in germanium

Temperature, °C	K_0, 10^{36} cm^6	K_A^*, 10^{50} cm^9	K_{DA}^A, 10^{10} cm^3	K_D^*, 10^{36} cm^6	K_{DA}^D, 10^{19} cm^3
500	2.04	0.40	1.40	2.10	1.94
600	11.24	16.60	19.55	8.20	1.35

Table 3. Experimental data and the values of solubility of a donor element in a Ge–Cu–Sb system as calculated from the isotherm of a charged complex

Temperature, °C	Crosscut at the Gibbs triangle $N_A : N_D$	Solubility N_{Sb}, 10^{16} cm^{-3}	
		experiment	calculation
500	3 : 1	0.11	0.18
	2 : 1	2.97	3.32
600	3 : 1	2.22	2.33
	2 : 1	14.83	18.54

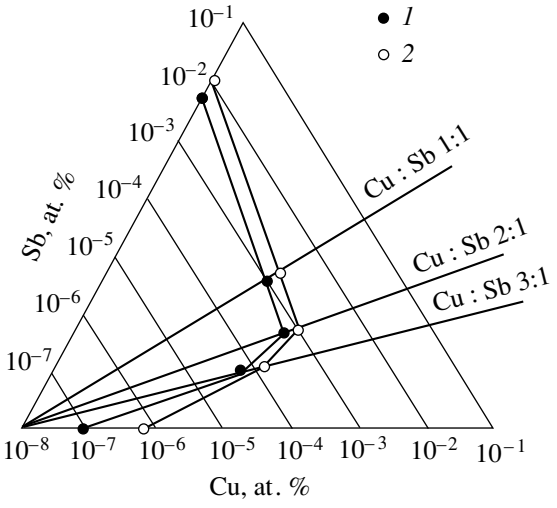

Fig. 4. The solubility isotherms for copper and antimony in germanium at the temperatures of (*1*) 600 and (*2*) 500°C.

$$\frac{a}{4} + \left[\frac{2}{3}(2N_A K_{DA}^A - K_0) - \frac{1}{9}(N_A + K_{DA}^A)^2\right]^3 < 0. \quad (23)$$

Therefore, formula (17) may be represented as

$$y = \frac{1}{K_A^*}\left[\frac{N_A + K_{DA}^A}{6} + \sqrt{\frac{2}{3}(K_0 - 2N_A K_{DA}^A) + \frac{1}{9}(N_A + K_{DA}^A)^2}\cos\frac{\varphi}{3}\right], \quad (24)$$

where

$$\cos\varphi = \left\{\frac{1}{3}(K_0 - 2N_A K_{DA}^A)(N_A K_{DA}^A) + 2[K_A^* + N_A K_{DA}^A(N_A + K_{DA}^A)] + \frac{1}{27}(N_A + K_{DA}^A) - \frac{K_0^2 N_A K_{DA}^A}{2K_A^*}\right\} \Big/ \sqrt{\left[\frac{2}{3}(K_0 - 2N_A K_{DA}^A) + \frac{1}{9}(N_A + K_{DA}^A)^2\right]^3}. \quad (25)$$

The results of calculations and experimental data to be compared with are listed in Table 3.

A strict consistency in derivation of the isotherm equations $N_D = f(N_A)$ and $N_A = f(N_D)$, along with good agreement between the results of calculations and experimental data, verify the adequacy of the suggested model for interaction between acceptor and donor elements in the case of formation of charged complexes in ternary solid solutions of the considered type. The isothermal equations $N_D = f(N_A)$ and $N_A = f(N_D)$ make it possible to theoretically (by calculations) trace the cosolubility of donor and acceptor elements in the case of the combined doping of germanium in the entire range of temperatures and concentrations used.

REFERENCES

1. V. M. Glazov and V. S. Zemskov, *Physicochemical Principles of Semiconductor Doping* (Nauka, Moscow, 1967; Israel Program for Scientific Translations, Jerusalem, 1968).
2. V. M. Glazov, A. Ya. Potemkin, and A. I. Kiselev, Dokl. Akad. Nauk SSSR **223** (2), 377 (1975).
3. V. M. Glazov, A. I. Kiselev, and A. Ya. Potemkin, Zh. Fiz. Khim. **51** (11), 2788 (1977).
4. V. M. Glazov, A. I. Kiselev, and A. Ya. Potemkin, Élektron. Tekh., Ser. Mater., No. 9, 64 (1975).
5. F. A. Kreger, *The Chemistry of Imperfect Crystals* (Wiley, New York, 1964; Mir, Moscow, 1969).
6. N. I. Shadeev, T. I. Grekhova, and A. Ya. Potemkin, Élektron. Tekh., Ser. Mater., No. 3, 63 (1974).
7. H. Reiss and C. Fuller, Phys. Rev. **97**, 559 (1956).
8. H. Reiss and C. Fuller, J. Met. **8**, 256 (1956).
9. H. Reiss, C. Fuller, and F. Morin, Bell Syst. Tech. J. **35**, 535 (1956).
10. V. M. Glazov, G. M. Malyutina, and A. I. Kiselev, Zh. Fiz. Khim. **44**, 1051 (1970).
11. V. M. Glazov, G. L. Malyutina, and A. I. Kiselev, Élektron. Tekh., Ser. 14: Mater., No. 2, 53 (1968).
12. V. M. Glazov and A. I. Kiselev, Élektron. Tekh., Ser. 14: Mater., No. 2, 52 (1970).
13. V. M. Glazov, A. I. Kiselev, and V. N. Chernyaev, Élektron. Tekh., Ser. 14: Mater., No. 3, 37 (1970).
14. A. G. Kurosh, *A Course in Higher Algebra* (Nauka, Moscow, 1968).
15. L. N. Okunev, *Higher Algebra* (Prosveshchenie, Moscow, 1966).
16. A. Yu. Potemkin and V. I. Potapov, Fiz. Tverd. Tela (Leningrad) **2** (1960).
17. A. Yu. Potemkin and E. V. Mel'nikov, in *Doped Semiconductors* (Nauka, Moscow, 1975).
18. V. M. Glazov and V. N. Vigdorovich, *Microhardness of Metals and Semiconductors* (Metalurgiya, Moscow, 1969).
19. A. S. Okhotin, A. S. Pushkarskiĭ, and V. V. Gorbachev, *Thermal Properties of Semiconductors* (Atomizdat, Moscow, 1972).
20. G. B. Bokiĭ, A. Ya. Ugaĭ, *et al.*, *Crystallochemical, Physicochemical, and Physical Properties of Semiconductors* (Izd. Standartov, Moscow, 1973).

Translated by A. Spitsyn

Semiconductors, Vol. 34, No. 5, 2000, pp. 502–509. Translated from Fizika i Tekhnika Poluprovodnikov, Vol. 34, No. 5, 2000, pp. 519–525.

ATOMIC STRUCTURE AND NONELECTRONIC PROPERTIES OF SEMICONDUCTORS

Special Features of the Sublimational Molecular-Beam Epitaxy of Si and Its Potentialities for Growing Si:Er/Si Structures

V. P. Kuznetsov and R. A. Rubtsova

Physicotechnical Research Institute, Nizhni Novgorod State University, Nizhni Novgorod, 603600 Russia

Submitted July 23, 1999; accepted for publication September 16, 1999

Abstract—The concentration of charge carriers and their Hall mobility in Si:Er/Si layers grown by sublimational molecular-beam epitaxy were investigated as functions of temperature in the range of 300–77 K. No electric activity of Er-containing luminescent centers was observed. The feasibility of precise control over impurity profiles in growing the p^+–n–n^+ electroluminescent structures is demonstrated. © *2000 MAIK "Nauka/Interperiodica".*

INTRODUCTION

Interest in growing and investigating Si:Er/Si epitaxial layers is caused by their potential use in optoelectronics.

The multiple ion implantation of Er and O impurities and also shallow-level donors and acceptors into bulk or epitaxial silicon is often used [1–4] with the aim of producing p^+–n–n^+ electroluminescent structures. To do this, it is necessary to use high-energy ions (0.5–4 MeV); irradiation with such ions results in the generation of high-density radiation defects, which cannot be completely eliminated in the subsequent high-temperature annealing. This technology is expensive, the ion range is restricted, and there are traditional constraints in producing the layers with given distributions of Er and of dopants of Groups III and V, in particular, abrupt junctions. Following the erbium implantation and annealing, a high concentration of electrically active centers (10–90% of the Er concentration) is observed in the Si layers [1, 2], which also restricts the practical use of this technology.

If the molecular-beam epitaxy (MBE) is used [5, 6], the crystallographic perfection of the Si:Er layers is improved, the diffusion broadening of the concentration profiles is reduced, and the time required for the structures to grow decreases. Distinctive features of this method are an ultrahigh initial vacuum (10^{-11}–10^{-10} mbar), the electron bombardment for evaporating silicon, effusion cells for evaporating the impurities, multichamber setups, and liquid-helium traps. The disadvantages and difficulties of this method are known [7]; these are the high cost of technological equipment, a limited choice of dopants (Sb and B) and poor control over their fluxes from the effusion cells, a high temperature of the heated parts inside the vacuum chamber, low deposition rates of 0.1–0.2 μm/h, and a high level of contamination by electrically active impurities ($\approx 10^{15}$–10^{16} cm^{-3}). The problem of obtaining a given distribution of impurities in this method is of major importance and has remained unsolved until now [7, 8]. The main difficulty is the accumulation of impurities on the surface of a growing layer.

The accumulation effect was discovered for the first time in 1973 [9], and, in 1979, one way of eliminating this phenomenon was demonstrated [10] by the example of doping silicon with phosphorus using the sublimational MBE. The main distinction of this method consists in the fact that the fluxes of dopants are formed by heating the silicon wafers preliminarily doped with desired impurities at temperatures lower than the Si melting point. The accumulation (surface segregation) of P, Sb, and Al, as well as Ga, As, and B impurities was investigated in a wide range of growth conditions for the Si(100), Si(110), and Si(112) layers [10–16]. The parameters controlling the accumulation were determined. In the case where the accumulation of impurities is absent, the opportunity arises to obtain virtually arbitrary impurity profiles with a reduced density of defects in the layers. For the first time, this possibility was realized for obtaining heavily doped Si layers (to $n \simeq 2 \times 10^{20}$ cm^{-3}) [12, 15, 16], δ-doped Si layers [12, 17], and extremely abrupt concentration profiles [12, 14] without interrupting the growth, without using ion implantation, electric fields and other methods of stimulation, and also without solid-phase recrystallization.

The purpose of this work is to analyze the special features of the sublimational MBE of silicon, to investigate the electrophysical properties of Si:Er epitaxial layers, and to consider the possibility of producing the controlled concentration profiles of Er, P, B, O, and C impurities in the Si:Er/Si structures.

1063-7826/00/3405-0502$20.00 © 2000 MAIK "Nauka/Interperiodica"

EXPERIMENTAL PROCEDURE. SPECIAL FEATURES OF THE SUBLIMATIONAL MOLECULAR-BEAM EPITAXY

The silicon layers were grown in the setup designed in the Physicotechnical Research Institute of the Nizhni Novgorod State University. The silicon wafers (used as sources of fluxes of silicon and impurity atoms and also as substrates) were heated resistively. The setup was evacuated by an oil-diffusion pump with a liquid-nitrogen trap. The pressure of residual gases in the growth chamber during the epitaxy was $(2–9) \times 10^{-7}$ mbar. The layers were grown on Si(100) substrates at temperatures of 400–600°C at a rate of 0.2–5 μm/h. The type of doping impurities and their depth distribution were determined by secondary-ion mass spectroscopy (SIMS). The distribution of charge-carrier concentration over the depth of layers was investigated by the electrochemical capacitance–voltage (CV) method and the Hall method. The concentration and the mobility of electrons in the range of 77–300 K were found from the Hall measurements.

The partial pressure of gases in the process of epitaxy was measured with an IPDO-1 omegatron and amounted to (in mbar), $\sim 2 \times 10^{-7}$ for H_2, $\sim 2 \times 10^{-7}$ for N_2, $\sim 10^{-8}$ for N, $\sim 10^{-9}$ for H_2O, $\sim 10^{-9}$ for O_2, $\sim 10^{-9}$ for O (or CH_4), and $\sim 4 \times 10^{-9}$ for lightweight hydrocarbons. It is known [3] that the atoms of each aforementioned gas introduced by implantation enhance the photoluminescence (PL) intensity of Er in Si. In our layers, all these gas atoms have a chance (and without forcing) to form a luminescent complex with Er. The indicated partial pressure of gases can give rise to a concentration of 10^{19}–10^{21} cm^{-3} for the complexes with Er in the epitaxial layer.

A low vacuum during the growth of our structures posed no negative consequences. In fact, the temperature of growing perfect Si layers (density of etch pits was 10^2–10^4 cm^{-2}) of a thickness to 20 μm was reasonably low (500°C) [13, 18]. This value of the growth temperature coincides approximately with that of the MBE layers grown in an ultrahigh vacuum. A temperature limit for growing perfect Si layers, as was first noted in [18], can be considerably lower than 500°C if the layer thickness is less than 1 μm. In our layers, the background concentration of electrically active centers was less than 2×10^{13} cm^{-3} [13, 19]. The lifetime of minority charge carriers in lightly doped layers exceeded 2 μs [12]. Values of the Hall mobility of carriers in high-resistivity and heavily doped ($n = 3 \times 10^{19}$ cm^{-3}) silicon layers [12, 15] coincide in the range from 77 to 500 K with their values in the corresponding single crystals. The ionization energy of P, Sb, As, Al, B, and Ga impurities in layers differs insignificantly from their values in a bulk silicon [12].

There are two causes of contamination of the Si layers in the setup: thermal evaporation and the gas transport from heated parts in the growth chamber. Therefore, when the technology was being developed [20], much attention was given to reducing their temperature (below 600°C), which, in our opinion, gave the opportunity to obtain perfect Si layers in a relatively low vacuum.

In the sublimational MBE, a large number of dopants can be used: P, Sb, As, B, Al, Ga, etc. The doping regularities were investigated for a wide range of parameters: the temperature and the rate of epitaxy, the impurity flux, the crystallographic orientation of the substrate, and the angle of deviation of the substrate surface from a singular face [12, 19, 20, 22–25]. We also investigated the causes and regularities of formation of defects in a crystal structure [9–11, 24, 25].

ELECTROPHYSICAL PROPERTIES OF EPITAXIAL Si:Er LAYERS

In Fig. 1, we present the concentration n and the Hall mobility μ_H of electrons in Si:Er layers. For comparison, we present the data for a Sb-doped layer only. The layers were grown on p-type substrates (10 Ω cm). Rates v_g and temperatures T_g of growth, thicknesses d, and erbium concentrations N_{Er} in the layers are presented in the table. The sources for doping these layers were cut from silicon ingots with a different content of Er and shallow-level impurities. Among them, there are also the ingots with an erbium concentration below the SIMS detection limit $N_{Er} < 1 \times 10^{16}$ cm^{-3}. The electrophysical properties were investigated in the layers deposited at a temperature lower than 500°C. We note that, in this case, a large number of crystal defects are formed in thick layers even if the latter were grown using Si sources with an impurity concentration of $\sim 10^{12}$ cm^{-3}. For layer 996 ($d \cong 6$ μm and $T_g = 450$°C), we observed a change in the slope of the dependence $n(T)$ (Fig. 1a), which can be interpreted as being due to the presence of a shallow energy state (~0.03 eV) and a deeper energy state (~0.15 eV). More detailed measurements of the energy spectrum of local levels in our Si:Er layers were carried out by deep-level transient

Table

Series no. of the sample	T_g, °C	v_g, μm/h	d, μm	N_{Er}, cm^{-3}	Annealing, 900°C, 30 min
977	430	0.34	0.5	2.5×10^{18}	Yes
978	560	0.24	0.4	5×10^{18}	Yes
994	500	1.6	4.8	$<1 \times 10^{16}$	Yes
995	500	1.5	1.5	$<1 \times 10^{16}$	Yes
996	450	2	6	$<1 \times 10^{16}$	No
996_0	450	2	6	$<1 \times 10^{16}$	Yes
1016	450	1	2	1×10^{16}	No
546(Sb)	600	5.1	7.6	0	No

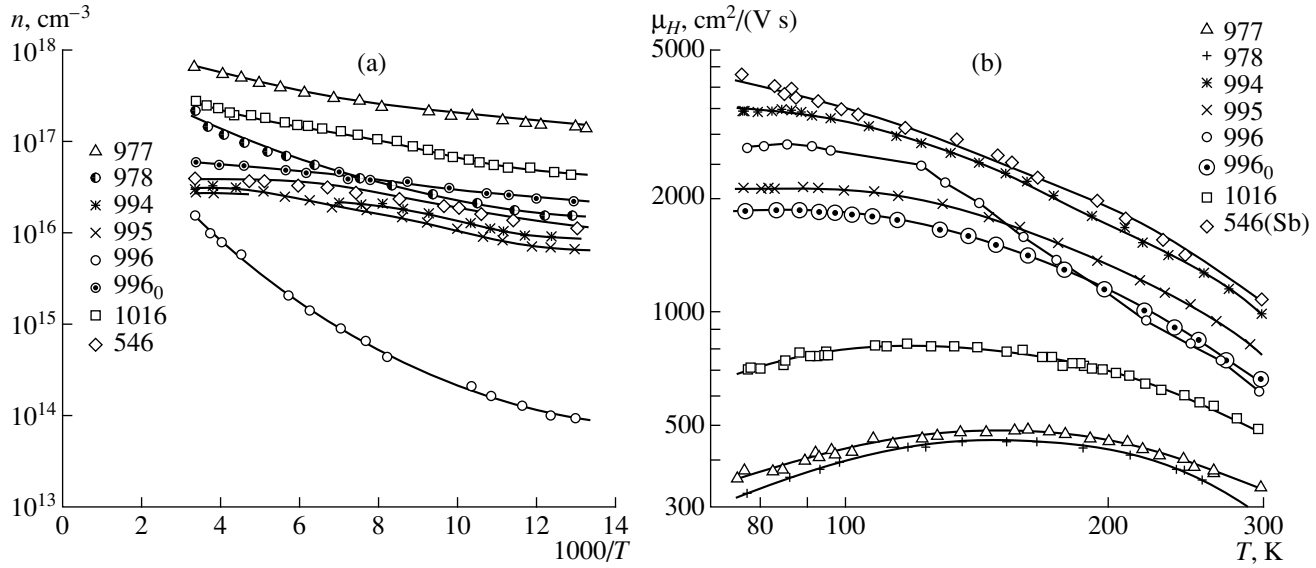

Fig. 1. Temperature dependences for (a) the concentration and (b) the Hall mobility of electrons in the Si:Er layers.

spectroscopy [26] and by admittance spectroscopy. A general pattern was observed; namely, following the annealing of the layers at 900°C for 30 min, deep-level centers of 0.15 eV disappeared, and only shallow levels of ~0.03 eV remained. We assume that the shallow levels in our layers are caused by the presence of conventional donors, for example, P, while the gentle slope of the dependence $\log n(1000/T)$ can be attributed to depletion of these donors near room temperature for $n < 10^{17}$ cm^{-3} and by a decrease in the ionization energy at higher concentrations. The dependence $n(T)$ differed insignificantly for the Si:Sb layer as compared with those for the Si:Er layers. Conversely, in the annealed erbium-implanted samples, a wide spectrum of deep and shallow energy levels is observed; it can be assumed that these are the 0.15-eV donor centers [4] that are responsible for the photoluminescence in these samples. The presence of one or two energy levels ($T_g < 500$°C without annealing) in our Si:Er layers was observed irrespective of the presence [$(1–5) \times 10^{18}$ cm^{-3}] or the absence ($<10^{16}$ cm^{-3}) of erbium atoms in them. This means that none of the donor levels in our layers belong to the Er-containing center.

The depth distribution of the charge-carrier concentration of the Er-doped layers was investigated by the electrochemical CV method. For a uniform erbium distribution at a level of 3×10^{18} cm^{-3}, the charge-carrier concentration in the layer was typically within 10^{15}–10^{16} cm^{-3}, while the type of conduction in one layer can be either *p* or *n*. The charge-carrier sources in our layers can probably be the phosphorus and boron impurities, which were indeed present in the layers and the Si:Er sources at a level of $\approx 10^{16}$ cm^{-3}, according to the SIMS data.

The free-electron concentration in the implanted layers is high (10^{18}–10^{19} cm^{-3}) and amounts to a large fraction (10–90%) of the erbium concentration [1, 2]. For example, it was assumed [1] that the electrically active center is the one containing Er and O. For the MBE layers, there are no data about the electrical activity of erbium centers. The charge-carrier concentration in our layers (usually 10^{15}–10^{16} and to 6×10^{17} cm^{-3} in initial experiments) was not correlated with the erbium concentration; i.e., as distinct from the implantation, in the case of sublimational MBE, the electrical activity of Er centers was less than 0.03%.

Thus, as a result of investigating the electrophysical properties for the sublimational-MBE Si:Er layers, we conclude that the centers containing Er can be electrically inactive.

Nowadays, a number of models are proposed for explaining the excitation of the photoluminescence of erbium in silicon. In some of them, the donor nature of the Er centers plays an important role. Such models are apparently unsuitable for explaining the photoluminescence in our layers.

The Hall mobility of electrons in certain Si:Er layers (Fig. 1b) is somewhat lower than that in a bulk Si sample with the same concentration of electrons: by 20–30% at 300 K and several times at 77 K. According to SIMS, this distinction can be explained by the presence of the boron impurity with a concentration as high as 4×10^{16} cm^{-3}.

IMPURITY PROFILES IN THE p^+–n–n^+ STRUCTURE WITH THE Er-DOPED *n*-BASE

As was noted above, one of the principal unsolved problems in the MBE method is the formation of con-

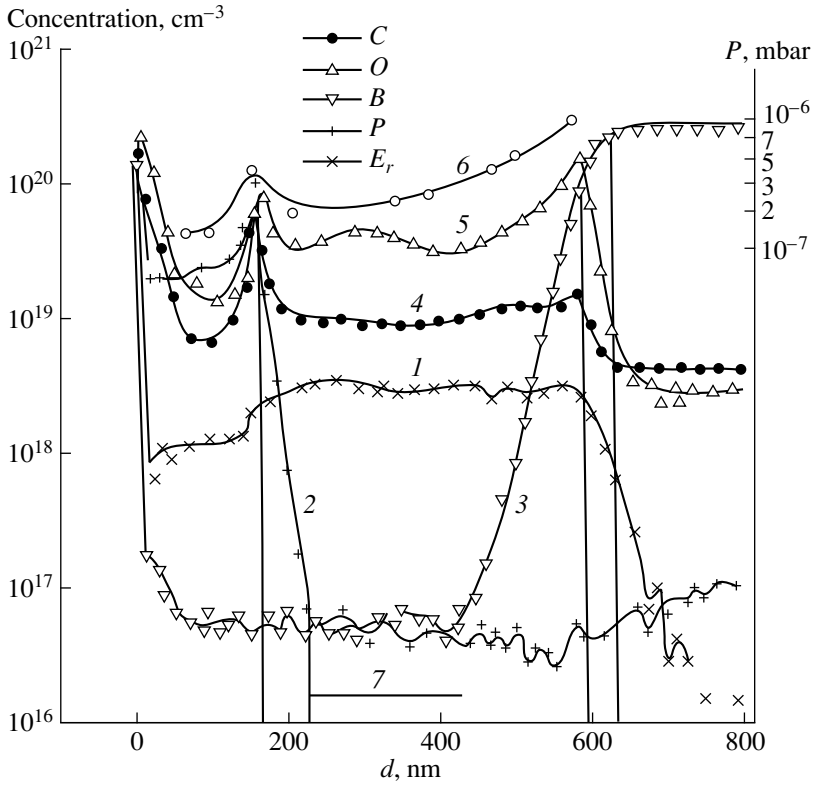

Fig. 2. SIMS profiles of the following impurities in the p^+–n–n^+ Si structure: (*1*) Er, (*2*) P, (*3*) B, (*4*) C, (*5*) O. Curve *6* represents the residual-gas pressure, and curve *7* corresponds to the CV profile of the electron concentration.

trolled impurity profiles, in particular, obtaining heavily doped n^+ layers and abrupt n–n^+ junctions. This problem is the consequence of the accumulation effect of dopants on the surface of a growing layer. The essence of this phenomena consists in the fact that not all the impurity atoms impinging on the layer surface are incorporated in its bulk simultaneously with Si atoms. A significant fraction of impurity atoms is accumulated on the surface and, proportionally to the growing surface concentration, is incorporated into the layer [10]. Near the interface with a substrate (or with a previous layer), a transition region with increasing impurity concentration is formed. An increase in the concentration of a dopant or of a background impurity at the surface and also an increase in its flux into the layer bulk to steady-state values occurs until the impurity flux from the source (or from vacuum) becomes equal to the flux leaving the bulk. The thickness d_n of the layer region with a varying concentration is a measure of the impurity accumulation. However, the steady state is not necessarily reached. Thus, for large fluxes of an impurity from the source, the growth of the surface concentration of this impurity is restricted by the density of Si atoms at the surface ($n_s \simeq 10^{15}$ cm^{-2}). For example, for an impurity concentration of 10^{20} cm^{-3} in the silicon source and for a layer-growth rate of 1 μm/h, the impurity density at the growth surface reaches 10^{15} cm^{-2} within 5 min; i.e., d_n is equal to 0.1 μm. In fact, d_n can be even smaller. Our investigations [10, 11] show that, for a surface impurity density of $\simeq 10^{14}$ cm^{-2}, defects arise in the layer in such a number that the crystal structure of this layer is modified along with the mechanism of incorporation of this impurity, its flux into the layer, and also the position of impurity atoms in the crystal lattice. The impurity concentration in the layer is no longer constant but decreases [11] or increases. Such behavior of the impurity concentration in Si layers along with the presence of a transition region d_n is a second indication of the accumulation phenomenon.

In Fig. 2, we present the SIMS profiles for Er, O, C, B, and P impurities in the p^+–n–n^+ structure and also the CV profile of the charge-carrier concentration in the base n layer and a pressure P of residual gases during the layer growth. The n-type layer was deposited onto the Si(100) boron-doped substrate (0.001 Ω cm) with a rate of 1 μm/h from the Si:Er source at 600°C. Following the deposition of the Er-doped n layer, the temperature was lowered to 500°C and an additional P-impurity source was activated with the aim of depositing the n^+ layer; thereafter, the erbium flux was reduced.

If we take a depth beginning from which the B-impurity concentration becomes constant at a level of 2×10^{20} cm^{-3} as a layer–substrate interface, a maxi-

mum concentration of O, C, and Er in this layer, according to Fig. 2, is attained at a distance of ≃30 nm, identical for different aforementioned impurities and their various concentrations. Moreover, this distance turns out to coincide with d_n for the n^+–n junction in Fig. 2, which is certainly much larger than its actual width, because the n^+ region was grown by us using the δ-doping procedure. The observed value of $d_n \simeq 30$ nm is overestimated due to limitations of the SIMS method; for more details, see the next section. One way or another, it may be assumed that a maximum of concentrations of the impurities Er, O, and C is attained rather rapidly. The calculation shows that, in this case, the Er density at the layer surface is lower than 10^{13} at/cm^2, which is much less than the surface density of Si atoms. Also taking into account that the Er distribution over the n-layer thickness is uniform (Fig. 2), we can state that the Er accumulation at the surface plays no significant role.

The Er distribution in the layer does not correlate with the oxygen distribution (Fig. 2). Along with this, trapping of erbium by an MBE layer is known to increase in the presence of oxygen [6]. If the last statement is also true for the sublimational-MBE layers, the oxygen concentration in our layers should be considered to be higher than that necessary for Er trapping. The O and C concentrations in the layer correlate with the value of a residual-gas pressure in the chamber (Fig. 2) and exceed the typical concentrations of O and C in a melt-grown silicon. We assume that the O and C sources in our layers are represented by oxygen and lightweight hydrocarbons from a residual gas in the operating chamber. According to data of other experiments, the O and C concentrations in the layers were not changed with a layer-growth temperature varying from 600 to 900°C and with the replacement of the Si:Er source for the Si:P one (0.3 Ω cm) containing no erbium. The mechanism of O and C adsorption by the Si layer surface is apparently chemical and is not related to the Er adsorption.

The boron concentration in the layer (Fig. 2) gradually decreases from 2×10^{20} cm^{-3} in the substrate to a background value of $\sim 5 \times 10^{16}$ cm^{-3} at a depth of 200 nm. The cause of this is the phenomenon inverse to the accumulation; that is, a gradual incorporation of boron accumulated at the substrate surface in the course of its preepitaxy annealing (at 1250°C for 20 min) into the layer bulk. Our investigations show that the thickness of the transition region with boron at the p^+ substrate can be considerably decreased. To verify this under somewhat different conditions, we grew the n-type layer with a concentration of $\sim 3 \times 10^{17}$ cm^{-3} and the n-type δ layer in its midsection on a heavily boron-doped silicon substrate. The electrochemical CV measurements for this layer showed that the thickness of the region between the p^+ substrate and the δ layer (0.1 μm) coincided with that calculated from the rate and time of its growth; i.e., virtually no push-out of boron was observed. The existence of a charge-carrier concentration of 1.5×10^{16} cm^{-3} in the n layer of the structure (Fig. 2) or a charge-carrier concentration in the range of 10^{15}–10^{16} cm^{-3} in other Si:Er layers can be considered as a result of compensation of the P and B impurities, whose traces are actually present in our layers according to the SIMS data. The sources of these impurities are the Si:Er sources themselves.

In [5], the SIMS profiles are reported for the Er, P, O, and B impurities in the p^+–n–n^+ structure grown by the MBE. This structure is similar to ours (Fig. 2); however, the width of the junctions ($d_n \simeq 0.1$ μm) for the P, Er, B, and O impurities is markedly larger in [5] than in our case, while the phosphorus-doping level of the n^+ layer is by an order of magnitude lower. A probable cause of this fact is the accumulation (segregation) of impurities at the growth surface. In [7], the same authors investigated the possibility of obtaining thin heavily phosphorus-doped Si layers by the MBE. Similar to us [12, 15, 16], they used the sublimational Si:P source (the authors of [7], published in 1995, thought erroneously that they pioneered the use of these sources). Other growth conditions were different from ours [12, 15, 16]; for this reason, the authors of [7] succeeded in obtaining a thin Si:P layer ≃0.1 μm thick with $n = 2 \times 10^{18}$ cm^{-3} only at a very low temperature of 310–350°C. Our Si:(P, As, Sb) layers of the same thickness were grown with concentrations as high as $\simeq 2 \times 10^{20}$ cm^{-3} at $T_g = 500$°C.

δ-DOPED LAYERS

The electrochemical CV profiles for our silicon δ layers doped in the sublimational MBE process by P, Sb, and Ga are reported in [12, 17]. We also obtained similar profiles for δ layers with As, B, and Al. All these profiles differ only slightly from the profiles for the Si(100) δ layers grown by the solid-phase recrystallization or by the low-temperature MBE (150–270°C) [8]; however, our δ layers have the Hall mobility of charge carriers twice as high for the same surface densities (10^{13}–10^{14} cm^{-2}). Moreover, contrary to [8], our layers can be grown with various impurities and on a Si substrate of virtually arbitrary crystallographic orientation. Under a selective etching of our thick periodic structures with the δ layers on Si(100), etch pits are often not observed at all. This means that the δ-layer defects, if they exist, do not penetrate into the adjoining regions. A disadvantage of the electrochemical CV profiling of the δ layers is the impossibility of determining the maximum doping level. Therefore, the distribution of charge carriers in the δ-region of the layer was measured by the Hall method and the layer-by-layer etching with a step of 0.8 nm (Fig. 3). To do this, the δ layer was grown for 5 s within the n layer that had a concentration of $\simeq 10^{17}$ cm^{-3} and was deposited on a p-type high-resistivity Si(100) substrate. The measured surface conductivity σ_s, the Hall coefficient R_{Hs}, and also the surface

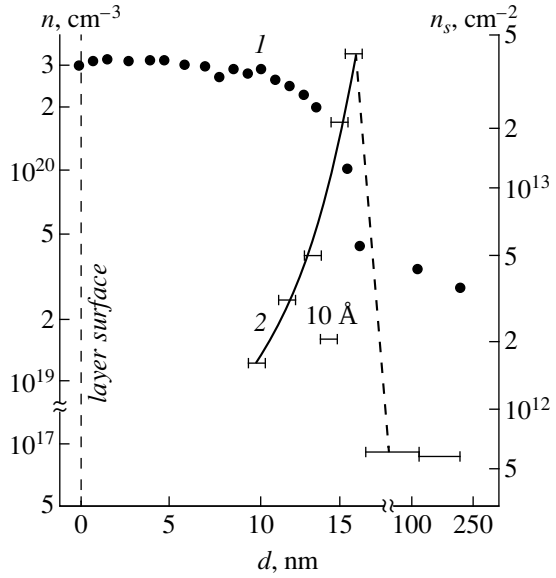

Fig. 3. Profiles of (*1*) surface and (*2*) bulk concentrations of electrons in the Si structure with the δ layer. The impurity is P.

concentration n_s remained virtually unchanged until the δ-layer region was etched off. In this case, σ_s and n_s changed abruptly (Fig. 3), and, then, their variation became weaker, because we now etched off only the region with a concentration of 10^{17} cm^{-3}. It can be seen from Fig. 3 that the δ-layer concentration is as high as 3.5×10^{20} cm^{-3}. The concentration gradient $\Delta N/d_n$ from the surface side amounted to 1.3×10^{27} at/cm^4 in the range from 3.5×10^{19} to 3.5×10^{20} cm^{-3}. For comparison, the gradient at the n–n^+ junction [5] was 10^{24} at/cm^4.

We failed to measure the carrier-concentration profile in the δ layer (Fig. 3) from the substrate side. It is too abrupt for the etch step of 0.8 nm. Actually, even if impurity accumulation occurs, the phosphorus concentration at the Si-layer surface and, consequently, in its bulk can increase only during 5s. After that, the flux was switched off, and the P concentration on the surface and in the bulk only decreased. Therefore, the width of the n–n^+ junction in the δ layer from the substrate side cannot exceed 1.4 nm (the dashed line in Fig. 3), which corresponds to the δ-layer technological thickness d_t equal to the product of the growth rate and the time of existence of the P flux. Generally speaking, the width of both junctions in our δ layer must be identical, like their growth conditions. We observed precisely this [12, 17], as did other investigators [8], in the δ-layer profiling by the electrochemical CV method and by the SIMS method. The value of d_t can be considered as a good estimate for not only the width of the n–n^+ junction but also for the δ-layer thickness, whose values must be independent of the impurity type and of its ability to segregate (of the growth conditions). Another issue is what maximum concentration n_{max} can

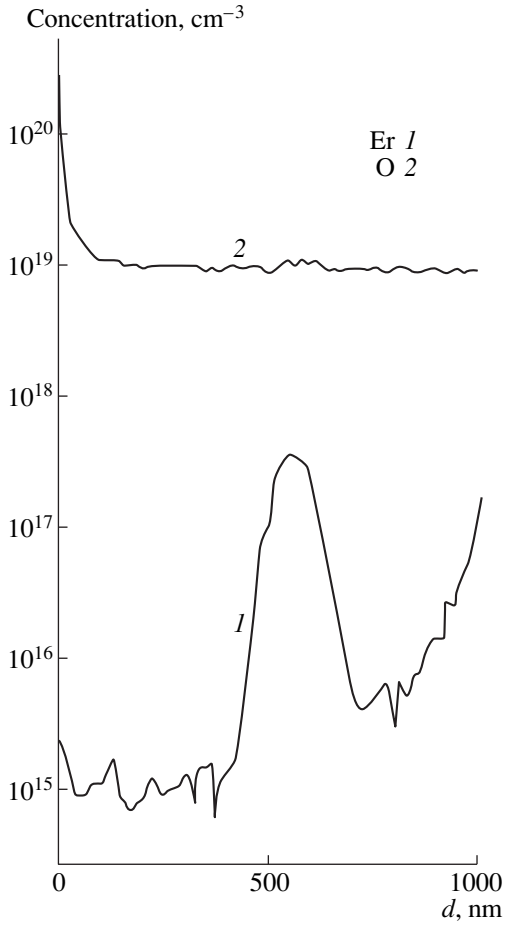

Fig. 4. SIMS profiles of (*1*) Er-doped and (*2*) O-doped Si structures with the δ layer.

be attained in the δ layer. A difference of n_{max} in the δ layer from the concentration expected according to the impurity flux at the growing-layer surface or from the concentration in thick layers represents the third attribute of the presence of impurity accumulation. In the δ layer under consideration, $n_{max} = 3.5 \times 10^{20}$ cm^{-3} somewhat exceeds the concentration in thick n^+ layers [16]. Therefore, the P accumulation in the case of growing the δ layer can be considered as being virtually absent, while the n–n^+ junction in the δ layer is extremely abrupt with a gradient of 2.5×10^{27} at/cm^4. From the above analysis it follows that the transition concentration regions for P and also for O, C, and Er in our p^+–n–n^+ structures are thinner than 30 nm measured by SIMS (Fig. 2).

In Fig. 4, we present the SIMS profiles for erbium in the δ layer grown at 500°C on Si(100). Owing to the limitations of the SIMS method, the junctions in the δ layer are equally wide in Fig. 4 as the junction for Er in Fig. 2. The analysis of the abruptness of the junction in the Er δ layer is the same as that carried out above for the P δ layer. This analysis is true for arbitrary impurity; i.e., the width of the Er δ layer is ≅2 nm (technological

thickness). A maximum Er surface density N_s in the δ layer can be estimated by integrating the profile (Fig. 4) as $N_s = 3.4 \times 10^{12}$ cm^{-2}. Taking into account the technological thickness, we found that the Er concentration in the δ layer is equal to 1.7×10^{19} cm^{-3}. This value is even somewhat higher than the Er concentration of $(3–5) \times 10^{18}$ cm^{-3} in our thick Si:Er layer grown at temperatures of 400–600°C. Therefore, the Er accumulation at the surface can be considered as virtually absent under growth conditions in our experiments.

CONCLUSION

Our investigations showed that the method of sublimational MBE has a number of undeniable advantages. A major advantage is the opportunity to precisely control the doping profiles. The concentrations of an impurity of Groups III and V can be varied from 10^{13} to 3.5×10^{20} cm^{-3}, with the thickness of uniformly doped regions ranging from ~1 nm to ~10 μm. The impurity-concentration gradient $\Delta N/d_n$ in the concentration profiles and δ-doped regions can be extremely large and can reach 2.5×10^{27} at/cm^4.

The erbium concentration in the layers we grew ($\leq 5 \times 10^{18}$ cm^{-3}) was one to two orders of magnitude less than the Er concentration in the implanted and MBE layers, with the PL intensity in the sublimational MBE layers being at least an order of magnitude higher than that in the implanted and MBE Si:Er/Si layers. The PL intensity in the sublimational-MBE layers varies only slightly with the concentration of electrically active impurities. The structure of the PL spectrum differs from that of the Er-containing centers in the case of other doping methods [27]. It is possible that, in our layers, the Er PL center is surrounded by various atoms of gases present in the operating volume. The positions of Er atoms in the crystal-lattice matrix are apparently also different. The analysis of the Rutherford-backscattering-spectroscopy data [26] and the PL spectrum [27] suggests that Er atoms in the crystal lattice of our layers are located at substitutional sites.

The method makes it possible to vary the thickness of the erbium-doped region in a wide range, the charge-carrier concentration in this region (from ~10^{15} to ~3.5×10^{20} cm^{-3}), and the conductivity type, as well as to use selective doping, in particular, erbium δ doping. All this creates new possibilities for optimizing the parameters of PL and electroluminescence in the Si:Er/Si structures. It is also important to note that the sublimational MBE technology is inexpensive. Its cost can be comparable with that of the technology of vacuum deposition of metallic contacts.

ACKNOWLEDGMENTS

The SIMS measurements were carried out in the Ioffe Physicotechnical Institute of the RAS in St. Petersburg. We thank the staff members of this institute M.S. Bresler and I.N. Yassievich for their collaboration. We also thank B.A. Andreev, A.Yu. Andreev, Z.F. Krasil'nik, O.A. Kuznetsov, M.V. Stepichova, E.A. Uskova, V.B. Shmagin, and L.T. Shchipkova for help in this work. This work was supported by the Russian Foundation for Basic Research, project nos. 98-02-16619 and 99-03-32757, and by the Ministry of Scientific and Technological Policy under the program "Fundamental Spectroscopy," project no. 08.02.043.

We especially thank the director of the AO "Kopernik" M.V. Kuznetsov for consistent financial and moral support.

REFERENCES

1. S. Coffa, G. Franzo, F. Priolo, *et al.*, Appl. Phys. Lett. **73**, 93 (1998).
2. L. Palmetshofer, Yu. Suprun-Belevich, and M. Stepikhova, Nucl. Instrum. Methods Phys. Res., Sect. B **127–128**, 479 (1997).
3. J. Michel, J. L. Benton, R. F. Ferrante, *et al.*, J. Appl. Phys. **70**, 2672 (1991).
4. V. V. Emtsev, V. V. Emtsev, Jr., D. Ts. Poloskin, *et al.*, Fiz. Tekh. Poluprovodn. (St. Petersburg) **33**, 649 (1999) [Semicond. **33**, 603 (1999)].
5. Y. Stimmer, A. Reittinger, J.F. Nützel, *et al.*, Appl. Phys. Lett. **68**, 3290 (1996).
6. K. Serna, Jung H. Shin, M. Lohmeier, *et al.*, J. Appl. Phys. **79**, 2658 (1996).
7. J. F. Nützel and G. Abstreiter, J. Appl. Phys. **78**, 937 (1995).
8. H.-J. Gossman and E.F. Schubert, CRC Crit. Rev. Solid State Mater. Sci. **18**, 1 (1993).
9. V. P. Kuznetsov, Extended Abstract of Candidate's Dissertation (Gorki, 1973).
10. V. P. Kuznetsov, V. A. Tolomasov, and A. V. Tumanova, Kristallografiya **24**, 1028 (1979) [Sov. Phys. Crystallogr. **24**, 588 (1979)].
11. V. P. Kuznetsov, R. A. Rubtsova, T. M. Isaeva, *et al.*, Izv. Vyssh. Uchebn. Zaved., Fiz., No. 7, 3 (1983).
12. V. P. Kuznetsov, A. Yu. Andreev, and N. A. Alyabina, Élektron. Promyshlennost' **9**, 57 (1990).
13. V. P. Kuznetsov, R. A. Rubtsova, A. Yu. Andreev, *et al.*, Kristallografiya **31**, 1180 (1986) [Sov. Phys. Crystallogr. **31**, 697 (1986)].
14. A. Yu. Andreev, V. P. Kuznetsov, and V. A. Tolomasov, Zh. Tekh. Fiz. **57**, 1204 (1987) [Sov. Phys. Tech. Phys. **32**, 710 (1987)].
15. V. P. Kuznetsov, V. V. Postnikov, and V. A. Tolomasov, Kristallografiya **15**, 391 (1970) [Sov. Phys. Crystallogr. **15**, 335 (1970)].
16. V. P. Kuznetsov, A. Yu. Andreev, and O. A. Kuznetsov, Phys. Status Solidi A **127**, 371 (1991).
17. V. P. Kuznetsov, A. Yu. Andreev, and N. A. Aleshina, in *Proceedings of 8th All-Union Conference on Growth of Crystals, Kharkov, 1992*, p. 81.
18. V. P. Kuznetsov, V. V. Postnikov, T. D. Komrakova, *et al.*, Kristallografiya **20**, 626 (1975) [Sov. Phys. Crystallogr. **20**, 382 (1975)].

19. A. Yu. Adreev, N. V. Gudkova, V. P. Kuznetsov, *et al.*, Izv. Akad. Nauk SSSR, Neorg. Mater. **24**, 1423 (1988).

20. V. P. Kuznetsov, USSR Inventor's Certificate No. 343324 (2 Feb. 1970), Byull. Izobret., No. 38 (1989).

21. V. P. Kuznetsov, R. A. Rubtsova, T. N. Sergievskaya, *et al.*, Kristallografiya **16**, 432 (1971) [Sov. Phys. Crystallogr. **16**, 357 (1971)].

22. V. P. Kuznetsov, R. A. Rubtsova, A. Yu. Andreev, *et al.*, Kristallografiya **31**, 135 (1986) [Sov. Phys. Crystallogr. **31**, 76 (1986)].

23. V. P. Kuznetsov and V. V. Postnikov, Kristallografiya **19**, 346 (1974) [Sov. Phys. Crystallogr. **19**, 211 (1974)].

24. V. P. Kuznetsov and V. A. Tolomasov, Kristallografiya **26**, 647 (1981) [Sov. Phys. Crystallogr. **26**, 369 (1981)].

25. V. P. Kuznetsov, A. Yu. Andreev, V. A. Tolomasov, *et al.*, Kristallografiya **33**, 1227 (1988) [Sov. Phys. Crystallogr. **33**, 727 (1988)].

26. A. Yu. Andreev, B. A. Andreev, M. N. Drozdov, *et al.*, Izv. Ross. Akad. Nauk, Ser. Fiz. **63**, 392 (1999).

27. B. A. Andreev, A. Yu. Andreev, D. M. Gaponova, *et al.*, in *Proccedings of the Conference on Nanophotonics, Nizhni Novgorod, 1999*, p. 81.

Translated by V. Bukhanov

Semiconductors, Vol. 34, No. 5, 2000, pp. 510–513. Translated from Fizika i Tekhnika Poluprovodnikov, Vol. 34, No. 5, 2000, pp. 526–529.

ATOMIC STRUCTURE AND NONELECTRONIC PROPERTIES OF SEMICONDUCTORS

The Influence of Electrically Inactive Impurities on the Formation of Donor Centers in Silicon Layers Implanted with Erbium

O. V. Aleksandrov*, A. O. Zakhar'in*, N. A. Sobolev, and Yu. A. Nikolaev****

** State Electrotechnical University, St. Petersburg, 197376 Russia*

*** Ioffe Physicotechnical Institute, Russian Academy of Sciences, Politekhnicheskaya ul. 26, St. Petersburg, 194021 Russia*

Submitted November 18, 1999; accepted for publication November 22, 1999

Abstract—The influence of the additional implantation of electrically inactive impurities of carbon, oxygen, nitrogen, and fluorine on the formation of donor centers in silicon implanted with erbium was studied. It is shown that additional implantation brings about an increase in the concentration of donor centers formed during anneals. Variation in the concentration of donor centers depends on the type of introduced impurity. The results indicate that electrically inactive impurities are involved in the formation of donor centers. © *2000 MAIK "Nauka/Interperiodica".*

INTRODUCTION

If silicon is doped with an Er rare-earth element by the method of double implantation, electrically and optically active centers are formed [1–4]. Optically active centers are responsible for photoluminescence and electroluminescence at a wavelength of 1.54 μm corresponding to a minimum in the losses and dispersion in optical fiber links, which makes a Si:Er system promising for silicon optoelectronics. It has been found that the luminescence intensity correlates with the concentration of Er-containing donor centers formed in Er-implanted silicon layers during thermal annealing [5, 6]. In connection with this, it is of great interest to study a coimplantation of ions of rare-earth elements and those of electrically inactive impurities (C, O, N, and F), which causes the photoluminescence intensity to increase [6–9]. It was found that implantation of O impurity brought about an increase in the donor-center concentration (N_d) in Si layers implanted preliminarily with Er, Ho, Dy, and Yb rare-earth elements [5, 10–12], whereas implantation of carbon ions led to an increase in N_d in Si layers implanted preliminarily with Er [5].

In this work, we studied the influence of annealing on the electrical properties of silicon layers implanted with Er ions and electrically inactive impurities of C, O, N, and F intensifying the photoluminescence.

EXPERIMENTAL

As the substrates, we used the *p*-Si wafers with a resistivity of ~40 Ω cm. Er^+ ions with an energy of 1 MeV and a dose of $Q_{Er} = 1 \times 10^{13}$ cm^{-2} were implanted in a K2MV High Voltage Engineering Europe heavy-ion accelerator. Coimplantation of O, C, N, and F ions was carried out with a dose of $Q = 1 \times 10^{14}$ cm^{-2} and energies in the range of 135–180 keV. The energies were chosen so that the projected ion ranges of coimplanted impurities and erbium coincided ($R_p \approx 0.32$ μm). The samples were annealed isochronally for 30 min in the temperature range of $T = 700$–900°C in a chlorine-containing ambient (1 mol % of CCl_4 in O_2). The sheet resistance R_s was measured by the four-point probe method. The depth profiles of charge-carrier concentration $n(x)$ were determined from the measurements of the capacitance–voltage characteristics of the Hg–Si Schottky barrier using a mercury probe. The effective activation coefficient for electrically active centers was calculated from the relationship $k = (e\mu_e R_s)^{-1}/Q_{Er}$, where e is the elementary charge and μ_e is the electron mobility ($\mu_e = 1350$ cm^2 V^{-1} s^{-1}).

RESULTS

Annealing of silicon implanted first with Er ions and then with ions of electrically inactive N, F, C, and O impurities gives rise to an *n*-type layer, i.e., to the formation of donor centers. Annealing at $T = 700$°C results in an increase in the concentration of the formed donor centers for all the impurities studied (Fig. 1). The concentration increases in the following order: Er ⟶ F ⟶ N ⟶ C ⟶ O; here, Er signifies the implantation of Er alone, and the succeeding element's designations signify the impurity implanted in combination with erbium. The largest value of the effective activation coefficient ($k = 0.215$) is observed in Si:(Er, O) (curve *3*). As the annealing temperature is increased to $T = 800$°C, the effective activation coefficient remains virtually unchanged in Si:(Er, O), Si:(Er, N), and Si:(Er, C) (curves *3*–*5*). In the samples Si:Er (and, especially, Si:(Er, F)), a decrease in the concentration of

1063-7826/00/3405-0510$20.00

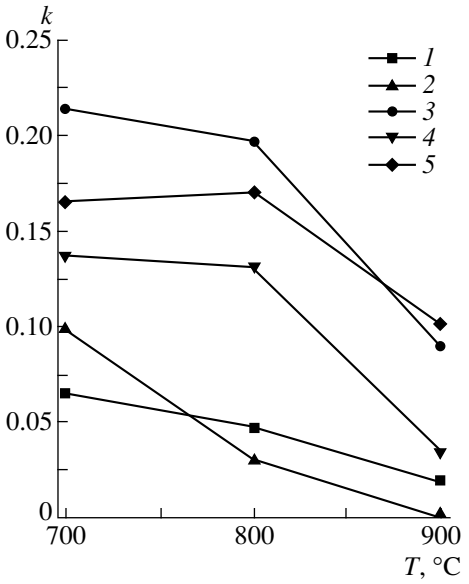

Fig. 1. Dependences of the activation coefficient on the annealing temperature in the case of implantations of (*1*) erbium, (*2*) erbium and fluorine, (*3*) erbium and oxygen, (*4*) erbium and nitrogen, and (*5*) erbium and carbon.

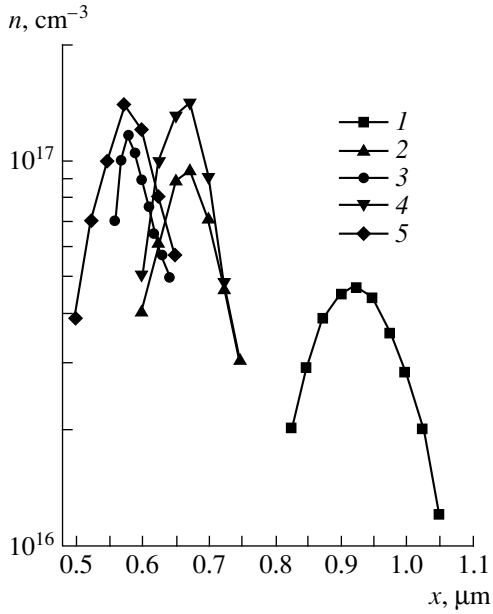

Fig. 2. Concentration profiles of donor centers in (*1*) Si:Er, (*2*) Si:(Er, F), (*3*) Si:(Er, O), (*4*) Si:(Er, N), and (*5*) Si:(Er, C) after implantation and annealing for 30 min at $T = 700$°C.

introduced donor centers is observed (curves *1*, *2*). An increase in the annealing temperature to $T = 900$°C results in a decrease in the effective activation coefficient in the case of all implanted impurities. In the Si:(Er, F) samples, the donor centers are not formed at all ($k \approx 0$).

The depth profiles of the donor-center concentration are represented by the curves with peaks (Fig. 2). Implantation of all additional impurities results in an increase in the peak concentration of the donor centers n_m (Fig. 3). Furthermore, the positions of the peaks x_m in the donor-center concentration distributions shift towards the surface (Fig. 4), i.e., towards the peaks in the concentrations of implanted impurities ($R_p \approx 0.32$ μm). Such a shift in the concentration profiles of donor centers in the case of combined implantation of Er and oxygen was first reported in [10].

An increase in the annealing temperature leads to a decrease in the values of n_m in all the samples studied. The most rapid decrease in the values of n_m is observed in Si:(Er, F) (Fig. 3, curve *2*) and in Si:Er (Fig. 3, curve *1*), which correlates well with the behavior of $k(T)$ in these samples (Fig. 1).

Figure 4 shows the dependences of positions of peaks in the profiles of donor-center concentrations x_m on the annealing temperature. As the annealing temperature increases from 700 to 800°C, a drastic increase in x_m is observed in Si:(Er, F) alone (curve *2*). An increase in the annealing temperature to 900°C affects only slightly the positions of peaks in the concentration profiles of donor centers in Si:(Er, O) and Si:(Er, C) (curves *3*, *5*) and, in the case of Si:Er and Si:(Er, N) (curves *1*, *4*), results in a significant increase in x_m.

DISCUSSION

Thus, as a result of the studies, we revealed the following trends observed for all coimplanted electrically inactive impurities: first, an increase in k and n_m and a decrease in x_m in the case of coimplantation of electrically inactive impurities as compared to implantation of Er alone, and, second, a decrease in k and n_m and an increase in x_m as the annealing temperature increases, with the rate of these changes being different for dissimilar impurities.

It was previously concluded [3] that native point defects produced during annealing of implantation-induced defects were involved (along with Er atoms) in the formation of donor centers in the ion-implanted silicon layers. A decrease in k and n_m and also a shift of x_m farther from the surface was explained by the fact that an increasingly larger fraction of excess native point defects migrates to the surface as the annealing temperature is raised to higher than 700°C. In a quantitative model developed in [10], it was assumed that the donor centers are complexes of erbium atoms with self-interstitial atoms. Apparently, the native point defects formed in the course of annealing are involved in the formation of donor centers in the case of coimplantation of Er and electrically inactive C, O, N, and F impurities as well. An increase in k and n_m (Figs. 1, 3) is accounted for by the appearance of additional implantation-induced defects during coimplantation and, cor-

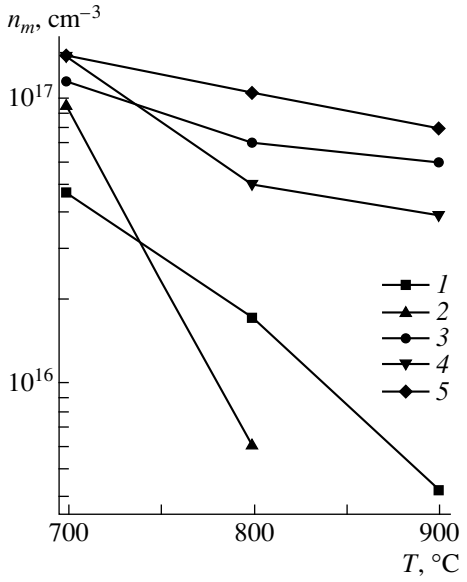

Fig. 3. Dependences of the peak concentration of donor centers on the annealing temperature in (*1*) Si:Er, (*2*) Si:(Er, F), (*3*) Si:(Er, O), (*4*) Si:(Er, N), and (*5*) Si:(Er, C).

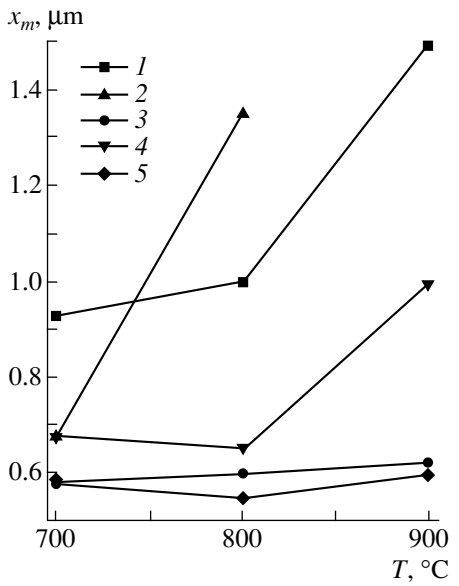

Fig. 4. Position of the peak in the concentration profile of donor centers as a function of the annealing temperature in (*1*) Si:Er, (*2*) Si:(Er, F), (*3*) Si:(Er, O), (*4*) Si:(Er, N), and (*5*) Si:(Er, C).

respondingly, additional native point defects during subsequent annealings. Such an interpretation is also supported by a shift of peaks in the spatial distribution of donor centers to the surface (Fig. 2). Native point defects formed as a result of the decomposition of implantation-introduced defects are involved in the formation of donor centers in the case of coimplantation of electrically inactive impurities as well.

At the same time, there are marked differences in the characteristics of donor centers in relation to the type of coimplanted impurity, with these differences being related to special features of the behavior of these impurities in silicon. A rapid decrease in k and n_m with an increase in the annealing temperature in the case of coimplantation of F ions may be explained by the tendency of F towards escape from the silicon lattice by back diffusion as a result of low solubility. Thus, according to [13, 14], only ~80% of implanted fluorine is retained in silicon after annealing at T = 800°C, and fluorine is not detected in the ion-implanted layer at all after annealing at T = 1000°C. Nitrogen impurity diffuses from the ion-implanted layer to the bulk at T > 800°C [15], which accounts for an appreciable increase in x_m for T = 900°C (Fig. 4, curve *4*). In the range of annealing temperatures used, C and O impurities become redistributed within the ion-implanted layer and do not leave this layer [16]. This accounts for the weak influence of the annealing temperature on the position of the peak in the spatial distribution of donor centers. Oxygen impurity tends to form complexes both with Si atoms (in the form of SiO_x thermodonors) and with Er atoms (Er–O) [17]. The results obtained in [18] also support the concept of the formation of two types of donor centers (erbium- and oxygen-containing). A decrease in k after annealing at T > 700°C is apparently indicative of the low thermal stability of thermodonors and (or) Er–O complexes. The result worth noting is the fact that, after annealing at $T \geq 800$°C, k and n_m decrease to values smaller than those corresponding to implantation of Er alone in the case of coimplantation of the F impurity (curves *2* in Figs. 1, 3). This result can be explained by assuming that the escape of F atoms from the Si lattice is conducive to an increase in the concentration of vacancies and, correspondingly, to a decrease in the concentration of self-interstitial silicon atoms incorporated (according to [3, 10]) into the donor centers.

CONCLUSION

Thus, we showed that coimplantation of electrically inactive C, N, and F, as well as coimplantation of an O impurity, results in an increase in the effective activation coefficient, maximization of the donor-center concentration, and a shift of the peak in the donor-center spatial distribution to the surface as compared to the implantation of Er alone. As the annealing temperature increases, the effective activation coefficient and the peak concentration of donor centers decrease, and the peak in the donor-center concentration shifts to the bulk of the sample for all coimplanted impurities, with the rate of these changes being different for dissimilar impurities. The annealing-induced behavior of the donor-center concentration in the Si:Er layers with coimplanted electrically inactive impurities of C, O, N,

and F correlates with the known individual behavior of these impurities. The results obtained indicate that not only Er and native point defects but also the implanted electrically inactive impurities are involved in the formation of donor centers.

ACKNOWLEDGMENTS

We thank E.O. Parshin and A.V. Shestakov for performing the implantations.

This work was supported by the Russian Foundation for Basic Research, project no. 99-02-17750.

REFERENCES

1. H. Ennen, J. Schneider, G. Pomrenke, and A. Axmann, Appl. Phys. Lett. **43**, 943 (1983).
2. N. A. Sobolev, Fiz. Tekh. Poluprovodn. (St. Petersburg) **29**, 1153 (1995) [Semicond. **29**, 595 (1995)].
3. O. V. Aleksandrov, N. A. Sobolev, E. I. Shek, *et al.*, Fiz. Tekh. Poluprovodn. (St. Petersburg) **30**, 876 (1996) [Semicond. **30**, 468 (1996)].
4. J. Michel, L. V. C. Assali, M. T. Morse, *et al.*, *Semiconductors and Semimetals* (Academic, San Diego, 1998), Vol. 49, p. 111.
5. F. Priolo, S. Coffa, G. Franzo, *et al.*, J. Appl. Phys. **74**, 4936 (1993).
6. J. Michel, J. Palm, X. Duan, *et al.*, Mater. Sci. Forum **258–263**, 1485 (1997).
7. P. N. Favennec, H. L. Haridon, D. Moutonnet, *et al.*, Jpn. J. Appl. Phys. **29**, L524 (1990).
8. J. Michel, J. L. Benton, R. F. Ferrante, *et al.*, J. Appl. Phys. **70**, 2672 (1991).
9. S. Libertino, S. Coffa, G. Franzo, *et al.*, J. Appl. Phys. **78**, 3867 (1995).
10. N. A. Sobolev, O. V. Alexandrov, and E. I. Shek, Mater. Res. Soc. Symp. Proc. **442**, 237 (1997).
11. O. V. Aleksandrov, A. O. Zakhar'in, N. A. Sobolev, *et al.*, Fiz. Tekh. Poluprovodn. (St. Petersburg) **32**, 1029 (1998) [Semicond. **32**, 921 (1998)].
12. N. A. Sobolev, A. M. Emel'yanov, R. N. Kyutt, *et al.*, in *Proceedings of Conference on "Nanophotonics", Nizhni Novgorod, 1999*, p. 71.
13. Byoung gon Yu, N. Konuma, and Eichi Arai, J. Appl. Phys. **70**, 2408 (1991).
14. J. Michel, J. Palm, F. Gan, *et al.*, Mater. Sci. Forum **196–201**, 585 (1995).
15. R. S. Hockett, Appl. Phys. Lett. **54**, 1793 (1989).
16. H. Koyama, J. Appl. Phys. **51**, 3202 (1980).
17. V. F. Masterov, F. S. Nasredinov, P. P. Seregin, *et al.*, Fiz. Tekh. Poluprovodn. (St. Petersburg) **32**, 708 (1998) [Semicond. **32**, 636 (1998)].
18. V. V. Emtsev, V. V. Emtsev, Jr., D. S. Poloskin, *et al.*, J. Lumin. **80**, 374 (1999).

Translated by A. Spitsyn

Semiconductors, Vol. 34, No. 5, 2000, pp. 514–516. Translated from Fizika i Tekhnika Poluprovodnikov, Vol. 34, No. 5, 2000, pp. 530–532.

ELECTRONIC AND OPTICAL PROPERTIES OF SEMICONDUCTORS

Carbon-Stimulated Increase in the Concentration of Gallium Divacancies in Semi-Insulating Undoped GaAs Crystals

K. D. Glinchuk*, N. M. Litovchenko, A. V. Prokhorovich, and O. N. Stril'chuk

Institute of Semiconductor Physics, National Academy of Sciences of Ukraine, Kiev, 252028 Ukraine

** e-mail: glinchuk@class.semicond.kiev.ua*

Submitted October 19, 1999; accepted for publication October 28, 1999

Abstract—It is shown that an increase in carbon content in semi-insulating undoped GaAs crystals leads to a substantial rise of the concentration of gallium divacancies in these crystals. This effect seems to be related to the process of carbon atoms occupying the arsenic vacancies involved in the As-divacancy–Ga-divacancy complex. © *2000 MAIK "Nauka/Interperiodica".*

1. INTRODUCTION

It is known that, in semi-insulating undoped GaAs (hereafter referred as SIUN GaAs) crystals, the luminescence band is observed at 4.2 K with a peak of emission at 1.5099 eV [1]. This band is caused by the radiative annihilation of *X* excitons bound by *d* defects (gallium divacancies $(V_{Ga})_2$) [1].[1] In this work, we are going to show that the concentration of gallium divacancies involved in the above (*d*, *X*) centers substantially increases with the rise of carbon content in SIUN GaAs crystals and consider a possible model explaining the observed phenomenon.[2]

2. EXPERIMENTAL

The experiments were performed with the SIUN GaAs crystals with the known concentration of carbon atoms $N_C = 2 \times 10^{15}$–3×10^{16} cm^{-3}. The carbon concentration was determined with an accuracy of ±30% from the spectra of low-temperature photoluminescence (one can find details of the method, for example, in [7]). The crystals were grown by the Czochralski method in argon atmosphere with a pressure of 3 atm using a B_2O_3 coating and were almost stoichiometric. The resistivity ρ of the crystals (ρ ≈ 10^8 Ω cm at 300 K and ρ $\longrightarrow \infty$ at 4.2–200 K) was determined by the thermal ionization of deep donors *EL*2 partially compensated by carbon atoms (electrical properties of the crystals were discussed in detail in [8]).

The luminescence was excited by a strongly absorbed radiation of a He–Ne laser under the following conditions: the energy of quanta was 1.96 eV, the absorption coefficient of light was $k = 4 \times 10^4$ cm^{-1}, the effective penetration depth of radiation was $1/k$ = 0.25 μm, and the intensity of illumination was L = 10^{18}–10^{21} photon/(cm^2 s). Prior to the measurements of luminescence, the surface of the crystals was treated in a mixture of $3H_2SO_4 : 1H_2O_2 : 1H_2O$. The concentrations of the excess electrons δ*n* and holes δ*p* generated by a laser were determined by the rate of volume recombination of nonequilibrium charge carriers at the deep centers. These concentrations differed only slightly (no more than by ±20%) in the crystals with various carbon content; i.e., $\delta n, \delta p \neq \varphi(N_C)$ [8].

The exciton-luminescence spectra of the SIUN GaAs crystals with various carbon content were studied at 4.2 K. The ratios between intensities of various bands in the spectra were virtually independent of the illumination intensity *L*. An MDR-23 monochromator with a resolution no lower than 0.2 meV was used to obtain the spectra. The signal was detected using a cooled FEU-62 photomultiplier. The spectra included the commonly known bands of the luminescence, in particular, the band related to the annihilation of free excitons with a peak at $h\nu_m$ = 1.5156 eV. The intensity I_{FE} (the accuracy of the determination of I_{FE} was ±25%) can be obviously estimated as $I_{FE} \sim \delta n \delta p$ [9]. In addition to conventional bands, there was also observed an unconventional luminescence band (see Fig. 1) peaked at $h\nu_m$ = 1.5099 eV and caused, as was mentioned above, by the radiative annihilation of excitons bound by gallium

[1] The gallium divacancies introduce deep acceptor centers with the ionization energy of ε_a = 68 eV [1].

[2] Carbon atoms occupy preferentially the sites in the arsenic sublattice of gallium arsenide (the concentration of carbon atoms at the sites of gallium sublattice and at interstitial positions is extremely low) [2–6]. The substitutional carbon atoms are the shallow acceptors with an ionization energy of ε_a = 26 meV [7]. Their diffusion occurs over the arsenic vacancies [3].

1063-7826/00/3405-0514$20.00 © 2000 MAIK "Nauka/Interperiodica"

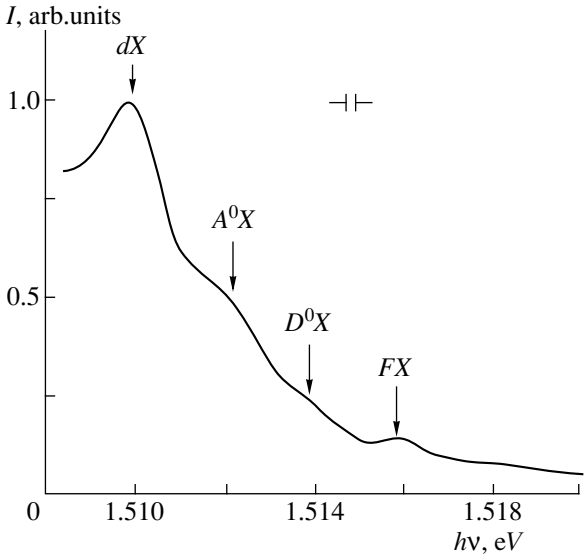

Fig. 1. Exciton luminescence spectra of the SIUN GaAs crystal with a carbon concentration of $N_C = 1.3 \times 10^{16}$ cm^{-3} at 4.2 K. Arrows show the emission bands resulting from the annihilation of free excitons (*FX*), excitons bound by gallium-divacancies (*dX*), shallow-acceptor excitons (A^0X), and shallow-donor excitons (D^0X) [1]. The spectrum is taken under the intensity of illumination $L = 10^{19}$ photon/(cm^2 s).

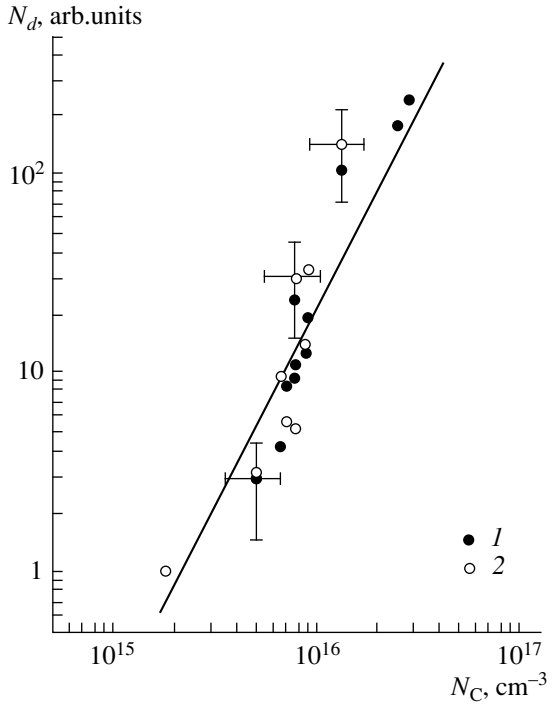

Fig. 2. The concentration of gallium divacancies as a function of the carbon atom concentration in the SIUN GaAs crystals; the relations (*1*) $N_d \sim I_{dX}$ and (*2*) $N_d \sim I_{dX}/I_{FE}$ were used. The straight line corresponds to the $N_d \sim N_C^2$ dependence; for convenience, the experimental error in determination of N_d and N_C is shown only for some crystals.

divacancies. The intensity I_{dX} of this band (determined with an accuracy of ±25%) can be estimated as $I_{dX} \sim N_d \delta n \delta p$ [9] (see Fig. 1).[3] The measurement of the intensity I_{dX} of this new luminescence band or the ratio I_{dX}/I_{FE} allows for the determination (with an accuracy of ±50%) of the concentration of gallium divacancies N_d in the crystals studied: $N_d \sim I_{dX}$, because $\delta n \delta p$ = const (see above) and $N_d \sim I_{dX}/I_{FE}$ (both methods of determination of N_d yielded almost the same results, see Fig. 2).

3. RESULTS AND DISCUSSION

In Fig. 2, the dependence of the concentration of gallium divacancies involved in (*d*, *X*) centers on the concentration of carbon atoms in the SIUN GaAs crystals is shown. It can be seen that an increase in carbon concentration results in an appreciable increase in the concentration of gallium divacancies. This increase is superlinear ($N_d \sim N_C^2$).

These data unquestionably show that carbon atoms are conducive to the formation of gallium divacancies. This cannot be related to the displacement of gallium atoms from their lattice sites due to the perturbing effect of carbon atoms. Indeed, the covalent radius of a carbon atom $R_C = 0.77 \times 10^{-18}$ cm is much smaller than the covalent radius of an arsenic atom $R_{As} = 1.20 \times 10^{-8}$ cm. Thus, the doping of gallium arsenide with carbon results in a relatively small displacement of gallium atoms (over the distance of 0.14×10^{-8}–0.38×10^{-8} cm) towards the neighboring carbon atoms that replace arsenic atoms [2, 4–6].

The most probable process which accounts for the carbon-stimulated increase in gallium divacancy concentration consists in the following. We assume that gallium arsenide crystals, along with isolated gallium and arsenic vacancies, can also contain various complexes, such as the complexes of vacancies of different elements $(V_{Ga}V_{As})_2$ [1]. Then, the successive occupation by the migrating carbon atoms of arsenic vacancies involved in the $(V_{Ga}V_{As})_2$ complexes will result in the appreciable generation of, first, vacancies and of, second, gallium divacancies $(V_{Ga})_2$ during the growth of the crystal. Obviously, the change in the concentration

[3] The given relation for the intensity I_{dX} is valid if (i) only a small number of free excitons become bound by gallium divacancies, and (ii) gallium divacancies are predominantly neutral, i.e., occupied by holes [9]. These conditions were strictly met in the experiment. In particular, for $T = 4.2$ K and $L = 10^{18}$–10^{21} photon/(cm^2 s), gallium divacancies were actually completely filled with holes, which unquestionably followed from the experiment, because the ratio I_{dX}/I_{FE} was found to be independent of L.

of gallium divacancies under the variation of carbon concentration obeys the law $N_d \sim N_C^2$.

To summarize the discussion of the experimental relationships $N_d = \varphi(N_C)$, we should emphasize the following. The aforementioned interaction of the As-substituting carbon atoms and $(V_{Ga}V_{As})_2$ complexes, which accounts for the carbon-stimulated increase in the concentration of gallium divacancies, results in the generation of Ga divacancies bound by As-substituting carbon atoms rather than by isolated Ga divacancies. It is very likely that the properties of the isolated and bound-to-carbon gallium divacancies differ only slightly from each other.

4. CONCLUSION

Carbon atoms stimulate the formation of gallium divacancies (an increase in carbon content results in an increase in the concentration of gallium divacancies according to the $N_d \sim N_C^2$ law) in SIUN GaAs crystals. This effect is determined by the occupation of arsenic vacancies involved in the complex $(V_{Ga}V_{As})_2$ by the carbon atoms. In order to verify this explanation of the experimentally observed dependence $N_d = \varphi(N_C)$, one needs to perform a theoretical calculation of the concentration of gallium divacancies generated due to the interaction of substitutional carbon atoms with vacancy complexes $(V_{Ga}V_{As})_2$ and to compare the calculated value of N_d with the experimentally obtained value of N_d.

REFERENCES

1. Chao Chen, V. A. Bykovskiĭ, and M. I. Tarasik, Fiz. Tekh. Poluprovodn. (St. Petersburg) **28**, 35 (1994) [Semicond. **28**, 19 (1994)].
2. L. M. Scolfaro, R. Pintanel, V. M. Gomes, *et al.*, Phys. Rev. B: Condens. Matter **34**, 7135 (1986).
3. B. T. Guningham, L. J. Guido, and J. E. Baker, Appl. Phys. Lett. **55**, 687 (1989).
4. I. Fujimoto, S. Nishine, and T. Yamada, Jpn. J. Appl. Phys. **31**, L296 (1992).
5. K. J. Chang and B. H. Cheong, Phys. Rev. B: Condens. Matter **49**, 17436 (1994).
6. T. M. Schmidt, P. M. Venezuela, M. J. Caldas, *et al.*, Appl. Phys. Lett. **66**, 2715 (1995).
7. K. D. Glinchuk, N. M. Litovchenko, O. N. Sril'chuk, *et al.*, in *Optoelectronics and Semiconductor Technology* (Naukova Dumka, Kiev, 1998), No. 33, p. 204.
8. K. D. Glinchuk, N. M. Litovchenko, O. N. Strilchuk, *et al.*, Phys. Status Solidi B **213**, 233 (1999).
9. T. Schmidt and K. Lischka, Phys. Rev. B: Condens. Matter **45**, 8989 (1992).

Translated by A. Zalesskiĭ

Semiconductors, Vol. 34, No. 5, 2000, pp. 517–520. Translated from Fizika i Tekhnika Poluprovodnikov, Vol. 34, No. 5, 2000, pp. 533–536.

ELECTRONIC AND OPTICAL PROPERTIES OF SEMICONDUCTORS

Effect of Diffusion Length and Surface Recombination on the Photopleochroism of Anisotropic Crystals

G. A. Medvedkin

Ioffe Physicotechnical Institute, Russian Academy of Sciences, Politekhnicheskaya ul. 26, St. Petersburg, 194021 Russia

Submitted October 13, 1999; accepted for publication November 22, 1999

Abstract—Formulas were derived and numerical analysis was carried out for the dependences of photopleochroism coefficient P_i of the homogeneous anisotropic crystal on the diffusion length L and surface recombination rate. The polarization photoconductivity was considered in the region of both weak and strong optical absorption. The spectral contour of photopleochroism was shown to follow the optical dichroism curve at weak absorption and deviated from it or even reversed in sign in the case of appreciable recombination of charge carriers at the crystal surface at strong absorption. The limiting cases of zero and high surface recombination rates were considered for the dependence of the photopleochroism coefficient on the diffusion length. The dependences were analyzed by using the typical parameters of II–IV–V_2 ternary diamond-like semiconductors. *© 2000 MAIK "Nauka/Interperiodica".*

1. INTRODUCTION

Anisotropic crystals with a high photosensitivity provide the basis for optical detectors of polarized radiation. These crystals are of interest both as polarization-optical and as photoelectric semiconductor objects, which have interrelated specific features. In the development of the devices of polarization optics and optoelectronics, the high polarization photosensitivity $\Pi_i = P_i S_i$ (P_i is the photopleochroism coefficient, and S_i is the current sensitivity), as well as the fundamental parameter, polarization quantum efficiency $Q_p = |\Delta n_\parallel - \Delta n_\perp|/N_{\text{ph}}$ (N_{ph} is the number of photons, and $\Delta n_{\parallel,\perp}$ is the photocarrier density), are of importance in the general case. Hereinafter, the subscripts $\parallel$ and $\perp$ indicate the respective polarization directions $\mathbf{E} \parallel \mathbf{c}$ and $\mathbf{E} \perp \mathbf{c}$, where $\mathbf{E}$ is the electric vector of the wave and $\mathbf{c}$ is the optical axis of the crystal. The electrical and photoelectrical properties of anisotropic semiconductor crystals are subject to strong effects of all characteristic electronic parameters of material. Among the latter, the diffusion length of minority carriers L, surface recombination rate s, and electron–hole pair lifetime τ are of prime importance. In this paper, the dependences of the photopleochroism coefficient on the parameters L and $s\tau$ are studied for ternary diamond-like semiconductors, which are analogous to III–V and II–VI compounds.

2. PHENOMENOLOGICAL APPROACH

Let us consider a photoeffect arising in anisotropic crystal oriented along optic axis $\mathbf{c}$ at normal incidence of radiation on the surface. The following three arrangements of contacts at the sample are possible in the general case for the observation of polarization photoconductivity (see Fig. 1): (i) contacts at the illuminated and unilluminated sides (bulk longitudinal photoconductivity); (ii) contacts at the end planes (bulk transverse photoconductivity); and (iii) contacts at the illuminated or unilluminated surface (surface transverse photoconductivity). For arrangement 1, the Dember effect [1] occurs at zero external bias when the nonuniform illumination and diffusion of nonequilibrium carriers give rise to the electric charge gradients, which are different for two polarizations. The difference of the Dember emf for $\mathbf{E} \parallel \mathbf{c}$ and $\mathbf{E} \perp \mathbf{c}$ in the case of monopolar conduction (or for the relationship between the electron and hole mobilities $\mu_n > \mu_p$) is expressed as [2]

$$\Delta U_D = \frac{kT}{e} \ln\left(\frac{n_2}{n_1}\right)_\parallel \left(\frac{n_1}{n_2}\right)_\perp, \qquad (1)$$

where n_1 and n_2 are the photocarrier densities in the illuminated and unilluminated regions. In arrangement 2, the transverse Dember emf can be observed when the sample is cut at an angle to the crystallographic axes and the tensors of the diffusion coefficients become important [3]. The arising photoelectric voltage is too small to be of practical use, including application in polarization optoelectronics. At nonvanishing external biases, the polarization photoconductivity can be observed in arrangements 1 and 3 for crystals of different thickness, while, in arrangement 2, it appears only for thin transparent crystals with a thickness $d < 1/\alpha_{\parallel,\perp}$ ($\alpha_{\parallel,\perp}$ are the absorption factors).

3. POLARIZATION PHOTOCONDUCTIVITY

Let us consider in more detail the bulk photoconductivity arising in the homogeneous oriented crystal at

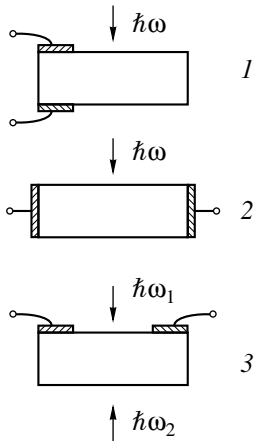

Fig. 1. The arrangement of contacts and the direction of propagation of the polarized light for the observation of polarization photoconductivity: (*1*) bulk longitudinal photoconductivity; (*2*) bulk transverse photoconductivity; and (*3*) surface transverse photoconductivity (the contacts are on the illuminated ($\hbar\omega_1$) or unilluminated ($\hbar\omega_2$) sides of the sample).

normal incidence of radiation onto the surface (arrangements 1 and 2). We assume that the condition for the linear recombination is met in the bulk of the crystal and that the surface recombination is absent ($s = 0$). If the absorption depth of light $1/\alpha_{\parallel,\perp}$ is smaller than the sample thickness d, equal densities of free nonequilibrium charge carriers are generated in the bulk of the semiconductor irrespective of the polarization of radiation. The different spatial distribution of these densities and the rate of carrier recombination do not produce the polarization photoconductivity in the conditions described. However, for thin crystals, the bulk photoconductivity may become anisotropic, provided that condition $d < (1/\alpha_\perp + L)$ is fulfilled and the dichroism is positive, i.e., $\alpha_\parallel > \alpha_\perp$. The difference in spatial distribution of charge carriers is evident in the latter case. The expression for photocurrent i can be written in the form proposed in [4]. Notice, however, that we present here more exact expression as compared to [4], since the dependence of radiation flux in the crystal on the polarization state is given in the explicit form

$$i_{\parallel,\perp} = \alpha_{\parallel,\perp}\beta\gamma\frac{e}{\hbar\omega}\int_0^d \Phi_{\parallel,\perp}(x)dx. \qquad (2)$$

Here, $\alpha_{\parallel,\perp}$, β, and γ are the optical absorption factor, the quantum efficiency of the photoeffect, and the separation factor of the electron–hole pairs, respectively; d is the thickness of the crystal; $\Phi_{\parallel,\perp}(x) = (1 - R)\Phi_0\exp(-\alpha_{\parallel,\perp}x)$ is the radiation power in the crystal; Φ_0 is the power of incident radiation; and R is the optical reflectivity. The parameters β and γ are assumed to be independent on the polarization of incident radiation. For many ternary diamond-like semiconductors, R depends only slightly (or much more weakly than α) on the polarization of radiation near the fundamental absorption edge. Therefore, the polarization dependence of R is not considered. On integrating (2) separately for two polarizations $\mathbf{E} \parallel \mathbf{c}$ and $\mathbf{E} \perp \mathbf{c}$, the photocurrent difference is written as

$$\Delta i = \beta\gamma\frac{e}{\hbar\omega}(1 - R)\Phi_0[e^{-\alpha_\perp d} - e^{-\alpha_\parallel d}]. \qquad (3)$$

To account for the surface recombination and charge carrier diffusion, one has to supplement the generation component of photocurrent (2) in accordance with the continuity equation for the minority carriers, e.g., for holes; thus, we have

$$\beta\gamma\frac{(1 - R)}{\hbar\omega}\Phi_0 e^{-\alpha x} - \frac{\Delta p}{\tau} + D\frac{d^2\Delta p}{dx^2} = 0, \qquad (4)$$

where D is the diffusion coefficient of charge carriers. The second term describes recombination and the third term accounts for carrier diffusion, which arises from nonuniform photogeneration and surface recombination. Using the general solution of (4) similarly to [5], we can express the polarization photocurrent difference in the form [6]

$$\Delta i = \Phi_1\left\{\frac{A_\perp}{(\alpha_\perp L)^2}(1 - e^{-\alpha_\perp d}) - \frac{A_\parallel}{(\alpha_\parallel L)^2}(1 - e^{-\alpha_\parallel d}) + \frac{LB}{L + s\tau}\left[A_\parallel - A_\perp + \frac{s\tau}{L^2}\left(\frac{A_\parallel}{\alpha_\parallel} - \frac{A_\perp}{\alpha_\perp}\right)\right]\right\}, \qquad (5)$$

where

$$\Phi_1 = \beta\gamma\frac{e}{\hbar\omega}(1 - R)\Phi_0\tau,$$

$$A = \frac{(\alpha L)^2}{(\alpha L)^2 - 1}, \quad B = (1 - e^{-d/L}).$$

The diffusion length in ternary diamond-like semiconductors is usually small ($L \le 1$ μm); thus, the term in square brackets in expression (5) is negative. It reduces the polarization photocurrent difference and even causes a reversal of its sign. This diffusion–recombination term plays a significant part in all anisotropic photoelectric phenomena, since it is responsible for the sign and amplitude of the basic polarization coefficients, such as P_i and Q_p. We now consider the limiting cases.

3.1. Photopleochroism at Weak Optical Absorption

In the range of small absorption factors, $\alpha d < 1$ and $\alpha L \ll 1$. In this case, $1 - e^{-\alpha d} \approx \alpha d$ and $e^{-d/L} \approx 0$ (because

$d \gg L$) and the photocurrent for each polarization (**E** ∥ **c** and **E** ⊥ **c**) has the following form:

$$i = \frac{\beta\gamma e(1-R)\Phi_0\tau}{\hbar\omega}\left(\alpha d - \frac{s_1\alpha L}{1+s_1}\right), \qquad (6)$$

where $s_1 = s\tau/L$ is the dimensionless surface recombination rate. Taking into consideration the conventional expression for the photopleochroism coefficient, we obtain

$$P_i = \frac{[d - s_1L/(1+s_1)](\alpha_\parallel - \alpha_\perp)}{[d - s_1L/(1+s_1)](\alpha_\parallel + \alpha_\perp)} = P_\alpha. \qquad (7)$$

At weak optical absorption, P_i is independent of the thickness of anisotropic crystal, diffusion length, and surface recombination and equals the coefficient of optical dichroism P_α. In other words, the photopleochroism in this spectral region is defined completely by the optical characteristics of the crystal and is independent of the electronic semiconductor parameters of material.

Thus, the spectral trend of P_i follows that of the coefficient of optical dichroism P_α in the region of weak absorption. This theoretical result is consistent with the experimental data, in particular, with the spectra of the photopleochroism coefficient of $CdSnP_2$ crystal (Fig. 2). In Fig. 2, two spectra $P_i(\hbar\omega)$ are presented. These spectra were derived from the photoconductivity spectra of crystals with low and very high surface recombination rates. It can be seen that, in the region of a weak optical absorption, the spectra are similar; they also follow a spectral profile of P_α (see, e.g., [7]). In a region of higher energy, the spectra become widely separated and even have opposite signs in some spectral regions. The surface recombination rate in some spectral regions where $\alpha d > 1$ may have a decisive effect on the amplitude of P_i. Because of this, one has to know the actual level of s in the experiment to estimate correctly the strength of the polarization-optical transitions obtained from the photoelectric measurements of the crystals at energies exceeding the energy gap, $\hbar\omega \geq E_g$. We emphasize that such a consideration is required not only in the case of natural anisotropy (in anisotropic semiconductors), but also in the case of "Brewster anisotropy" in isotropic conductors, i.e., at oblique incidence of light [8].[1]

3.2. Photopleochroism at Strong Optical Absorption

In the region of moderate and high optical absorption factors, when $\alpha d > 1$ and $\alpha L < 1$, the expression for a photocurrent takes the form

$$i = \frac{\beta\gamma(1-R)\Phi_0\tau}{\hbar\omega}\left(1 - \frac{\alpha L + s_1}{1+s_1}\alpha L\right). \qquad (8)$$

In the absence of surface recombination ($s_1 = 0$), the expression for the photopleochroism coefficient is written as form

$$P_i = \frac{P_\alpha}{1 - 2(\alpha_\parallel\alpha_\perp + 1/L^2)/(\alpha_\parallel + \alpha_\perp)^2}. \qquad (9a)$$

If the surface recombination rate equals or exceeds the bulk recombination rate, then $s_1 > \alpha L$ and formula (8) may be simplified. With due regard for the initial expression for the photopleochroism coefficient, we have

$$P_i = \frac{P_\alpha}{1 - 2(1+s_1)/s_1L(\alpha_\parallel + \alpha_\perp)}. \qquad (9b)$$

It can be seen that the photopleochroism is directly proportional to the optical dichroism but, due to the negative term in the denominators of expressions (9a) and (9b), it changes sign and the amplitude of P_i appears to be lower than that of P_α at low surface recombination

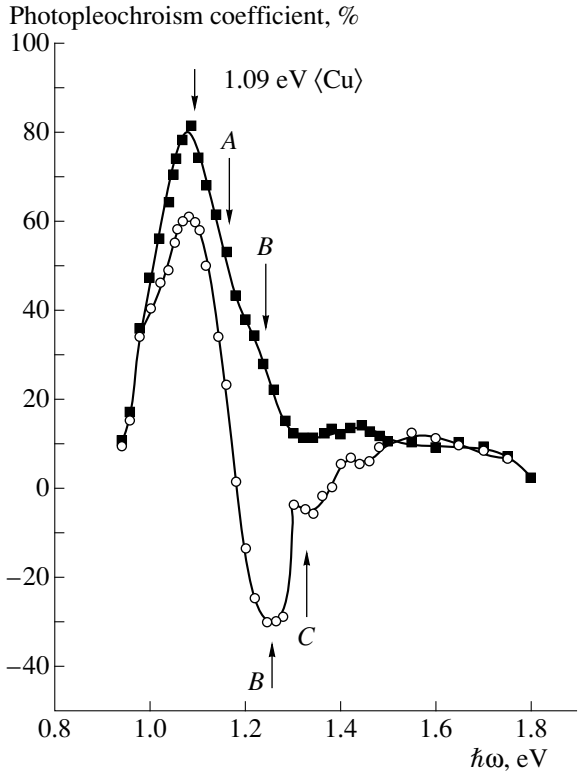

Fig. 2. Effect of surface recombination on the natural photopleochroism of $CdSnP_2\langle Cu\rangle$ crystals: $s_1 \cong 0$ (without a sign reversal, the upper curve), and $s_1 \gg 0$ (with a sign reversal, the lower curve). The impurity and interband transitions *A*, *B*, *C* are indicated by arrows.

[1] Notice that erroneous expressions, e.g., (9) and (10), were presented in [8] for the main discussed dependence $P_i(\alpha_0)$. The correct expressions can be found in the initial paper [9].

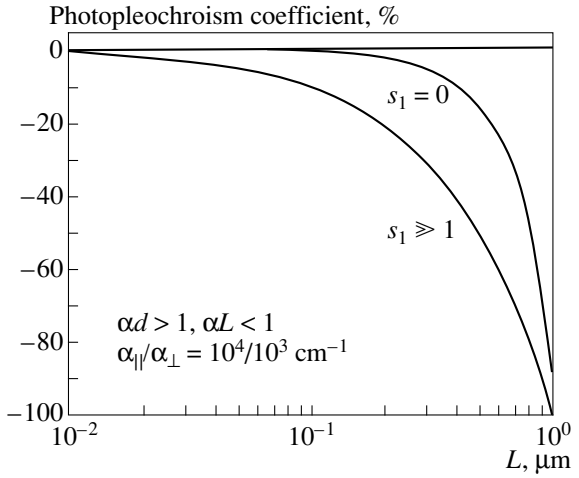

Fig. 3. Dependence of the photopleochroism coefficient on the diffusion length in the region of moderate and high optical absorption factors.

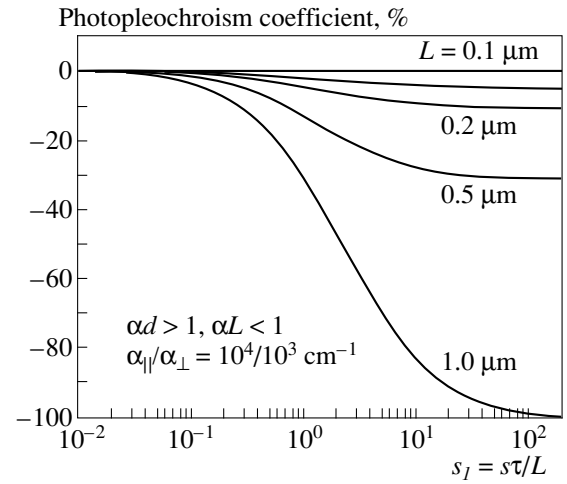

Fig. 4. Dependence of the photopleochroism coefficient on the surface recombination rate in the region of moderate and high optical absorption factors.

rates. For L comparable to the optical absorption depth, the magnitude of photopleochroism starts to increase quite rapidly in the negative range. The plots of the dependences $P_i(L)$ and $P_i(s_1)$ are shown in Figs. 3 and 4. For some relationships between the diffusion length and surface recombination rate in anisotropic semiconductor crystals, a significant increase in the negative photopleochroism is possible, which may be as high as 100%. This happens, for example, at a high surface recombination rate $s_1 \gg 1$ or at a large diffusion length (however, not exceeding $1/\alpha$, which amounts to $L \leq 1$ μm in this example). Similar reasoning is applicable to isotropic semiconductors if the so-called Brewster anisotropy is considered. An analysis of the polarization properties of the isotropic semiconductors will be carried out elsewhere. It is only worth noting here that, in the case of an isotropic semiconductor such as single-crystal silicon, the diffusion lengths of the minority carriers may amount to 100 μm and larger. Thus, the condition $L < 1/\alpha$ will be violated in the region of fundamental absorption.

4. CONCLUSION

The dependences obtained illustrate the great importance of considering the characteristic semiconductor parameters of anisotropic crystals, which are used in polarization optoelectronics. The diffusion length of the minority charge carriers and the recombination rate at the surface of the photoconductor vary the amplitude of the polarization factor P_i in a wide range (from –100% to +100%) depending on the sign of the optical dichroism of anisotropic crystal and the spectral range of excitation. In addition, the geometric layout of illumination and the arrangement of electrical contacts on the illuminated and unilluminated surfaces of the wafer may cause an additional spatial redistribution of photogenerated carriers for the polarizations **E** || **c** and **E** ⊥ **c**. This also has a significant effect on the sign and amplitude of the photopleochroism coefficient.

REFERENCES

1. S. M. Ryvkin, *Photoelectric Effects in Semiconductors* (Fizmatgiz, Leningrad, 1963; Consultants Bureau, New York, 1964).
2. G. A. Medvedkin, Yu. V. Rud', and M.A. Tairov, *Semiconductor Crystals for Photodetectors of Winearly Polarized Wight* (FAN, Tashkent, 1992).
3. I. P. Zhad'ko *et al.*, Fiz. Tverd. Tela (Leningrad) **7**, 1778 (1965) [Sov. Phys. Solid State **7**, 1440 (1965)].
4. G. A. Medvedkin, Yu. V. Rud, and M. A. Tairov, Phys. Status Solidi A **115**, 11 (1989).
5. K. V. Shalimova, *Physics of Semiconductors* (Énergiya, Moscow, 1976).
6. G. A. Medvedkin, Doctoral Dissertation (St. Petersburg, 1993).
7. G. A. Medvedkin, Yu. V. Rud', and M. A. Tairov, Fiz. Tverd. Tela (Leningrad) **31** (4), 108 (1989) [Sov. Phys. Solid State **31**, 606 (1989)].
8. F. P. Kesamanly, V. Yu. Rud', and Yu. V. Rud', Fiz. Tekh. Poluprovodn. (St. Petersburg) **33**, 513 (1999) [Semicond. **33**, 483 (1999)].
9. G. A. Medvedkin and Yu. V. Rud, Phys. Status Solidi A **67**, 333 (1981).

Translated by Yu. Aleshchenko

Semiconductors, Vol. 34, No. 5, 2000, pp. 521–524. Translated from Fizika i Tekhnika Poluprovodnikov, Vol. 34, No. 5, 2000, pp. 537–540.

ELECTRONIC AND OPTICAL PROPERTIES OF SEMICONDUCTORS

Effect of Diffusion Length and Surface Recombination on the Polarization Quantum Efficiency of Anisotropic Crystals

G. A. Medvedkin

Ioffe Physicotechnical Institute, Russian Academy of Sciences, Politekhnicheskaya ul. 26, St. Petersburg, 194021 Russia

Submitted October 13, 1999; accepted for publication November 22, 1999

Abstract—The formulas were derived and numerical analysis was carried out of the dependences of the polarization quantum efficiency Q_p and polarization photocurrent difference Δi in a homogeneous anisotropic crystal on the diffusion length L and surface recombination rate s_1. The polarization photoconductivity was considered in the region of both weak and strong optical absorption. The trends of $Q_p(L)$ and $Q_p(s_1)$ were shown to move in opposite directions. These curves are descending for small absorption factors α and ascending for high α. The limiting cases of zero, small, and high surface recombination rates were considered for $Q_p(L)$. The dependences were analyzed using the typical parameters of II–IV–V_2 ternary diamond-like semiconductors. © *2000 MAIK "Nauka/Interperiodica".*

1. INTRODUCTION

Anisotropic crystals with a high photosensitivity provide the basis for optical detectors of polarized radiation. These crystals are of interest both as polarization-optical and as photoelectric semiconductor objects, which have interrelated specific features. In the development of the devices of polarization optics and optoelectronics, the high polarization photosensitivity $\Pi_i = P_i S_i$ (where P_i is the photopleochroism coefficient and S_i is the current sensitivity) is of importance in the general case. Some other parameters are widely used in the basic research of anisotropic crystals. Among them are the polarization quantum efficiency $Q_p = |\Delta n_\parallel - \Delta n_\perp|/N_{\text{ph}}$ (N_{ph} is the number of photons, and $\Delta n_{\parallel,\perp}$ are the photocarrier density) and polarization photocurrent difference $\Delta i = (i_\parallel - i_\perp)$. Hereinafter, the subscripts $\parallel$, $\perp$ indicate the corresponding polarization directions $\mathbf{E} \parallel \mathbf{c}$ and $\mathbf{E} \perp \mathbf{c}$, where $\mathbf{E}$ is the electric vector of the wave and $\mathbf{c}$ is the optic axis of the crystal. The electric and photoelectric properties of anisotropic semiconductor crystals are strongly affected by all characteristic electronic parameters of the material. Among the latter, the diffusion length of minority charge carriers L, surface recombination rate s, and electron–hole pair lifetime τ are of prime importance. In this paper, the dependences of the polarization quantum efficiency on the L and $s\tau$ parameters were obtained and analyzed using the phenomenological approach [1], which was developed for studies of anisotropic semiconductors [2]. To our knowledge, the issues connected with polarization photoconductivity and discussed below have not previously been considered in the literature [3, 4].

2. POLARIZATION PHOTOCONDUCTIVITY

Let us assume that a linearly polarized radiation excites the bulk photoconductivity in the homogeneous oriented crystal at normal incidence. We suppose that the condition for the linear recombination is met in the bulk of the crystal and the surface recombination is absent ($s = 0$). If the absorption depth of light $1/\alpha_{\parallel,\perp}$ ($\alpha_{\parallel,\perp}$ are the absorption factors) is smaller than the sample thickness d, the similar densities of free nonequilibrium charge carriers are generated in the bulk of the semiconductor irrespective of the polarization of radiation. The different spatial distribution of these densities and the rate of carrier recombination would not induce the polarization photoconductivity in the conditions described. However, for thin crystals, the bulk photoconductivity may become anisotropic provided the condition $d < (1/\alpha_\perp + L)$ is fulfilled and the dichroism is positive, i.e., $\alpha_\parallel > \alpha_\perp$. The difference in the spatial distribution of carriers takes effect in the latter case. Similarly to [5], we use the general solution of the continuity equation, which includes the generation, recombination, and diffusion terms. The polarization photocurrent difference can be expressed in the form

$$\Delta i = \Phi_1 \left\{ \frac{A_\perp}{(\alpha_\perp L)^2}(1 - e^{-\alpha_\perp d}) - \frac{A_\parallel}{(\alpha_\parallel L)^2}(1 - e^{-\alpha_\parallel d}) + \frac{LB}{L + s\tau}\left[A_\parallel - A_\perp + \frac{s\tau}{L^2}\left(\frac{A_\parallel}{\alpha_\parallel} - \frac{A_\perp}{\alpha_\perp}\right)\right]\right\}, \quad (1)$$

1063-7826/00/3405-0521$20.00

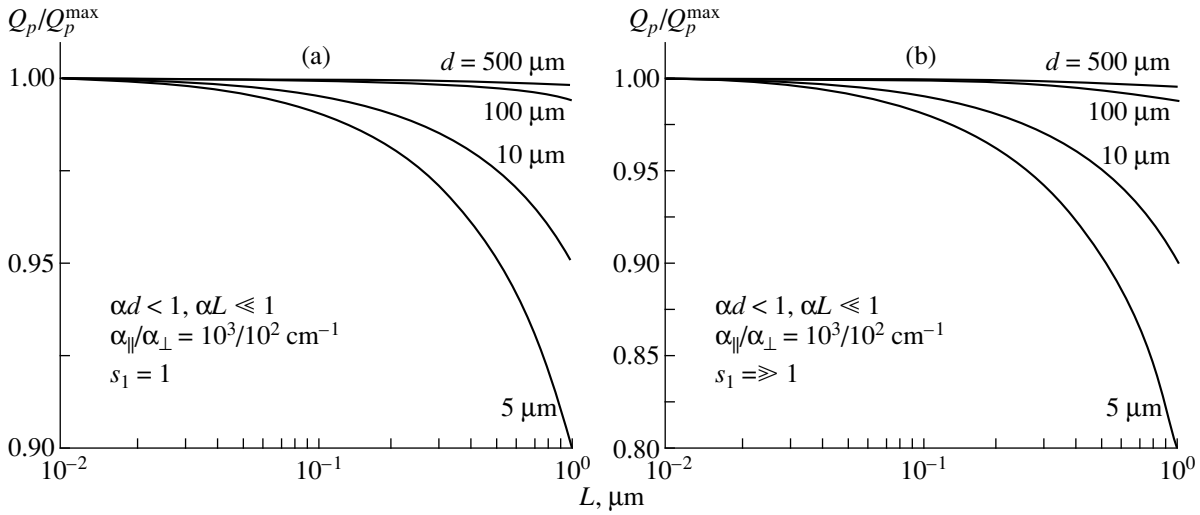

Fig. 1. Dependences of the polarization quantum efficiency normalized to the maximum value Q_p/Q_p^{max} in the region of weak optical absorption on the diffusion length for the cases of (a) low and (b) high surface recombination rate. The thickness of the crystal d is indicated at each curve.

where

$$\Phi_1 = \beta\gamma\frac{e}{\hbar\omega}(1-R)\Phi_0\tau,$$

$$A = \frac{(\alpha L)^2}{(\alpha L)^2 - 1}, \quad B = (1 - e^{-d/L}).$$

The diffusion length in ternary diamond-like semiconductors is usually small ($L \le 1$ μm); thus, the term in square brackets in expression (1) is negative. It reduces the difference in polarization photocurrent and even causes a reversal of its sign. This diffusion–recombination term plays a significant part in all anisotropic photoelectric phenomena, because it is responsible for the sign and amplitude of the polarization quantum efficiency. We now consider the limiting cases.

2.1. Polarization Quantum Efficiency at Weak Optical Absorption

In the region of small absorption factor, $\alpha d < 1$ and $\alpha L \ll 1$. In this case, $1 - e^{-\alpha d} \approx \alpha d$ and $e^{-d/L} \approx 0$, since $d \gg L$, and the photocurrent for each polarization (**E** ∥ **c** and **E** ⊥ **c**) has the following form:

$$i = \frac{\beta\gamma e(1-R)\Phi_0\tau}{\hbar\omega}\left(\alpha d - \frac{s_1\alpha L}{1+s_1}\right), \qquad (2)$$

where $s_1 = s\tau/L$ is the dimensionless surface recombination rate. Taking into consideration the conventional expression for the polarization quantum efficiency, we obtain

$$Q_p = \frac{\beta\gamma e(1-R)\tau}{\hbar\omega}\left|\left(d - \frac{s_1 L}{1+s_1}\right)\Delta\alpha\right|. \qquad (3)$$

In the region of a small absorption factor, the polarization quantum efficiency is directly proportional to the absolute value of dichroism $\Delta\alpha = (\alpha_\parallel - \alpha_\perp)$ and is linear in d. The recombination term reduces the amplitude of Q_p. According to (3), the dependence of the diffusion length follows the linear law for large L. In the absence of the surface recombination, the polarization quantum efficiency is independent of L. Figure 1 shows the dependences of $Q_p(L)$ for low ($s_1 = 1$) and high ($s_1 \gg 1$) surface recombination rates. The parameters and ranges of their variation characteristic of II–IV–V_2 ternary semiconductors [3, 4] were used to plot these curves. A comparison of Figs. 1a and 1b shows that a steeper decay of $Q_p(L)$ occurs with an enhanced surface recombination rate. Nevertheless, the resultant decrease in the amplitude of Q_p for the sample thicknesses d used in actual practice is moderate and amounts to 10–20%.

We now analyze the dependence of the polarization quantum efficiency on the dimensionless surface recombination rate $s_1 = s\tau/L$. We note that the parameter $s\tau/L$ represents the ratio between the bulk (τ) and surface lifetimes. According to (3), the dependence on s_1 is more complex than that on d and L. In Fig. 2, the parameter Q_p normalized to the maximum value Q_p^{max} is plotted as a function of s_1. It can be seen that thin crystals experience the most rapid decrease in Q_p as the surface recombination increases. The variation in Q_p for all actual samples ($d \ge 10$ μm) is small in this case. The value of Q_p for the bulk photoconductivity is also small. The curves in Fig. 2 show that a 10% reduction in Q_p occurs for thin crystals with an increase in the surface recombination rate by a factor of 1000.

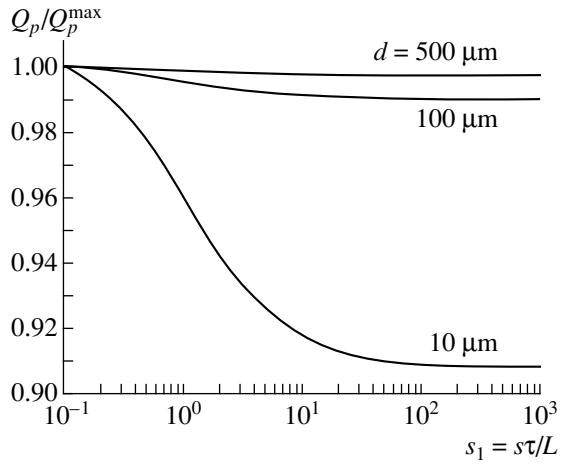

Fig. 2. The polarization quantum efficiency of bulk photoconductivity of an anisotropic crystal as a function of the dimensionless surface recombination rate. The diffusion length L = 1 μm, and the thickness of the crystal d is indicated at each curve.

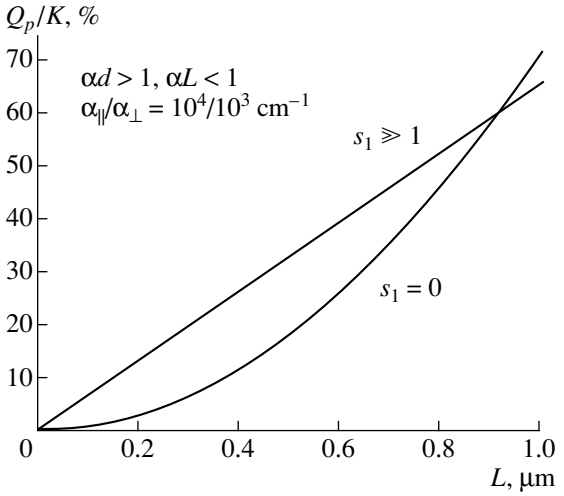

Fig. 3. Dependence of the polarization quantum efficiency on the diffusion length in the region of moderate and large optical absorption factors. R = 0.26 and $K = \beta\gamma\tau/\hbar\omega$.

Thus, in the region of weak absorption, the polarization quantum efficiency decreases only slightly with an increase in the surface recombination rate and the diffusion length of carriers. The surface recombination rate in some spectral regions where $\alpha d > 1$ may have a decisive effect on the increase in the Q_p magnitude. Because of this, one has to know the actual level of s_1 in the experiment to estimate correctly the strength of the polarization-optical transitions obtained from the photoelectric measurements at the energies exceeding the energy gap ($\hbar\omega \geq E_g$). We emphasize that such a consideration is required in the case of a so-called "Brewster anisotropy" in isotropic semiconductors (at oblique incidence of light) and is important for the correct evaluation of the peak response of polarization photodevices.

2.2. Polarization Quantum Efficiency at Strong Optical Absorption

In the region of moderate and large optical absorption factors, when $\alpha d > 1$ and $\alpha L < 1$, the expression for a photocurrent takes the form

$$i = \frac{\beta\gamma(1-R)\Phi_0\tau}{\hbar\omega}\left(1 - \frac{\alpha L + s_1}{1 + s_1}\alpha L\right). \qquad (4)$$

In the absence of the surface recombination ($s_1 = 0$), the expression for the polarization quantum efficiency is written as

$$Q_p = \frac{\beta_\gamma(1-R)\tau}{\hbar\omega}\left|\alpha_\parallel^2 - \alpha_\perp^2\right| L^2. \qquad (5)$$

If the surface recombination rate equals or exceeds the bulk recombination rate, then $s_1 > \alpha L$ and formula (4) may be simplified. With consideration of the initial expression for the polarization quantum efficiency, we have

$$Q_p = \frac{\beta\gamma(1-R)\tau}{\hbar\omega}\frac{s_1 L}{1 + s_1}|\Delta\alpha|. \qquad (6)$$

The magnitude of polarization quantum efficiency increases with the diffusion length (see Fig. 3). The dependence $Q_p(L)$ either follows square law (5) in the absence of the surface recombination ($s_1 = 0$) or obeys linear law (6) for $s_1 > \alpha L$ or for $s_1 \gg 1$. In anisotropic semiconductor crystals with the same L, the value of Q_p is found to be greater for the samples with a high sur-

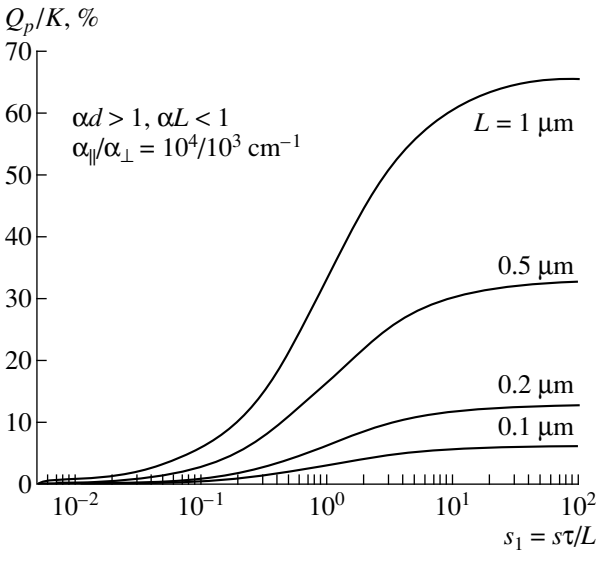

Fig. 4. Dependence of the polarization quantum efficiency on the surface recombination rate in the region of moderate and large optical absorption factors. R = 0.26 and $K = \beta\gamma\tau/\hbar\omega$.

face recombination rate almost without exception. This point can be explained as follows: the greater the difference in the photocarrier densities close to the surface ($\Delta n_{\parallel} - \Delta n_{\perp}$), the larger the Q_p magnitude.

The dependence of Q_p is nonlinear in s_1 (Fig. 4). The amplitude of Q_p reaches about 70% as the surface recombination rate increases. As can be seen from Fig. 4, the curves represent a sort of mirror image of the dependence $P_i(s_1)$ (compare with Fig. 4 in [5]). This property of the polarization coefficients is defined by the same recombination term $s_1(1 + s_1)$, which appears in the expressions for both polarization quantum efficiency and the photopleochroism coefficient [5].

3. CONCLUSION

The dependences obtained illustrate the great importance of considering the characteristic semiconductor parameters of anisotropic crystals, which are used in polarization optoelectronics. The diffusion length of the minority charge carriers and the recombination rate at the surface of the photoconductor vary the amplitude of the polarization quantum efficiency in a very wide range that depends on the sign of the optical dichroism of anisotropic crystal and the spectral range of excitation. In addition, the geometric layout of illumination and arrangement of electrical contacts at the illuminated and unilluminated surfaces of the wafer may cause an additional spatial redistribution of photogenerated carriers for the polarizations $\mathbf{E} \parallel \mathbf{c}$ and $\mathbf{E} \perp \mathbf{c}$. This also has a significant effect on the sign and amplitude of the polarization quantum efficiency.

REFERENCES

1. S. M. Ryvkin, *Photoelectric Effects in Semiconductors* (Fizmatgiz, Moscow, 1963; Consultants Bureau, New York, 1964).
2. G. A. Medvedkin, Doctoral Dissertation (St. Petersburg, 1993).
3. G. A. Medvedkin, Yu. V. Rud', and M. A. Tairov, *Semiconductor Crystals for Photodetectors of Winearly Polarization Wight* (FAN, Tashkent, 1992).
4. G. A. Medvedkin, Yu. V. Rud, and M. A. Tairov, Phys. Status Solidi A **115**, 11 (1989).
5. G. A. Medvedkin, Fiz. Tekh. Poluprovodn. (St. Petersburg) **34**, 533 (2000) [Semicond. **34**, 517 (2000)].

Translated by Yu. Aleshchenko

Semiconductors, Vol. 34, No. 5, 2000, pp. 525–526. Translated from Fizika i Tekhnika Poluprovodnikov, Vol. 34, No. 5, 2000, pp. 541–542.

ELECTRONIC AND OPTICAL PROPERTIES OF SEMICONDUCTORS

Thermoelectric Power of the *n*-InSb in a Transverse Quantizing Magnetic Field at a Large Temperature Gradient

M. M. Gadzhialiev

Institute of Physics, Dagestan Scientific Center, Russian Academy of Sciences, ul. 26 Bakinskikh komissarov, Makhachkala, 367003 Dagestan, Russia

Submitted October 27, 1999; accepted for publication November 25, 1999

Abstract—The thermoelectric power of the *n*-type indium antimonide was studied in the transverse magnetic field (0–80 kOe) at T_{av} = 160 K and different temperature gradients. It was found that the electron component of the thermoelectric power at a small temperature gradient is consistent with the theory that takes into account the electron spin, whereas, for a large temperature gradient, the value determined by the variation of the Benedicks thermoelectric power in the magnetic field is added to this component. © *2000 MAIK "Nauka/Interperiodica".*

The thermoelectric power of *n*-InSb was experimentally studied in the transverse quantizing magnetic field in [1–5]. It is shown that due to the quantization of the electron orbits ($\Omega\tau \gg 1$, $\hbar\Omega \gg kT$, and $\Omega = eH/m^*c$, where e is the elementary charge, H is the magnetic field strength, m^* is the electron effective mass, τ is the relaxation time, k is the Boltzmann constant, c is the speed of light, and T is temperature) in the transverse magnetic field both electron and phonon components of the thermoelectric power increase.

In [3–5], it is shown that the magnetothermoelectric power of *n*-InSb is consistent with the theory that takes into account the electron spin [6] provided that the phonon component is excluded.

The thermoelectric power of *n*-InSb has not yet been studied in the transverse quantizing magnetic field at a large temperature gradient (LTG). Interest in this study is caused by the fact that the thermoelectric power at LTG is usually measured at a high average temperature of the sample (T_{av} > 150 K). In this case, the phonon component of the thermoelectric power is absent, and this enables one to observe only the electron component of the magnetothermoelectric power for which there exists a detailed theory [7]. Besides, it is interesting to observe the simultaneous influence of the quantizing magnetic field and LTG on the thermoelectric power.

In this paper, the thermoelectric power of *n*-InSb ($n_{77} = 2 \times 10^{13}$ cm^{-3}) is measured as a function of the transverse magnetic field (0–80 kOe) at T_{av} = 160 K and temperature gradients equal to 2 and 10^3 K/cm.

LTG means a temperature gradient at which the relation $L_d \geq L_t$ is satisfied ($L_d = \sqrt{D\tau}$, D, and τ are the diffusion length, diffusion coefficient, and lifetime of the minority carriers, respectively; $L_t = \Delta x T/\Delta T$ is the reduced length; and Δx is part of the sample where the temperature gradient ΔT appears).

The method for producing the LTG and measuring the relevant coefficients was described in [8]. The condition $L_d > L_t$ is satisfied in InSb at T_{av} = 160 K provided that $\Delta T/\Delta x \geq 10^3$ K/cm in the sample with the dimensions of $(0.4 \times 0.05 \times 0.04)$ cm^3.

The magnetothermoelectric power of *n*-InSb at two of the above mentioned temperature gradients is presented in the figure. It can be seen that, in the region of the classical magnetic fields ($H \ll 55$ kOe at T_{av} = 160 K), the value of the magnetothermoelectric power is the same for the two temperature gradients. In the range of classically strong magnetic fields (20–55 kOe), the transverse thermoelectric power saturates; this is consistent with the theory [1].

It is interesting to study the behavior of the magnetothermoelectric power in the magnetic fields $H >$ 55 kOe. In this case, at average temperature T = 160 K, the conditions for quantization ($\hbar\Omega \gg kT$) and spin splitting of the Landau levels in the magnetic field ($g\mu_B H > kT$) are satisfied (g is the spectroscopic splitting factor, and μ_B is the Bohr magneton). It follows from the figure that, in the region of the quantizing magnetic fields (H > 55 kOe), the thermoelectric power increases, and its values at LTG (curve *2*) exceed the values of the thermoelectric power at a small temperature gradient (curve *1*).

The figure also shows (curve *3*) the quantum addition to the magnetothermoelectric power calculated according to the relation (1) from [6]

$$\alpha_h - \alpha_\infty = -\frac{k}{e}\left[\frac{1}{6} - \frac{1}{8}\left(\frac{m^*}{m_0}g\right)^2\right]\nu^2, \qquad (1)$$

where α_∞ is the thermoelectric power in the classically strong magnetic field (in our case, as can be seen from the figure, $|\alpha_\infty|$ = 37 μV/K), $\nu = \hbar\Omega/2kT$, and m_0 is the free electron mass.

1063-7826/00/3405-0525$20.00

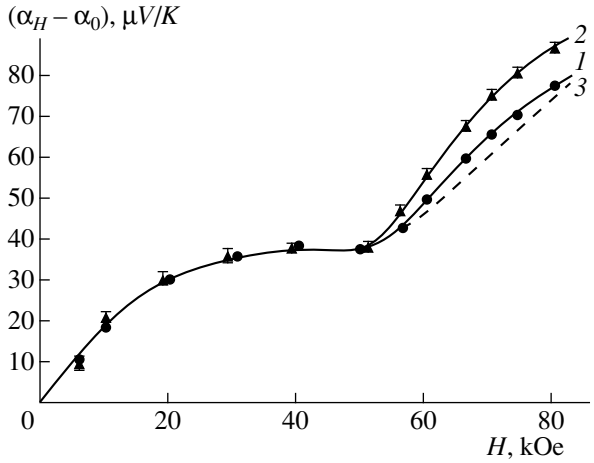

Thermoelectric power dependence on the transverse magnetic field in the *n*-type indium antimonide ($n_{77} = 2 \times 10^{13}$ cm^{-3}) at the temperature gradients of (*1*) 2 and (*2*) 10^3 K/cm, T_{av} = 160 K; (*3*) the values of the quantum components of the thermoelectric power, calculated according to (1).

It can be seen (curve *3*) that the experimental data at a small temperature gradient agree with the theory. This confirms the assumption that in this case only the electron component of the thermoelectric power is present, and its dependence on the magnetic field is consistent with the theory taking into account the electron spin (curves *1* and *3*).

As is shown in [8], in the case of LTG, the Benedicks thermoelectric power is added to the conventional thermoelectric power. An experimentally observed increase in the thermoelectric power in the quantizing magnetic field at LTG, in contrast to the thermoelectric power at a small temperature gradient, is caused, apparently, by the variation of the Benedicks thermoelectric power in the quantizing magnetic field. In the next paper we will perform the quantitative comparison of the thermoelectric power variation at LTG in the quantizing magnetic field with the theory and calculate the Benedicks thermoelectric power in the magnetic field.

In conclusion, we demonstrated experimentally that, in the quantizing magnetic field at a small temperature gradient, the electron component of the thermoelectric power is consistent with the theory considering the electron spin, and, in the case of LTG, the additional increase due to the variation of the Benedicks thermoelectric power in the magnetic field is observed.

REFERENCES

1. Kh. I. Amirkhanov, R. I. Bashirov, and M. M. Gadzhialiev, Fiz. Tverd. Tela (Leningrad) **3**, 3743 (1961) [Sov. Phys. Solid State **3**, 2713 (1961)].
2. I. L. Drichko and I. V. Mochan, Fiz. Tverd. Tela (Leningrad) **6**, 1902 (1964) [Sov. Phys. Solid State **6**, 1498 (1964)].
3. S. M. Puri and T. H. Geballe, Phys. Rev. **136**, 1767 (1964).
4. Kh. I. Amirkhanov, R. I. Bashirov, and M. M. Gadzhialiev, Fiz. Tekh. Poluprovodn. (Leningrad) **1**, 26 (1967) [Sov. Phys. Semicond. **1**, 19 (1967)].
5. M. M. Gadzhialiev, Izv. Vyssh. Uchebn. Zaved., Fiz., No. 3, 21 (1993).
6. A. I. Ansel'm and R. G. Tarkhanyan, Fiz. Tverd. Tela (Leningrad) **6**, 3357 (1964) [Sov. Phys. Solid State **6**, 2685 (1964)].
7. B. M. Askerov, *Electronic Phenomena in Semiconductors* (Nauka, Moscow, 1985).
8. M. M. Gadzhialiev and V. A. Elizarov, Fiz. Tekh. Poluprovodn. (St. Petersburg) **32**, 1313 (1998) [Semicond. **32**, 1168 (1998)].

Translated by I. Kucherenko

Semiconductors, Vol. 34, No. 5, 2000, pp. 527–533. Translated from Fizika i Tekhnika Poluprovodnikov, Vol. 34, No. 5, 2000, pp. 543–549.

ELECTRONIC AND OPTICAL PROPERTIES OF SEMICONDUCTORS

Influence of Annealing on the Dislocation-Related Electrical Conductivity of Germanium

S. A. Shevchenko

Institute of Solid-State Physics, Russian Academy of Sciences, Chernogolovka, Moscow oblast, 142432 Russia
e-mail: shevchen@issp.ac.ru

Submitted November 16, 1999; accepted for publication November 25, 1999

Abstract—Germanium *n*-type single crystals with a donor concentration of 3×10^{12} cm^{-3} were deformed at 760°C to strains of $\delta \le 71\%$ with a rate of 6×10^{-3} s^{-1}, cooled to room temperature, and then annealed for $t \le 20$ h at 900°C. Low-temperature static electrical conductivity due to holes trapped by dislocations and transported along a branching dislocation network was measured before and after annealing of the deformed samples. It was found that annealing enhances the dislocation-related electrical conductivity in the samples with $\delta < 50\%$ and diminishes this conductivity in the samples with $\delta > 60\%$. Selective etching and X-ray diffraction analysis showed that the main structural distinction of the samples with $\delta > 60\%$ is the presence of recrystallized regions. The influence of annealing on dislocation-related electrical conductivity is explained by an increase in connectedness of the dislocation network for $\delta < 50\%$ and by a decrease in this connectedness in the case of $\delta > 60\%$. © *2000 MAIK "Nauka/Interperiodica".*

INTRODUCTION

A search for and study of the objects demonstrating one-dimensional electronic properties and high electrical conductivity are of indubitable theoretical and application-oriented interest.

Motion of charge carriers trapped by dislocation cores and transported under the effect of an electric field is observed at low temperatures in the form of a specific electrical conduction in the microwave range in germanium and silicon [1, 2] and under dc conditions in germanium subjected to severe plastic deformation [3, 4]. Anisotropic dislocation-related microwave electrical conduction observed at $T < 30$ K in the germanium samples with relatively low ($N_D < 2 \times 10^7$ cm^{-2}) density of 60° dislocations is related to the transport of holes (if the Fermi level is within the donor dislocation band E_1) or electrons (if the Fermi level is within the acceptor dislocation band E_2) along rectilinear dislocation segments with the length on the order of 10 μm [4, 5]. The radius of the wave function of hole states in a transverse direction in the band E_1 located in germanium at a distance of ~0.1 eV above the top of the valence band E_v amounts to ~1 nm; i.e., the conducting region with such a radius and a length of more than 0.1 μm is equivalent to a quasi-one-dimensional quantum wire. According to [6], in one-dimensional metals at $T = 0$ K, the scattering of charge carriers by defects is conducive to the spatial localization of the carriers and, as a consequence, to the exponential decrease in the static electrical conductivity as the length of the conductor increases. Electrons or holes moving along a thin dislocation tube are scattered by bends, jogs, and other defects violating the translational symmetry along the dislocation cores in actual crystals; i.e., the extent of the translational localization of charge carriers in dislocation cores is found to be much less than the length of an individual dislocation. Therefore, in germanium at $T < 30$ K, the static electrical conductivity along the isolated 60° dislocations with a length larger than 0.1 mm is very low and is not observed experimentally [1, 7].

The static dislocation-related electrical conductivity (DEC) can manifest itself in a branching dislocation network with numerous intersections, which contribute to the destruction of the one-dimensional localization of charge carriers and make possible the charge transport over macroscopic distances [8]. For example, such a network is formed on high-temperature plastic deformation of germanium to large strains δ. Dislocations are largely located at the boundaries of cells (blocks) in the form of two-dimensional networks composed of segments of the screw and 60° dislocations with a length of ~0.1 μm [4, 9–11]. According to [4, 12], the DEC originates in lightly doped germanium of *n*- and *p*-types if a certain threshold value δ_0, for which the dislocation segments are found to be combined into a unified macroscopic network, is attained; the DEC then increases with a further increase in δ. For $\delta^* > \delta_0$, the Arrhenius dependence of DEC on temperature ceases to exist, and the temperature dependence of DEC can be described by the relation $\sigma(T) \sim T^y$ in a very wide temperature range (0.01–40 K). The values of y determined from various experiments are in the range of 0.08–1.5 and decrease with increasing δ [4, 11, 12]. For $y < 0.2$, the Hall emf becomes measurable in the DEC range, with the sign of the emf corresponding to the hole conduction [4]. Such an evolution of DEC with an

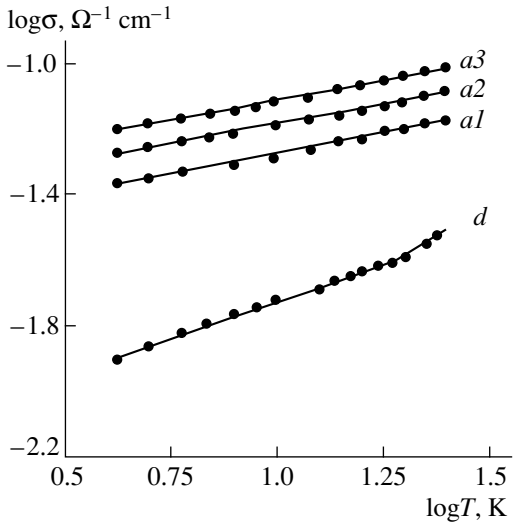

Fig. 1. Temperature dependence of dislocation-related electrical conductivity in deformed sample 1 (δ = 43%) (*d*) after deformation and after subsequent annealing at 900°C for (*a1*) 5, (*a2*) 12, and (*a3*) 20 h.

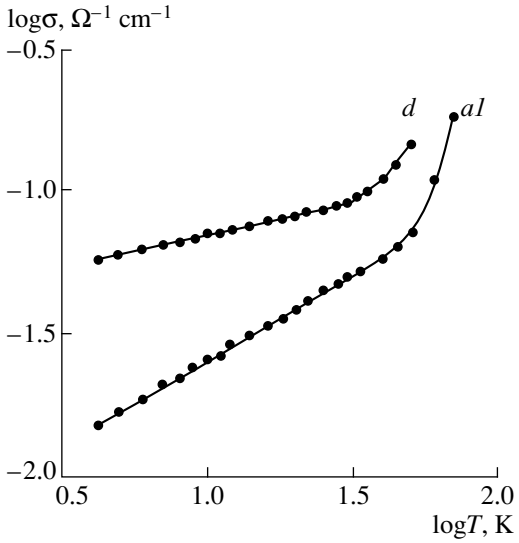

Fig. 2. Temperature dependence of dislocation-related electrical conductivity in deformed sample 2 (δ = 62%) (*d*) after deformation and (*a1*) after the subsequent annealing for 20 h at 900°C.

increase in δ is related to the insulator–metal transition put into effect by plastic deformation [11, 12].

A large difference between the values of δ_0, δ*, and *y* obtained in [4] and [12] can result from the different impurity composition of original single crystals or the change in the dislocation network itself under the different conditions of preparation of deformed samples. The issue concerning the influence of doping or residual technological impurities on physical properties of deformed crystals has always been discussed when studying the specific properties controlled by dislocations themselves. It was reasoned in [11] that impurities cannot significantly influence the DEC in lightly doped germanium samples. It was also shown [11] that, for a fixed strain, the value of static electrical conductivity related to the motion of electrons along a branching system of quasi-one-dimensional segments essentially depends on the geometrical characteristics of deformed germanium crystals and the high-temperature annealing of these crystals following deformation. This dependence was explained by a variation in the connectedness of the dislocation network.

In this work, we study the influence of the high-temperature annealing of germanium crystals deformed with a high rate on the value and temperature dependence of DEC related to hole transport.

EXPERIMENTAL RESULTS

In our studies, we used GSD-2a high-purity *n*-type germanium crystals with a net concentration of shallow chemical donors of $N_d = 3 \times 10^{12}$ cm^{-3} and a density of grown-in dislocations lower than 10 cm^{-2}. The samples in the form of parallelepipeds 10 mm × 5 mm × 2.5 mm in size oriented in the [011], [100], [$00\bar{1}$] crystallographic directions were deformed by compression at a temperature of T_d = 760°C in the [100] direction in the dynamic mode with a rate of $\nu = 6 \times 10^{-3}$ s^{-1} to the strains of δ = 20–71%. The deformed crystals were cooled in the chamber for the deformation to room temperature; the samples for electrical studies were then cut from these crystals. These samples were annealed in vacuum at a pressure of ~10^{-3} Pa for $5 \le t \le 20$ h at T_{ann} = 900°C (the melting point of germanium is equal to T_m = 937°C). The methods for preparing the samples and measuring the electrical characteristics were outlined in detail in [4].

According to [13], following plastic deformation and the annealing of deformation-introduced defects [14], the *n*-type germanium samples with $N_d = 3 \times 10^{12}$ cm^{-3} and a density of introduced dislocations of $N_D > 5 \times 10^6$ cm^{-2} change their conductivity to the *p*-type. The conductivity of the samples with δ > 20% ($N_D > 10^9$ cm^{-2}) at $T > 50$ K is due to free holes in the valence band whose concentration decreases exponentially with decreasing temperature. This contributes to the appearance of static DEC at $T < 30$ K related to the transport of holes trapped by dislocations [4].

Figures 1–3 show the temperature dependences of DEC for three rapidly ($\nu = 6 \times 10^{-3}$ s^{-1}) deformed germanium samples before and after annealings of various durations at 900°C. In unannealed samples with δ = 43, 62, and 71%, the DEC decreases with decreasing temperature as $\sigma(T) \sim T^y$, with y = 0.49, 0.25, and 0.36, respectively. The data shown in Fig. 4 make it possible to compare the values of DEC at 4.2 K ($\sigma_{4.2}$) in the rap-

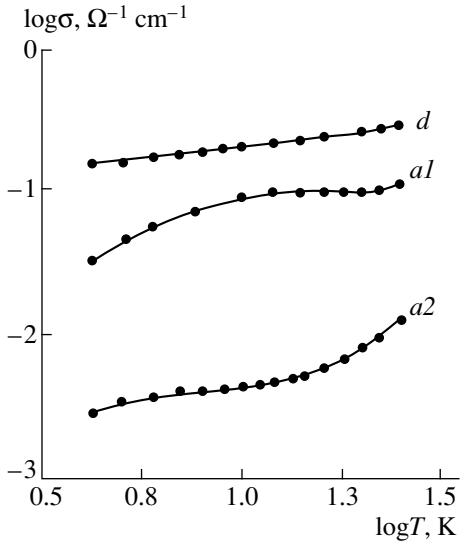

Fig. 3. Temperature dependence of dislocation-related electrical conductivity in deformed sample 3 (δ = 71%) (*d*) after deformation and after subsequent annealing at 900°C for (*a1*) 12 and (*a2*) 20 h.

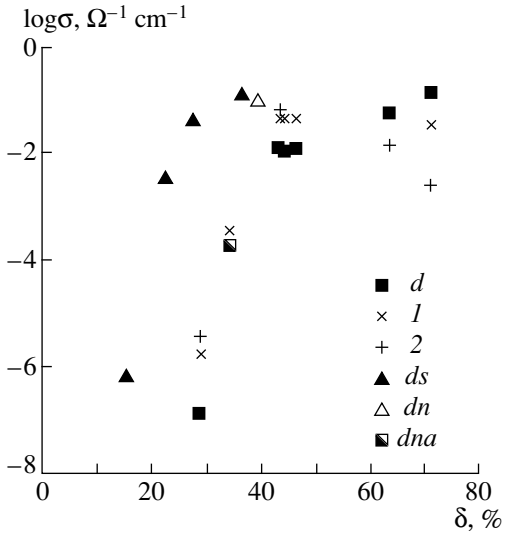

Fig. 4. Dislocation-related electrical conductivity measured at 4.2 K in the *n*-type germanium samples (*d*) after deformation with a strain rate of $\nu = 6 \times 10^{-3}$ s^{-1} to various strain levels δ and after subsequent annealing at 900°C for (*a1*) 12 and (*a2*) 20 h; (*dn*) in a sample cut from the same ingot and deformed with the strain rate of $\nu = 3 \times 10^{-5}$ s^{-1} to the strain level of δ = 39%; (*ds*) in the *p*-type germanium samples deformed with a rate of $\nu = 3 \times 10^{-5}$ s^{-1} (the data reported in [4]); and (*dna*) in the sample subjected to postdeformation annealing for 1 h at 900°C.

idly and slowly ($\nu = 3 \times 10^{-5}$ s^{-1}) deformed samples. The values of $\sigma_{4.2}$ for slowly deformed *p*-type samples with a net concentration of shallow chemical acceptors equal to $N_a = 10^{12}$ cm^{-3} were taken from [4]. It follows from Figs. 1–4 that the law $\sigma(T) \sim T^y$ and the threshold shape of the curve $\sigma_{4.2}(\delta)$ are retained after deformation with a high rate; however, the values of $\sigma_{4.2}$ decrease significantly for fixed values of δ.

It also follows from Figs. 1–4 that subsequent annealing of deformed samples at $T_{ann} = 900$°C for up to 20 h changes the value of DEC: the value of DEC increases in the samples with δ < 50% and decreases in the samples with δ > 60%. In the samples with δ < 50%, the law $\sigma(T) \sim T^y$ is retained after annealing; however, the value of *y* is decreased (for example, in sample 1 with δ = 43% as shown in Fig. 1). In the case of the samples with δ = 43–46%, the values of $\sigma_{4.2}$ increase as a result of annealing and become close to those typical of slowly deformed samples (Fig. 4). In sample 2 (δ = 62%), the law $\sigma(T) \sim T^y$ is obeyed both before and after annealing for 20 h (Fig. 2); however, the DEC decreases as a result of annealing, and the value of *y* increases to 0.62. It follows from Fig. 3 that, in the temperature range of 4.2–30 K, curves *a1* and *a2* for sample 3 (δ = 71%) cannot be described by a power law; i.e., a high-temperature annealing of this sample causes the form of the dependence $\sigma(T)$ to change. Tentative studies showed that such an annealing of an *n*-type sample deformed slowly to δ = 39% (Fig. 4) did not reduce the DEC.

In order to clarify the cause of the different influence of annealing at 900°C on the DEC of the samples with δ < 50% and δ > 60%, we conducted additional studies. Treatment of the surface, which was parallel to the principal glide plane {111}, in a Billig etchant [15] made it possible to reveal structural distinctions between the samples with δ < 50% and δ > 60%. Alternating dark and light areas 1–20 μm in size are observed on the surface of the samples with δ < 50% (before and after annealing) viewed with an optical microscope. The dark areas correspond to dislocation-enriched two-dimensional cell boundaries (the structure of the boundaries is resolved by transmission electron microscopy), and the light areas correspond to the cells where the dislocation density is much lower than that within the boundaries. Such an etch pattern was previously observed in silicon [10] and germanium [11] crystals subjected to severe plastic deformation. As δ increases to 71%, the size of the cells decreases almost to 1 μm, and the cells are now poorly resolved when viewed with an optical microscope. Following the deformation of sample 3 (δ = 71%), light, slightly elongated areas that were 20–40 μm in length and were separated by more than 50 μm were observed against the more or less uniform background corresponding to a cellular structure. Annealing at 900°C brings about a growth of these areas, and several light areas with a length exceeding 0.1 mm are observed on the surface of the sample annealed for 20 h (Fig. 5). Cells 2–10 μm in size can be seen in the upper part of Fig. 5. In the case of sample 2 (δ = 62%), individual light areas ~30 μm in length were observed only after annealing for 20 h at 900°C. In the samples with δ < 50%, such areas were

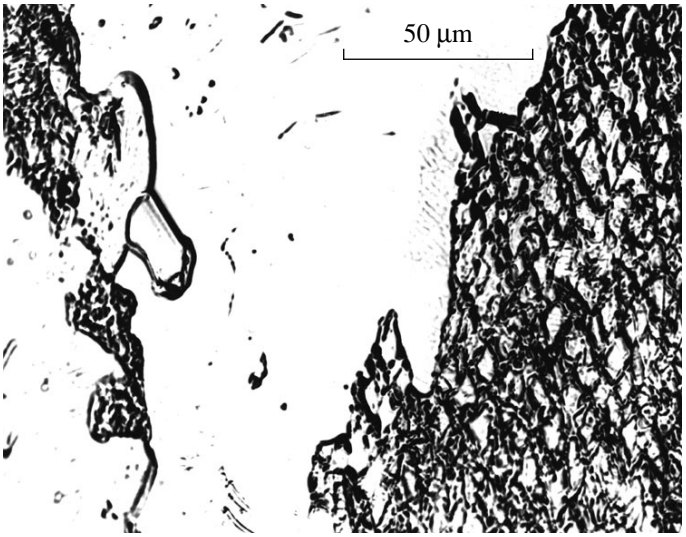

Fig. 5. Image of a {111} surface as obtained in an optical microscope for sample 3 after annealing at 900 °C (t = 20 h).

not observed either after deformation or after annealing for 20 h at 900°C. A body of evidence gained in experimental studies [16, 17] on the influence of annealing on the defect structure of fcc metals (Al, Cu, and Ni) subjected to severe plastic deformation at $T_d < 0.4T_m$ show that an annealing at $T_{ann} > 0.6T_m$ brings about an emergence of regions (the so-called recrystallized grains) with the crystal structure more perfect compared to the deformed matrix. Such grains can also be formed in the course of plastic deformation. Since the mechanisms of plastic deformation and annealing in fcc metals and covalent semiconductors have much in common [18, 19], it is very likely that the light areas in sample 3 correspond to recrystallized grains.

The assumption that recrystallized regions are present in sample 3 (δ = 71%) after annealing at 900°C is supported by the results of X-ray diffraction analysis. Annular reflections and separate point reflection spots can be seen in the back-reflection Laue diffraction pattern (CuK_α radiation) obtained after annealing at 900°C (t = 20 h) (Fig. 6). Annular reflections are observed in X-ray diffraction patterns of all samples with $\delta > 15\%$ and are composed of a large number of small spots corresponding to the reflection of X-ray radiation from certain planes in the cells 1–20 μm in size [4]. The intensity of these reflections changes with varying azimuthal angle; i.e., each ring involves several arcs. In the annealed sample with δ = 46%, the ring is composed of a single intense arc and two arcs of lower intensity; these arcs encompass ~20°. The angular extent of the arcs (the range of misorientation angles between the cells) increases with increasing δ, and, in sample 3 (Fig. 6), the inner ring is found to be almost continuous. Separate point reflections in the X-ray pattern for sample 3 are clearly pronounced after annealing for 12 and 20 h at 900°C, which correlates with the growth of light areas (Fig. 5). Therefore, we may assume that symmetrically arranged separate point reflections in Fig. 6 correspond to the reflection of X-rays from a {100} plane in one of the largest single-crystalline grains grown in the course of annealing. The arrangement of separate point reflections in the X-ray diffraction patterns corresponding to other areas of this sample differs from that shown in Fig. 6. This is related to changes in the orientation and number of grains grown in these areas. In the samples with $\delta < 50\%$, the point reflections were not observed either after deformation or after annealing at 900°C (t = 20 h).

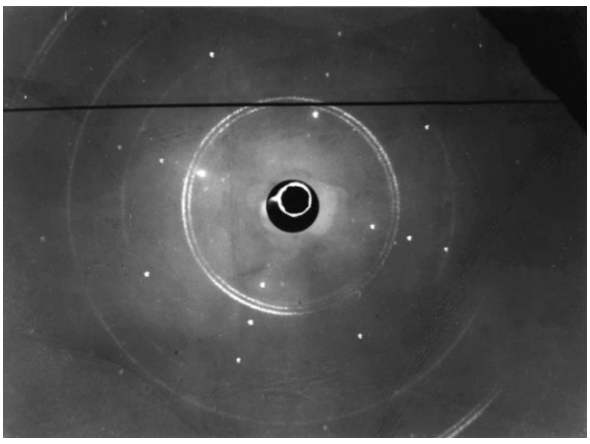

Fig. 6. The back-reflection X-ray diffraction pattern for sample 3 after annealing at 900°C (t = 20 h).

Thus, a decrease in the magnitude and a change in the form of temperature dependence of DEC in sample 3 (δ = 71%) as a result of annealing at 900°C correlate with an increase in the area of recrystallized grains.

DISCUSSION

According to [4, 11], in slowly deformed germanium samples, the DEC is independent of the type and concentration of doping impurities in the starting crystals for $N_a < 10^{16}$ cm^{-3} or $N_d < 10^{16}$ cm^{-3}. It is well known that grown-in residual impurities (oxygen, carbon, copper, and so on) in germanium and silicon are actively involved in the formation of various complexes and precipitates. Electrically active defects formed during the plastic deformation of germanium are the substitutional copper atoms and more complex associations containing copper and oxygen atoms; however, these disappear after a short-term annealing at ~700°C owing to the precipitation of copper [13, 14]. This suggests that, in the samples subjected to severe plastic deformation, the residual impurities at $T < 300$ K are largely in a bound state in the form of precipitates whose concentration is much lower than the density of dislocation-related states. Therefore, in order to interpret the results shown in Figs. 1–4, we should analyze the changes in the dislocation system itself. In a percolation system of dislocation segments, the static electrical conductivity depends exponentially on the parameter η that characterizes the connectedness of this system [8]. The above-outlined specificity of the dislocation-system formation in germanium samples subjected to severe plastic deformation makes it possible to consider a variation in the parameter η as the most probable cause of the influence of the strain rate and annealing at 900°C on the DEC.

At present, there is a body of experimental data supporting the existence of various, spatially inhomogeneous dislocation structures (lamellar, cellular, polygonized, fragmentated, etc.) in plastically deformed crystals [20–22]. According to [22], nonuniformity in the distribution of dislocations is a result of kinetic instability and self-organization, which are developed in the ensemble of dislocations owing to the interaction of dislocations with each other and with local obstacles. The spatial–temporal scale and morphology of forming dislocation structures depend on external and internal physical parameters. The former include the strain rate, the deformation temperature, the type of loading, and a single or multiple slip; the latter involve the crystallographic structure, the ability to cross-slip, the initial density of dislocations, the magnitude of the strain, and other such parameters [21]. Thus, for example, a single slip is conducive to the formation of lamellar structures, whereas, in the case of multiple slip, cellular structures are preferential. At a high deformation temperature ($T_d > 0.6T_m$), two processes are in competition with each other. One of the processes is the accumulation of dislocations in the crystal (in the form of chaotic clusters) under the effect of applied stress, and the second process consists in the rearrangement of these clusters into ordered low-energy dislocation structures (walls and networks) by slip and nonconservative motion of dislocations (i.e., the formation of polygonized structures [19, 21]). A cellular dislocation structure containing the fragments of polygonized structures was observed in germanium and silicon crystals subjected to plastic deformation at $T_d > 0.7T_m$ to large strains ($15 < \delta < 40\%$) with the strain rate of $\dot{\varepsilon} \leq 2 \times 10^{-4}$ s^{-1} [4, 10]. This structure was studied by transmission electron microscopy and was demonstrated to consist of a branching system of dislocations largely located within low-angle cell boundaries in the form of chaotic dislocation clusters and two-dimensional networks, with a fraction of regular fragments of dislocation networks increasing as δ increases. It is likely that the presence of chaotic dislocation clusters manifests itself also in the radial broadening of certain arcs in back-reflection X-ray diffraction patterns; these arcs correspond to the reflection of X-rays at the largest angles [4]. Since the deformation temperature and the strain rate exert the opposite effects on the rate of the dislocation-structure rearrangement [21], the degree of ordering in this structure depends heavily on the strain rate. If the strain rate is high, the accumulation of dislocations dominates over the process of ordering, and a highly unordered system of dislocation segments is formed as a result. In the case of slow deformation, the dislocation system has the opportunity to reduce its energy and become more ordered. Therefore, it might be expected that, in rapidly deformed germanium samples, the degree of connectedness in a system of dislocation fragments is lower than that in slowly deformed samples, and an infinite conducting cluster is formed for larger values of δ. This assumption is in conformity with a shift of the dependences $\sigma_{4.2}(\delta)$ for the samples deformed with different strain rates (Fig. 4). The samples subjected to rapid deformation feature larger values of δ_0, δ^*, and y (for fixed values of δ), which are found to be closer to the values reported in [12].

According to [16, 17], high-temperature annealing of fcc metals subjected to severe plastic deformation at $T_d < 0.4T_m$ causes the internal energy stored in the course of deformation to be reduced owing to polygonization and recrystallization. Polygonization is a lower temperature process and significantly changes the dislocation structure during heating. If deformation gives rise to a cellular structure and the cells are separated from each other by chaotic dislocation clusters, polygonization brings about a flattening of these dislocation regions and the formation of planar two-dimensional low-angle boundaries that separate the regions free of dislocations. It was mentioned above that polygonization could also occur in the course of deformation. It follows from the data reported in [10, 19] that, in silicon samples subjected to severe plastic deformation, the area occupied by regular dislocation networks increases appreciably after annealing at $T_{ann} > 0.7T_m$. Splitting of annular reflections corresponding to the CuK_α doublet in the back-reflection X-ray diffraction patterns (Fig. 6) indicates that internal stresses are relieved and, consequently, the dislocation structure is ordered in samples 1–3 as a result of anneal-

ing at 900°C. All the aforementioned makes it possible to assume that an increase in DEC in the samples with $\delta < 50\%$ after annealing at 900°C is a result of an increase in the connectedness of a system of dislocation segments. It is difficult to determine the value of parameter η from experimental data, because special features of the energy spectrum of dislocation-related states (in particular, the existence of a gap between the donor and acceptor states) were not taken into account in model calculations of static DEC in [8]. Some of the dislocation-system parameters are also unknown.

Recrystallization is effected by the formation and motion (or by motion alone) of large-angle boundaries ($\theta > 10°$) [16, 17]. Such boundaries can emerge in the case of deformation to large strains as a result of the appearance of a high dislocation density and can also be formed in the course of high-temperature annealing. In the latter case, low-angle boundaries are formed first and then move in the direction of the high volume density of dislocations; in the course of this motion, new dislocations become attached to these boundaries, thus increasing the misorientation angle θ between adjoining cells. The large-angle boundaries are formed in the regions where there are gradients in the angles θ (the orientation gradients). The important parameters affecting the character of changes in the dislocation structure during annealing are the magnitude and the rate of strain. According to [16, 17], recrystallization sets in metals and alloys only if a certain critical strain δ_c is attained. In the samples with $\delta < \delta_c$, annealing only induces polygonization, as a result of which the orientation mismatch between adjoining cells is reduced and the recrystallization is impeded. This is consistent with the absence of recrystallized grains and an increase in DEC after annealing germanium samples with $\delta < 50\%$ at 900°C. On a further increase in δ, the nonuniformity in the distribution of dislocations and other defects becomes more pronounced, the angles of misorientation between adjoining crystal regions increase, and the regions with a high stored energy emerge. The latter regions are characterized by large orientation gradients [20] and correspond to the sites where recrystallization nuclei appear, with their critical size exceeding 1 μm [17].

Taking into account the above, we may assume that the value of δ_c is in the range of 50–60% for rapidly deformed germanium samples. In sample 2 ($\delta = 62\%$), the recrystallization nuclei with larger than critical sizes are apparently formed only in the course of annealing; therefore, the size of recrystallized regions is rather small (~30 μm) even after annealing for 20 h at 900°C. In sample 3 ($\delta = 71\%$), such regions are already formed during deformation and grow appreciably in the course of subsequent annealing. The coexistence of macroscopic regions having a cellular structure with coarse recrystallized grains in this sample (Fig. 5) indicates that the plastic deformation is inhomogeneous. The back-reflection X-ray diffraction patterns for this sample are characterized by the largest azimuthal extent of annular reflections, which corresponds to a large spread in the misorientation angles; in this case, the existence of orientation gradients is believed to be more likely.

An increase in the strain rate results in an increase in the inhomogeneity of deformation and in a shift of δ_c to smaller values [16, 17]. This means that recrystallization in slowly deformed samples could occur for even larger values of δ.

The formation of recrystallized regions in the samples with $\delta > 60\%$ is a result of the disappearance of a fraction of dislocation segments and should cause the connectedness (the parameter η) of the dislocation system to decrease. As distinct from slowly deformed samples, for which the value of y decreases with increasing δ [4], in sample 3 ($\delta = 71\%$) subjected to deformation, the value of y ($y = 0.36$) is found to be larger than y ($y = 0.25$) in sample 2 ($\delta = 62\%$). This fact and also an increase in y to 0.62 in sample 2 after annealing at 900°C ($t = 20$ h) can be explained by a slight decrease in parameter η as a result of the formation of small-size (~30 μm) recrystallized regions after deformation (in sample 3) or after annealing (in sample 2). An increase in the volume of recrystallized regions in sample 3 with an increased duration of annealing brings about a further decrease both in parameter η and in the value of DEC. A change in the form of the temperature dependence of DEC in this sample (Fig. 3) after annealing is apparently related to the contribution of recrystallized regions and (or) their boundaries to the total electrical conductivity of the crystal.

CONCLUSION

The body of experimental data reported in this paper indicates that the DEC is sensitive to changes in the dislocation structure under various conditions of preparing germanium samples subjected to severe plastic deformation. The assumption that the connectedness of a dislocation system is improved with its ordering is supported by experimental data on the higher values of DEC in slowly deformed samples and an increase in DEC in rapidly deformed samples with $\delta < 50\%$ after high-temperature annealing. The absence of recrystallized regions in these samples makes it possible to ignore the possible contribution of electrical conductivity over large-angle boundaries to the total conductivity. A decrease in the stored internal energy in the samples with $\delta > 60\%$ as a result of high-temperature annealing is largely related to an increase in the size of recrystallized regions, which brings about a deterioration in the connectedness of the dislocation system and a decrease in DEC.

ACKNOWLEDGMENTS

I thank V.V. Kveder, M.P. Karpov, and G.E. Abrosimova for their participation in discussions of the results and for their valuable comments.

REFERENCES

1. Yu. A. Osip'yan, V. I. Tel'yanskiĭ, and S. A. Shevchenko, Zh. Éksp. Teor. Fiz. **72**, 1543 (1977) [Sov. Phys. JETP **45**, 810 (1977)].
2. V. A. Grazulis, V. V. Kveder, and V. Yu. Mukhina, Phys. Status Solidi A **43**, 407 (1977); **44**, 107 (1977).
3. Yu. A. Osip'yan and S. A. Shevchenko, Pis'ma Zh. Éksp. Teor. Fiz. **20**, 709 (1974) [JETP Lett. **20**, 328 (1974)].
4. V. A. Goncharov, Yu. A. Osip'yan, and S. A. Shevchenko, Fiz. Tverd. Tela (Leningrad) **29**, 1928 (1987) [Sov. Phys. Solid State **29**, 1110 (1987)].
5. V. V. Kveder, R. Labusch, and Yu. A. Ossipyan, Phys. Status Solidi A **92**, 293 (1985).
6. D. J. Thouless, Phys. Rev. Lett. **39**, 1167 (1977).
7. R. Labusch and J. Hess, Phys. Status Solidi A **146**, 145 (1994).
8. I. A. Ryzhkin, Fiz. Tverd. Tela (Leningrad) **20**, 3612 (1978) [Sov. Phys. Solid State **20**, 2087 (1978)].
9. H. G. Brion and P. Haasen, Philos. Mag. A **51**, 879 (1985).
10. S. A. Shevchenko, Yu. A. Ossipyan, T. R. Mchedlidze, *et al.*, Phys. Status Solidi A **146**, 745 (1994).
11. S. A. Shevchenko, Zh. Éksp. Teor. Fiz. **115**, 115 (1999) [JETP **88**, 66 (1999)].
12. I. V. Klyatskina, M. L. Kozhukh, S. M. Ryvkin, *et al.*, Fiz. Tekh. Poluprovodn. (Leningrad) **13**, 1089 (1979) [Sov. Phys. Semicond. **13**, 638 (1979)].
13. A. I. Kolyubakin and S. A. Shevchenko, Phys. Status Solidi A **63**, 677 (1981).
14. S. A. Shevchenko, Fiz. Tekh. Poluprovodn. (Leningrad) **20**, 275 (1986) [Sov. Phys. Semicond. **20**, 172 (1986)].
15. E. Billig, Proc. R. Soc. London, Ser. A **235**, 37 (1956).
16. S. S. Gorelik, *Recrystallization of Metals and Allows* (Metallurgiya, Moscow, 1967), Chap. 2–5, p. 17.
17. F. J. Humpreys and M. Hatherly, *Recrystallization and Related Annealing Phenomena* (Pergamon, Oxford, 1996), Chap. 5–7, p. 127.
18. H. Siethoff and W. Schroeter, Z. Metallkd. **75**, 475 (1984).
19. D. Gwinner and G. Packeiser, Philos. Mag. A **42**, 645 (1980).
20. V. V. Rybin, *Large Plastic Strains and Fracture of Metals* (Metallurgiya, Moscow, 1986), Chap. l, p. 14.
21. F. Loucher, Solid State Phenom. **35–36**, 57 (1994).
22. G. A. Malygin, Usp. Fiz. Nauk **169**, 979 (1999).

Translated by A. Spitsyn

Semiconductors, Vol. 34, No. 5, 2000, pp. 534–537. Translated from Fizika i Tekhnika Poluprovodnikov, Vol. 34, No. 5, 2000, pp. 550–554.

ELECTRONIC AND OPTICAL PROPERTIES OF SEMICONDUCTORS

Optical Spectroscopy of Excitonic States in $CuInSe_2$

A. V. Mudryĭ*, M. V. Yakushev, R. D. Tomlinson**, A. E. Hill**, R. D. Pilkington**, I. V. Bodnar'***, I. A. Viktorov*, V. F. Gremenok*, I. A. Shakin*, and A. I. Patuk***

** Institute of Solid-State and Semiconductor Physics, Belarussian Academy of Sciences, ul. Brovki 17, Minsk, 220072 Belarus*
e-mail: mudryi@ifttp.bas-net
*** University of Salford, M54WT Salford, UK*
**** Belarussian State University of Information Science and Radio Engineering, ul. Brovki 17, Minsk, 220072 Belarus*
Submitted November 24, 1999; accepted for publication December 1, 1999

Abstract—Optical properties of structurally perfect $CuInSe_2$ single crystals were studied in the temperature range of 4.2–300 K with the use of photoluminescence, optical absorption, optical reflection, and wavelength-modulated optical reflection (WMOR). The intense lines of free excitons *A* (~1.0414 eV) and *B* (~1.0449 eV) with a half-width of ~0.7 meV at 4.2 K are found to be related to two extrema of valence band split by a crystal field. The excitons emission line *C* (~1.2779 eV) in WMOR spectra are related to a lower valence band split-off by spin-orbit interaction. Within the context of the quasi-cubic Hopfield model, the parameters of valence band splitting Δ_{CF} = 5.2 meV and Δ_{SO} = 234.7 meV defined by the crystal and spin–orbit interaction, respectively, are calculated. In the region of the fundamental absorption edge, the lines of bound excitons are found with a half-width ~0.3 meV that is indicative of a high quality of grown $CuInSe_2$ crystals. © *2000 MAIK "Nauka/Interperiodica".*

INTRODUCTION

Ternary $CuInSe_2$ compound (CIS) belongs to the I–III–VI_2 semiconductor group and crystallizes in the chalcopyrite structure. The CIS compound is a direct-band semiconductor with an extremely large optical absorption coefficient ~$(3–6) \times 10^7$ m^{-1} and is recognized as a promising material for the fabrication of highly efficient solar cells [1]. To date, CIS is one of a most studied compounds of the I–III–VI_2 semiconductor group; however, many of its properties, especially, optical properties, have not been adequately studied. In most cases, data on the fundamental parameters and the energy band structure of CIS material are contradictory or are completely absent. This is especially true of the experimental data on free and bound excitonic states and impurity optical transitions in the region of the fundamental absorption edge [2–4]. Studies of CIS properties were limited until recently by the absence of structurally perfect single crystals. Polycrystals and single crystals of low structural quality with irreproducible parameters have both been studied. However, only recently have photoluminescence (PL) spectra of polycrystalline thin films, 1.0398 and 1.0432 eV lines related to the ground and excited states of free excitons, respectively, been observed [3]. The lines of free excitons 1.039 and 1.045 eV close in energy to those mentioned above were observed in the PL spectra of films grown by molecular-beam epitaxy [2]. We observed a series of excitonic lines that peaked at ~1.0408 eV (ground state) and ~1.0446 eV (excited state) in the PL spectra of CIS single crystals [4]; the energies are higher than those reported in [2, 3]. In this paper, we report new data and give a new interpretation of excitonic luminescence in high-quality CIS single crystals. For the first time, simultaneously in PL, optical absorption (OA), and optical reflection spectra, the structure of *A* and *B* excitonic lines is resolved, with these excitons related to two extrema of the valence band split-off by the crystal field in CIS single crystals.

EXPERIMENTAL

The CIS samples with perfect structure and *p*-type conduction were cut from the middle part of ingots grown by the vertical Bridgman–Stockbarger method at the University of Salford. The optical properties of CIS single crystals were studied using PL, optical absorption, optical reflection, and wavelength-modulated derivative optical reflection (WMOR) in the temperature range of 4.2–300 K. PL was observed from the as-cleaved crystal faces. Optical absorption was measured in single crystals ~2–3 μm thick, which were freely immersed in liquid helium. Preparation of such samples was accomplished by mechanical polishing with subsequent chemical etching in a 1% solution of bromine in methanol. An argon laser operating at a wavelength of 488 nm was used as a source of optical excitation of nonequilibrium charge carriers in the luminescence experiments. In experiments with light absorption and reflection, a 100-W halogen lamp with a strip filament was used. A Ge *p–i–n* diode cooled to liquid nitrogen temperature was employed as a detector. The wavelength modulation was accomplished by the mirror plane rocking with a frequency of 20 Hz along the vertical axis in an MDR23 monochromator.

1063-7826/00/3405-0534$20.00 © 2000 MAIK "Nauka/Interperiodica"

The energy position of lines in PL, optical absorption and reflection, and WMOR spectra was determined within an accuracy of ±0.2 and ±0.4 meV, respectively.

EXPERIMENTAL RESULTS AND DISCUSSION

The typical PL spectra taken at 4.2 K in the region of the fundamental absorption edge are presented in Fig. 1 for three samples cut from different ingots. The experiments show that, for structurally perfect samples cut either from different ingots or from different parts of the same ingot, the PL spectra can differ but their shape is mainly limited to the three types presented in Figs. 1a–1c. As can be seen, no less than five relatively intense narrow lines designated as *M*1–*M*5 can be observed in PL spectra. The energy positions of the most intense luminescence lines determined within an accuracy of ±0.0002 eV are 1.0386 (*M*1), 1.0353 (*M*2), 1.0341 (*M*3), 1.0324 (*M*4), and 1.0278 eV (*M*5). Depending on the technological process of crystal growth (various ingots, samples), the relative intensities of *M*1–*M*5 lines in PL spectra can significantly vary to the extent of the absence of detection for some of them (see, e.g., Figs. 1a, 1b). Such a of variation of the line relative intensities from ingot to ingot, or from crystal to crystal, allows us to assume that they are caused by the radiative recombination of nonequilibrium carriers at defect–impurity complexes differing in nature and structure. Intense narrow lines *M*1–*M*5 have a half-width of ~0.3 meV at 4.2 K, and this half-width always remains less than kT when the temperature varies in the range of 4.2–40 K. The intensity of lines *M*1–*M*5 strongly decreases, with the temperature increasing from 4.2 K, and, at 40 K, the lines are virtually not observed in the PL spectra. Taking into account these experimental data, we consider that lines *M*1–*M*5 are related to zero-phonon (purely electronic) transitions caused by the radiative annihilation of excitons localized at the corresponding impurity centers. It is of importance to note that the most intense lines of bound excitons *M*1 and *M*2 have narrow short-wavelength components *M*1' (1.396 eV), *M*1" (1.0405 eV), and *M*2' (1.0359 eV), respectively, with a half-width of ~0.3 meV. The presence of "non-hydrogen-like" convergence to the high-energy side of spectrum is characteristic of components of lines *M*1 and *M*2. In this case, the energy distance between the lines is dissimilar, namely, *M*1–*M*1' ~ 1.03 meV and *M*1'–*M*1" ~ 0.85 meV, whereas *M*2–*M*2' ~ 0.64 meV and *M*2'–*M*2" ~ 0.45 meV. The larger splitting of components is characteristic of centers responsible for line *M*1, which have lesser exciton binding energy as compared to *M*2 centers. The redistribution of intensities between components of *M*1 and *M*2 lines is observed with a temperature increase from 4.2 K and obeys the Boltzmann law. This allows us to interpret *M*1', *M*1" and *M*2', *M*2" lines as a manifestation of excited excitonic states of *M*1 and *M*2 centers, respectively. On the basis of the analysis of

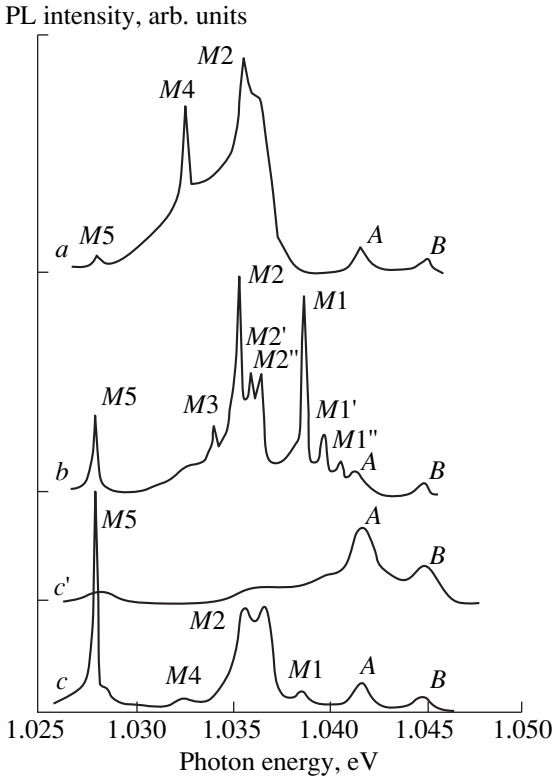

Fig. 1. Photoluminescence spectra for three various CIS single crystals (*a*, *b*, and *c*). The temperature of the crystals was (*a*, *b*, and *c*) 4.2 and (*c*') 40 K. Spectral resolution is 0.3 meV.

PL spectra and stoichiometric composition of the samples under study, we come to some conclusions about the nature of luminescent centers. Lines *M*1–*M*5 most probably appear as a result of annihilation of excitons bound by various neutral donors and acceptors, such as, e.g., Cu_i, Cu_{In}, In_i, etc., or atoms of uncontrollable residual impurities.

A most important experimental fact is the existence of two high-energy lines designated by us as *A* and *B* in Fig. 1. The experiments showed that the energy position of lines *A* and *B* does not change and their intensity increases practically linearly with an increase in excitation light intensity in the range from 0.2 to 20 W/cm^2. Lines *A* and *B* have the same half-width of ~0.7 meV (~2kT) at 4.2 K. The experiments showed that the intensity of lines *M*1–*M*5 diminishes much faster than that of *A* and *B* lines as the temperature increases. Taking this fact into account, it is reasonable to assume that the low-energy 1.0414-eV line is caused by the radiative recombination of free excitons (*A* excitons) and that a less intense high-energy line at 1.0449 eV (*B*) is caused by the radiative recombination of free excitons related to two extrema of valence band split-off owing to the influence of a noncubic crystal field in CIS single crystals. A temperature analysis of energy positions of lines *M*1–*M*5, lines *A* and *B*, and their half-width and intensities in the temperature range of 4.2–300 K confirms

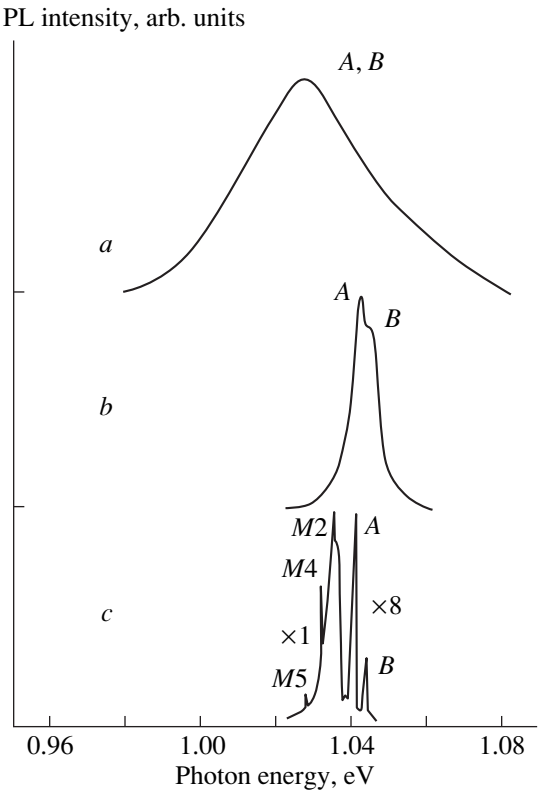

Fig. 2. Photoluminescence spectra of CIS single crystals at (*a*) 300, (*b*) 78, and (*c*) 4.2 K.

this interpretation. The PL spectra taken at various temperatures are presented in Fig. 2 for one of the samples (see the PL spectra of this sample also in Fig. 1). The experiments show that the low-energy intense lines *M*1–*M*5 completely disappear from PL spectra at temperatures of 40–45 K, which is caused by the dissociation of bound excitons and that lines *A* and *B* are related to the annihilation of free excitons and exist in the spectra up to room temperature. The absence of lines *M*1–*M*5 in PL spectra at $T \sim 40$ K is also clearly seen from data presented for another sample in Fig. 1 (curve *c*, *c*'). The spectra measured at 78 K include only two weakly resolved lines of free excitons *A* (~1.0426 eV) and *B* (~1.0459 eV) with a half-width of ~7 meV. PL spectra at 300 K consist of a single line with a peak at 1.028 eV and a half-width of 40 meV; this line is a contour of unresolved *A* and *B* lines of free excitons (Fig. 2). Experiments show that the energy position of lines *M*1–*M*5 and *A* and *B* depends on temperature. As the temperature increases (in the region of <80 K), all the lines shift similarly to higher energies in the spectrum and their relative energy positions are retained. This indicates that the energy position of the *M*1–*M*5 lines of bound excitons is defined by the temperature shift of band energy states. In particular, it is established that the energy of the ground state of *A* exciton increases from the value of ~1.0414 eV at 4.2 K up to the value of 1.0426 eV at 78 K and then decreases slowly to 1.028 eV at 300 K. A similar temperature dependence is characteristic of a 1.0449-eV line caused by *B* excitons. Such an anomalous temperature change of the bandgap E_g can be caused by the combined effect of the lattice constant change and electron–phonon interaction. A similar temperature dependence of E_g was established for other chalcopyrite semiconductor compounds, namely, $CuGaSe_2$, $AgInSe_2$, etc. (see, e.g., [4–6]). In addition to PL measurements, we measured the absorption and reflection spectra with a high spectral resolution of ~0.1 meV at low temperatures. The results of these measurements are shown in Fig. 3. We succeeded in resolving clearly the lines of free excitons *A* and *B* in the optical absorption and reflection spectra, and, within the accuracy of ±0.0002 eV, their energy positions corresponded to the luminescence data. The half-width of *A* and *B* lines in absorption and reflection spectra turned out to be ~0.7–0.8 meV at 4.2 K, which is consistent with PL data. It is established also that *A* and *B* lines in absorption, reflection, and in PL spectra have the same temperature dependence of energy positions in the range of 4.2–78 K. We observed the third exciton transition *C* caused by a spin–orbit interaction in CIS material only when measuring the reflection with the wavelength modulation. At 4.2 K, the energy position of the *C* exciton line was 1.2779 eV. Measurements of polarization dependence of spectra for orientation of the electrical vector of analyzing polarizer $E \parallel Z$ and $E \perp Z$, where *Z* is the optical axis of CIS crystals, showed that the intensities of components *A*, *B*, and *C* were consistent with the quasi-cubic model [7, 8]. Employing the Hopfield quasi-cubic model for the splitting of a three-fold degenerate valence band with consideration of the effect of the noncubic (tetragonal) crystal field and spin–orbit interaction, we calculated the corresponding parameters of the valence band Δ_{CF} and Δ_{SO} [7, 8]. According to this model, the energy of Γ_7 levels with respect to the energy of the Γ_6 level for the valence band of ternary chalcopyrite semiconductors is described by the following equations:

$$\Delta_{CF} = -1/2(E_1 + E_2) - 1/2[(E_1 + E_2)^2 - 6E_1E_2]^{1/2}, \quad (1)$$

$$\Delta_{SO} = -1/2(E_1 + E_2) + 1/2[(E_1 + E_2)^2 - 6E_1E_2]^{1/2}, \quad (2)$$

where Δ_{SO} is the magnitude of the spin–orbit splitting of the valence band in a cubic field; Δ_{CF} is the magnitude of splitting caused by the crystal field in the absence of spin–orbit splitting; and $E_1 = E_A - E_B$ and $E_2 = E_A - E_C$ are the energy distances between the two upper and lower valence bands, respectively [9, 10]. Using the energies found in our experiments for *A*, *B*, and *C* transitions, 1.0414, 1.0449, and 1.2779 eV, respectively, we determined the values of $\Delta_{CF} = 5.2$ meV and $\Delta_{SO} = 234.7$ meV from expressions (1) and (2). We note that two lines *A* and *B* with significantly lower values of energy were observed previously in electroreflectance spectra of CIS single crystals at 77 K [8]. The energy

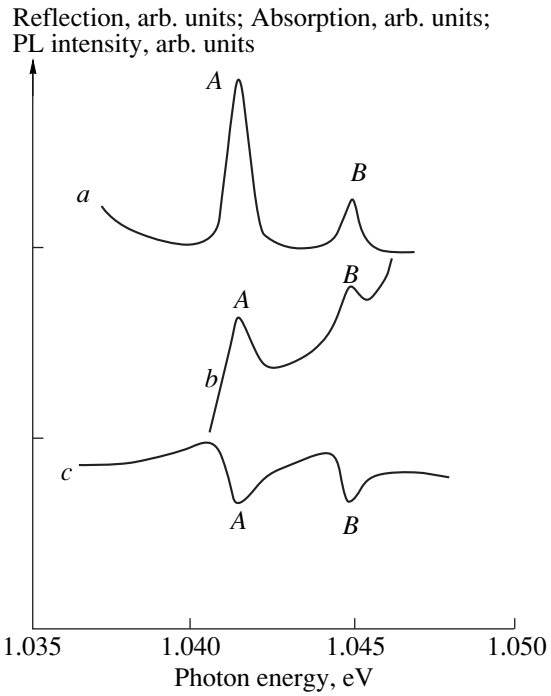

Fig. 3. Photoluminescence (*a*), absorption (*b*), and reflection (*c*) spectra of high-quality CIS single crystals at 4.2 K. Spectral resolution is 0.1 meV.

separation between the lines was equal to 3.8 meV, which agrees satisfactorily with the value of 3.5 meV obtained in our experiments.

We should mention some important facts. First, in experiments with PL, absorption, and reflection, the half-width of exciton lines *A* and *B* was 0.7 meV at 4.2 K, which is the smallest half-width thus far determined for CIS material. Second, the half-width of lines for bound excitons *M*1–*M*5 was also small and was 0.3 meV at 4.2 K. It is known that, at low temperatures (~1–4.2 K), a typical line half-width for free and bound excitons is 0.7–1.0 and 0.1–0.3 meV, respectively, in structurally perfect semiconductor single crystals (GaAs, ZnS, ZnSe, CdS, InSe etc.). Third, only free exciton lines are present in PL spectra of CIS single crystals at 78 K. These experimental facts are indicative of the structural perfection of the CIS single crystals we studied. The results obtained in this work suggest another interpretation of line *B*; namely, this line may be assigned to free *B* excitons, as distinct from its previous assignment to the first excited state of *A* excitons [2–4]. The following facts support such an interpretation: (i) the different polarization of lines *A* and *B*, and (ii) the unusually high intensity of line *B* with respect to line *A* ($I_A/I_B \approx 1/3$) in optical spectra. If line *B* is related to the first excited state of *A* excitons, then, according to the exciton theory, its intensity would amount to less than $I_A/8$ according to the expression $I_n = n^{-3}[(E^0_{ex} - E_g)/n^2kT]$; i.e., it would diminish faster than n^{-3}, where *n* is the principal quantum number.

CONCLUSION

Thus, it is established that, for structurally perfect CIS single crystals at low temperatures (<40 K), the photoluminescence spectra involve the well-resolved lines of free and bound excitons with a half-width comparable to that for other high-quality and well-studied semiconductors. Based on the absorption and reflection measurements, we verified for the first time the existence of valence band splitting in CIS material due to the influence of a noncubic crystal field. Using the quasi-cubic Hopfield theory, we determined the numerical values of parameters $\Delta_{CF} = -5.2$ meV and $\Delta_{SO} = 234.7$ meV of valence band splitting caused by the crystal-field and spin–orbit splitting, respectively.

ACKNOWLEDGMENTS

This work was supposed by EPSRC (grant no. GR/L 62757), INTAS (grant no. 634), and the Foundation for Basic Research of the Republic of Belarus (grant no. F98-201).

REFERENCES

1. H. W. Schock, Sol. Energy Mater. Sol. Cells **34**, 19 (1994).
2. S. Niki, H. Shibata, P. J. Fons, *et al.*, Appl. Phys. Lett. **67**, 1289 (1995).
3. J. H. Schön, V. Alberts, and E. Bucher, J. Appl. Phys. **81**, 2799 (1997).
4. A. V. Mudryĭ, I. V. Bodnar, V. F. Gremenok, *et al.*, Sol. Energy Mater. Sol. Cells **53**, 247 (1988).
5. J. J. Binsma, L. J. Giling, and J. Bloem, J. Lumin. **27**, 55 (1982).
6. V. A. Aliyev, G. D. Gusseinov, F. L. Mamedov, *et al.*, Solid State Commun. **59**, 745 (1986).
7. J. J. Hopfield, J. Phys. Chem. Solids **15**, 97 (1960).
8. J. L. Shay and J. W. Wernick, *Ternary Chalcopyrite Semiconductors: Growth, Electronic Properties, and Applications* (Pergamon, New York, 1975).
9. J. L. Shay and B. Tell, Surf. Sci. **37**, 748 (1973).
10. N. Yamamoto, H. Horinaka, K. Okada, and T. Miyauchi, Jpn. J. Appl. Phys. **16**, 1817 (1977).

Translated by T. Galkina

Semiconductors, Vol. 34, No. 5, 2000, pp. 538–540. Translated from Fizika i Tekhnika Poluprovodnikov, Vol. 34, No. 5, 2000, pp. 555–557.

ELECTRONIC AND OPTICAL PROPERTIES OF SEMICONDUCTORS

Effect of Uniaxial Deformation on Electrophysical Parameters of 6*H*-SiC *p–n* Structures

A. A. Lebedev

Ioffe Physicotechnical Institute, Russian Academy of Sciences, Politekhnicheskaya ul. 26, St. Petersburg, 194021 Russia

Submitted November 26, 1999; accepted for publication December 1, 1999

Abstract—The effect of uniaxial pressure on the electroluminescence (EL) spectrum and current–voltage (*I–V*) characteristics of a 6*H*-SiC *p–n* structure was studied. Under the effect of pressure, a fast quenching of the excitonic EL is observed and a slower quenching of the impurity EL bands. Uniaxial pressure also distorts the shape of the forward *I–V* characteristic and shifts it to lower voltages. A conclusion is made that the application of pressure leads to the transformation of thermal injection currents into tunneling currents. © *2000 MAIK "Nauka/Interperiodica".*

INTRODUCTION

Uniaxial deformation of semiconductor crystals is widely used in studying luminescence spectra and optical absorption, electron paramagnetic resonance spectroscopy of local centers, and deep-level transient spectroscopy [1–3]. Application of a uniaxial pressure in certain directions changes the crystal symmetry and (or) the forbidden gap, which furnishes additional information about the crystal structure of a semiconductor and its defect centers.

The effect of uniaxial stress on the photoluminescence of 6*H*-SiC single crystals was studied in [4]. It was found that a uniaxial pressure of ~10–30 kbar shifted the energy position of some impurity luminescence lines characteristic of 6*H*-SiC and caused their doubling. The exact magnitudes of the shifts as well as the estimates of possible variations in the bandgap were not reported.

SAMPLES

In this work, we studied 6*H*-SiC *p–n* structures prepared by sublimational epitaxy in an open system [5] and used to fabricate various SiC-based semiconductor devices [6]. The *p–n* structures were grown on the (0001)Si face of single-crystal n^+ silicon carbide substrates of the 6*H* polytype. Al (*p*-type) and N (*n*-type conduction) were used as dopants. The thickness of *p*-type epitaxial layers was 1–2 μm, and that of the *n*-type layers was 5–10 μm. The area of the *p–n* structures was $\sim 2.5 \times 10^{-3}$ cm^2.

The capacitance–voltage characteristics of the diodes under study were linear when plotted as C^{-2} as a function of U. The related cutoff voltage was 2.55 V at room temperature. The current–voltage (*I–V*) characteristics of the diodes taken in the current range 10^{-6}–5×10^{-4} A were exponential $J = J_0 \exp(qU/\beta kT)$, where $\beta \sim 1.2$, q is the elementary charge, k is the Boltzmann constant, and T is the absolute temperature.

EXPERIMENT

For investigations, we selected *p–n* structures exhibiting well pronounced excitonic electroluminescence (EL). Pressure was applied to the upper and lower non-

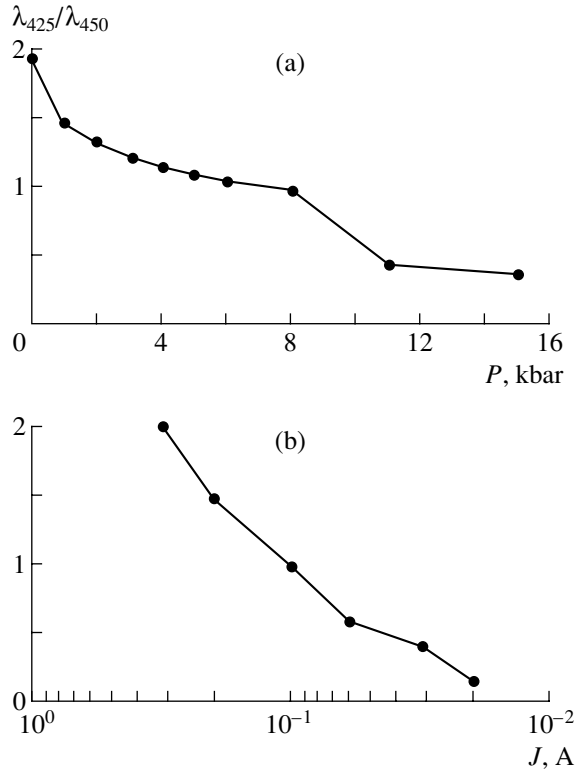

Fig. 1. Relative intensity of excitonic EL in 6*H*-SiC *p–n* as a function of (a) applied uniaxial pressure and (b) forward current.

1063-7826/00/3405-0538$20.00 © 2000 MAIK "Nauka/Interperiodica"

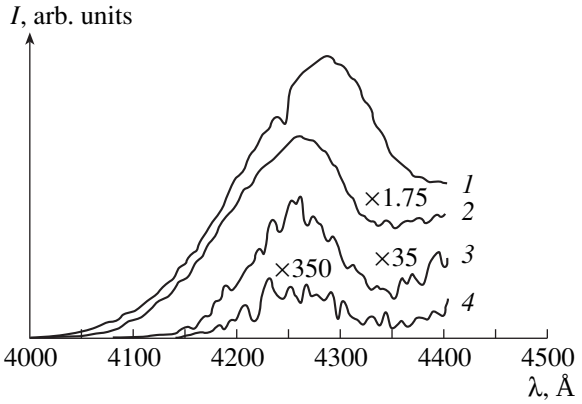

Fig. 2. Spectra of excitonic EL of a 6*H*-SiC *p–n* structure, taken at uniaxial pressures P = (*1*) 0, (*2*) 5, (*3*) 11, and (*4*) 15 kbar.

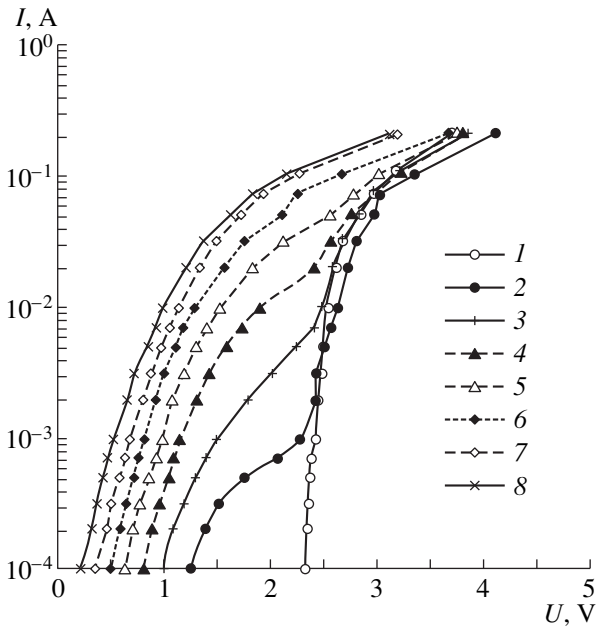

Fig. 3. Forward *I–V* characteristics of a 6*H*-SiC *p–n* structure in relation to the applied uniaxial pressure P = (*1*) 0, (*2*) 0.2, (*3*) 1, (*4*) 3, (*5*) 5, (*6*) 8, (*7*) 10, (*8*) 15 kbar.

rectifying contacts in the direction parallel to the *c*-axis of the crystal. Emission was extracted through its lateral face. In this experimental configuration, the uniaxial strain had no effect on the crystal lattice symmetry but could change the bandgap, i.e., could induce a shift of the excitonic band peak.

It was found that, with increasing applied pressure P (at a fixed forward current J), the intensity of the excitonic EL decreased rapidly, while that of other EL bands decreased more slowly. An increase in pressure led to the same change in the EL spectrum as a decrease in J (resulting in a lower concentration of carriers injected into the base) [7]. Figure 1 shows variation in the ratio of EL intensities at 4250 and 4500 Å ($I_{425/450}$) with pressure. It can be seen that the application of a uniaxial pressure of ~15 kbar reduces the $I_{425/450}$ value approximately to the same extent as does a decrease by an order of magnitude in the current through the *p–n* structure at $P = 0$.

In studying the effect of pressure on the EL spectrum, the forward current through the *p–n* structure was maintained constant. For the excitonic band to be well distinguishable at high pressures P as well, a rather high current was chosen (400 mA). With such a current passing through the *p–n* structure, the latter was self-heated to a temperature of ~500 K. For this reason, the excitonic band had a peak (λ_{max}) at 4280 Å at $P = 0$ (Fig. 2). With increasing applied pressure, the peak was shifted to shorter wavelengths (to $\lambda_{max} \approx 4250$ Å at P = 15 kbar).

A separate investigation was performed of the effect of pressure on the *I–V* characteristics of the diodes. It was found that, with increasing P, the shape of the $I(V)$ curve was distorted strongly—the value of β increased—and the characteristic itself was shifted to lower voltages in the region of low currents (Fig. 3). Up to pressures of ≅30 kbar, the *I–V* characteristics typically returned to their initial shape after the uniaxial pressure was removed. In some cases, an irreversible distortion of the exponential shape of the *I–V* characteristics was observed for currents $\leq 3 \times 10^{-3}$ A, which was presumably due to irreversible changes in the crystal, that appeared under pressure. A further increase in pressure typically led to the fracture of crystals.

CONCLUSION

Thus, it was found that application of a uniaxial pressure (parallel to the *c*-axis of the crystal) to 6*H*-SiC *p–n* structures decreases the EL intensity at a fixed current. In our opinion, a decrease in the EL intensity may be due to a decrease in the concentration of holes injected into the base (i.e., to a transformation of thermal injection currents into tunneling currents). The *I–V* characteristics observed in this case are typical of tunneling currents that are predominant in neutron-irradiated SiC *p–n* structures [8] and also in unirradiated structures at low temperatures. We note that the *I–V* characteristics of this kind (with leakage currents) are also possible in unirradiated structures at higher temperatures. The observed reversibility of distortion of the *I–V* characteristics suggests that strain fields arising in SiC in the course of *p–n* junction growth may be a reason for the appearance of such leakage currents.

In addition, it was found that the peak of the excitonic EL band was shifted by ≈20 meV under the effect of a pressure of 15 kbar. We note, however, that this shift may be at least partly due to a weaker self-heating of the structure. Among the conceivable reasons are both a decrease in the applied voltage at the same current (because of the changed shape of the *I–V* charac-

teristic) and the possible improvement of the heat sink. Thus, a conclusion can be made that the change in the bandgap of 6*H*-SiC on applying a pressure of 15 kbar does not exceed 20 meV.

REFERENCES

1. A. A. Kaplyanskiĭ, Opt. Spektrosk. **10**, 165 (1961).
2. A. A. Kaplyanskiĭ, N. A. Moskvin, and A. K. Przhevuskiĭ, Opt. Spektrosk. **10**, 368 (1961).
3. A. A. Lebedev, N. A. Sultanov, and V. Ékke, Fiz. Tekh. Poluprovodn. **21**, 321 (1987) [Sov. Phys. Semicond. **21**, 193 (1987)].
4. Ch. Haberstroh, R. Helbig, and R. A. Stein, J. Appl. Phys. **76**, 509 (1994).
5. M. M. Anikin, A. A. Lebedev, S. N. Pyatko, *et al.*, Mater. Sci. Eng., B **11**, 113 (1992).
6. M. M. Anikin, P. A. Ivanov, A. A. Lebedev, *et al.*, in *Semiconductor Interfaces and Microstructures*, Ed. by Z. C. Feng (World Scientific, Singapore, 1990), p. 280.
7. A. A. Lebedev and V. E. Chelnokov, Diamond Relat. Mater. **3**, 1393 (1994).
8. V. V. Evstropov and A. M. Strel'chuk, Fiz. Tekh. Poluprovodn. **30**, 92 (1996) [Semicond. **30**, 52 (1996)].

Translated by M. Tagirdzhanov

Semiconductors, Vol. 34, No. 5, 2000, pp. 541–544. Translated from Fizika i Tekhnika Poluprovodnikov, Vol. 34, No. 5, 2000, pp. 558–561.

ELECTRONIC AND OPTICAL PROPERTIES OF SEMICONDUCTORS

Deep-Level Centers in Undoped *p*-GaAs Layers Grown by Liquid Phase Epitaxy

L. S. Berman, V. G. Danil'chenko, V. I. Korol'kov, and F. Yu. Soldatenkov

Ioffe Physicotechnical Institute, Russian Academy of Sciences, Politekhnicheskaya ul. 26, St. Petersburg, 194021 Russia

Submitted December 2, 1999; accepted for publication December 6, 1999

Abstract—Deep-level centers in GaAs-based *p–n* junctions, which were fabricated by a liquid phase epitaxy in hydrogen or argon ambients, were investigated. The minority charge carrier lifetime for *p*-layers grown in hydrogen is an order of magnitude larger than that for *p*-layers grown in argon. It is demonstrated that disimilar deep-level centers are formed in different gas media. Two types of deep-level centers, which act as hole traps, are found in the samples grown in hydrogen. The Arrhenius dependences for these centers are close to known dependences for *HL*2 and *HL*5 centers, suggesting that the centers observed can be identified as *HL*2 and *HL*5 centers. One type of deep-level center, which is a hole trap, is found in the samples grown in argon. This center is identified as arsenic in the gallium sublattice. © *2000 MAIK "Nauka/Interperiodica".*

1. INTRODUCTION

At present, liquid phase epitaxy is one of the major methods for obtaining the undoped GaAs layers and formation of high-voltage p_0–n_0 junctions on their basis. The p_0–n_0 junctions obtained in this way find expanding application in the development of fast diodes and thyristors. The mechanism of formation of the undoped GaAs-based *p–n* structures by the background impurities was considered in [1, 2]. It was found that the static and dynamic device characteristics depend significantly on the parameters of the *p*-layers. For this reason, the aim of this work was to investigate the interface between the *n*-substrate and *p*-layer as well as the *p*-layer itself.

2. SAMPLES

The high-voltage p_0–n_0 structures were grown on the n^+-GaAs:Sn substrates with the donor concentration $N_d = 10^{18}$ cm^{-3} using a liquid phase epitaxy (LPE) from the limited volume of a solution–melt in a quartz vessel in the range from 900°C to room temperature in an atmosphere of hydrogen (group 1) or argon (group 2). Except for the gas medium, the samples of both groups were prepared identically.

During the growth, first the *p*-layer and then the *n*-layer was formed on the substrate because of self-doping [1]. Subsequent to that, the *n*-layer was removed by etching, and the p^+-GaAs:Ge layer with the acceptor concentration $N_a = 10^{18}$ cm^{-3} was grown on the *p*-layer. The ohmic contact layers Au + Zn and Au + Ge were formed on the p^+- and n^+-layers, respectively. The samples 2×2 mm^2 in size were cleaved from the obtained epitaxial wafers with contact layers.

The evaluation of the possible Sn diffusion from the n^+-substrate demonstrates that the penetration of Sn in the *p*-layer can be neglected and, consequently, the n^+–*p* junction is virtually abrupt.

3. MEASUREMENT TECHNIQUES

The current–voltage (*I–V*) characteristics, the capacitance–voltage (*C–V*) characteristics, the DLTS signals [3], and minority carrier lifetime were measured. The automated equipment for capacitance transient spectroscopy of semiconductors was used [4]. The electron lifetime τ_n in the *p*-base was measured using a Lax technique with regard to a finite base thickness [5].

The concentration of shallow acceptors N_{da} and deep-level centers N_t was determined by measuring the *C–V* characteristics at two temperatures T_1 and T_2:

(a) $T_1 > 350$ K, when the steady-state occupancy of deep-level centers by electrons or holes keeps pace with the variation of the dc voltage;

(b) $T_2 < 80$ K, when the initial occupancy of deep-level centers remains unchanged during measurements [6].

The concentration of ionized impurities N_i in the space charge region (except for the layer of incompletely ionized deep-level centers, the so-called λ-layer) at T_1 can be determined from the expression

$$N_i(T_1) = N_{da} + N_{ta} - N_{d0}, \quad (1)$$

and at T_2, with the increase of the reverse bias from zero, it can be determined from the expression

$$N_i(T_2) = N_{da} - N_{td} - N_{d0}, \quad (2)$$

where N_{da} is the dopant concentration (shallow acceptors), N_{ta} and N_{td} are the concentrations of deep level acceptors and donors in the lower half of the bandgap, and N_{d0} is the concentration of donors in the upper half of the bandgap.

1063-7826/00/3405-0541$20.00

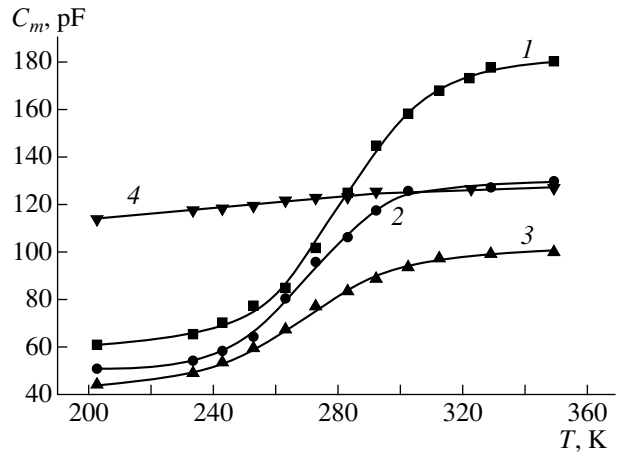

Fig. 1. Temperature dependences of the measured capacitance C_m for the samples of group 1 at reverse voltages V (*1*) 5, (*2*) 10, and (*3*, *4*) 20 V.

Subtracting (2) from (1), we find the concentration of deep-level centers in the lower half of the bandgap:

$$N_i(T_1) - N_i(T_2) = N_{ta} + N_{td}. \quad (3)$$

4. RESULTS OF MEASUREMENTS AND THEIR DISCUSSION

4.1. Samples of Group 1

The value of the $N_i(T_1)$ quantity for all of the samples was in the range of $(0.9–1.2) \times 10^{15}$ cm^{-3} and varied only slightly within the space charge region thickness w = 1.2–5.1 μm.

For T_1 = 350 K, the value of w found from the formula

$$C_m = \varepsilon/Aw \quad (4)$$

coincides (within an error of 10%) with the value calculated from the formula for an abrupt n^+–p junction

$$w = \sqrt{\frac{2\varepsilon(V + V_{bi})}{qN_i(T_1)}}, \quad (5)$$

where C_m is the experimental value of capacitance, A is the n^+–p junction area, ε is the dielectric constant, V is the reverse voltage, V_{bi} is the contact potential difference between the n^+ and p regions, and q is the elementary charge. This result confirms that the n^+–p junction is virtually abrupt.

The temperature dependences of capacitance at dc reverse voltages were investigated. The measured capacitance C_m for some of the samples varied substantially in the temperature range T = 260–330 K. The dependences $C_m(T)$ for one of these samples at several reverse voltages are shown in Fig. 1 (curves *1–3*). These dependences are defined by the presence of the overcompensated layer in the diode base, which manifests itself in an abrupt increase in the layer resistance on cooling. We determined the capacitance and thickness d of the overcompensated layer for a given sample using the C_m values at $T > 350$ K and $T < 200$ K. No dependence of the d value on the voltage is observed in the reverse bias range of $5 < V < 20$ V: $d = 5.2 \pm 0.3$ μm. This result demonstrates that a partially compensated layer exists between the overcompensated layer and the space charge region. This can be explained by the gradual decrease in the dopant concentration along the base depth. The dependence $C_m(T)$ for another sample of group 1 is also shown in Fig. 1 (curve *4*). The observed weak temperature dependence of the capacitance, which is characteristic of the barrier capacitance [7], points to the absence of the overcompensated layer. Since the spread in $N_i(T_1)$ is small (see above), the presence or absence of the overcompensated layer is apparently defined by the spread in N_{td} over the wafer area.

For the samples without overcompensated layer, we analyzed the C–V characteristics at T = 80 K and found that $N_i(T_2) = (0.2–0.3) \times 10^{15}$ cm^{-3}. Subsequently, from (3), we found $N_{ta} + N_{td} = (0.7–0.8) \times 10^{15}$ cm^{-3}.

The DLTS signals were measured for the samples without overcompensated layer in the temperature range of $80 < T < 350$ K. Two DLTS peaks, which were identical for all of the samples, were observed in the range of $230 < T < 350$ K after switching from 0.1 to 10 V. These peaks correspond to two hole-trap deep-level centers. The temperature dependences of the thermal emission time $\tau_{th}(T)$ (Arrhenius plots) for holes were found from these peaks for two deep-level centers (Fig. 2, curves *1*, *2*). Ignoring the temperature dependences of the hole-capture cross sections, we determine the energies of ionization E_{t1} and E_{t2}, the hole-capture cross sections σ_{p1} and σ_{p2}, and concentrations N_{t1} and N_{t2} for these two centers. We found $E_{t1} = E_v + (0.83 \pm 0.02)$ eV, $N_{t1} = 0.3 \times 10^{15}$ cm^{-3}, $\sigma_{p1} = 10^{-(14 \pm 1)}$ cm^2, $E_{t2} = E_v + (0.47 \pm 0.02)$ eV, $N_{t2} = 0.4 \times 10^{15}$ cm^{-3}, and $\sigma_{p2} = 10^{-(12 \pm 1)}$ cm^2. Consequently, $N_{t1} + N_{t2} \approx N_{ta} + N_{td}$. Hence, the concentrations of deep-level centers measured using the methods of the C–V characteristics and DLTS coincide.

Similar DLTS signals were obtained after switching from the forward voltage, which corresponded to a current of 10 mA, to the reverse voltage of 10 V. The Arrhenius plots for both deep-level centers are close to dependences for the *HL*2 (*B*) and *HL*5 (*HB*5, *A*) centers according to reviews and reference books [8–12] (Fig. 2, straight lines *3* and *4*). It is known that *HL*2 and *HL*5 centers are observed in certain GaAs layers grown by LPE in an H_2 atmosphere (see, for example, [2, 8, 11]). We note that the significant spread of the data on ionization energies and capture cross sections was observed in [2, 8, 11]. It is possible that this spread is caused by different growth conditions [11]. Another possible cause of the spread of the parameters reported in publications is the fact that even a small error in mea-

suring the Arrhenius plot can bring about a significant error in the ionization energy and capture cross section. The analysis performed allows us to suppose that the deep-level centers of type 1 and deep-level centers of type 2, which were observed in our work, are identical to *HL*2 and *HL*5 centers, respectively.

The values of τ_n at a current density of 1–10 A/cm^2 are equal to 200–250 ns. The electron-capture cross section for the *HL*5 center is $\sigma_n = 8 \times 10^{-17}$ cm^2 and for the *HL*2 center is $\sigma_n = 2 \times 10^{-19}$ cm^2 at $T = 300$ K [15]. Let us use the known formula $\tau_n = (\sigma_n v_{Tn} N_t)^{-1}$. Here, v_{Tn} is the thermal velocity of electrons ($v_{Tn} = 4.5 \times 10^7$ cm/s at $T = 300$ K). In this case, we have $\sigma_n \approx$ 700 ns for the center concentration $N_t = 0.4 \times 10^{15}$ cm^{-3}, and, hence, the *HL*5 center in our samples is an efficient recombination center.

4.2. Samples of Group 2

The value $N_i(T_1) = (2–3) \times 10^{15}$ cm^{-3} was determined from measurements. The weak temperature dependence of the capacitance (the temperature coefficient of the capacitance is equal to 2×10^{-4} K^{-1}) points to the absence of the overcompensated layer in the base. One DLTS peak, from which the dependence $\tau_{th}(T)$ was determined (Fig. 2, curve *5*), was observed in the range of $80 < T < 350$ K. We determined the ionization energy $E_t = E_v + (0.62 \pm 0.02)$ eV and $N_t = 0.2 \times 10^{15}$ cm^{-3} for this center (deep-level center of type 3). The $\tau_{th}(T)$ dependence coincided with the $\tau_{th}(T)$ dependence for Fe in GaAs [13] with an error less than 15% (Fig. 2, curve *6*). However, it is known that Fe is a rare background impurity in the GaAs epitaxial layer [16]. This can be explained by a low segregation coefficient of iron (on the order of 10^{-7}) at the temperature of epitaxial growth ($T < 800$–900°C) [13]. Using this value of the segregation coefficient, we can demonstrate that the iron concentration in our epitaxial layers cannot exceed 10^{11} cm^{-3}. The $\tau_{th}(T)$ dependence for a deep-level center, which is denoted as *HM*1 and is supposedly an antisite defect (arsenic in the gallium sublattice) [14], is also shown in Fig. 2 (curve *7*). The τ_{th} value for this deep-level center at room temperature is approximately two times less than for the observed deep-level center of type 3. However, the Schottky diodes with the shallow-impurity concentration in the base lower than $(5–10) \times 10^{16}$ cm^{-3} were used in [14]. This means that the field reaches a value several times higher than 10^5 V/cm even for the reverse voltage of several volts, and the thermal emission can be several times more intense in these fields [6, 17]. For this reason, we identify the deep-level center of type 3 hypothetically as *HM*1 (i.e., as arsenic in the gallium sublattice) rather than iron.

The electron lifetime at a current density of 1–50 A/cm^2 is $\tau_n = 25$–30 ns.

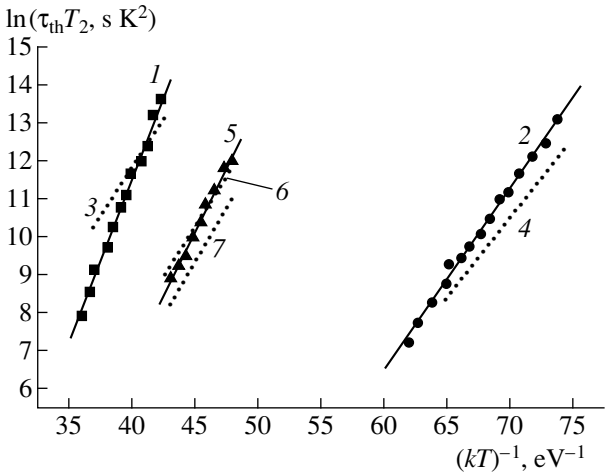

Fig. 2. Arrhenius plots. The sample of group 1: (*1*) deep-level centers of type 1 and (*2*) deep-level centers of type 2 (our results), (*3*) *HL*2 and (*4*) *HL*5 (*HB*5) centers according to [8]. The sample of group 2: (*5*) deep-level centers of type 3, (*6*) Fe in GaAs according to [13], and (*7*) As in the Ga sublattice according to [14].

Hence, different deep-level centers are formed in the samples belonging to groups 1 and 2, although the conditions of fabricating these samples were identical except for the gas medium. Let us consider the possible reasons for these distinctions. The GaAs layers are saturated with silicon, oxygen, and their compounds from the Ga melt during growth in the hydrogen atmosphere mainly because of quartz reduction by hydrogen with formation of silicon oxide and water vapor. As a result, the silicon and oxygen content in an inactive state can reach 10^{17}–10^{18} cm^{-3} in undoped GaAs layers. Contamination of the Ga melt with these impurities should be substantially lower during GaAs growth in the argon atmosphere. This leads to a significant difference in the impurity background in the Ga melt and, consequently, in the GaAs layer during the growth in the flows of H_2 or Ar.

It is also known that the impurity type and concentration additionally affect the concentration of electrically active defects. In addition, silicon and oxygen are the active complex-forming agents. The aforementioned suggests that the appearance of deep-level centers of type 1 (*HL*2) and deep-level centers of type 2 (*HL*5) in the samples of group 1 is related to the influence of silicon and oxygen. We can also suppose that deep-level centers of type 1 and deep-level centers of type 2 can contain the atoms of these elements. According to [18], the concentrations of *HL*2 and *HL*5 centers are defined mainly by the growth temperature in H_2. However, our results point to the significant influence of impurities on the concentration of these deep-level centers, all other factors being the same.

5. CONCLUSION

All n^+–p junctions are virtually abrupt.

Different deep-level centers are formed in the p-layers grown in hydrogen and argon; the concentration of deep-level centers is substantially lower in the latter case. This can be explained by the substantially lower concentration of oxygen and silicon. Deep-level centers in the samples grown in hydrogen are apparently identical to the *HL*2 and *HL*5 centers. As for samples grown in argon, these centers are identical to arsenic in the gallium sublattice (*HM*1).

The absence of deep-level centers *HL*2 and *HL*5 in the samples grown in argon points to the significant influence of the impurity medium on the formation of these centers. The minority carrier lifetime for the samples grown in argon is substantially less than for the samples grown in hydrogen.

REFERENCES

1. V. G. Nikitin, I. Rachinska, E. P. Seel', *et al.*, in *Proceedings of Third All-Union Conference on Physical Processes in Semiconductor Heterostructures, Odessa* (1982), Vol. 2, p. 146.
2. M. M. Sobolev, P. N. Brunkov, S. G. Konnikov, *et al*., Fiz. Tekh. Poluprovodn. (Leningrad) **23**, 1058 (1989) [Sov. Phys. Semicond. **23**, 660 (1989)].
3. D. V. Lang, J. Appl. Phys. **45**, 3023 (1974).
4. L. S. Berman, A. D. Remenyuk, and M. G. Tolstobrov, Preprint No. 974, FTI (Physicotechnical Institute, Russian Academy of Sciences, Leningrad, 1985).
5. Yu. R. Nosov, *Switching in Semiconductor Diodes* (Nauka, Moscow, 1968; Plenum Press, New York, 1969).
6. L. S. Berman, *Capacitance Spectroscopy of Deep Centers in Semiconductors* (Nauka, Moscow, 1981).
7. L. S. Berman, *Introduction to the Physics of Varactors* (Nauka, Moscow, 1968; Israel Program for Scientific Translations, Jerusalem, 1970).
8. A. Mitoneau, G.M. Martin, and A. Mircea, Electron. Lett. **13**, 666 (1977).
9. Landolt-Börstein, *Impurities and Deep Defects in Group IV Elements and III–V Compounds* (Springer-Verlag, 1989), New Series, Vol. 22b.
10. J. C. Bourgoin, H. T. Bardeleben, and D. Stievenard, J. Appl. Phys. **64**, R65 (1988).
11. D. Pons and J.C. Bourgoin, J. Phys. C **18**, 3839 (1985).
12. F. Hasegava and A. Majerfield, Electron. Lett. **11**, 286 (1975).
13. M. Kleverman, P. Omling, L.-A. Ledebo, *et al.*, J. Appl. Phys. **54**, 814 (1983).
14. G. Lagovski, D. G. Lin, T. P. Chen, *et al.*, Appl. Phys. Lett. **47**, 929 (1985).
15. C. H. Henry and D. V. Lang, Phys. Rev. B: Condens. Matter **15**, 989 (1977).
16. V. M. Andreev, L.M. Dolginov, and D. N. Tret'yakov, *Liquid-Phase Epitaxy in the Technology of Semiconductor Devices* (Sov. Radio, Moscow, 1975).
17. L. S. Berman, *Purity Control of Semiconductors by the Method of Capacitance Transient Spectroscopy* (St. Petersburg, 1995).
18. S. I. Ponomarev, A. B. Raĭtsyn, T. V. Rossina, *et al.*, in *Proceedings of Seventh All-Union Conference on Growth and Synthesis of Semiconductor Crystals and Films, Novosibirsk* (1986), Chap. 2, p. 246.

Translated by N. Korovin

Semiconductors, Vol. 34, No. 5, 2000, pp. 545–549. Translated from Fizika i Tekhnika Poluprovodnikov, Vol. 34, No. 5, 2000, pp. 562–566.

SEMICONDUCTOR STRUCTURES, INTERFACES, AND SURFACES

Photocapacitance Effect in a Monopolar Metal–Insulator–Semiconductor Capacitor at Low Temperatures

N. A. Penin

Lebedev Institute of Physics, Russian Academy of Sciences, Leninskiĭ pr. 53, Moscow, 117924 Russia

Submitted October 13, 1999; accepted for publication November 16, 1999

Abstract—The photocapacitance effect was theoretically studied in the case of optical ionization of impurity atoms in a monopolar MIS capacitor at low temperatures. Analytical expressions were derived for capacitance–voltage and photocapacitance–voltage characteristics of the MIS capacitor with a *p*-type semiconductor electrode. The dependence of photocapacitance sensitivity on bias was shown to exhibit a relatively narrow peak whose height and position depend on donor concentration. Capacitance and photocapacitance characteristics were calculated for the MIS capacitor with an indium-doped silicon electrode. © *2000 MAIK "Nauka/Interperiodica"*.

INTRODUCTION

The photocapacitance effect (PCE) in monopolar metal–insulator–semiconductor (MIS) capacitors has been observed [1–8] during photoexcitation in the semiconductor fundamental absorption band at temperatures sufficiently high to ionize dopant atoms almost completely. Under these conditions, the MIS device capacitance varies due mainly to changes in the concentration of carriers of both signs, i.e., in the bipolar mode.

The PCE can arise in the MIS capacitor during photoexcitation in the impurity absorption band at low temperatures due to variations in the concentration of ionized impurity atoms and free carriers of the same sign, i.e., in the monopolar mode.

In this work, we theoretically study the PCE in the monopolar MIS capacitor at low temperatures when dopant atoms are mostly unionized and at barrier bias voltages on the order of the ionization potential of impurity atoms, which almost corresponds to the mode of flat bands. The dependence of the MIS device capacitance and photocapacitance sensitivity on the bias magnitude and sign, the compensating impurity concentration, and temperature is considered.

MIS DEVICE CAPACITANCE

We consider a one-dimensional model of the MIS capacitor with a monopolar-conduction extrinsic semiconductor as an electrode (see Fig. 1). An applied voltage induces the semiconductor surface potential φ_0 and charge $Q(\varphi_0)$ per unit capacitor area. Surface charges at the insulator–semiconductor interface are assumed to be absent. The charge induced in the semiconductor is related to the potential φ_0 as

$$Q^2(\varphi_0) = \frac{\varepsilon}{2\pi}\int_{\varphi_0}^{0}\rho(\varphi)d\varphi, \quad (1)$$

where $\rho(\varphi)$ is the space charge density [9].

By definition, the differential static barrier capacitance in the semiconductor is given by

$$C_b = -\frac{dQ(\varphi_0)}{d\varphi_0}. \quad (2)$$

Differentiating equation (1) and substituting it into (2), we arrive at the general definition of the barrier capacitance

$$C_b = \frac{\varepsilon}{4\pi}\frac{\rho(\varphi_0)}{Q(\varphi_0)}. \quad (3)$$

We use relationship (1)–(3) to calculate the barrier capacitance in a *p*-type semiconductor doped by an acceptor impurity with the ionization energy E_i and partially compensated by a donor impurity with a shallow energy level. We assume that the concentration of minority carriers (electrons) is negligible compared to the hole concentration. Let N_a and N_d be, respectively, acceptor and donor concentrations. Hereafter, we assume impurities to be on average uniformly distributed.

The energy level and hole transition diagram is shown in Fig. 2. Henceforth, c is the coefficient of hole capture by an indium ion, q is the indium photoionization cross section, ϕ is the photon flux density, $p_1 = (N_v/g)\exp(-E_i/kT)$ is the Schockley–Read concentration, and g is the acceptor-impurity degeneracy factor.

1063-7826/00/3405-0545$20.00

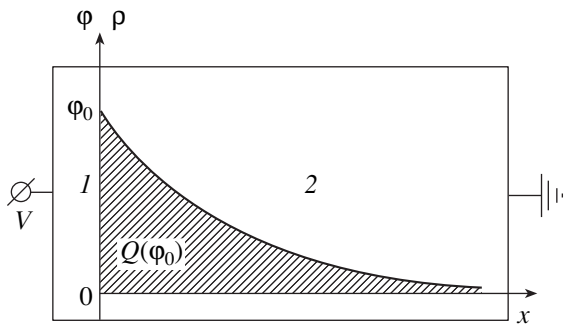

Fig. 1. Schematic of the MIS capacitor: (*1*) insulator and (*2*) semiconductor; V is the bias, φ_0 is the semiconductor surface potential, and $Q(\varphi_0)$ is the charge induced in the semiconductor.

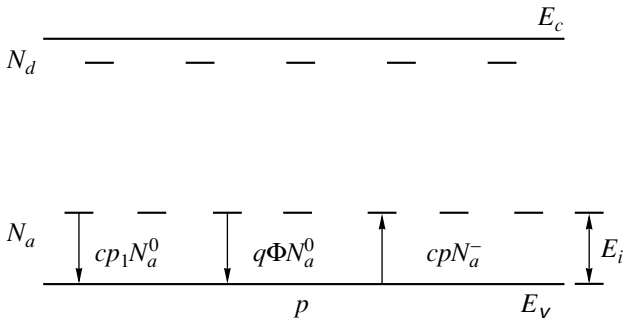

Fig. 2. Diagram of energy levels and hole transitions.

In the absence of an electric field, in a steady-state mode, and at a given temperature and a illumination intensity, concentrations of holes p, ionized acceptors N_a^-, and neutral atoms N_a^0 are defined by the set of equations

$$\begin{aligned} cp_1N_a^0 + q\phi N_a^0 &= cpN_a^-, \\ p + N_d &= N_a^-, \\ N_a^0 + N_a^- &= N_a \end{aligned} \tag{4}$$

and are given by

$$p = \frac{1}{2}\left(\left((N_d + p_1^*)^2 + 4(N_a - N_d)p_1^*\right)^{1/2} - (N_d + p_1^*)\right), \tag{5}$$

$$N_a^- = N_a p_1^*/(p_1^* + p), \quad N_a^0 = N_a p/(p_1^* + p), \tag{6}$$

where $p_a^* = p_1 + q\phi/c$.

If an electric field is applied, the semiconductor acquires the space charge density

$$\rho(\varphi) = e[p(\varphi) + N_d - N_a^-(\varphi)]. \tag{7}$$

We assume that the hole concentration p at a point with potential φ is defined by the Boltzmann formula

$$p(\varphi) = p_0\exp(-\alpha\varphi), \tag{8}$$

where p_0 is the hole concentration for $\varphi = 0$ and $\alpha = e/kT$. Then the space charge density is given by

$$\rho(\varphi_0) = e\left[p_0\exp(-\alpha\varphi_0) + N_d - N_a\frac{p_1^*}{p_1^* + p_0\exp(-\alpha\varphi_0)}\right]. \tag{9}$$

Substituting $\rho(\varphi_0)$ into (1) and integrating it, we find the induced charge as

$$Q^2(\varphi_0) = \frac{\varepsilon kT}{2\pi}\left[N_a\ln\frac{p_1^* + p_0\exp(-\alpha\varphi_0)}{p_1^* + p_0} + (N_a + N_d)\alpha\varphi_0 + p_0\exp(-\alpha\varphi_0) - p_0\right]. \tag{10}$$

Then, substituting $\rho(\varphi_0)$ and $Q(\varphi_0)$ into (3), we find an analytical expression for the barrier capacitance $C_b(\varphi_0)$ and its dependences on the potential φ_0, temperature T, and photoexcitation intensity ϕ.

However, the capacitance C_c is formed by a series connection of insulator-layer and barrier capacitances (C_d and C_b), so that

$$C_c = \frac{C_dC_b}{C_d + C_b}. \tag{11}$$

The voltage applied to the capacitor is a sum of the voltages across the insulator layer and across the barrier (U_d and φ_0),

$$V = U_d + \varphi_0, \tag{12}$$

where $U_d = Q(\varphi_0)/C_d$. Expressions (11) and (12) compose a parametric representation of the dependence of the capacitance C_c on the bias V with parameter φ_0. Here, C_d is assumed to be independent of U_d, temperature, and illumination intensity.

PHOTOCAPACITANCE EFFECT

We define the photocapacitance effect as the ratio of the capacitance change dC_c to the variation dI in the intensity of radiation that causes ionization of impurities; thus, we have

$$S_c = \frac{dC_c}{dI} = \frac{dC_c}{d\phi}\frac{d\phi}{dI} = \frac{1}{h\nu}\frac{dC_c}{d\phi}, \tag{13}$$

where $I = h\nu\phi$ is the illumination intensity. Taking into account (11), the photocapacitance sensitivity at a constant voltage is written as

$$S_c = \frac{1}{h\nu}\frac{C_d^2}{(C_d + C_b)^2}\frac{dC_b}{d\phi}, \quad (14)$$

where

$$\frac{dC_b}{d\phi} = \frac{\varepsilon}{4\pi}\frac{\rho}{Q}\left(\frac{1}{\rho}\frac{d\rho}{d\phi} - \frac{1}{Q}\frac{dQ}{d\phi}\right). \quad (15)$$

More detailed formulas simplifying calculations are given in the appendix.

Capacitance and photocapacitance characteristics were numerically calculated for the MIS capacitor with an electrode made of indium-doped silicon partially compensated by a donor impurity with a shallow energy level. There, the following values of the parameters were used. The insulating layer capacitance was $C_d = 100$ nF cm^{-2} that corresponded to a SiO_2 layer approximately 35 nm thick. The indium concentration was $N_a = 10^{16}$ cm^{-3}. The indium atom ionization energy in silicon was $E_1 = 160$ meV. The rate of hole capture by an indium ion was 2.5×10^{-6} cm^3 s^{-1} and the cross section of indium photoionization in silicon by light with $\lambda = 4$ μm was $q = 5 \times 10^{-16}$ cm^2. The indium acceptor level degeneracy factor was $g = 6$.

Then we varied the compensating impurity concentration N_d, temperature T, and illumination intensity I.

DISCUSSION

***C–V* characteristics in the absence of photoexcitation.** Figure 3 shows a family of *C–V* characteristics calculated for $T = 70$ K and various compensating impurity concentrations N_d used as a parameter. The following features are noteworthy.

(i) There exists a C_c maximum with height almost independent of N_d. As N_d decreases, the position of the maximum shifts towards positive (depleting) voltages. In particular, for $N_d = N_a/2$, the maximum is at $V = \varphi_0 = 0$. As N_d further decreases, the C_c maximum shifts towards positive voltages. In this case, as the positive voltage increases, the capacitance initially increases, reaches a maximum, and then decreases. For $\varphi_0 > \varphi_{max}$, the *C–V* characteristic becomes similar to that of the Schottky barrier at reverse voltages.

At a given temperature, the maximum capacitance C_{cmax} weakly depends on compensating impurity concentration and can be estimated from C_{cmax} at $N_d = N_a/2$. In this case, the capacitance maximum is at $V = \varphi_0 = 0$ and the barrier capacitance C_b is controlled by

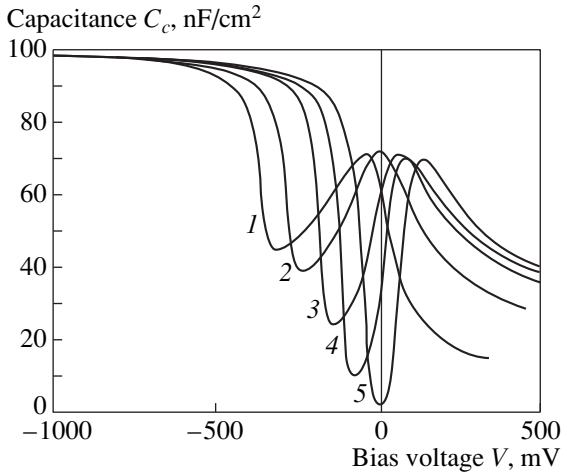

Fig. 3. *C–V* characteristics of the MIS capacitor for N_d = (*1*) 9×10^{15}, (*2*) 5×10^{15}, (*3*) 1×10^{15}, (*4*) 1×10^{14}, and (*5*) 0.0 cm^{-3}; $N_a = 1 \times 10^{16}$ cm^{-3}; $T = 70$ K.

the Debye screening length L_{db}. At a low temperature, when $p_1 \ll N_d$, the screening length is given by

$$L_{db}^2 = \frac{\varepsilon kT}{4\pi e^2}\frac{N}{N_d(N_a - N_d)}. \quad (16)$$

Therefore, for $N_d = N_a/2$, we have $L_{db}^2 = \varepsilon kT/\pi e^2 N_a$; hence,

$$C_{b\max} = \frac{\varepsilon}{4\pi L_{db}} = \frac{1}{4}\left(\frac{\varepsilon e^2 N_a}{\pi kT}\right)^{1/2}. \quad (17)$$

Substituting C_{cmax} for $V = 0$ and C_d into (11), we find C_{bmax}. Thus, one can estimate the majority-dopant concentration from the known values of C_{cmax} and C_d irrespective of N_d.

(ii) There exists a relatively broad C_c minimum at a negative (enhancing) voltage bias. The C_c minimum and its position depend on N_d. As N_d decreases, the C_c minimum deepens and shifts toward positive voltages. In particular, for $N_d = 0$, the minimum is observed at exactly $V = \varphi_0 = 0$. At $N_d > 0$, as the magnitude of the negative voltage increases, the capacitance initially decreases, reaches a minimum, and then increases steeply, so that the device capacitance becomes limited by the insulator layer capacitance.

In the voltage range where the capacitance reaches a minimum, the space charge density is controlled mainly by the compensating impurity concentration.

***C–V* Characteristics in the presence of photoexcitation.** Figures 4 and 5 show sets of *C–V* characteristics in the case of photoexcitation by light of various intensities; these characteristics were calculated for the

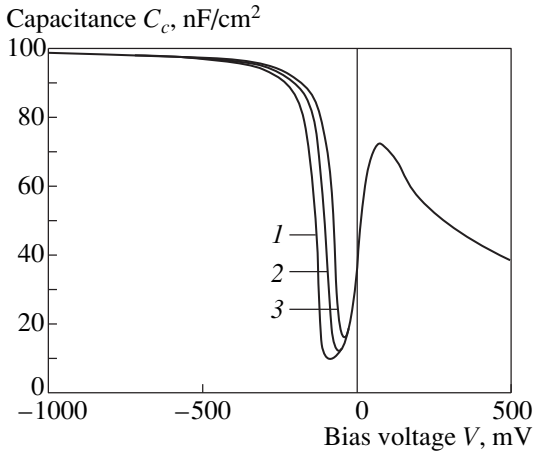

Fig. 4. C–V characteristic for $N_d = 1 \times 10^{14}$ cm^{-3} and I = (*1*) 0, (*2*) 1×10^{-2}, and (*3*) 1×10^{-1} W/cm^2; $N_a = 1 \times 10^{16}$ cm^{-3}; T = 60 K.

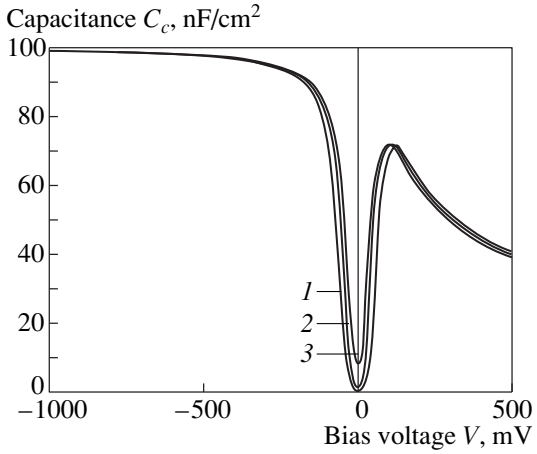

Fig. 5. C–V characteristics at $N_d = 0$ and I = (*1*) 0, (*2*) 1×10^{-3}, and (*3*) 1×10^{-1} W/cm^2; $N_a = 1 \times 10^{16}$ cm^{-3}; T = 60 K.

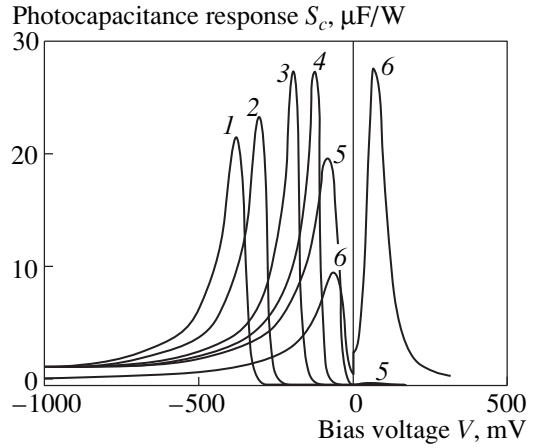

Fig. 6. S_c–V characteristics of the MIS capacitor for N_d = (*1*) 9×10^{15}, (*2*) 5×10^{15}, (*3*) 1×10^{15}, (*4*) 1×10^{14}, (*5*) 1×10^{12}, and (*6*) 0 cm^{-3}; $N_a = 1 \times 10^{16}$ cm^{-3}; T = 60 K.

two most typical compensating impurity concentrations $N_d = 0$ and $N_d = 1 \times 10^{14}$ cm^{-3} at T = 60 K.

Figure 4 shows that, at $N_d = 1 \times 10^{14}$ cm^{-3}, the left portion of the C–V characteristic shifts to positive voltages as the light intensity I increases, so that light of a given intensity increases the capacitance in a relatively narrow bias range. At the same time, the effect of light on the capacitance is absent in the right-hand portion of the C–V characteristic, i.e., at positive biases, since there we have $N_a^0 \ll N_a$ at a given concentration N_d.

Figure 5 shows a similar set of C–V characteristics for $N_d = 0$; it can be seen that illumination changes C_c in the entire range of voltage variation. For $V < V_{max}$, hence, for $\varphi_0 < \varphi_{max}$, the capacitance C_c increases as the photoexcitation intensity I increases, whereas, for $V > V_{max}$ and $\varphi_0 > \varphi_{max}$, the effect of I is the opposite. This is caused by almost complete ionization of impurity atoms N_a in the barrier at a positive voltage when $\varphi_0 > \varphi_{max}$. Therefore, light ionizes neutral atoms N_a^0 outside the barrier layer, which expands the barrier and decreases the capacitance.

Photocapacitance sensitivity. Dependences of the photocapacitance sensitivity S_c on bias were calculated for various values of N_d at T = 70 K (Fig. 6). It can be seen that the photocapacitance sensitivity manifests itself as a relatively sharp peak whose position depends on compensating impurity concentration. The value of S_c reaches a maximum in the range $N_d = (1 \times 10^{13}$–$1 \times 10^{14})$ cm^{-3}. As N_d further decreases, the S_c maximum decreases at negative voltages and the S_c maximum appears at a relatively low positive voltage. In the case of $N_d = 0$, S_c at positive voltages is virtually equal to the largest value of S_c at negative voltages. Dependences of S_c on bias are highly asymmetrical. A slow decrease in S_c in the left-hand portion is caused by the effect of a partial voltage drop across the insulator layer.

CONCLUSION

Analytical formulas have been derived for the capacitance and photocapacitance sensitivity of the monopolar MIS capacitor with a semiconductor electrode doped with an acceptor impurity with a deep energy level. C–V characteristics of the monopolar MIS capacitor were shown to become nonmonotonic at low temperatures when impurity atoms in the semiconductor electrode are weakly ionized. For instance, a capacitance maximum arises at depleting biases under low compensation ($K \ll 1$) by a donor impurity, while a capacitance minimum is observed at enriching voltages for high compensation ($1 - K \ll 1$). The photocapacitance sensitivity of the monopolar capacitor at low temperatures was shown to manifest itself as a relatively sharp peak, with height and position depending on the

compensating impurity concentration. The capacitance and photocapacitance characteristics of the MIS capacitor with an indium-doped silicon electrode were considered.

The monopolar MIS capacitor with an indium-doped silicon electrode can be used as a photodetector of modulated infrared emission, with sensitivity limited by a narrow range of bias variation ("selectivity" with respect to bias).

ACKNOWLEDGMENTS

This work was supported by the Russian Foundation for Basic Research, project no. 99-02-16675, as well as by the Federal Programs "Physics of Solid-State Nanostructures (project no. 97-1050) and "Promising Technologies and Devices of Micro- and Nanoelectronics."

APPENDIX

Calculation of the MIS capacitor photocapacitance sensitivity. To simplify calculations of S_c, we transform formula (15) by introducing the notation

$$F_1 = p_0\exp(-\alpha\varphi) + N_d - N_a\frac{p_1^*}{p_1^* + p_0\exp(-\alpha\varphi)},$$

$$F_2 = N_a\ln\frac{p_1^* + p_0\exp(-\alpha\varphi)}{p_1^* + p_0}$$

$$+ (N_a - N_d)\alpha\varphi + p_0[\exp(-\alpha\varphi) - 1].$$

Then

$$\rho(\varphi) = eF_1, \quad Q^2(\varphi) = \frac{\varepsilon kT}{2\pi}F_2,$$

and

$$C_b = e\left(\frac{\varepsilon}{8\pi kT}\right)^{\frac{1}{2}}\frac{F_1}{\sqrt{F_2}},$$

$$\frac{dC_b}{d\phi} = \frac{C_b}{2}\left(2\frac{1}{F_1}\frac{dF_1}{d\phi} - \frac{1}{F_1}\frac{dF_2}{d\phi}\right),$$

where

$$\frac{dF_1}{d\phi} = \frac{q}{c}\exp(-\alpha\varphi)\left[S_p - N_a\frac{p_0 - p_1^*S_p}{[p_1^* + p_0\exp(-\alpha\varphi)]^2}\right],$$

$$\frac{dF_2}{d\phi} = \frac{q}{c}[\exp(-\alpha\phi) - 1]$$

$$\times\left[S_p - N_a\frac{p_0 - p_1^*S_p}{[p_1^* + p_0\exp(-\alpha\varphi)](p_1^* + p_0)}\right],$$

$$S_p = \frac{N_a - N_d - p_0}{2p_0 + N_d + p_1^*}.$$

REFERENCES

1. R. F. Pierret and S. T. Sah, Solid-State Electron. **13**, 269 (1970).
2. A. V. Sachenko, V. A. Zuev, V. G. Litovchenko, *et al.*, Phys. Status Solidi A **21**, 345 (1974).
3. N. F. Kovtonyuk, Fiz. Tekh. Poluprovodn. (Leningrad) **9**, 2386 (1975) [Sov. Phys. Semicond. **9**, 1540 (1975)].
4. V. G. Litovchenko and A. P. Gorban', *Physical Basics of MIS-Based Microelectronic Systems* (Naukova Dumka, Kiev, 1978), Chap. 1.
5. A. Sher, Y. H. Tsuo, J. A. Moriarty, *et al.*, J. Appl. Phys. **51**, 2137 (1980).
6. A. A. Lebedev, N. A. Sobolev, and V. Ékke, Fiz. Tekh. Poluprovodn. (Leningrad) **15**, 1438 (1981) [Sov. Phys. Semicond. **15**, 832 (1981)].
7. V. A. Zuev and V. G. Popov, *Photoelectric MIS Devices* (Radio i svyaz', Moscow, 1983), Chap. 4, p. 89.
8. N. F. Kovtonyuk and E. N. Sal'nikov, *Photosensitive MIS Devices for Processing of Images* (Radio i Svyaz', Moscow, 1990), Chap. l, p. 8.
9. N. A. Penin, Fiz. Tekh. Poluprovodn. (Leningrad) **17**, 431 (1983) [Sov. Phys. Semicond. **17**, 266 (1983)].

Translated by A. Kazantsev

Semiconductors, Vol. 34, No. 5, 2000, pp. 550–554. Translated from Fizika i Tekhnika Poluprovodnikov, Vol. 34, No. 5, 2000, pp. 567–571.

SEMICONDUCTOR STRUCTURES, INTERFACES, AND SURFACES

Conditions for Negative Differential Resistance and Switching in a Tunnel Diode under the Effect of an External Microwave Signal

D. A. Usanov, A. V. Skripal', N. V. Ugryumova, S. B. Venig, and V. E. Orlov

Saratov State University, ul. Astrakhanskaya 83, Saratov, 410026 Russia

Submitted November 22, 1999; accepted for publication November 26, 1999

Abstract—Experimentally observed phenomenon of the origination of the mode of negative differential resistance and switching in a tunnel diode under the effect of external microwave signal is theoretically interpreted. The reasons for the existence of the ranges of bias voltages applied to the diode and the power levels of microwave signal for which the phenomenon is observed are clarified. © *2000 MAIK "Nauka/Interperiodica".*

INTRODUCTION

A high-strength microwave field substantially affects the characteristics of charge transport in the structures based on *p–n* junctions [1–3]. In [4, 5], the phenomenon of variation in the shape of current–voltage (*I–V*) characteristics of tunnel diodes under the effect of large-amplitude microwave signals was observed experimentally and interpreted theoretically. In particular, it was found that, as a result of the appearance of a thermal current of hot charge carriers and the detector phenomenon under the effect of microwave power, the peak value of current in the forward *I–V* characteristic decreases and the portion with negative differential resistance disappears for a certain level of microwave signal. If a tunnel diode energized by a dc voltage power supply was used as an active element in a self-excited oscillator, the above resulted in the suppression of autooscillations [6].

The use of load resistances in the feed circuits of tunnel diodes or a series connection of several tunnel diodes causes the dc voltages to be redistributed between the elements of an electric circuit under the effect of the microwave signal [7]. In particular, such a process can give rise to the mode of negative differential resistance and switching in the tunnel diode under the effect of an external microwave signal in the case where the voltage applied to the diode is much lower than the peak value. Such phenomena are the objects of this study.

EXPERIMENTAL

We studied experimentally the influence of high-power microwave radiation on the shape of low-frequency *I–V* characteristics of 1I308 tunnel diodes, with a constant series resistance of 50 Ω being connected in the feed circuit of these diodes.

The tunnel diode was mounted on a holder in a resonator based on a section of a short-circuit waveguide with a cross-sectional area of 7.2×3.4 mm^2. The frequency of microwave radiation was 38 GHz.

In order to reduce the effect of thermal heating of a diode structure, we used the ac voltage power supply with a frequency of 100 Hz.

The value of the supply voltage V_d of positive polarity applied to the series connected tunnel diode and resistance was chosen so that, in the absence of a microwave signal, the bias voltage V_0 applied to tunnel diode did not exceed the peak value V_p.

Figure 1 shows the experimental *I–V* characteristics of the tunnel diode measured for various power levels of the microwave signal and within the same range of voltages V_d.

It follows from the results obtained that, as the power level of microwave radiation increases to a certain value, the bias voltage V_0 applied to the tunnel diode increases abruptly and the operating point falls first in the region of negative differential resistance and then in the diffusion portion of the *I–V* characteristic of the tunnel diode; i.e., the mode of negative differential resistance and the switching mode occur in the tunnel diode as a result of microwave irradiation.

Figure 2 shows experimental dependences of the bias voltage V_0 applied to the tunnel diode on the value of voltage V_d; they suggest that the switching voltage corresponding to an abrupt transition of the tunnel diode from the low-resistance state to the high-resistance state decreases with the increasing power of microwave radiation.

With a further substantial increase in the power of microwave radiation, the region of negative differential resistance disappeared and the *I–V* characteristic of the tunnel diode became almost linear (Fig. 1, curve *6*).

1063-7826/00/3405-0550$20.00 © 2000 MAIK "Nauka/Interperiodica"

MODEL USED IN CALCULATIONS

When simulating the behavior of a tunnel diode incorporated into the microwave resonator, we used the equivalent circuit shown in Fig. 3. The elements of this equivalent circuit simulate the semiconductor diode structure in the form of parallel connection of the capacitance C and nonlinear resistance R [3]. The diode case is simulated by the elements L_c and C_c, and the waveguide section is represented by the input admittance in the plane of the diode Y_0.

It was assumed that the resistance of the diode base was independent of the current and is much less than the resistance R of the p–n junction for the bias voltages V no greater than the contact-potential difference V_{cont}. For $V > V_{cont}$, the value of R was assumed to be constant and was defined as $R = \rho\frac{l}{S}$, where ρ, l, and S are the resistivity, thickness, and area of the base of the diode structure.

The nonlinear resistance R was defined as the average resistance of the p–n junction for the first harmonic of microwave current; i.e.

$$R = \frac{\tilde{V}}{\tilde{I}}, \quad \text{where } \tilde{I} = \sqrt{A^2 + B^2},$$

$$A = \frac{2}{T}\int_0^T I(V)\sin\omega t dt,$$

$$B = \frac{2}{T}\int_0^T I(V)\cos\omega t dt,$$

$$V = V_0 + \tilde{V}\sin\omega t.$$

Here, V_0 and $\tilde{V}$ are the constant bias voltage and the amplitude of alternating microwave voltage applied to the tunnel diode, I is the current through the resistance R, and $T = 2\pi/\omega$ is the period of microwave oscillations.

In the context of the model suggested, the constant bias voltage V_0 is identified with the instantaneous value of the low-frequency alternating bias voltage applied to the tunnel diode in the experiments; this low-frequency voltage may be regarded as constant compared to the microwave voltage.

When simulating the current through the tunnel diode, we used an expression for the I–V characteristic derived with allowance made for variations in the tunnel (I_T), excess (I_X), and diffusion (I_D) components of the total current I due to heating of the free charge carriers [5]; i.e., we have

$$I(V) = I_T + I_X + I_D.$$

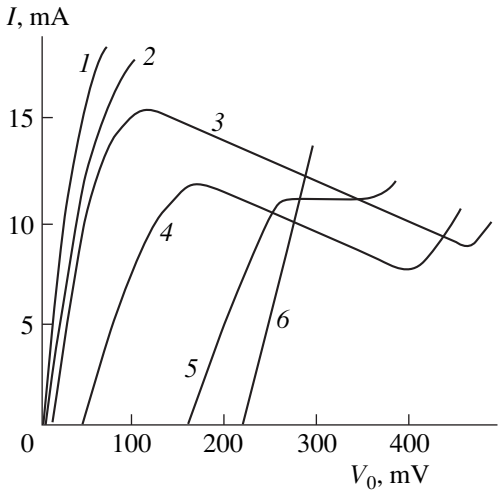

Fig. 1. Experimental I–V characteristics of the tunnel diode for the power levels of microwave radiation P_0 equal to (*1*) 0, (*2*) 50, (*3*) 100, (*4*) 400, (*5*) 800, and (*6*) 1200 mW for V_d = 900 mV.

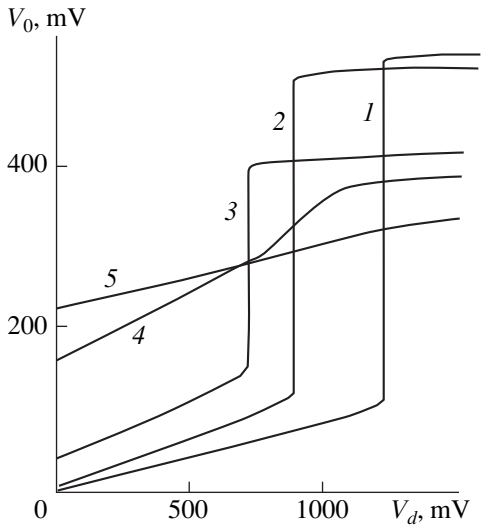

Fig. 2. Experimental dependences of the bias voltage V_0 applied to the tunnel diode on the supply voltage V_d for the power levels of microwave radiation P_0 equal to (*1*) 0, (*2*) 100, (*3*) 400, (*4*) 800, and (*5*) 1200 mW.

Here,

$$I_T = AT_T\int_{\varepsilon_c}^{\varepsilon_v}[f_{CT}(\varepsilon) - f_{VT}(\varepsilon)]g_c(\varepsilon)g_v(\varepsilon)d\varepsilon,$$

$$I_X = A_1 D_x S\exp(-a_x\varepsilon_x),$$

$$I_D = \frac{qSD_n n_{p0}}{L_n}\left\{\frac{kT_n}{\zeta_n(T_n) - \varepsilon_c}\frac{\zeta_n(T_0) - \varepsilon_c}{kT_0}\right.$$

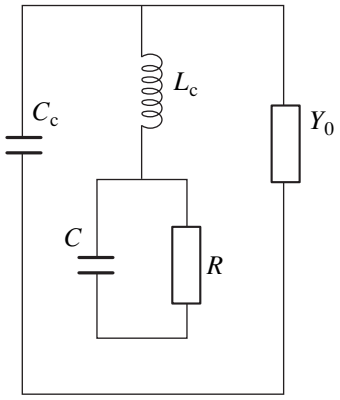

Fig. 3. Equivalent microwave circuit of a tunnel diode mounted in a microwave resonator.

$$\times \exp\left(\frac{qV_{\text{cont}}}{kT_0} - \frac{\zeta_n(T_0) - \varepsilon_c}{kT_0}\right)$$

$$\times \ln\left[1 + \exp\left(\frac{\zeta_n(T_n) - \varepsilon_c}{kT_n} - \frac{qV_{\text{cont}}}{kT_n} + \frac{qV}{kT_n}\right)\right] - 1\Bigg\}$$

$$+ \frac{qSD_p p_{n0}}{L_p}\Bigg\{\frac{kT_p}{\varepsilon_v - \zeta_p(T_p)}\frac{\varepsilon_v - \zeta_p(T_0)}{kT_0}$$

$$\times \exp\left(\frac{qV_{\text{cont}}}{kT_0} - \frac{\varepsilon_v - \zeta_p(T_0)}{kT_0}\right)$$

$$\times \ln\left[1 + \exp\left(\frac{\varepsilon_v - \zeta_p(T_p)}{kT_p} - \frac{qV_{\text{cont}}}{kT_p} + \frac{qV}{kT_p}\right)\right] - 1\Bigg\},$$

where $f_{CT}(\varepsilon)$ and $f_{VT}(\varepsilon)$ are the Fermi–Dirac distribution functions for electrons in the conduction and valence bands for the electron temperature T_n; T_p is the hole temperature; T_0 is the lattice temperature; A, A_1, and a_x are constants; T_T is the probability of tunneling transit through the potential barrier between the p-region and the n-region; $g_c(\varepsilon)$ and $g_v(\varepsilon)$ are the densities of energy states in the conduction and valence bands; ε_c and ε_v are the energies corresponding to the bottom of the conduction band and to the top of the valence band; ε_g is the bandgap; ζ_n and ζ_p are the quasi-Fermi levels in the n- and p-type semiconductors; D_x is the density of occupied states located in the forbidden band above the top of the valence band by the energy ε_x defined as

$$\varepsilon_x \approx \varepsilon_g - qV + (\zeta_n(T_n) - \varepsilon_c) + (\varepsilon_v - \zeta_p(T_p));$$

D_n and D_p are the diffusion coefficients for electrons and holes; S is the cross-sectional area of the p–n junction; and V is the voltage applied to the diode.

We calculated the I–V characteristic of the diode taking into account the detector effect and using the relationship

$$I_c = \frac{1}{T}\int_0^T I(V)dt.$$

It was taken into account in calculations that the constant resistance R_l connected in series with the tunnel diode was included in the feed circuit. The current–voltage characteristic $I_c(V_0)$ was determined by solving the equation

$$V_d = V_0 + I_c R_l,$$

where V_d is the supply voltage applied to the series-connected tunnel diode and the resistance.

The amplitude of microwave voltage $V^{\sim}$ was determined from the value of microwave power P absorbed by the diode; i.e.,

$$P = \frac{(V^{\sim})^2}{2R}.$$

In order to calculate the power absorbed by the diode mounted in the resonator, we used the expression [8]

$$P = P_0(1 - |N|^2),$$

where P_0 is the power of microwave radiation incident on the diode, $N = \dfrac{Y - Y_0}{Y + Y_0}$ is the coefficient of the reflection of microwave radiation from the diode, and $Y = j\omega C_c + \left[\dfrac{R}{1 + j\omega RC} + j\omega L_c\right]^{-1}$ is the admittance of the tunnel diode.

RESULTS OF CALCULATIONS

The calculations showed that, if the microwave signal was absent and a small-amplitude forward voltage was applied, most of the applied voltage dropped across a 50-Ω resistor connected in series with the tunnel diode. As the forward voltage V_d increases, a steady increase in the bias voltages across the tunnel diode V_0 and across the series resistor V_l occurs, with the ratio between these voltages equal to the ratio of the corresponding resistances under the dc conditions (Fig. 4, curve *1*). If the voltage V_0 reaches the peak value V_p (in the case under consideration, $V_p \approx 110$ mV), an abrupt redistribution of voltages between the tunnel diode and the resistor occurs: as V_d increases from 1220 to 1240 mV, the voltage V_0 increases from 110 to 420 mV; i.e., the tunnel diode switches from the low-resistance state to the high-resistance one, in which case the operating point is abruptly transferred along the load line from one ascending portion of the I–V characteristic to another ascending portion of this characteristic.

When the microwave signal is applied to the tunnel diode, a decrease in the total-current tunnel component, a sharp increase in the diffusion component, and an insignificant increase in the excess component of the total current through the tunnel diode are observed [5]. This causes the peak current I_p in the forward portion of the tunnel-diode I–V characteristic to decrease as the bias voltage V_p corresponding to this peak current is increased somewhat. Consequently, the effect of the microwave signal on the tunnel diode consists in an increase of the tunnel-diode dc resistance in the range of predominance of the tunnel component of the total current and in a decrease of this resistance in the range of predominance of the diffusion component of the total current.

Such changes in the I–V characteristic of the tunnel diode cause the voltage V_0 across the tunnel diode to increase with increasing microwave power and with V_d kept constant in the range of positive slope of the I–V characteristic in the vicinity of zero bias. As the microwave power increases to a certain value P_p, the voltage V_0 reaches the value corresponding to the starting point of the descending portion in the I–V characteristic of the tunnel diode, and an abrupt redistribution of dc voltages between the tunnel diode and the series resistance occurs (Fig. 5, curves *3*, *4*); as a result, the operating point is transferred along the load line through the region of negative differential resistance to a point located at the ascending portion of the tunnel-diode I–V characteristic. It is this effect that was observed in the experiment outlined above.

As was mentioned above, a further increase in the microwave power causes the tunnel-diode resistance to decrease in the region of predominance of the diffusion component of the total current (i.e., at the second ascending portion of the tunnel-diode I–V characteristic). This leads to a slight decrease in the bias voltage V_0 applied to the tunnel diode for a fixed value of V_d.

Figure 6 shows the tunnel-diode I–V characteristics calculated for various power levels of microwave radiation and for the same range of voltages V_d.

It is noteworthy that the changes in the I–V characteristic of the tunnel diode caused by microwave irradiation with increasing power result in a shift of the region of abrupt increase in V_0 in the dependence $V_0(V_d)$ to smaller values of V_d (Fig. 4, curves *2*–*4*).

Since, as follows from the results of calculations illustrated in Fig. 5, the value of P_p for which V_0 reaches the value corresponding to the starting point of the descending portion of the I–V characteristic is defined by the voltage V_d and increases with decreasing V_d, the effect of abrupt redistribution of voltages is bound to be observed at higher levels of microwave power for small values of V_d. On the other hand, an appreciable increase in the microwave power causes the current to decrease in the maximum of the tunnel-diode I–V characteristic and to increase in the minimum of this characteristic to such an extent that the I–V characteristic ceases to have an N-shape and becomes similar to the forward I–V characteristic of an inversed diode. For a still larger magnitude of the microwave signal, the I–V characteristic of the diode becomes almost linear.

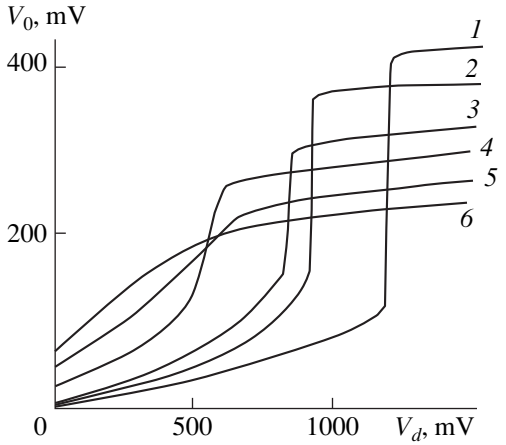

Fig. 4. Calculated dependences of bias voltage V_0 applied to the tunnel diode on the supply voltage V_d for the power levels P_0 of microwave radiation equal to (*1*) 0, (*2*) 50, (*3*) 100, (*4*) 400, (*5*) 800, and (*6*) 1200 mW.

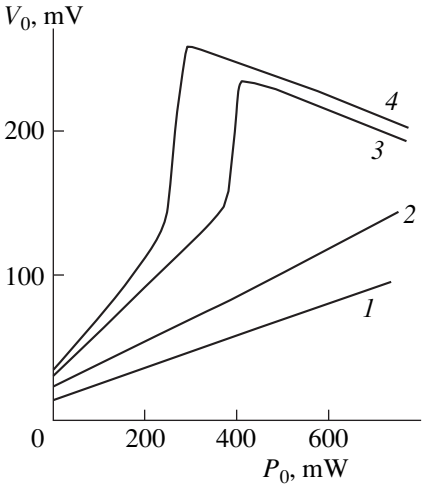

Fig. 5. The bias voltage V_0 applied to the tunnel diode as a function of the power level P_0 of microwave signal for the supply voltages V_d equal to (*1*) 250, (*2*) 350, (*3*) 500, and (*4*) 550 mV.

Such a change in the I–V characteristic causes the effect of abrupt switching of the tunnel diode from the low-resistance state to the high-resistance state to disappear and the region of negative differential resistance to cease to exist. In this case, abrupt changes in V_0 in the dependences $V_0(P)$ (Fig. 5, curves *1*, *2*) and $V_0(V_d)$ (Fig. 4, curves *5*, *6*) are no longer observed.

Consequently, for a given type of tunnel diode and a chosen value of series resistance, there exist a minimal

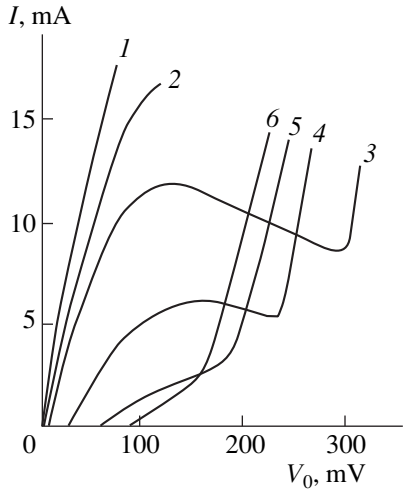

Fig. 6. The tunnel-diode *I–V* characteristics calculated for the microwave-radiation power levels P_0 = (*1*) 0, (*2*) 50, (*3*) 100, (*4*) 400, (*5*) 800, and (*6*) 1200 mW.

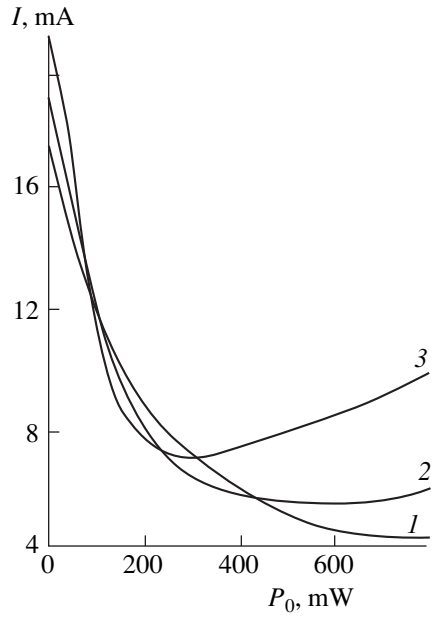

Fig. 7. The direct current of tunnel diode as a function of the power level of microwave radiation for V_d = (*1*) 250, (*2*) 270, and (*3*) 300 mV.

value V_{dm} of the voltage and a corresponding value V_{0m} of the bias voltage for which the phenomenon of negative differential resistance and switching under the effect of external microwave signal becomes possible. In the absence of a microwave signal, the value of current I_{0m} for a 1I308 diode is equal to $0.5I_p$ for $V_0 = V_{0m}$ and $R_l = 50\ \Omega$.

It is worth noting that, choosing the bias voltage at the positive-slope portion of the *I–V* characteristic $V_{0m} < V_0 < V_p$ and connecting a resistance of $R_l = 50\ \Omega$ in series with the diode (so that R_l is much larger than the tunnel-diode resistance R_0 in the vicinity of zero bias), we can use the external microwave signal to switch the tunnel diode over the region of negative differential resistance with respect to voltage (Fig. 4, curves *2*, *3*, *4*); if the resistor with $R_l = 10\ \Omega$ comparable to R_0 is employed, one can use the microwave signal to switch the tunnel diode over the region of negative differential resistance with respect to current (Fig. 7).

The results of the calculations are in good qualitative and quantitative agreement with the experimental data obtained.

CONCLUSION

Thus, we demonstrated experimentally and substantiated theoretically the possibility of initiating the mode of negative differential resistance and switching in a tunnel diode exposed to microwave radiation for supply voltages lower than the peak value.

REFERENCES

1. A. I. Veĭnger, L. G. Paritskiĭ, É. A. Akopyan, *et al.*, Fiz. Tekh. Poluprovodn. (Leningrad) **9** (2), 216 (1975) [Sov. Phys. Semicond. **9**, 144 (1975)].
2. N. A. Ablyazimova, A. I. Veĭnger, and V. S. Pitanov, Fiz. Tekh. Poluprovodn. (Leningrad) **22**, 2001 (1988) [Sov. Phys. Semicond. **22**, 1267 (1988)].
3. D. A. Usanov, A. V. Skripal', and N. V. Ugryumova, Fiz. Tekh. Poluprovodn. (St. Petersburg) **32**, 1399 (1998) [Semicond. **32**, 1248 (1998)].
4. D. A. Usanov, B. N. Korotin, V. E. Orlov, *et al.*, Pis'ma Zh. Tekh. Fiz. **16** (8), 50 (1990) [Sov. Tech. Phys. Lett. **16**, 303 (1990)].
5. D. A. Usanov, A. V. Skripal', B. N. Korotin, *et al.*, Pis'ma Zh. Tekh. Fiz. **19** (7), 81 (1993) [Tech. Phys. Lett. **19**, 220 (1993)].
6. D. A. Usanov, B. N. Korotin, V. E. Orlov, *et al.*, Izv. Vyssh. Uchebn. Zaved., Radiofiz. **34** (1), 98 (1991).
7. D. A. Usanov, A. V. Skripal', V. E. Orlov, *et al.*, Izv. Vyssh. Uchebn. Zaved., Élektron. **1–2**, 129 (1996).
8. J. Helszajn, *Passive and Active Microwave Circuits* (Wiley, New York, 1978; Radio i svyaz', Moscow, 1981).

Translated by A. Spitsyn

Semiconductors, Vol. 34, No. 5, 2000, pp. 555–557. Translated from Fizika i Tekhnika Poluprovodnikov, Vol. 34, No. 5, 2000, pp. 572–575.

SEMICONDUCTOR STRUCTURES, INTERFACES, AND SURFACES

Hot Carrier Electromotive Force Caused by Surface Potential Modulation in a Strong Microwave Field

G. Gulyamov, M. G. Dadamirzaev, and S. R. Boĭdedaev

Engineering–Pedagogical Institute, Namangan, 716003 Uzbekistan

Submitted September 6, 1999; accepted for publication December 7, 1999

Abstract—The effect of a heating wave distortion on recombination currents and electromotive force generated at the *p–n* junction in a strong microwave field was studied. High-frequency perturbations of the surface potential and the *p–n* junction height by the heating wave under the conditions of short and open circuits were shown to decrease the effective barrier height and to cause an anomalously high electromotive force, respectively.

Currents and electromotive force (emf) generated in the *p–n* junction subjected to a strong microwave field are accounted for by two complementary mechanisms. One is electron and hole heating by a strong microwave field [1, 2]. Another mechanism is distortion of the electric component **E** of the microwave field; i.e, a change in the field direction relative to the initial one $\mathbf{E}_0$ inside a sample [3, 4]. The wave electric field inside a diode can be resolved into perpendicular ($E_\perp$) and parallel ($E_\parallel$) components relative to the sample surface (see Fig. 1). The basic effect of the parallel component $E_\parallel$ is limited to electron and hole heating. This is taken into account by corresponding temperatures T_e and T_h. The perpendicular component $E_\perp$ heats carriers and changes the *p–n* junction potential barrier height and the surface potential. The barrier height modulation in a strong microwave field increases the *p–n* junction currents and emf [3]. The wave modulates not only by the *p–n* junction potential φ but also by the surface potential φ_s. However, the effect of surface potential modulation on currents and the emf generated at the *p–n* junction in a strong microwave field has not been discussed in the available publications. This work is aimed at studying the effect of surface potential modulation on currents and the emf generated at the *p–n* junction in the microwave field.

The perpendicular component $E_\perp$ modulates the *p–n* junction barrier height φ and the surface potential φ_s with the microwave frequency as

$$\varphi = \varphi_0 + U_{-v} + U_{\sim v}\cos\omega t,$$
$$\varphi_s = \varphi_{s0} + U_{\sim s}\cos\omega t,$$

where φ is the *p–n* junction potential barrier height, φ_0 is its equilibrium value in the absence of a microwave field, U_{-v} is the dc voltage at the *p–n* junction, $U_{\sim v}$ is the ac voltage that drops across the *p–n* junction and is caused by $E_\perp$, and $U_{\sim s}$ is the ac voltage drop across the surface layer. The *p–n* junction band diagram in the microwave field is shown in Fig. 2. Voltages are related to $E_\perp$ by the following formulas:

$$U_{\sim v}(t) = \int_{-l_p}^{l_n} E_\perp(t)dx, \quad U_{\sim s}(t) = \int_{d-l}^{d} E_\perp(t)dx. \quad (1)$$

Here, l_p and l_n are boundaries of the *p–n* junction space-charge region and $(d - l)$ and d are space charge near-surface regions. As shown in [5], the surface recombination rate S strongly depends on carrier temperatures and the surface potential φ_s. The current j in a strong microwave field is given by

$$j(U, T_e, T_h) = e\frac{D_p p_n}{L_p}F_h(U, T_h) + \frac{eSn_p}{1 + d/L_s}F_e(U, T_e) + \frac{eq_s^0}{1 + d/L_s}. \quad (2)$$

Here,

$$F_h(U, T_h) = \exp\left[\frac{e\varphi_0}{kT} - \frac{e(\varphi_0 - U)}{kT_h}\right] - 1,$$

$$F_e(U, T_e) = \exp\left[\frac{e\varphi_0}{kT} - \frac{e(\varphi_0 - U)}{kT_e}\right] - 1;$$

other notation is conventional and corresponds to that used in [3, 4]. For $\Delta n \ll p_0 + n_0$, the surface recombination rate is written as

$$S = \frac{N_s\gamma_{1s}\gamma_{2s}(p_0 + n_0)\exp[(e\varphi_s/k)(1/T_h - 1/T_e)]}{\gamma_{1s}n_1 + \gamma_{2s}p_1 + F_{es}(\gamma_{1s}, U, T_e) + F_{hs}(\gamma_{2s}, U, T_h)}, \quad (3)$$

1063-7826/00/3405-0555$20.00 © 2000 MAIK "Nauka/Interperiodica"

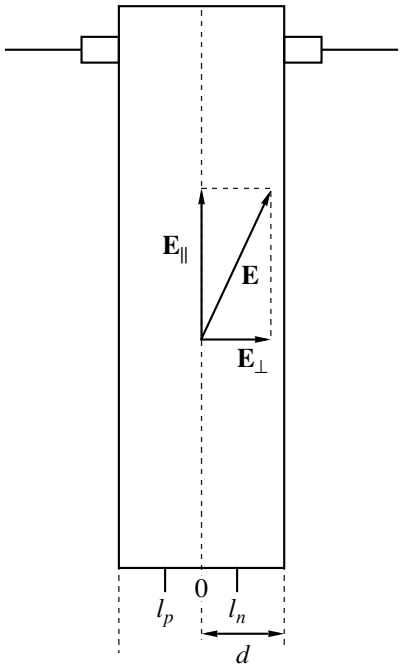

Fig. 1. Origination of the perpendicular component of the wave electric field.

where

$$F_{es}(\gamma_{1s}, U, T_e) = \gamma_{1s} n_0 \exp\left[\frac{e\varphi_0}{kT} - \frac{e(\varphi_0 - U)}{kT_e}\right],$$

$$F_{hs}(\gamma_{2s}, U, T_h) = \gamma_{2s} p_0 \exp\left[\frac{e\varphi_0}{kT} - \frac{e(\varphi_0 - U)}{kT_h} + \frac{e\varphi_0}{kT_h}\right].$$

Thus, the surface recombination rate strongly depends on the surface potential φ_s. Both the surface recombination rate and the voltage drop $U = U_{-v} + U_{\sim v}\cos\omega t$ across the *p–n* junction appear in formula (2) for the dark current. Thus, the microwave field distortion changes the *p–n* junction barrier height and the surface potential. This induces a high alternating current through the diode. Its average value is given by

$$\bar{j} = \frac{1}{T_\sim}\int_0^{T_\sim} j_r(U, T, T_e, U_{\sim v}, U_{\sim s})dt = \bar{j}_r + \frac{e\bar{S}n_p}{1 + d/L_s}\bar{F}_e(U, T_e) + \frac{e\bar{q}_s^0}{1 + d/L_s}, \quad (4)$$

where j_r is the recombination current in the *p–n* junction and

$$\bar{F}_e(U, T_e) = \exp\left[\frac{e\varphi_0}{kT} - \frac{e(\varphi_0 - U - \bar{U}_{\sim v})}{kT_e}\right] - 1.$$

To derive the latter formula, the mean-value theorem was used [6]. In (4), quantity $\bar{S}$ is given by

$$\bar{S} = N_s\gamma_{1s}\gamma_{2s}(p_0 + n_0) \times \frac{\exp\{[e(\varphi_{s0} + \bar{U}_s)/k](1/T_h - 1/T_e)\}}{\gamma_{1s}n_1 + \gamma_{2s}p_1 + \bar{F}_{es}(\gamma_{1s}, \bar{U}, T_e) + \bar{F}_{hs}(\gamma_{2s}, \bar{U}, T_h)}, \quad (5)$$

where

$$\bar{F}_{es}(\gamma_{1s}, \bar{U}, T_e) = \gamma_{1s} n_0 \exp\left[\frac{e\varphi_0}{kT} - \frac{e(\varphi_0 - U_{-v} - \bar{U}_{\sim v})}{kT}\right],$$

$$\bar{F}_{hs}(\gamma_{2s}, \bar{U}, T_h) = \gamma_{2s} p_0 \exp\left[\frac{e\varphi_0}{kT} - \frac{e(\varphi_0 - U_{-v} - \bar{U}_{\sim s})}{kT_h} + \frac{e\varphi_{s0}}{kT_h}\right].$$

For $U_{-v} = 0$, we find the short circuit current through the diode as

$$j_{sc} = \bar{j}_r + \frac{e\bar{S}(U = 0)n_p}{1 + d/L_s} \times \left\{\exp\left[\frac{e\varphi_0}{kT} - \frac{e(\varphi_0 - \bar{U}_{\sim v})}{kT_e}\right] - 1\right\} + \frac{e\bar{q}_s^0}{1 + d/L_s}. \quad (6)$$

When the surface recombination dominates over the bulk one, the first term in (6) can be neglected. It follows from (6) that the dependence of the short circuit current on the inverse temperature of carriers is controlled by the *p–n* junction barrier effective height. Then, the potential barrier effective height is written as $\varphi_0 - \bar{U}_{\sim v}$. Hence, the effect of the barrier height modulation in the short circuit mode is reduced to a decrease in the potential-barrier effective height. The latter was determined in [7, 8] from the dependence of the short circuit current on the inverse temperature of electrons. The measurements in the short circuit mode have shown the potential barrier effective height to be approximately twice lower than its true value φ_0. Thus, variations in the *p–n* junction barrier height and the surface potential decrease the former. Hence, both the recombination in the *p–n* junction region and the surface recombination during modulation of the *p–n* junction barrier and of the surface potential height lead to a decrease in the *p–n* junction barrier effective height and the surface potential, as well as to an increase in the short circuit current. The surface potential modulation enhances generation and recombination currents, which follows from (4). When the *p–n* junction barrier height φ and the surface potential φ_s are varied in phase with the wave, the surface recombination rate strongly increases. This leads to a drastic increase in forward and reverse currents of the *p–n* junction, which was indeed observed in [7, 8] in the presence of a strong microwave field. It follows from (4) that an increase in the forward and reverse currents can be accounted for

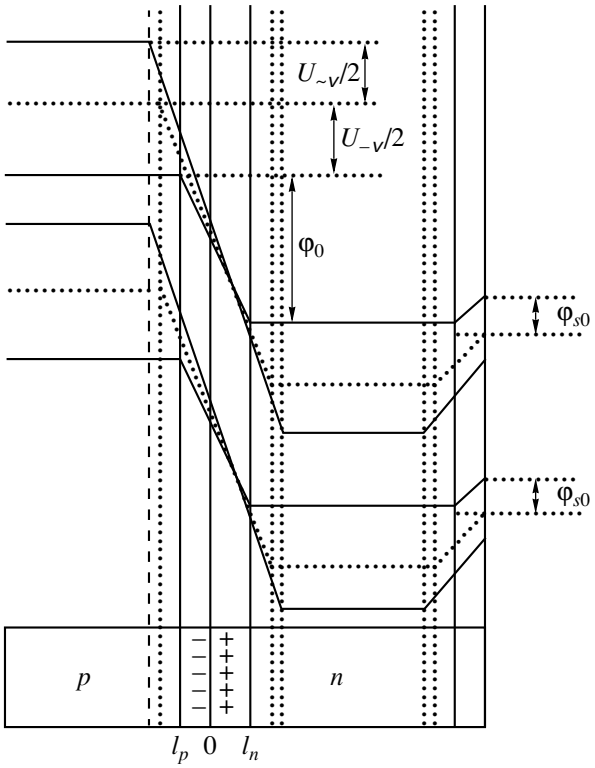

Fig. 2. Band diagram of the *p–n* junction in the strong microwave field.

by modulation of the *p–n* junction potential barrier and the surface potential.

We now analyze the open circuit voltage U_{oc} generated at the *p–n* junction in a strong microwave field. The open circuit voltage can be found by setting $\bar{j}$ in (4) equal to zero. For the sake of simplicity, we consider the case $T_e = T_h$, for which

$$U_{oc} = -\left(\frac{T_e}{T} - 1\right)\varphi_0 - \bar{U}_{\sim V} + \frac{kT_e}{e}\ln\left[1 + \frac{e\bar{q}_s^0/(1 + d/L_s)}{j_s + en_p\bar{S}/(1 + d/L_s)}\right], \quad (7)$$

where the first term $-(T_e/T - 1)\varphi_0$ corresponds to the emf generated at the *p–n* junction due to carrier heating. The second and third terms account for the surface carrier recombination and the surface potential modulation. It follows from (7) that the modulation of the *p–n* junction barrier height and surface potential strongly increases the emf. As is evident from (7), the emf can be generated even in the absence of heating merely due to the modulation of the *p–n* junction barrier height and the surface potential. As the microwave power increases, the emf can take on anomalously high values. The anomalously large values of emf generated at the *p–n* junction in the microwave field even in the case of weak heating, as observed in [7, 8], were apparently caused by the barrier height modulation by microwaves and the carrier recombination at surface states. Based on the above, we can conclude that the surface potential modulation caused by microwave distortion in the short- and open-circuit modes leads to a decrease in the effective barrier height and to the anomalously high emf generated at the *p–n* junction even in the case of weak heating.

REFERENCES

1. A. I. Veĭnger, L. G. Paritskiĭ, É. A. Akopyan, and G. Dadamirzaev, Fiz. Tekh. Poluprovodn. (Leningrad) **9** (2), 216 (1975) [Sov. Phys. Semicond. **9**, 144 (1975)].
2. S. P. Ashmontas, *Electromagnetic Phenomena in Semiconductors* (Mosklas, Vil'nyus, 1984).
3. G. Gulyamov, Fiz. Tekh. Poluprovodn. (St. Petersburg) **30**, 1279 (1996) [Semicond. **30**, 673 (1996)].
4. G. Gulyamov and B. Khamidova, Fiz. Tekh. Poluprovodn. (St. Petersburg) **30**, 769 (1996) [Semicond. **30**, 413 (1996)].
5. G. Gulyamov, Fiz. Tekh. Poluprovodn. (St. Petersburg) **30**, 569 (1996) [Semicond. **30**, 311 (1996)].
6. V. I. Smirnov, *A Course of Higher Mathematics* (Nauka, Moscow, 1974; Addison-Wesley, Reading, 1964), Vol. 1.
7. N. A. Ablyazimova, A. I. Veĭnger, and V. S. Pitanov, Fiz. Tekh. Poluprovodn. (St. Petersburg) **26**, 1041 (1992) [Sov. Phys. Semicond. **26**, 583 (1992)].
8. N. A. Ablyazimova, A. I. Veĭnger, and V. S. Pitanov, Fiz. Tekh. Poluprovodn. (Leningrad) **22**, 2001 (1988) [Sov. Phys. Semicond. **22**, 1267 (1988)].

Translated by A. Kazantsev

Semiconductors, Vol. 34, No. 5, 2000, pp. 558–562. Translated from Fizika i Tekhnika Poluprovodnikov, Vol. 34, No. 5, 2000, pp. 576–581.

SEMICONDUCTOR STRUCTURES, INTERFACES, AND SURFACES

Photosensitivity of Thin-Film Structures Based on $(CuInSe_2)_x(2ZnSe)_{1-x}$ Solid Solutions

V. Yu. Rud'*, Yu. V. Rud', R. N. Bekimbetov**, V. F. Gremenok***, I. V. Bodnar'****, and L. V. Rusak******

** St. Petersburg State Technical University, Politekhnicheskaya ul. 29, St. Petersburg, 195251 Russia*
e-mail: rudvas@uniys.hop.stu.neva.ru
*** Ioffe Physicotechnical Institute, Russian Academy of Sciences, Politekhnicheskaya ul. 26, St. Petersburg, 194021 Russia*
****Institute of Solid-State and Semiconductor Physics, Belarussian Academy of Sciences, ul. Brovki 17, Minsk, 220072 Belarus*
***** Belarussian State University of Information Science and Radio Engineering, ul. Brovki 17, Minsk, 220072 Belarus*
Submitted December 6, 1999; accepted for publication December 7, 1999

Abstract—Polycrystalline $(CuInSe_2)_x(2ZnSe)_{1-x}$ films (x = 0.6–1.0) with p-type conductivity and a thickness of 0.5–0.9 μm were obtained by pulsed laser evaporation. It is shown that a chalcopyrite–sphalerite transition occurs in the above system for x = 0.7. The obtained films were used to fabricate the photosensitive structure of the In/p-$(CuInSe_2)_x(2ZnSe)_{1-x}$ and InSe(GaSe)/$(CuInSe_2)_x(2ZnSe)_{1-x}$ types. Spectral dependences of photovoltaic-conversion quantum efficiency were studied, and the photosensitivity of the structures in relation to the type of energy barrier and the composition was analyzed. It is concluded that the structures under consideration can be used as broadband photovoltaic converters. © *2000 MAIK "Nauka/Interperiodica".*

1. INTRODUCTION

Ternary I–III–VI_2 semiconductor compounds are the closest crystallochemical analogs to the binary II–VI semiconductors and are formed by replacement of two atoms from Group II by one atom from Group I and one atom from Group III [1]. Studies of ternary and multinary compounds expand appreciably the potentialities of the science of semiconductor materials. Thus, for example, the use of ternary and multinary phases with chalcopyrite structure has made it possible to develop thin-film Cu(In, Ga)Se_2-based solar cells with conversion efficiency as high as 18% [2, 3]. Further improvement in the characteristics of such photovoltaic converters would rely on the studies of the relation of the properties of specific structures to technological processes and also on utilization of new systems of solid solutions based on I–III–VI_2 semiconductors. In the context of these studies, solid solutions based on ternary and binary compounds have recently attracted the attention of the designers of solar cells [4–7]. In particular, it was shown [4–7] that, in a $CuInSe_2$–2ZnSe system, there exists a continuous series of solid solutions whose bandgap varies continuously with changes in composition and ranges from 2.67 (for ZnSe) to 1.04 eV (for $CuInSe_2$).

In this work, we used the method of pulsed laser evaporation to obtain thin films of $CuInSe_2$–2ZnSe solid solutions, on the basis of which we fabricated and studied for the first time the photosensitive structures of several types.

2. EXPERIMENTAL

As targets in the laser evaporation for the formation of the films, we used the crystals of $(CuInSe_2)_x(2ZnSe)_{1-x}$ solid solutions obtained by planar crystallization in a vertical one-zone furnace [5]. The source components of high purity (copper, indium, and zinc of 99.999% purity, and selenium of 99.99999% purity) were mixed in stoichiometric ratio and charged into quartz ampules, which were preliminarily subjected to chemical treatment (etching in a mixture HNO_3 : HCl = 1 : 3 of acids, rinsing in distilled water, and drying at 400 K). After the stoichiometric mixture of the components was charged, the ampules were evacuated to a residual pressure of 10^{-3} Pa, sealed, and put in the furnace. The phases were synthesized by raising the temperature to 1100 K with a rate of 50 K/h; in order to homogenize the alloy, it was then kept for about 2 h at the above temperature under conditions of continuous vibration. Next, the temperature of the alloy was raised to 1270–1470 K (depending on the solid-solution composition) with the same rate as above, and the alloy was kept again for 1 h at the aforementioned temperatures. Afterwards, the vibration was terminated, and the planar crystallization of the alloy was effected by lowering the furnace temperature with a rate of 2 K/h until the alloy was completely solidified. In order to homogenize the ingots obtained, we had to subject them to additional heat treatment at 1070 K for 300 h. The resulting ingots with the aforementioned composition range had a pronounced mosaic structure and were 14 mm in diameter and 40 mm in length.

1063-7826/00/3405-0558$20.00 © 2000 MAIK "Nauka/Interperiodica"

The atomic composition of solid solutions was determined by chemical analysis; the results showed that the composition of crystallized phases was in satisfactory agreement with the charge composition [5].

The homogeneity of $(CuInSe_2)_x(2ZnSe)_{1-x}$ solid solutions was determined by X-ray diffraction using a DRON-3M diffractometer (filtered Cu radiation was employed). Studies showed that a structural phase transition occurs in the solid-solution system under consideration in the vicinity of $x = 0.7$. Within the range of $x = 1.0$–0.7, the crystallized solid solution has a chalcopyrite structure, whereas the cubic sphalerite structure was found in the solid solutions with $x < 0.7$. Variation in the unit-cell parameters obeys the Vegard law in the studied system of solid solutions.

The system of pulsed laser evaporation of semiconductor materials that we developed includes a commercial free-running laser ($\lambda = 1.06$ μm and $\tau_{puls} = 10^{-3}$ s). The laser beam was focused onto the $(CuInSe_2)_x(2ZnSe)_{1-x}$ target surface using a glass lens with a focal length of 500 mm. Typically, the surface of semiconductor wafers was set at an angle of 45° with respect to the direction of the laser beam. The repetition rate of laser pulses was 3×10^{-2} Hz, with the energy of a pulse being 150–180 J. The films were deposited in a vacuum chamber at a residual pressure of 2×10^{-5} Pa, and the condensation rate was 20–40 μm/s. As the substrates, we used plates of Corning 7059 glass, whose temperature during deposition was kept in the range of 770–790 K; the plates were preliminarily cleaned using conventional chemical methods. The thickness of deposited films was 0.5–0.9 μm over the active area of 2 cm^2.

The X-ray studies showed that the diffraction patterns of $(CuInSe_2)_x(2ZnSe)_{1-x}$ solid-solution films featured a system of lines corresponding to the chalcopyrite or sphalerite structures, depending on the composition. The films were polycrystalline with a preferred orientation in the (112) plane for $0.7 \le x \le 1$. The values of the unit-cell parameters are consistent with the data for bulk crystals and vary linearly with x, which indicates that the composition of the films corresponds to that of the target. These studies suggest that pulsed laser evaporation is a promising method for producing films of ternary and quaternary semiconductor phases.

3. RESULTS AND DISCUSSION

Tentative studies of phenomena at the contacts of various metals with p-type $(CuInSe_2)_x(2ZnSe)_{1-x}$ solid-solution films suggested that the photovoltaic effect was reproducibly observed in the structures consisting of a thin vacuum-deposited indium film ($d = 0.5$ μm) in contact with the surface of the obtained solid solutions. Indium was deposited onto the surface of laser-sputtered films without any additional treatment of this surface. The thus obtained structures feature reproducibly the rectification effect (typically, the ratio of forward and reverse currents is ≤10 for the bias voltage of $U = 2$–3 V). The conducting direction corresponds to positive polarity of external bias applied to the solid-solution films. As can be seen from Table 1, the residual resistance R_0 is much lower in the barriers involving the solid solutions than in that involving the positionally ordered $CuInSe_2$ phase. This fact can result from extension of acceptor behavior of zinc atoms (characteristic of $CuInSe_2$ compound) to the solid solutions [1].

In the Schottky barriers obtained, the photovoltaic effect is observed reproducibly; this effect is dominant in the case of illumination of such structures from the side of the indium layers that are always negatively charged, which corresponds to the rectification direction. The voltage photosensitivity in the highest quality structures reaches 1 V/W at $T = 300$ K. The highest relative quantum efficiency of photovoltaic conversion η_m is observed in the barriers involving the solid-solution films with $x = 0.7$ (Table 1); however, it should be noted that the value of η_m for the barriers involving films of almost the same atomic composition may vary within a rather wide range (Table 1, samples 3, 4), which is apparently related to the effects of differences in technological conditions of preparing the solid-solution films.

Spectral dependences of relative quantum efficiency $\eta(\hbar\omega)$ for the Schottky barriers in relation to the atomic composition of $(CuInSe_2)_x(2ZnSe)_{1-x}$ films at room temperature under conditions of illumination from the side of the barrier contact are shown in Fig. 1. The values of a number of the photosensitivity parameters of the structures under consideration are listed in Table 1. The long-wavelength edge of photosensitivity in the barriers based on both the solid-solution films and the positionally ordered $CuInSe_2$ compound is exponential (Fig. 1), and its slope $S = \delta(\ln\eta)/\delta(\hbar\omega)$ ranges from 15 to 30 eV^{-1} in different structures (Table 1), which is characteristic of vertical band-to-band transitions [8–10]. As x increases, the long-wavelength edge of photosensitivity and the energy position $\hbar\omega_m$ of the peak tend to shift to shorter wavelengths, which corresponds to the formation of $(CuInSe_2)_x(2ZnSe)_{1-x}$ solid solutions [11]. The full width of the spectra $\eta(\hbar\omega)$ at half maxi-

Table 1. Photoelectric properties of In/p-$(CuInSe_2)_x(2ZnSe)_{1-x}$ thin-film surface-barrier structures at $T = 300$ K

Serial no. of the film	x, mol %	R_0, 10^{-3} Ω	$\hbar\omega_m$, eV	S, eV^{-1}	$\delta_{1/2}$, eV	η_m, arb. units
1	1	100	1.3	14	1.36	5
2	0.9	1.2	1.3	18	0.8	1
3	0.7	1.7	1.7	18	1.24	380
4	0.7	6.7	1.7	26	1.19	1.2
5	0.6	5.0	1.3	25	0.34	0.5
6	0.6	1.7	–	–	–	–

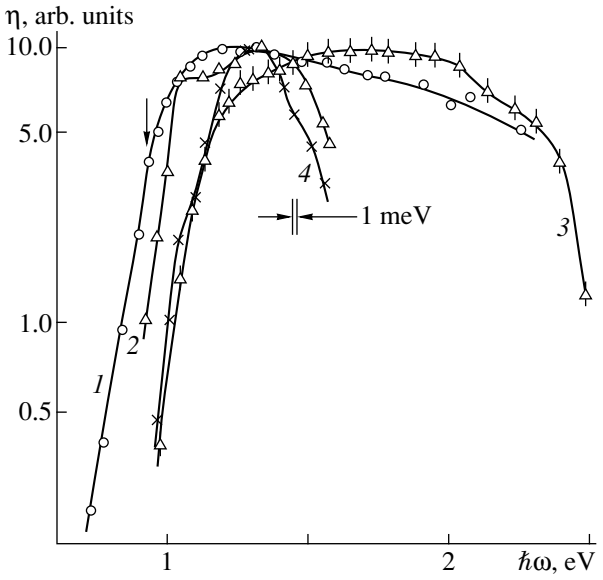

Fig. 1. Spectral dependences of the relative quantum efficiency of photovoltaic conversion by In/*p*-$(CuInSe_2)_x(2ZnSe)_{1-x}$ Schottky barriers for unpolarized light at $T = 300$ K for $x =$ (*1*) 1, (*2*) 0.9, (*3*) 0.7, and (*4*) 0.6 mol %. The structures were illuminated from the side of the barrier contact.

mum $\delta_{1/2}$ (Fig. 1, Table 1) indicates that the photovoltaic conversion is broadband in such structures and corresponds to the solar radiation spectrum. It is noteworthy that the narrowest band spectra $\eta(\hbar\omega)$ were observed for the barriers based on the films of solid solutions with sphalerite structure (Fig. 1, curve *4*). Apparently, in the range of compositions corresponding to the occurrence of the chalcopyrite–sphalerite phase transition, the photosensitivity processes may be affected by variation in the type of ordering in the structure of the material. Obviously, this issue should be given further consideration.

With the aim of obtaining the photosensitive structures, we also studied the possibility of bringing the as-grown mirror surface of the films into a direct optical contact with cleaved platelets of lamellar III–VI semiconductors (InSe and GaSe). As in the case of indium layers, such heterostructures do not require any heat treatments for their fabrication; this is especially appealing when applied to the chalacogenide films under consideration, because the above procedure does not induce additional changes in the atomic composition and crystal structure of as-grown materials [12, 13]. When fabricating these heterostructures, we used electrically homogeneous single crystals of *n*-InSe ($n = 10^{16}$ cm^{-3}) and *p*-GaSe ($p = 10^{14}$ cm^{-3}) compounds; platelets with average dimensions of 3 mm × 3 mm × 0.02 mm can be easily obtained by cleaving the above crystals [14]. Direct contact of the platelets with $(CuInSe_2)_x(2ZnSe)_{1-x}$ chalcogenide films makes it possible to produce heterostructures that exhibit rectifying properties and a photovoltaic effect. It was found that the photosensitivity of the highest quality *n*-InSe/*p*-$(CuInSe_2)_x(2ZnSe)_{1-x}$ and *p*-GaSe/*p*-$(CuInSe_2)_x(2ZnSe)_{1-x}$ structures for all x was two–three orders of magnitude higher than that in the case of Schottky barriers in the same structures. The maximal voltage photosensitivity (measured at 300 K) of heterostructures based on *n*-InSe was as high as 10^2 V/W, and, in the case of *p*-GaSe, it was even higher (5×10^2 V/W).

Table 2. Photoelectric properties of InSe(GaSe)/$(CuInSe_2)_x(2ZnSe)_{1-x}$ heterostructures

Serial no. of the film	x, mol %	Hetero-compound	$\hbar\omega_m$, eV	S, eV^{-1}	$\delta_{1/2}$, eV	η_m, arb. units
1	1	InSe	2.25	46	0.6	4
2	0.9	″	2.0–2.07	27	0.9	2
3	0.7	″	1.41	40	0.8	58
4	0.7	″	1.6	38	1.0	150
5	0.6	″	1.4	26	0.6	5
6	0.6	″	1.4	51	0.5	21
3	0.7	GaSe	2.0–2.07	38	>0.7	–

Figure 2 shows the spectra $\eta(\hbar\omega)$ of typical heterostructures based on *n*-InSe and the solid-solution films with differing compositions. In order to eliminate the effect of optical absorption in the heteropair layers adjoining the active heterostructure layers and having almost the same values of bandgaps E_G [11], we recorded the $\eta(\hbar\omega)$ spectra in the configuration where the radiation was directly incident on the heteroboundary. In order to avoid superimposition, the $\eta(\hbar\omega)$ spectra for different heterostructures in Fig. 2 were shifted along the vertical axis.

The main special features of the $\eta(\hbar\omega)$ spectra consist in the following.

Energy positions of the long-wavelength exponential edge of $\eta(\hbar\omega)$ and the narrow peak (Fig. 2, curves *1*, *2*) or the kink for the photon energy of $\hbar\omega = 1.21$ eV (Fig. 2, curves *3*, *4*) were found to be close to the value of E_G for InSe [11, 12]. Therefore, we may assign the long-wavelength photosensitivity cutoff for heterostructures, which is the same for all values of x in $(CuInSe_2)_x(2ZnSe)_{1-x}$ films used in the heterostructures, to interband absorption in an InSe crystal [12]. It should be emphasized that the long-wavelength cutoff of $\eta(\hbar\omega)$ in the InSe-based heterostructures is found to be shifted to shorter wavelengths as compared to that for Schottky barriers in the same $(CuInSe_2)_x(2ZnSe)_{1-x}$ films (Figs. 1, 2). This may be attributed to the fact that the active region of the structures under consideration is largely located in the binary compound as a result of the higher doping level of polycrystalline solid-solution films as compared to InSe. For this reason, the photosensitivity of the heterostructures in the spectral region

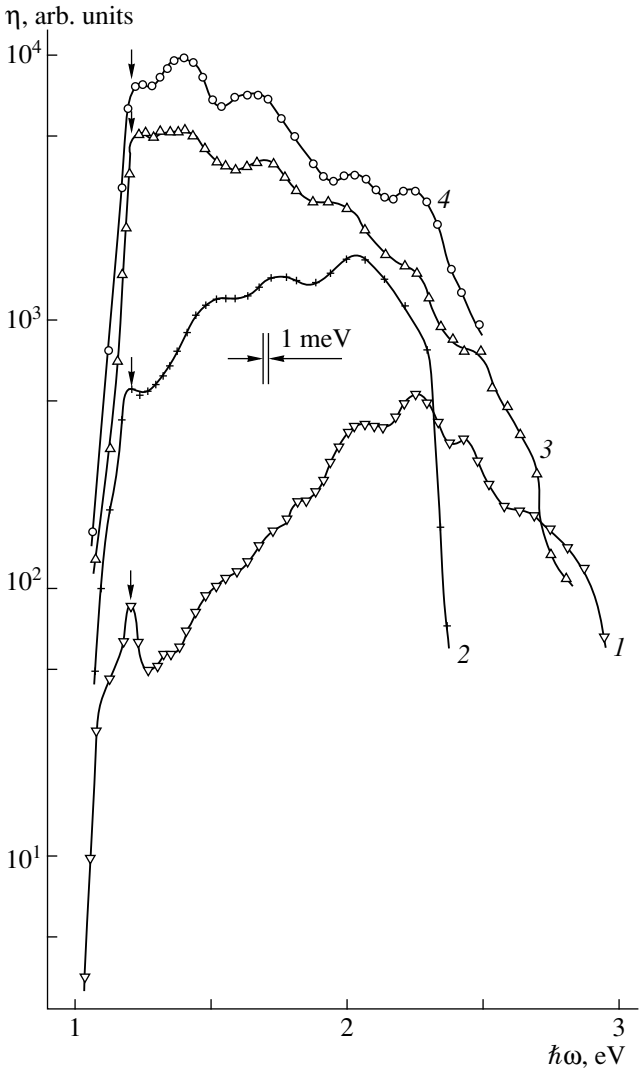

Fig. 2. Spectral dependences of relative quantum efficiency of photovoltaic conversion by *n*-InSe/$(CuInSe_2)_x(2ZnSe)_{1-x}$ heterostructures for unpolarized light at T = 300 K for x = (*1*) 1, (*2*) 0.9, (*3*) 0.7, and (*4*) 0.6 mol %. The structures were illuminated over the area of interface between InSe and the solid solution. Arrows indicate the peaks of the spectra for $\hbar\omega$ = 1.21 eV.

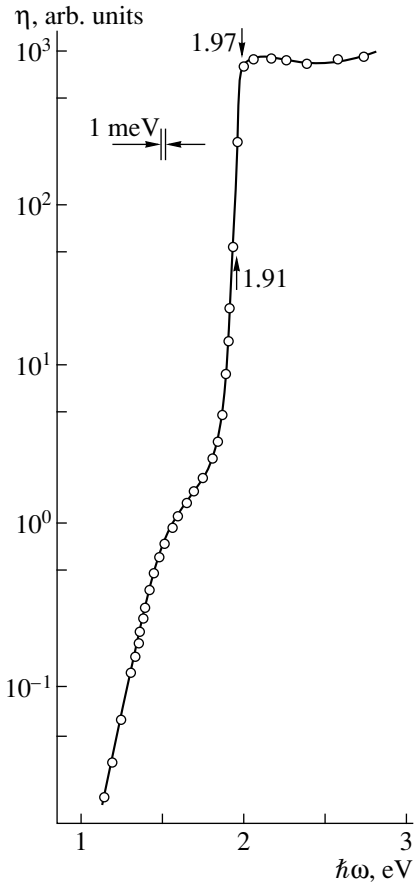

Fig. 3. Spectral dependence of the relative quantum efficiency of photovoltaic conversion for the *p*-GaSe/$(CuInSe_2)_x(2ZnSe)_{1-x}$ heterostructure at T = 300 K. The structure was illuminated from the GaSe side.

of optical absorption by the material of $(CuInSe_2)_x(2ZnSe)_{1-x}$ films hardly affects the $\eta(\hbar\omega)$ spectra of these heterostructures (Fig. 2).

High steepness of $\eta(\hbar\omega)$ spectra of InSe-based structures is determined by vertical optical transitions (Table 2). It can be seen that the absolute maximum of η in such heterostructures is attained deep inside the fundamental absorption region of InSe; as a result, experimental values of $\hbar\omega_m$ exceed the bandgap of the InSe compound.

For all values of x, the photosensitivity of the structures, as in the case of Schottky barriers formed with $(CuInSe_2)_x(2ZnSe)_{1-x}$ films, is found to be broadband and is characterized by the value of $\delta_{1/2}$ = 0.5–1.2 eV (Table 2). As follows from Table 2, the maximal photosensitivity η_m is observed in heterostructures based on the films with x = 0.7.

The presence of pronounced oscillations in photosensitivity is the most interesting feature of the $\eta(\hbar\omega)$ spectra of InSe/$(CuInSe_2)_x(2ZnSe)_{1-x}$ structures. It can be seen from Fig. 2 that the energy positions of extrema in the case of different heterostructures involving the contacts of the same InSe platelet with the films of dissimilar solid solutions are close to each other. Taking this into consideration, we may relate the observed features to interference of incident radiation in the InSe single crystal. As in the case of the Schottky barriers, it should be noted that the $\eta(\hbar\omega)$ spectra of InSe/$(CuInSe_2)_x(2ZnSe)_{1-x}$ heterostructures match the solar-radiation spectrum.

The photovoltaic effect and rectification were also observed in *p*-GaSe/*p*-$(CuInSe_2)_x(2ZnSe)_{1-x}$ heterostructures. Typical spectral dependence $\eta(\hbar\omega)$ for one such structure illuminated from the GaSe side is shown in Fig. 3. As for the InSe-based heterostruc-

tures, the dependence $\eta(\hbar\omega)$ is largely determined by photoactive absorption in GaSe, and the highest voltage photosensitivity of such structures is observed if the structures are illuminated from the side of the binary compound and, in this case, attains a value on the order of 5×10^2 V/W at 300 K. The energy position of the exponential photosensitivity edge in *p*-GaSe/*p*-$(CuInSe_2)_x(2ZnSe)_{1-x}$ structures is consistent with band-to-band transitions in GaSe [11, 14].

If all the structures considered above were illuminated with linearly polarized radiation incident normally to the photosensitive surface, the short-circuit current was independent of the polarization-plane position in the entire range of photosensitivity. Consequently, there is no natural photopleochroism in such structures [14]. This is consistent with the fact that the detected radiation is incident on the active heterostructure region along the isotropic direction for III–VI single crystals and that the $(CuInSe_2)_x(2ZnSe)_{1-x}$ solid solutions are polycrystalline.

4. CONCLUSION

Thus, we fabricated photosensitive structures on the basis of $(CuInSe_2)_x(2ZnSe)_{1-x}$ films obtained by laser evaporation and deposition of indium layers and by bringing these films into optical contact with the cleaved InSe and GaSe surfaces. The results of our studies indicate that solid-solution films can be used for fabrication of broadband photovoltaic natural-radiation converters whose long-wavelength cutoff can be controlled by atomic composition of III–VI compounds. The results we obtained also indicate that it is expedient to continue the efforts to grow III–VI layers on the surface of $(CuInSe_2)_x(2ZnSe)_{1-x}$ thin films in order to develop thin-film solar-radiation converters.

REFERENCES

1. N. A. Goryunova, *The Chemistry of Diamond-Like Semiconductors* (Izd. Len. Gos. Univ., Leningrad, 1963; Chapman and Hall, London, 1965).
2. H. W. Schock, Appl. Surf. Sci. **92**, 606 (1996).
3. T. Negami, Solid State Phenom. **67–68**, 349 (1999).
4. I. Luck, W. Henrion, R. Scheer, *et al.*, Cryst. Res. Technol. **31**, 841 (1996).
5. I. V. Bodnar, I. A. Victorov, and I. V. Chibusova, Cryst. Res. Technol. **31**, 119 (1996).
6. Th. Doering, W. Schmitz, and I. V. Bodnar, in *7 Jahrestangung der DGK, Leipzig, Germany, March 8–10, 1999*, p. 121.
7. *Electroluminescence*, Ed. by J. I. Pankove (Springer-Verlag, Berlin, 1977).
8. Yu. V. Rud' and V. Yu. Rud', Fiz. Tekh. Poluprovodn. (St. Petersburg) **31**, 1336 (1997) [Semicond. **31**, 1151 (1997)].
9. V. Yu. Rud' and H. W. Schock, Solid State Phenom. **67–68**, 391 (1999).
10. *Physicochemical Properties of Semiconducting Materials: A Reference Book* (Nauka, Moscow, 1978).
11. V. Yu. Rud', Yu. V. Rud', V. F. Gremenok, *et al.*, Solid State Phenom. **67–68**, 415 (1999).
12. V. Yu. Rud', Yu. V. Rud', R. M. Bekimbetov, *et al.*, Fiz. Tekh. Poluprovodn. (St. Petersburg) **33**, 824 (1999) [Semicond. **33**, 757 (1999)].
13. N. M. Mekhtiev, Yu. V. Rud', and É. Yu. Salaev, Fiz. Tekh. Poluprovodn. (Leningrad) **12**, 1566 (1978) [Sov. Phys. Semicond. **12**, 924 (1978)].
14. F. P. Kesamanly, V. Yu. Rud', and Yu. V. Rud', Fiz. Tekh. Poluprovodn. (St. Petersburg) **30**, 1921 (1996) [Semicond. **30**, 1001 (1996)].

Translated by A. Spitsyn

Semiconductors, Vol. 34, No. 5, 2000, pp. 563–567. Translated from Fizika i Tekhnika Poluprovodnikov, Vol. 34, No. 5, 2000, pp. 582–587.

LOW-DIMENSIONAL SYSTEMS

Shallow Acceptors in Strained Ge/$Ge_{1-x}Si_x$ Heterostructures with Quantum Wells

V. Ya. Aleshkin*, B. A. Andreev*, V. I. Gavrilenko*, I. V. Erofeeva*, D. V. Kozlov*, and O. A. Kuznetsov**

** Institute for Physics of Microstructures, Russian Academy of Sciences, Nizhni Novgorod, 603600 Russia*

*** Physicotechnical Research Institute, Nizhni Novgorod State University, Nizhni Novgorod, 603600 Russia*

Submitted September 6, 1999; accepted for publication September 16, 1999

Abstract—The energies of localized acceptor states in quantum wells (strained Ge layers in Ge/$Ge_{1-x}Si_x$ heterostructures) were analyzed theoretically in relation to the quantum well width and the impurity position in the well. The impurity absorption spectrum in the far IR range is calculated. Comparison of the results of the calculation with experimental photoconductivity spectra allows an estimation of the acceptor distribution in the quantum well to be made. In particular, it was concluded that acceptors may largely concentrate near the heterointerfaces. The absorption spectrum is calculated taking into account the resonance impurity states. This allows the features observed in the short-wavelength region of the spectrum to be interpreted as being due to transitions into the resonance energy levels "linked" to the upper size-quantization subbands. © *2000 MAIK "Nauka/Interperiodica".*

1. INTRODUCTION

The electronic structure of shallow impurities in semiconductor heterostructures with quantum wells (QWs) is known to depend significantly on the well width and the position of an impurity center within the well. In the case of donors, the wave function confinement by barriers leads to stronger electron localization near the impurity ion, thereby making the binding energy higher in comparison with the bulk semiconductor. The binding energy is the highest if the impurity is situated at the QW center and decreases markedly when it is shifted toward the QW boundary [1, 2]. An additional factor reducing the binding energy appears in the case of the acceptor: the hole effective mass at the bottom of the first subband decreases because of the heavy and light hole subband splitting due to the size-quantization effects. In strained structures, the built-in strain also influences the shallow acceptor spectrum, leading to an additional subband splitting and decreasing the effective mass of holes. All these factors allow the acceptor binding energy in the QW to be varied, with the heterostructure parameters changed, which is of interest for creating extrinsic photodetectors for the far-infrared (FIR) range.

This work is concerned with shallow acceptors in QWs in strained multilayer Ge/$Ge_{1-x}Si_x$ heterostructures grown on the Ge substrate in the (111) crystallographic direction. In these structures, the Ge layers acting as QWs for holes are compressed in the plane perpendicular to the growth direction because of the lattice mismatch for the materials constituting the heterostructure [3].

A method for calculating the spectra of shallow acceptors in QWs is developed in this work. This method made it possible to obtain the wave functions for both localized and delocalized states, to calculate binding energies for the ground and excited states, and to find spectra of free hole photogeneration in heterostructures for the FIR range. The calculation method used was proposed in [4]. It is based on an expansion of the acceptor wave function in free hole wave functions in QWs. However, the incorrect choice of the basis functions in [4] led to qualitatively erroneous results: it was predicted that the twofold degeneracy of acceptor states is lifted in strained QWs (see also [5]). An integral equation was derived in [6] for the coefficients of the acceptor wave function expansion mentioned above. Unfortunately, the authors of [6] solved this equation using the variational technique, which, first, impaired the calculation accuracy (especially for excited states) and, second, gave no way of finding the continuum spectrum states and, therefore, failed to produce the optical absorption coefficient and photogeneration spectra.

A comparison of the experimental photoconductivity spectra of the QW Ge/$Ge_{1-x}Si_x$ heterostructures with the photogeneration spectra calculated for various impurity positions in the QWs suggested that a significant number of acceptors may concentrate at the heterointerface.

2. CALCULATION TECHNIQUE

The energies of acceptor states were found by solving the Schrödinger equation. The Hamiltonian was chosen as a sum of the kinetic energy (Luttinger's

Hamiltonian), the potential energy of a hole in the QW, the deformation term, and the energy of the Coulomb interaction with the charged acceptor [7]. Similarly to [6], the axial approximation was used; i.e., the hole dispersion law was assumed to be isotropic in the QW plane. For this purpose, the terms proportional to $(\gamma_2 - \gamma_3)$ (γ_2 and γ_3 are the Luttinger parameters [7]) were dropped in the nondiagonal elements of the Luttinger Hamiltonian. We note that the first-order perturbation correction to the energy, associated with the dropped terms, is zero.

Within the axial approximation, the component of the total angular momentum $\pm J$ normal to the QW plane is conserved and the acceptor spectrum is doubly degenerate with respect to the sign of this component (i.e., $\pm J$). Note that, in accordance with group theory, the electronic structure of an acceptor in a QW grown on the (001) or (111) plane must be doubly degenerate even with account taken of the hole dispersion law anisotropy in the QW plane.

The acceptor wave function was sought for as an expansion in the eigenfunctions of holes in the QW containing no acceptor:

$$\Psi_J(\mathbf{r}) = \sum_{k, n, s} C_J(k, n, s)\frac{\varphi(\mathbf{k}, n, s, \mathbf{r})}{\sqrt{k}}, \qquad (1)$$

where k is the hole wave vector; n is the number of a size-quantization subband; $s = \pm 1$ is the parity with respect to reflection in the plane containing the wave vector k and the normal to the QW plane; and $\varphi(\mathbf{k}, n, s, \mathbf{r})$ is the eigenfunction of a hole in the QW. Taking into account that the dependence of the coefficients $C_J(\mathbf{k}, n, s)$ on the wave vector is given by [4]

$$C_J(\mathbf{k}, n, s) = C_J(k, n, s)\exp\left[i\alpha\left(J - \frac{3}{2}\right)\right], \qquad (2)$$

where α is the angle characterizing the wave vector direction, we can derive the following equation for determining $C_J(k, n, s)$:

$$[\varepsilon(k, n) - E]C_J(k, n, s) + \sum_{n', s'}\int_0^\infty dk'\sqrt{kk'}C_J(k', n', s') \times V(k', n', s', k, n, s) = 0, \qquad (3)$$

where $\varepsilon(k, n)$ is the hole dispersion law in the nth subband, E is the energy,

$$V(k', n', s', k, n, s) = -\frac{e^2}{\chi}\int_0^{2\pi} d\beta\exp\left[i\beta\left(J - \frac{3}{2}\right)\right] \times \int d^3\mathbf{r}\left\langle \varphi(\mathbf{k}', n', s', \mathbf{r})\left|\frac{1}{r}\right|\varphi(\mathbf{k}, n, s, \mathbf{r})\right\rangle, \qquad (4)$$

β is the angle between the wave vectors k and k', χ is the semiconductor's permittivity, and e is the elementary charge. The heterointerface polarization due to a slight permittivity mismatch between the quantum well and barrier materials is not taken into account here. Note that the kernel of the integral operator in the equation for $C_J(k, n, s)$ is symmetric with respect to the variables k, n, s, k', n', s', and V is real. This enables us to solve equation (4) diagonalizing the symmetric real matrix. Indeed, if the step in k' is chosen less than the Bohr radius, the integrand varies only slightly in a single step. In this case, the integral can be written as a sum over discrete k' values. Also, $C_J(k, n, s)$ are apparently small for k much larger than the inverse Bohr radius. Therefore, the series can be truncated without any significant error. It is also clear that, if the QW depth much exceeds the acceptor ionization energy and the acceptor is located inside the QW, the contribution to the wave function from the three-dimensional (above-barrier) states can be neglected. Thus, the problem of finding the localized and delocalized acceptor states is reduced to diagonalization of a finite symmetric matrix.

Energy eigenvalues have been found for states corresponding to the angular momentum components $J = \pm 3/2, \pm 1/2$, and $\pm 5/2$ in the $Ge/Ge_{1-x}Si_x$ heterostructures. For the acceptor ground state, we have $J = \pm 3/2$; and for the lower excited states, $J = \pm 1/2, \pm 3/2$, and $\pm 5/2$. Anisotropy-related corrections to the level energies were calculated in terms of the second-order perturbation theory. For heterostructures grown on the (111) plane, the anisotropy leads to an interaction between the states with the angular momentum components J and $J \pm 3$. The strongest influence is exerted by the anisotropy on the ground state of the acceptor. For Ge/GeSi heterostructures, consideration of the second-order correction increases the acceptor binding energy by 3.0–3.5%. Consideration of the anisotropy changes the energy of the excited states of acceptors by less than 1% in these structures.

The described method yields wave functions both for localized states and for states belonging to the continuum, which enables calculation of the probabilities of the dipole-optical transitions between impurity levels beyond the Born approximation. This makes it possible to describe not only the position but also the shape of lines in the observed photoconductivity spectrum of the Ge/GeSi heterostructures and, therefore, to study impurities in these structures in more detail. The photoconductivity signal is proportional to the free-hole generation intensity per unit volume (I_{hg}). Under the effect of electromagnetic radiation, a hole makes a transition into the continuum or is transferred to excited localized states. In the former case, the free-hole generation intensity per unit volume is given by

$$I_{hg} = nW, \qquad (5)$$

where n is the impurity concentration and W is the probability of a hole transition from the ground state into the continuum per unit time under the influence of radiation. In the latter case, a hole that has been transferred to an excited state may pass into the continuum

upon absorbing an acoustic phonon (thermal ionization); then, the free carrier generation intensity is given by

$$I_{hg} = P_{\text{ph}} n W, \tag{6}$$

where W is the probability of hole transition to the excited state per unit time and P_{ph} is the thermal ionization probability.

The transition probability per unit time under the action of circularly polarized electromagnetic radiation is written as

$$W = \frac{\sqrt{2}\pi(eE)^2}{\hbar}\int |\langle \Psi_i(J)|x \pm iy|\Psi_f(J \pm 1)\rangle|^2 \times \frac{G(E_f)}{[E_i + \hbar\omega - E_f]^2 + (h\nu)^2}, \tag{7}$$

where x and y are the Cartesian coordinates in the QW plane, E is the electric field strength of the electromagnetic wave, $h\nu$ is the half-width of the energy levels, E_i is the ground state energy, E_f is the final state energy, and $G(E_f)$ is the density of states. Note that transitions are allowed between the ground state and the states with total angular momentum components $J = 5/2$ and $-1/2$ for one direction of circular polarization and $J = 1/2$ and $-5/2$ for the other.

As already noted, not all carriers transferred to the excited states can be found in the continuum; that is why the photoconductivity spectrum differs essentially from the transition intensity spectrum. The probability of thermal ionization of a level for $E \gg kT$ can be expressed as [8, 9]

$$P_{\text{ph}} = A\exp(-E/kT), \tag{8}$$

where A is temperature-dependent. The calculated free-hole photogeneration spectra agree well with the experimental photoconductivity spectra if we assume that, for deep excited states (such that $E \gg kT$, with $kT \approx 0.4$ meV at $T = 4.2$ K), $A \approx 1$ [in equation (8)], and, for shallow states (such that $E < kT$), $P_{\text{ph}} \approx 1$.

3. RESULTS AND DISCUSSION

3.1. Calculation of Energy Levels

Shallow acceptor spectra calculated for Ge/GeSi heterostructures are shown in Figs. 1 and 2. As can be seen from Fig. 1, the ionization energy of the ground state of acceptors at the QW center decreases with increasing QW width, which is due to a weakening of the Coulomb interaction between a hole and an acceptor. However, for $d_{QW} = 350$ Å, the binding energy is lower than that in the bulk Ge subjected to biaxial compression equal to the compression of Ge layers in the heterostructures under consideration (indicated by an arrow in Fig. 1). Such a nonmonotonic dependence of the binding energy on the QW width reflects the dual effect of spatial confinement on the binding energy of

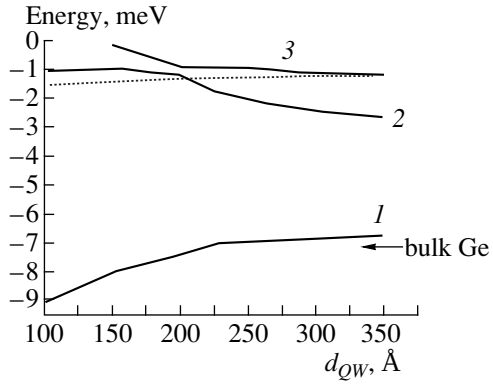

Fig. 1. Calculated binding energies of the ground and lower excited states of an acceptor at the center of a QW in a $Ge/Ge_{0.88}Si_{0.12}$ heterostructure ($\varepsilon = 2.1 \times 10^{-3}$) in relation to the QW width. Solid line: $J = \pm 3/2$ (curve *1* is for the ground state, and curves *2* and *3* are for the lower excited states corresponding to this angular momentum component). Dashed line: $J = \pm 1/2, \pm 5/2$. The arrow indicates the acceptor binding energy in bulk Ge subjected to "equivalent" uniaxial tension.

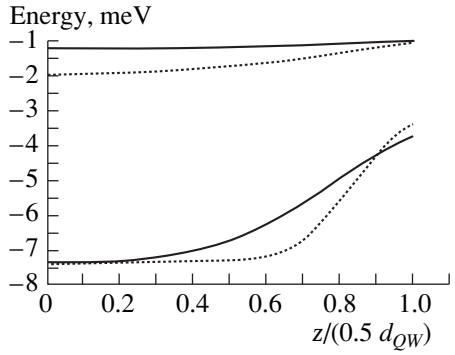

Fig. 2. Calculated binding energies of the ground and lower excited states for Ge/GeSi samples 306 (solid line) and 308 (dashed line) in relation to the impurity position in the QW (sample parameters as in Fig. 3).

shallow acceptors. The curves for two excited state energies are also shown in Fig. 1. The ionization energies of the lower excited states with the angular momentum components $J = 5/2$ and $1/2$ are seen to increase with decreasing QW width, which is due to a stronger wave function localization at the acceptor and, therefore, to an increasing Coulomb energy. However, it should be noted that the ionization energies of excited states with the angular momentum component $J = 3/2$ decrease with decreasing QW width. The structure of the excited state wave functions with this angular momentum component has to be considered in more detail in order to gain insight into the origin of this effect. The expansions of the acceptor wave function in the wave functions of free holes in the QW include functions related to different size-quantization subbands. Note that, if the QW width is large, the lower

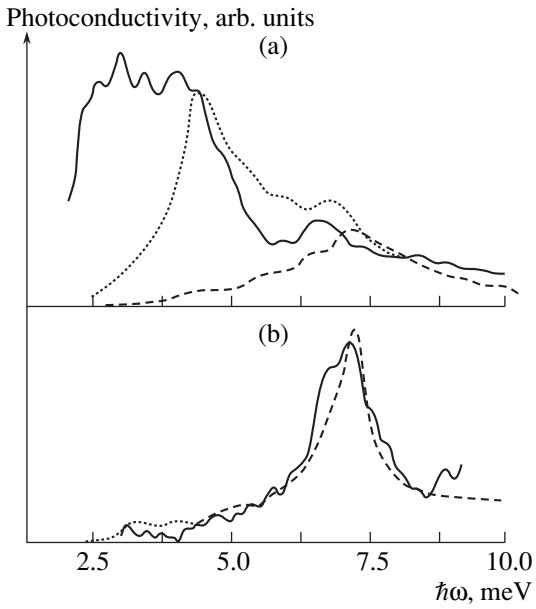

Fig. 3. FIR photoconductivity spectra of multilayer $Ge/Ge_{1-x}Si_x$ heterostructures with QWs, (a) no. 306 (x = 0.12; d_{QW} = 200 Å, $\varepsilon = 2.1 \times 10^{-3}$; and N_{QW} = 162) and (b) no. 308 (x = 0.09, d_{QW} = 355 Å, $\varepsilon = 0.34 \times 10^{-3}$; and N_{QW} = 162). Solid lines represent the experimental data; dashed lines represent the free-hole generation spectra calculated under assumption of a uniform impurity distribution over the QWs of heterostructures under study. The dotted line in (a) represents the free-hole generation spectrum calculated under the assumption that a delta-layer of acceptors is present at the heterointerfaces along with the uniform impurity distribution. The surface density of the impurity in this layer is half the integrated concentration of the uniformly distributed impurity.

state (*2*) is mainly formed by the functions of the second size-quantization subband, while the upper state (*3*), mainly by those belonging to the first subband. When the QW width decreases, the ionization energy of the state (*2*) (which is linked to the second size-quantization subband) decreases fast. For a QW width of about 200 Å, the states (*2*) and (*3*) approach each other to the largest extent and "exchange" their wave functions. For an even smaller QW width, the state (*2*) is already formed by the wave functions of the first size-quantization subband. Because of this, the dependence of the ionization energy of state (*2*) on the QW width becomes smoother (see Fig. 1), with the state (*3*) formed by functions of the second size-quantization subband pushed upwards into the continuum.

The dependence of the ground and lower excited state energies on the acceptor position in the QW is shown in Fig. 2. The ionization energy of the ground state of the acceptor is clearly seen to decrease nearly twofold in moving from the QW center to the heterointerface, which is also associated with a decrease in the Coulomb energy. Note that the binding energy starts to change significantly when the impurity approaches the QW edge to a distance of about 50 Å, which corresponds to the spatial scale of localization of the acceptor ground state wave function in the growth direction.

It can also be seen in Fig. 2 that the ionization energy of the excited states decreases only slightly as the heterointerface is approached. The reason is that the QW width is comparable with the localization scale of the acceptor's excited-state wave function and, consequently, even an impurity located at the QW edge "feels" both the heterointerfaces.

3.2. Spectra of Free-Hole Generation from Impurity in a QW in Ge/GeSi Heterostructures

The outlined method presents an opportunity to describe the generation spectrum of free (i.e., delocalized) holes under the action of FIR radiation beyond the Born approximation. The generation is associated with excitation of shallow acceptor centers located in the QWs in the heterostructure.

Most of the investigated heterostructures were not intentionally doped; they contained only residual acceptors (with a concentration on the order of $\sim 10^{14}$ cm^{-3}). It seems reasonable to suppose that these impurities are distributed uniformly in the QW. However, some features of the growth process favor accumulation of impurities near the heterointerfaces. Indeed, a heterointerface is a source of point defects, and a vacancy can behave as a shallow acceptor in germanium.

The experimental photoconductivity spectra of two samples with different QW widths (solid lines) are shown in Fig. 3. The dashed lines represent the free-hole generation spectra calculated under the assumption of a uniform distribution of impurities over the QWs in the heterostructures under study. These generation spectra are mainly due to the transitions between the levels of an impurity residing at the QW center. The reason is that the quantum wells in the heterostructures under study contain a substantial layer of impurities with ionization energies close to the acceptor ionization energy at the QW center (for sample no. 308, E_i = 7.4 meV; for no. 306, E_i = 7.35 meV; see Fig. 2). The layer thickness is about 75% of the total QW width in sample no. 308 and about 50% in sample no. 306. It can be seen that both the position and the shape of the photoconductivity spectral lines of sample no. 308 can be described in terms of the uniform impurity distribution model.

At the same time, it should be noted that the occurrence of a strong long-wavelength band in the photoconductivity spectrum of sample no. 306 cannot be explained in terms of a uniform impurity distribution over the QW. We have to assume that, in addition to the uniformly distributed impurities, there is a considerable amount of acceptors concentrated near the heterointerface, since their ionization energy corresponds to the short-wavelength photoconductivity band. The dotted

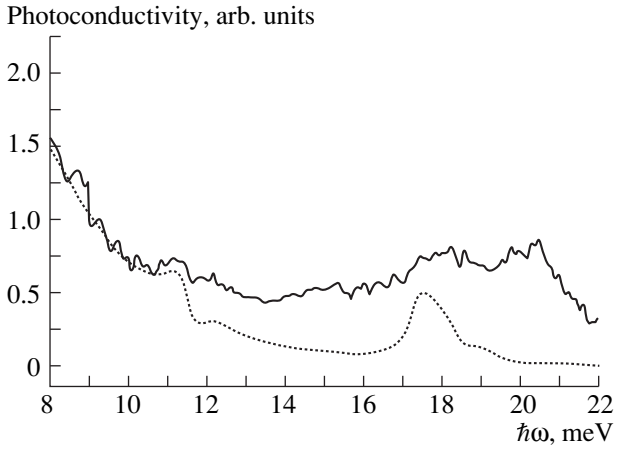

Fig. 4. Short-wavelength region of the photoconductivity spectrum of sample no. 306. The solid line represents the experimental photoconductivity spectrum. The dashed line corresponds to the hole generation spectrum calculated for an impurity at the QW center in sample no. 306.

line in Fig. 3a represents the free-hole generation spectrum calculated, assuming that, in addition to the uniform impurity distribution, there is a delta-layer of acceptors near the heterointerfaces. It can be seen that the short-wavelength features and the right-hand edge of the long-wavelength band of the photoconductivity spectrum of sample no. 306 are well described by this model. The long-wavelength wing of the photoconductivity spectrum of sample no. 306 (as already mentioned in [10]) can be related to ionization of acceptors in the barrier and also to excitation of A^+ centers located in QWs.

The short-wavelength region of the photoconductivity spectrum of sample no. 306 is shown in Fig. 4. The dashed line represents the free-hole generation spectrum calculated for an impurity residing at the center of the QW in sample no. 306, with account taken of the resonance impurity levels. The peak in this spectrum coincides with the short-wavelength edge of the 17–20 meV photoconductivity band in the experimental spectrum. This photoconductivity peak is associated with transitions from the ground state to the resonance levels mainly formed by the states of the third size-quantization subband. The appearance of a broad photoconductivity band instead of the narrow line in the experimental spectrum can be explained by the variance of the QW width. The theoretical curve also exhibits some features at photon energies of 11 and 12 meV; their positions coincide with the weakly pronounced lines in the experimental spectrum. These lines are associated with transitions from the ground state to the resonance levels mainly formed by states of the second size-quantization subband. Thus, short-wavelength features of the absorption spectrum present an opportunity to study the positions of resonance levels linked to the upper size-quantization subbands.

ACKNOWLEDGMENTS

We thank M.D. Moldavskaya for her assistance in measurements and her helpful participation in discussions, E.A. Uskova for sample preparation for measurements, and Yu.N. Drozdova for X-ray analysis of the samples.

This work was supported by the Ministry of Policy in Science and Technology under the Programs “Physics of Solid-State Nanostructures” (project nos. 97-1069 and 97-2022) and “Physics of Microwaves” (project no. 4.5), the State Scientific and Technological Program “Physics of Quantum and Wave Processes/Fundamental Spectroscopy” (project no. 8/02.08), the Russian Foundation for Basic Research (project no. 97-02-16326), the Special Federal Program “Integration” (project nos. 540 and 541), and NATO (grant no. CLG 975592).

REFERENCES

1. A. A. Reeder, J. M. Mercy, and B. B. McCombe, IEEE J. Quantum Electron. **24**, 1690 (1988).
2. C. Guillemot, Phys. Rev. B: Condens. Matter **31**, 1428 (1985).
3. O. A. Kuznetsov, L. K. Orlov, and R. A. Rubtsova, Pis’ma Zh. Tekh. Fiz. **15** (21), 77 (1989) [Sov. Tech. Phys. Lett. **15**, 863 (1989)].
4. J. P. Loehr and J. Singh, Phys. Rev. B: Condens. Matter **41**, 3695 (1990).
5. J. P. Loehr, Y. C. Chen, *et al.*, in *Proceedings of 20th International Conference on the Physics of Semiconductors, 1990*, Vol. 2, p. 1401.
6. A. Pasquarello, L. C. Andreani, and R. Buczko, Phys. Rev. B: Condens. Matter **40**, 5602 (1989).
7. G. M. Bir and G. E. Pikus, *Symmetry and Strain-Induced Effects in Semiconductors* (Nauka, Moscow, 1972; Wiley, New York, 1975).
8. V. N. Abakumov and I. N. Yassievich, Zh. Éksp. Teor. Fiz. **70**, 657 (1976) [Sov. Phys. JETP **44**, 345 (1976)].
9. A. V. Osutin, Candidate’s Dissertation in Physics and Mathematics (Leningrad, 1988).
10. V. Ya. Aleshkin, V. I. Gavrilenko, I. V. Erofeeva, *et al.*, Fiz. Tekh. Poluprovodn. (St. Petersburg) **32**, 1240 (1998) [Semicond. **32**, 1106 (1998)].

Translated by S. Ktitorov

Semiconductors, Vol. 34, No. 5, 2000, pp. 568–574. Translated from Fizika i Tekhnika Poluprovodnikov, Vol. 34, No. 5, 2000, pp. 588–594.

LOW-DIMENSIONAL SYSTEMS

Exciton Energy States and Photoluminescence Spectra of the Strained-Layer ZnS–ZnSe Superlattices

N. V. Bondar', V. V. Tishchenko*, and M. S. Brodin

Institute of Physics, National Academy of Sciences of Ukraine, Kiev, 258650 Ukraine

** e-mail: vvti@iop.kiev.ua*

Submitted September 9, 1999; accepted for publication September 16, 1999

Abstract—Excitonic photoluminescence spectra in the ZnS–ZnSe strained-layer superlattices with imperfect heterointerfaces were studied experimentally. It is shown that the energy states of excitons in these structures are affected both by interface imperfections and internal strain caused by the lattice mismatch between the semiconductors composing the superlattice layers. *© 2000 MAIK "Nauka/Interperiodica".*

1. INTRODUCTION

It is known that the optical and electrical properties of semiconductor devices with quantum wells (QWs) and superlattices (SLs) depend substantially on the degree of the in-plane uniformity of the layer thicknesses [1–7]. Uncontrolled fluctuations result in the formation of QW domains with thicknesses differing from the design value L_W by an integer number of the lattice constants. As a consequence, heterointerfaces between the semiconductors composing the structure appear in the form of growth islands or valleys [2]. As distinct from the case of a QW with ideal interfaces, the energy spectrum and behavior of excitons in actual QWs and SLs are determined by the ratio between the island lateral size D_x and the exciton radius R [3]. If $D_x \sim R$, the intrinsic QW luminescence originates from the recombination of excitons localized in the wells of the potential relief formed due to the thickness fluctuations. The common feature shared by all disordered QWs is the existence of the Stokes shift of the photoluminescence (PL) spectrum with respect to the absorption spectrum maximum (correspondingly, to the reflection spectrum minimum), so that the PL line falls within the QW forbidden band, where the absorption coefficient is small [8–12]. Investigating the samples with individual ZnS–ZnSe QWs, we established that the shape of their reflection and PL spectra is largely determined by the imperfections in the interface [7–9]. Analyzing the PL line shape, we found that the scale of fluctuations in those samples does not exceed the ZnSe lattice constant (5.6684 Å).

If the lateral size and thickness of the islands are increased significantly ($D_x \gg R$), a drastic transformation of the exciton PL and reflection spectra is observed. Substantial deviations from the two-dimensional (layer-by-layer) growth can be caused simply by an improper choice of the parameters in the growth chamber, such as the temperature, flux rates of the reactants, etc. [10]. Another, more fundamental reason is related to the internal strain in the quantum structure, which inevitably appears if the structure is composed from lattice-mismatched semiconductor materials. In our case, the lattice constant difference between ZnS and ZnSe amounts to 4.6%. Thus, elastic energy can be accumulated in the ZnSe layers due to the contraction of its unit cells, and the initial two-dimensional growth can turn into the three-dimensional growth with the island formation, the so-called Stranski–Krastanov mode [1]. Because of insufficient information available on the surface adsorption processes, we cannot *a priori* specify unambiguously which of these two reasons lead to the formation of the island interface structure in the strained ZnS–ZnSe QWs and SLs.

In this paper, we report the results of experimental studies of the exciton energy spectra in the strained-layer ZnS–ZnSe SLs grown by the photostimulated gas-phase epitaxy [10]. It is established that fluctuations result in the formation of QW regions of increased thickness (exceeding the design value by several ZnSe lattice constants) with lateral dimensions two order of magnitude greater than the exciton size. Since the exciton coherence length is substantially increased within such regions, these SLs can be treated as a set of separate QWs with discrete thicknesses. Different QW regions give rise to different components of the PL band, a phenomenon which has been confirmed experimentally. It is shown that the spectral position of these components is largely affected by the internal strain in the ZnS–ZnSe SLs under consideration. It is emphasized that, due to the strain, the height of the potential barrier for electrons depends considerably on the QW thickness, which should be taken into account when analyzing the PL spectra.

1063-7826/00/3405-0568$20.00 © 2000 MAIK "Nauka/Interperiodica"

2. ENERGY SPECTRUM OF THE STRAINED-LAYER ZnS–ZnSe QUANTUM STRUCTURES

Let us characterize the strain state of the ZnS–ZnSe SL by the following three parameters: the in-plane lattice constant $a_\parallel$ and the two lattice constants $a_\perp^{1,2}$ in the growth direction (indices 1 and 2 refer to ZnSe and ZnS, respectively). In the case of pseudomorphic growth, $a_\parallel = a_0$, where a_0 is the lattice constant of the substrate (e.g., GaAs). The other situation, when the SL can be considered free-standing, occurs if its total thickness is well above the critical value [15, 16]. Then,

$$a_\parallel = \frac{a^1 G^1 L + a^2 G^2 L_b}{G^1 L + G^2 L_b}, \quad (1)$$

$$a_\perp^{1,2} = a^{1,2}\left\{1 - \left(D^{1,2}\frac{a_\parallel}{a^{1,2}} - 1\right)\right\}, \quad (2)$$

where $D^{1,2} = 2\dfrac{C_{11}^{1,2}}{C_{12}^{1,2}}$, $C_{11}^{1,2}$, and $C_{12}^{1,2}$ are the elastic constants; $G^{1,2}$ are the shear moduli; and $a^{1,2}$ are the bulk lattice constants of ZnSe and ZnS, respectively. The SL strain is described by the strain tensor ε, whose diagonal components are given by [16]

$$\varepsilon_{xx}^{1,2} = \varepsilon_{yy}^{1,2} = \frac{a_\parallel}{a^{1,2}} - 1, \quad (3)$$

$$\varepsilon_{zz}^{1,2} = \frac{a_\perp^{1,2}}{a^{1,2}} - 1. \quad (4)$$

The internal strain can be expressed as a sum of isotropic and uniaxial components, which differ qualitatively in their effect on the semiconductor band structure. The isotropic strain results in the energy shift of the edges of conduction band E_c and valence band E_v with respect to the corresponding equilibrium positions. The magnitude of the shift is determined by the electron and hole deformation potentials a_c and a_v, respectively; their sum gives the full isotropic deformation potential $a = a_c + a_v$. The uniaxial strain results in the splitting of the ZnSe valence band, which is degenerate at the Γ-point, into the heavy- and light-hole subbands E_{vh} and E_{vl}, respectively. The magnitude of the splitting is determined by the uniaxial deformation potential b [15, 16].

Recently, the "model-solid" theory, developed in [15, 16], became the most widely used in calculations. It combines simplicity with efficiency and enables one to calculate the heterostructure characteristics from the parameters of the binary semiconductors. Strain may or may not be included in the calculation; i.e., both lattice-mismatched and lattice-matched materials may be considered [5, 16]. Employing the principles of this theory,

ZnS and ZnSe material parameters

Parameter	ZnSe	ZnS	Source
a, Å	5.6684	5.4093	[5]
a_c, a_v, eV	–3.65, 1.67	–4.09, 2.31	[5, 15]
E_g, eV	2.823	3.84	[15, 16]
C_{11}, C_{12}, Mbar	0.859, 0.506	1.066, 0.666	[5–7]
b, eV	–1.2	–0.7	[5, 7, 15]
G	1.447	1.803	[15]
Δ_0, eV	0.143	0.070	[5, 6]
E_{av}, eV	–8.37	–9.15	[15]

let us first calculate the conduction- and valence-band-edge discontinuities ΔE_{fc} and ΔE_{fv} in the unstrained ZnS–ZnSe structure [16]:

$$\Delta E_{fv} = \Delta E_{av} + \frac{\Delta_0^1}{3} + \frac{\Delta_0^2}{3}, \quad (5)$$

$$\Delta E_{fc} = E_c^2 - (E_g^1 + \Delta E_{fv}). \quad (6)$$

Here, $\Delta E_{av} = E_{av}^1 - E_{av}^2$, where E_{av} is the energy position of the valence band "centroid" related to E_v by $E_v = E_{av} + \dfrac{\Delta_0^{1,2}}{3}$ (here, $\Delta_0^{1,2}$ is the spin–orbit energy splitting); $E_g^{1,2}$ is the bandgap energy; and $E_c^2 = E_g^2 + \dfrac{\Delta_0^2}{3}$. Substituting the corresponding numerical values, given in the table, we obtain $\Delta E_{fc} \sim 0.14$ eV and $\Delta E_{fv} \sim 0.9$ eV.

Next, inclusion of the deformation changes the internal state of the SL, and the new values for the band-edge discontinuities ΔE_c and ΔE_v are related to ΔE_{fc} and ΔE_{fv} in terms of the respective deformation potentials [5]:

$$\Delta E_c = \Delta E_{fc} + a_c\frac{\Delta\Omega}{\Omega}, \quad (7)$$

$$\Delta E_v = \Delta E_{fv} + a_v\frac{\Delta\Omega}{\Omega} + E_{vh}; \quad (8)$$

for $\varepsilon_{ij} \ll 1$, the relative volume change is given by $\dfrac{\Delta\Omega}{\Omega} \approx (\varepsilon_{xx} + \varepsilon_{yy} + \varepsilon_{zz})$. The last term in (8) is related to the uniaxial deformation component [16]:

$$E_{vh} = \frac{\Delta_0^1}{3} + \frac{1}{2}\delta E_{001}, \quad (9)$$

$$\delta E_{001} = 2b(\varepsilon_{zz} - \varepsilon_{xx}). \quad (10)$$

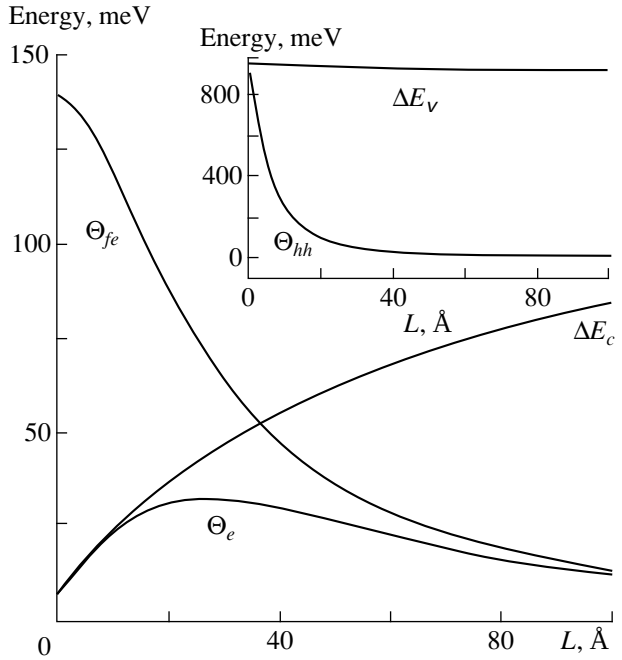

Fig. 1. Variation of Θ_e, ΔE_c, and Θ_{fe} in relation to the quantum well width L. Insert: Θ_{hh} and ΔE_v as functions of the well width.

Using equations (1)–(10), we can calculate the well-width dependence of the potential barrier heights ΔE_c and ΔE_v, as well as the energies Θ_e and Θ_{hh} of the first ($n = 1$) quantum-confined electron and heavy-hole levels, in the free-standing SL approximation at $L_b = 60$ Å; the results of calculations are shown in Fig. 1. The $\Delta E_c(L)$ and $\Delta E_v(L)$ dependences were calculated from equations (7) and (8), and $\Theta_e(L)$ and $\Theta_{hh}(L)$ were determined from the transcendental equation

$$(L)^2 = \left(\frac{\hbar^2}{2m_j\Theta_j(L)}\right) \times\left(\pi - 2\arcsin\left[\frac{\Theta_j(L)}{\Delta E_{c(v)}}\right]^{1/2}\right)^2 \quad j = e, hh, \tag{11}$$

where $m_e = 0.17m_0$ and $m_{hh} = 0.6m_0$ are the bulk ZnSe electron and hole masses, respectively.

The dependence of the heavy-hole exciton binding energy on the well width in the ZnS–ZnSe structures, with the internal strain accounted for, is given by

$$E_{hh}(L) = E_g^1 + \Theta_e(L) + \Theta_{hh}(L) - E_{2x}(L), \tag{12}$$

where $E_x(L)$ is the heavy-hole exciton binding energy, which also depends on L. This dependence can be obtained from the solution of the Schrödinger equation in the "fractional dimension" model and expressed in terms of the parameter α, which determines the electron-hole interaction anisotropy [7]:

$$E_{2x} = \frac{E_x}{\left\{n - \frac{1}{2}(\alpha - 3)\right\}^2}, \tag{13}$$

$$\alpha = 3 - \exp\left(-\frac{L^*}{2a_B}\right), \tag{14}$$

where $E_x = 21$ meV and $a_B = 50$ Å are the bulk ZnSe exciton binding energy and the Bohr radius, respectively, and L^* is the effective QW width accounting for the penetration of electron and hole wave functions into the barrier:

$$L^* = L_e^* + L_{hh}^* + \frac{1}{k_e} + \frac{1}{k_{hh}}, \tag{15}$$

$$L_j^* = \left(\frac{\hbar^2 L^2}{8\Delta E_{c(v)} m_j}\right)^{1/4}, \tag{16}$$

$$\frac{1}{k_j} = \left[\frac{2m_j(\Delta E_{c(v)} - \Theta_j)}{\hbar^2}\right]^{1/2}. \tag{17}$$

It can be seen from Fig. 1 that, if the well-width dependence of ΔE_c is taken into account, Θ_e approaches a maximum at $L \sim 20$ Å and then decreases; this can be compared to the electron energy level dependence $\Theta_{fe}(L)$ calculated for the constant $\Delta E_{fc} \sim 0.14$ eV, as shown in Fig. 1. Such behavior of $\Theta_e(L)$ is caused by an increase in the electron potential barrier height with increasing QW thickness.

Due to the partial penetration of electron and heavy-hole wave functions into the barrier, the effective well width L^*, which is "felt" by the particles, differs from the geometric width. For $L = 5.66$ Å, $\Delta E_c = 10$ meV, and $\Delta E_v = 930$ meV, we find from equation (16) that $L_e^* \sim 12.3$ Å and $L_{hh}^* \sim 2.7$ Å. Thus, since the extension of the electron wave function decreases with increasing L, the initial growth of $\Theta_e(L)$, which is also caused by the accompanying increase in ΔE_c, occurs. At the same time, for the heavy holes, $L_{hh}^* < L$ in the entire range of the QW widths and, consequently, the dependence $\Theta_{hh}(L)$ is proportional to the conventional $1/L^2$. It can be easily found that the $\Theta_e(L)$ dependence transforms into the conventional $1/L^2$ if the initial value of ΔE_c exceeds 0.1 eV. At first glance, it would seem that, since $\Delta E_c \ll \Delta E_v$, the $E_{hh}(L)$ dependence should be entirely determined by the behavior of $\Theta_{hh}(L)$; however, because the large heavy-hole mass $\Theta_{hh}(L)$ decreases rapidly as L increases and for $L > 24$ Å, $\Theta_e \approx \Theta_{hh}$, the behavior of $E_{hh}(L)$ is determined by the electron component (see Fig. 1).

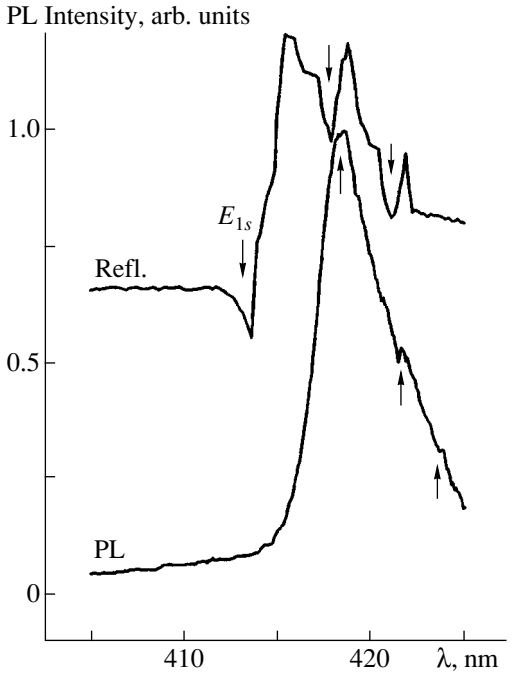

Fig. 2. Reflection and photoluminescence spectra of a ZnS–ZnSe superlattice at T = 4.5 K.

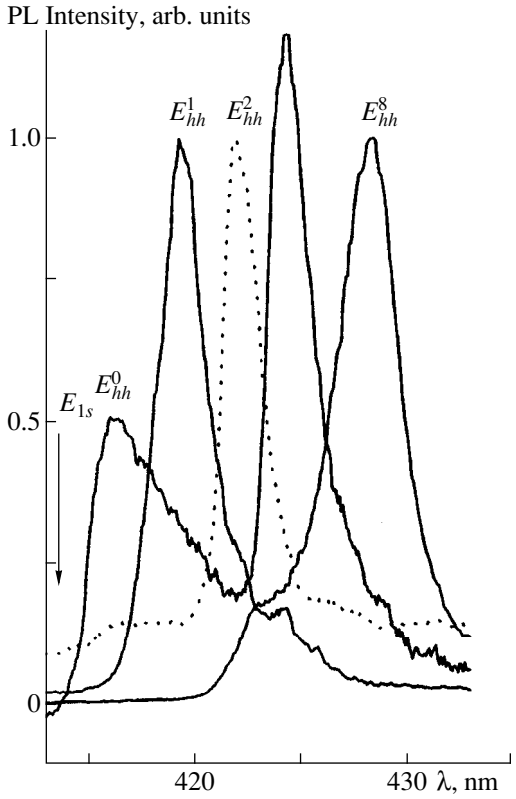

Fig. 3. Components of the photoluminescence band corresponding to different areas of the ZnS–ZnSe SL surface (T = 4.5 K).

3. EXPERIMENTAL RESULTS AND DISCUSSION

1. The ZnS–ZnSe SLs under study were grown by photostimulated gas-phase epitaxy on GaAs(001) substrates and were composed of 80 11-Å-thick ZnSe QWs separated by 60-Å-thick ZnS barriers; the thicknesses were determined from the growth rates measured for ZnSe and ZnS epitaxial films deposited on GaAs(001). To reduce the influence of the GaAs substrate on the SL, a ZnS_xSe_{1-x} buffer layer (with x = 0.07) of ~ 0.4 μm thickness was grown between them. A He–Cd laser (λ = 325 nm) with 10 mW average power was used as an excitation source, and a halogen lamp was used to record the reflection spectra. The samples were mounted in a cryostat with working temperatures T = 4.5–300 K, and the spectra were taken with a DFS-12 monochromator equipped with an FEU-79 photomultiplier operating in the photon counting mode.

2. In Figs. 2 and 3, we present the reflection and PL spectra originating from the heavy-hole exciton transitions for one of the selected SLs. Similar spectra related to the light-hole excitons are shifted to shorter wavelengths by ~ 200 meV [7]. Let us discuss some features of the spectra obtained. Along with the main minimum at E_{1s} = 2.997 eV, the reflection spectrum exhibits a number of additional minimums; those at 2.963 and 2.936 eV reveal themselves most clearly (see Fig. 2). The PL band, presented in the same figure, has a width at half-maximum of ~ 50 meV and an asymmetric shape with an extended long-wavelength wing, where several peaks (indicated by arrows) can be seen. The existence of these peaks suggests that the band is not elementary but consists of several components. Each component reveals itself most clearly in a certain area of the SL; thus, to determine their spectral positions more precisely, we performed a scan of the SL surface with the laser excitation spot (r ~ 30 μm). In doing so, we found nine distinct components of the PL band (denoted as E^0_{hh}, E^1_{hh}, E^2_{hh}, …, E^8_{hh}) corresponding to the nine different areas on the SL surface; four of them are shown in Fig. 3. We found that the spectral position of each component is independent of temperature over the range where the ZnSe bandgap is independent of T (i.e., below 100 K). The spectral position of each component is also independent of excitation intensity up to the levels where the exciton–exciton collisions become important (maximum excitation level ~10^{21} photon/(cm^2 s)). These results suggest that different components in the PL spectra originate from the recombination of the free heavy-hole excitons residing in different QW regions. Because of the increased lateral size of these regions, the exciton coherence length also increases, which makes possible observation of the separate components in the PL spectra. In Fig. 4, we present the dependence $E^p_{hh}(L)$ (where p = 0, 1, 2, …, 8), which was deduced

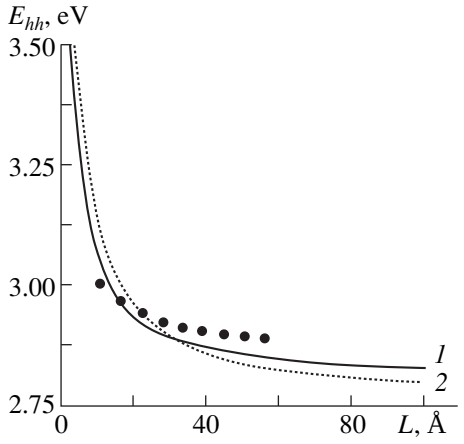

Fig. 4. Dependence of the exciton energy E_{hh} on the well width L: (*1*) calculation accounting for the internal strain; (*2*) calculation neglecting the internal strain, performed with $\Delta E_c = 0.14$ eV, $\Delta E_v = 0.9$ eV, and $E_{2x} = 42$ meV [7]. Experimental results are represented by dots.

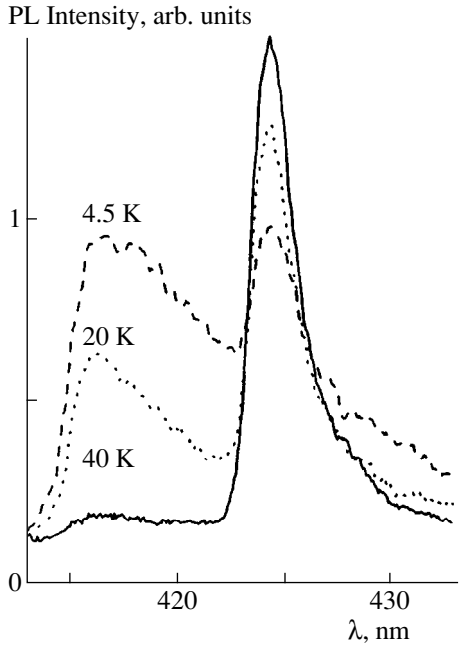

Fig. 5. Temperature variation of the shape of the E_{hh}^0 spectral component.

from the experimental data under the assumption that an exciton energy of 2.997 eV corresponds to the QW regions with width equal to the rated value $L_w = 11$ Å and that the lower energy minimums in the reflection spectra (respectively, peaks in the PL spectra) correspond to the QW regions of width $L = L_w + na^1$ ($n = 1, 2, 3, \ldots$). The similarity between the experimental and theoretical plots in Fig. 4 favors the conclusion that the shape of the reflection and PL spectra of the samples considered is determined by the width fluctuations in the QWs composing the SL.

The theoretical dependences $E_{hh}(L)$ presented in Fig. 4 by curves *1* and *2* deviate from the experimental points for $L > 20$ Å. One can see that the QW exciton energy calculated without taking into account the internal strain effect (curve *2*) equals about 2.803 eV (which corresponds to the ground-state exciton energy in the bulk ZnSe) even for $L \sim 80$ Å. However, our data, along with the results of other authors [13, 14], indicate that heavy-hole excitons in ZnS–ZnSe QWs and SLs are influenced by strain and the quantum-confinement effect even for $L > 100$ Å. Taking strain into account, we can improve the agreement between theoretical and experimental $E_{hh}(L)$ dependences for $L > 30$ Å. However, even in this case, complete agreement cannot be achieved. Possibly, this is explained by the fact that the calculation of the $E_{hh}(L)$ dependence has been performed in the free-standing SL approximation. It is valid if the total SL thickness greatly exceeds the critical value, which is more than 1 μm for the ZnS–ZnSe system [6]. Since the total thickness of the SLs studied here is about 0.6 μm, the calculations based on the model of [15, 16] can result in appreciable errors for structures not in their equilibrium state.

3. Degradation of the quality of QW interfaces results in an enhancement of the nonradiative processes and the appearance of additional channels for exciton scattering. Because of the formation of the QW regions of different widths, a number of resonant levels appear in the SL and the exciton system tends to occupy the lowest energy state during the exciton lifetime τ_0. We now consider the two cases characteristic of the exciton behavior in the disordered SLs studied here. The temperature dependence of the E_{hh}^0 PL component is shown in Fig. 5. At low T, this component consists of two peaks separated by ~55 meV. The asymmetric shape of the higher energy peak and its spectral position (this peak is at 2.977 eV, which falls between the main and the first additional reflection minima) indicate that the interfaces in the corresponding QW domain contain microislands with a lateral size smaller than the exciton radius: $D_x < R$. These microislands are "averaged" by excitons in the course of their motion, and, thus, the spectral position of the high-energy peak of the E_{hh}^0 component corresponds to the QW thickness that is not equal to a integer number of ZnSe lattice constants [2, 3]. The low-energy peak position, according to calculations, corresponds to the QW region with width differing from the rated value by an integer number of ZnSe lattice constants, namely, by $3a^1$. When the temperature is raised to 40 K, the high-energy peak almost vanishes and a simultaneous increase in the low-energy peak integrated intensity is observed, which takes place due to the redistribution of excitons between the QW regions with different thicknesses, which proceeds via diffusion on the characteristic length scale $L_D = (\tau_0 D)^{1/2}$ (where D is the diffusion coefficient) [2]. The complete disappearance of the

high-energy peak of the E^0_{hh} component occurs if excitons can reach the boundary of the QW region responsible for this peak within their lifetime, i.e., if $2L_D \sim D_x$. Taking into account that $L_D(T) = v(T)\tau_0$, where $v(T) = (kT/2\pi M_{hh})^{1/2}$ is the average thermal velocity of excitons (here, $M_{hh} = m_e + m_{hh}$), we find that, at $T = 40$ K, $D_x \cong 1$ μm; thus, the lateral size of the formed regions exceeds the exciton diameter (100 Å) in the bulk ZnSe by about two orders of magnitude.

Another kind of behavior is observed for the component $E^1_{hh}(T)$ (Fig. 6). This component consists of two peaks that are separated by ~ 17 meV and that are also related to two macroislands differing in width by $\sim a^1$. On raising the temperature to 60 K, the low-energy peak intensity increases slightly, while, for $T > 100$ K, the component vanishes with no changes in its shape. In the insert to Fig. 6, we demonstrate the dependence of the integrated intensity I^1_{hh} of the high-energy peak of this component on T^{-1}. Unlike the case considered previously, the $I^1_{hh}(T)$ dependence can be characterized by two activation energies: $E_{a1} \sim 8$ meV and $E_{a2} \sim (35 \pm 2)$ meV. The former energy is related to the thermal delocalization of excitons from the microislands, which are always present at the interfaces. The latter energy is equal to the difference between the energies E_{1s} and E^1_{hh} and is, evidently, related to the thermal emission of excitons into the free state from the macroislands corresponding to the QW width of 11 Å + a^1. Similar behavior is also observed for the other components of the PL band.

Mechanisms of the PL quenching in the quantum structures were investigated in a number of works [14, 18]. It has been established that the main quenching mechanism is the thermal emission of excitons from the QW into the barrier. However, in the ZnS–ZnSe SLs under study, the $n = 1$ heavy-hole exciton level is about 850 meV deep; this renders exciton escape into the barrier impossible, and such structures, provided that high quality is achieved, are ideally suited to accumulate excitons up to high temperatures [14]. Thus, the observed temperature dependence of the PL band components should be related to the features in the ZnS–ZnSe interface structure. Appearance of the coupled regions in the QW (macroislands) with discrete widths and significant lateral dimensions results in the formation of additional resonance levels of the heavy-hole excitons. Then, reduction in the integrated intensity of any component with increasing T is explained by the special features of the spatial motion of excitons and their redistribution between these levels. This leads to a gradual disappearance of the short-wavelength components and an increase in the integrated intensities of the long-wavelength components, as in the case of E^0_{hh}. On the other hand, if the uncoupled (quantum-dot-like) macroislands prevail, the exciton motion in the QW plane is characterized by the activation energy (as in the case of the component E^1_{hh}) that, in general form, can be defined as

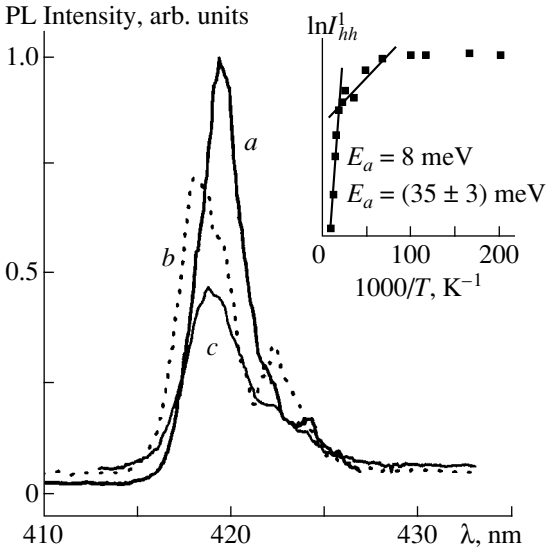

Fig. 6. Temperature variation of the shape of the E^1_{hh} spectral component; temperature equals (*a*) 4.5, (*b*) 40, and (*c*) 60 K. Insert: temperature dependence of the integrated intensity I^1_{hh} of the component's main peak.

$$E_{an} = E_{1s} - E^p_{hh}(L_w + na^1).$$

4. Finally, let us formulate some conclusions. It is established that a number of resonance levels can exist in ZnS–ZnSe SL with a rated thickness of 11 Å due to the significant fluctuations of the QW widths. The lateral dimensions of the resulting regions exceed the exciton size by two orders of magnitude; thus, exciton coherence is restored and the entire SL can be described as a set of separate QWs with discrete L. Variation of the heavy-hole exciton energy with the QW width is largely determined by the electron energy, which, in the range of small ΔE_c and L, behaves quite differently from the hole energy. This could possibly explain the disagreement between experimental and theoretical dependences of the heavy-hole exciton energy on the QW width in the strained-layer ZnS–ZnSe structures.

ACKNOWLEDGMENTS

We thank A.V. Kovalenko for supplying the ZnS–ZnSe SL samples. This work was supported by the State Foundation for Basic Research of Ukraine (project no. 2.4/86/).

REFERENCES

1. N. N. Ledentsov, V. M. Ustinov, and D. Bimberg, Fiz. Tekh. Poluprovodn. (St. Petersburg) **32**, 385 (1998) [Semicond. **32**, 343 (1998)].
2. M. A. Herman, D. Bimberg, and J. Christen, J. Appl. Phys. **70**, R1 (1991).
3. C. A. Warwick and R. F. Kopf, Appl. Phys. Lett. **60**, 386 (1992).
4. V. P. Kochereshko, G. L. Sandler, and V. Yu. Davydov, Fiz. Tverd. Tela (St. Petersburg) **38**, 2253 (1996) [Phys. Solid State **38**, 1242 (1996)].
5. T. Taguchi, Y. Kawakami, and Y. Yamado, Physica B **191**, 23 (1993); T. Taguchi, Y. Kawakami, and A. Hiraki, J. Cryst. Growth **93**, 714 (1988).
6. K. Shachzad, D. J. Olego, and Ch. G. van der Walle, Phys. Rev. B: Condens. Matter **38**, 1417 (1988).
7. V. V. Tishchenko, Y. S. Raptis, E. Anastassakis, and N. V. Bondar, Solid State Commun. **96**, 793 (1995).
8. V. V. Tishchenko, N. V. Bondar', and A. V. Kovalenko, Fiz. Tekh. Poluprovodn. (St. Petersburg) **31**, 1440 (1997) [Semicond. **31**, 1244 (1997)].
9. V. V. Tishchenko, N. V. Bondar', A. V. Kovalenko, *et al.*, Superlattices Microstruct. **25**, 143 (1998).
10. V. V. Tishchenko, N. V. Bondar', and A. V. Kovalenko, Fiz. Tekh. Poluprovodn. (St. Petersburg) **31**, 1350 (1997).
11. N. N. Ledentsov, S. V. Ivanov, and V. M. Maksimov, Fiz. Tekh. Poluprovodn. (St. Petersburg) **29**, 65 (1995) [Semicond. **29**, 34 (1995)].
12. J. A. Kash, M. Zachau, and E. E. Méndez, Phys. Rev. Lett. **66**, 2247 (1991); A. L. Efros, C. Wetzel, and L. M. Worlock, Phys. Rev. B: Condens. Matter **52**, 8384 (1995).
13. B. Gil, M. Di Blasio, and T. Cloitre, Phys. Rev. B: Condens. Matter **50**, 18231 (1994); S. K. Chang, C. D. Lee, and S. J. Min, J. Cryst. Growth **159**, 112 (1996).
14. Yi-hong Wu, K. Arai, and T. Yao, Phys. Rev. B: Condens. Matter **53**, R10485 (1996); T. Yao, S. A. Chang, and H. Tanino, J. Cryst. Growth **111**, 823 (1991).
15. T. Nakayama, J. Phys. Soc. Jpn. **59**, 1029 (1990).
16. Ch. G. van der Walle, Phys. Rev. B: Condens. Matter **39**, 1871 (1989); A. Qteish and R. J. Needs, Phys. Rev. B: Condens. Matter **45**, 1317 (1992).
17. H. Mathieu, P. Lefebvre, and P. Christol, Phys. Rev. B: Condens. Matter **46**, 4092 (1992); H. Mathieu, P. Lefebvre, and P. Christol, J. Appl. Phys. **72**, 300 (1992).
18. S. Weber, W. Limmer, G. Bacher, *et al.*, Phys. Rev. B: Condens. Matter **52**, 14739 (1995); G. Bacher, H. Schweizer, H. Nichel, *et al.*, Phys. Rev. B: Condens. Matter **43**, 9312 (1991).

Translated by M. Skorikov

Semiconductors, Vol. 34, No. 5, 2000, pp. 575–582. Translated from Fizika i Tekhnika Poluprovodnikov, Vol. 34, No. 5, 2000, pp. 595–601.

LOW-DIMENSIONAL SYSTEMS

Zero-Phonon and Dipole Γ–*X* Electron Transitions in GaAs/AlAs Quantum-Well Heterostructures in a Longitudinal Electric Field

V. Ya. Aleshkin and A. A. Andronov

Institute for Physics of Microstructures, Russian Academy of Sciences, Nizhni Novgorod, 603600 Russia

e-mail: aleshkin@ipm1.sci.nnov.ru

Submitted September 6, 1999; accepted for publication November 22, 1999

Abstract—The probabilities of zero-phonon and dipole electron transitions between the Γ and *X* subbands in a GaAs/AlAs quantum-well heterostructure subjected to a high longitudinal electric field are calculated. It is shown that the electric field significantly affects the probabilities of both the zero-phonon and the direct dipole Γ–*X* transitions. In addition, the electric field changes the spectral dependence of the Γ–*X* intersubband light-absorption coefficient; i.e., an intersubband analogue of the Franz–Keldysh effect takes place. © *2000 MAIK "Nauka/Interperiodica".*

INTRODUCTION

In recent years, considerable progress has been made in the development of lasers operating by intersubband transitions with vertical transport [1] and optical pumping [2]. A scheme has been proposed for designing an interband laser with longitudinal electron transport in a GaAs/AlAs heterostructure in high electric fields [3, 4]. An important role in the operation of such a laser is played by the interaction of the electron states in the Γ- and *X*-valleys at the heterointerface [5]. It is evident that this interaction renders direct optical transitions of electrons between these two valleys allowed. Furthermore, it gives rise to additional Γ–*X* electron transitions, namely, zero-phonon transitions [6].

Our work is devoted to finding the probabilities of the zero-phonon Γ–*X* transition and the optical dipole Γ–*X* transition in a GaAs/AlAs quantum well (QW) heterostructure subjected to a high longitudinal electric field. It is shown that the electric field significantly affects the probabilities of both the zero-phonon and the direct dipole Γ–*X* transitions. In addition, the electric field changes the spectral dependence of the intersubband light-absorption coefficient; i.e., we actually have an intersubband analogue to the Franz–Keldysh effect.

ZERO-PHONON TRANSITIONS IN A LONGITUDINAL FIELD

Let us consider a periodic heterostructure comprising narrow alternating GaAs and AlAs layers grown on the (001) plane. We choose the *z*-axis aligned with the growth direction. In such a heterostructure, the GaAs layers constitute potential wells for Γ-valley electrons and barriers for *X*-valley electrons, while the AlAs layers, conversely, represent potential wells for *X*-valley electrons and barriers for Γ-valley electrons. We assume that the barrier transparency for Γ- and *X*-electrons is low, so that the widths of minibands arising from electron tunneling are smaller than the level broadening due to collisions. In this case, an electron is scattered several times during the time between tunneling transitions, and, therefore, there is no coherence of the wave functions of electrons in different GaAs (AlAs) layers. This means that the heterostructure can be treated as a set of independent QWs for *X*- and Γ-electrons.

Collision of an electron with the heterointerface changes the electron quasi-momentum component normal to the interface. Therefore, Γ-valley electrons can interact at the heterointerface directly (i.e., with no phonons or defects involved) with electrons of the *X*-valley, which is shifted away from the center of the Brillouin zone in the [001] direction (hereinafter referred to as X_z). This interaction gives rise to zero-phonon transitions between neighboring GaAs and AlAs layers [6]. As a result of such a transition, an electron located in the Γ-valley of GaAs may find itself in the *X*-valley of the neighboring AlAs layers. If the transition probability is low (and it is this case that is considered here), then, owing to the lack of phase coherence of the wave functions in different AlAs layers, zero-phonon transitions into the two nearest neighboring layers may be thought of as occurring independently of one another. Therefore, to describe the zero-phonon transitions, it suffices to consider the Γ–*X* interaction at a single heterointerface, i.e., the transitions

1063-7826/00/3405-0575$20.00 © 2000 MAIK "Nauka/Interperiodica"

into one of the two nearest layers. To describe this interaction, we use the Hamiltonian [5]

$$\hat{H}_{\text{int}} = \begin{pmatrix} \hat{H}_\Gamma & \alpha\delta(z-z_0) \\ \alpha\delta(z-z_0) & \hat{H}_X \end{pmatrix}, \quad (1)$$

where $\hat{H}_\Gamma$ and $\hat{H}_X$ are the Hamiltonians describing the electron motion in the Γ- and X-valleys, $\alpha \approx 0.155$ eV Å is the Γ–X coupling constant for the GaAs/AlAs heterostructure [5], and z_0 is the z-coordinate of the heterointerface.

Let us consider the in-plane electron motion in a QW subjected to a longitudinal electric field. Under the effect of the field, the electron quasi-momentum increases with time. Owing to the translation-invariance of the Γ–X interaction Hamiltonian in the heterointerface plane, the zero-phonon transitions occur with quasi-momentum conservation. The most intense transitions occur in those regions of the quasi-momentum space where the Γ and X subbands intersect or approach each other to the maximum extent (in the absence of intersections). Indeed, two types of electron waves correspond to the Γ and X subbands. At the intersection points of the Γ and X subbands, the condition of phase synchronism of these waves is satisfied (their frequencies and wave vectors coincide), which is necessary for their effective interaction. If there is no intersection, the condition for phase synchronism cannot be satisfied, while, at the points of the closest approach of the subbands, it is violated to the minimum extent.

Consider a pair of interacting Γ and X subbands. The electron wave function can be sought for as a sum of two wave functions $\Psi = C_\Gamma\Psi_\Gamma + C_X\Psi_X$, where $\Psi_{\Gamma, X}$ are the wave functions in the relevant subbands. The solution to the time-independent Schrödinger equation in the absence of an electric field has the form

$$C_\Gamma^\pm(k) = \frac{V}{\sqrt{[E_\pm(k)-\varepsilon_\Gamma(k)]^2 + V^2}},$$
$$C_X^\pm(k) = \frac{E_\pm(k)-\varepsilon_\Gamma(k)}{\sqrt{[E_\pm(k)-\varepsilon_\Gamma(k)]^2 + V^2}}, \quad (2)$$

where $\varepsilon_\Gamma(k)$ and $\varepsilon_X(k)$ are the dependences of the energy on the wave vector in the Γ and X subbands, $E_\pm(k)$ are the dependences of the energy on the quasi-wave vector in the new subbands arising from the Γ and X subbands owing to their interaction

$$E_\pm(k) = \frac{\varepsilon_\Gamma(k)+\varepsilon_X(k)}{2} \pm \sqrt{\left(\frac{\varepsilon_\Gamma(k)-\varepsilon_X(k)}{2}\right)^2 + V^2}, \quad (3)$$

$V = \alpha\Psi_\Gamma(0)\Psi_X(0)$ is the effective interaction energy of the Γ- and X-valleys, and $\Psi_{\Gamma, X}(0)$ are the values of the corresponding wave functions at the heterointerface.

It can be seen from (3) that the interaction lifts the degeneracy of the electronic structure at the point of intersection of the Γ and X subbands. At this point there occurs a gap of $2V$, which is the minimum distance between the new subbands for fixed k.

Before finding the probability of the zero-phonon Γ–X transition in an electric field of arbitrary magnitude, we consider two limiting cases. In low electric fields, the electron motion is adiabatic and occurs entirely within a subband with energy $E_\pm(k)$. In this case, the probability of the zero-phonon Γ–X transition is zero if the electron has passed two points (or none) of intersection of the Γ and X subbands in k space and unity if the electron has passed one such point. In high electric fields, the Γ–X interaction scarcely affects the electron motion, since the time required to traverse the region in k space where the Γ–X interaction is effective is small. In this case, the probability of the zero-phonon transition is low.

We now find the probability of the Γ–X transition for the electron wave vector component along the electric field changing from k_0 to k_1. We assume that at an instant of time $t = t_0$ an electron resides in any one of the Γ or X subbands. The time-dependent Schrödinger equation reduces to a set of equations in $C_{\Gamma, X}$:

$$\varepsilon_\Gamma(\mathbf{k})C_\Gamma(\mathbf{k}, t) - iF\frac{\partial}{\partial k_1}C_\Gamma(\mathbf{k}, t)$$
$$+ VC_X(\mathbf{k}, t) = i\hbar\frac{\partial}{\partial t}C_\Gamma(\mathbf{k}, t),$$
$$VC_\Gamma(\mathbf{k}, t) + \varepsilon_X(\mathbf{k})C_X(\mathbf{k}, t)$$
$$- iF\frac{\partial}{\partial k_1}C_X(\mathbf{k}, t) = i\hbar\frac{\partial}{\partial t}C_X(\mathbf{k}, t), \quad (4)$$

where $F = eE$ is the force acting on the electron in the electric field E. The solution to (4) is conveniently sought for in the form [7]

$$C_j(k_1, k_2, t) = a_j(k_1, k_2)\delta[k_1 - k_0 - F(t-t_0)]$$
$$\times \exp\left\{-\frac{i}{F}\int_0^{k_1}\varepsilon_j(k_1', k_2)dk_1'\right\}, \quad (5)$$

where k_2 is the wave vector component perpendicular to the electric field. The squared absolute value of $a_j(k_1, k_2)$ is the probability of finding the electron in the jth band at the instant of time when its wave vector component along F equals k_1. The equations for a_j take the form

$$-i\frac{\partial}{\partial k_1}a_\Gamma(\mathbf{k})$$

$$+\frac{V}{F}\exp\left\{\frac{i}{F}\int_0^{k_1}(\varepsilon_\Gamma(k_1', k_2)-\varepsilon_X(k_1', k_2))dk_1'\right\}a_X(\mathbf{k}) = 0,$$
$$\frac{V}{F}\exp\left\{-\frac{i}{F}\int_0^{k_1}(\varepsilon_\Gamma(k_1', k_2)-\varepsilon_X(k_1', k_2))dk_1'\right\}a_\Gamma(\mathbf{k}) \quad (6)$$
$$-i\frac{\partial}{\partial k_1}a_X(\mathbf{k}) = 0.$$

It is convenient to introduce in (5) instead of k a new variable $\eta = kL_{FK}$, where $m = m_\Gamma m_X/(m_\Gamma - m_X)$; m_Γ and m_X are the electron masses in the Γ- and X_z-valleys, respectively; and $L_{FK} = (\hbar^2/2mF)^{1/3}$. Then, (6) takes the form

$$-i\frac{\partial}{\partial\eta}a_\Gamma(\eta, k_2)+\frac{V}{V_{FK}}\exp\left\{i\left(\frac{\eta^3}{3}-\eta\frac{\Delta_{X\Gamma}(k_2)}{V_{FK}}\right)\right\}$$
$$\times a_X(\eta, k_2) = 0,$$
$$-i\frac{\partial}{\partial\eta}a_X(\eta, k_2)+\frac{V}{V_{FK}}\exp\left\{-i\left(\frac{\eta^3}{3}-\eta\frac{\Delta_{X\Gamma}(k_2)}{V_{FK}}\right)\right\} \quad (7)$$
$$\times a_\Gamma(\eta, k_2) = 0,$$

where $\Delta_{X\Gamma}(k_2) = \varepsilon_X(0, k_2) - \varepsilon_\Gamma(0, k_2)$, and $V_{FK} = (\hbar^2F^2/2m)^{1/3}$ is the Franz–Keldysh energy. It is worth noting that the characteristic lengths across which the electron wave functions vary in noninteracting Γ and X subbands in an electric field are $(\hbar^2/2m_{X,\Gamma}F)^{1/3}$ [8].

The characteristic length across which the zero-phonon transitions occur is L_{FK}, and the change of the kinetic energy across this length equals V_{FK}. It is apparent that the region in k space in which the zero-phonon transitions occur most intensely has a size on the order of L_{FK}^{-1} along k_1 (i.e., on the order of unity in η units). This size increases as $F^{1/3}$ with increasing electric field. It can be seen from (7) that, as the electric field increases, the magnitude of the effective interaction between the Γ and X subbands decreases. Therefore, it would be expected that the probability of zero-phonon transitions decreases with increasing electric field. In addition, it is obvious that the dependence of the probability of zero-phonon transitions on k_2 is governed by the dependence $\Delta_{X\Gamma}(k_2)$.

In fairly high electric fields, the probability of zero-phonon transitions with the electron moving from k_0 to k_1 is low and can be calculated using the perturbation theory; i.e.,

$$D(k_0, k_1, k_2) = \frac{V^2}{F^2}\left|\int_{k_0}^{k_1}d\tilde{k}_1\right.$$
$$\left.\times\exp\left\{\frac{i}{F}\int_0^{\tilde{k}_1}dk_1''(\varepsilon_\Gamma(k_1'', k_2)-\varepsilon_X(k_1'', k_2))\right\}\right|^2. \quad (8)$$

Using (8), we find for the probability of a zero-phonon transition in motion from –∞ to +∞

$$D_0(k_2) = D(-\infty, \infty, k_2) = \left(\frac{2\pi V}{V_{FK}}\right)^2\mathrm{Ai}\left(-\frac{\Delta_{X\Gamma}(k_2)}{V_{FK}}\right),$$
$$\mathrm{Ai}(x) = \frac{1}{\pi}\int_0^\infty\cos\left(\frac{t^3}{3}+xt\right)dt, \quad (9)$$

where Ai(x) is the Airy function [9]. It follows from (9) that for those k_2 for which $\Delta_{X\Gamma} > 0$ and, hence, there are intersection points of the Γ and X subbands D_0 is an oscillating function of $\Delta_{X\Gamma}$, which results from the interference of transitions corresponding to two intersection

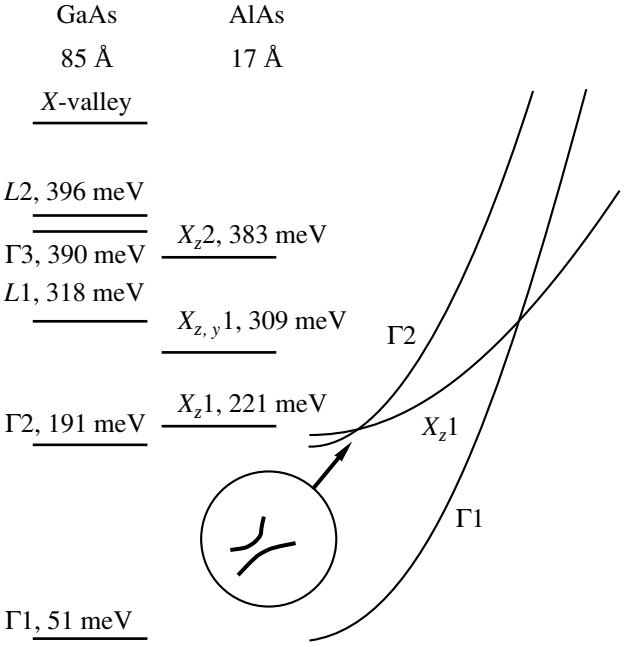

Fig. 1. Electron size-quantization subband edge profiles for a periodic GaAs/AlAs heterostructure. The layer thickness is 85 Å for GaAs and 17 Å for AlAs. The letters denote the valleys, and numerals, the subbands numbers. The energy is reckoned from the bottom of the Γ-valley in GaAs. The symbols X_x and X_y denote the two X-valleys displaced from the center of the Brillouin zone in the [100] and [010] directions, respectively. The wave vector dependences of the electron energies for the Γ1, Γ2, and X_z1 subbands are shown in the right-hand part of the figure.

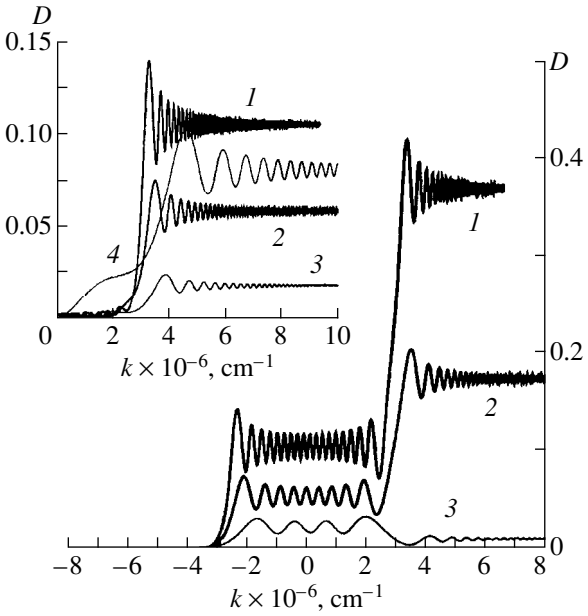

Fig. 2. Probability of the zero-phonon transition from the Γ2 to the X_z1 subband vs. the wave vector component along the electric field $D(-\infty, k, k_2 = 0)$ and $D(0, k, k_2 = 0)$ (in the insert) for the GaAs/AlAs heterostructure having the electronic structure shown in Fig. 1 ($\Delta_{X\Gamma} = 30$ meV). Numbers *1–4* correspond to the electric fields of 1, 2, 5, and 15 kV/cm. The probability for 15 kV/cm is increased tenfold.

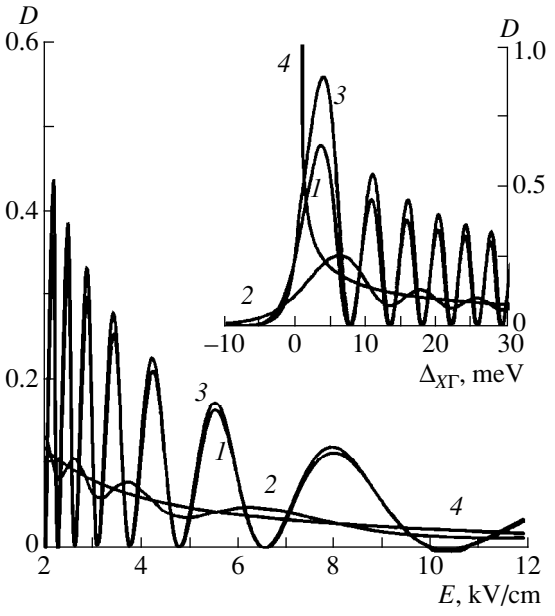

Fig. 3. Probability of the Γ2–X_z1 zero-phonon transition in the electron motion from $k_0 = -\infty$ to $k_1 = \infty$ (line *1*) and from $k_0 = 0$ to $k_1 = \infty$ (line *2*) vs. the electric field strength. The electron wave vector component perpendicular to the field is zero. Curves *3* and *4* are obtained using (9) and (10), respectively. The insert shows the zero-phonon transition probability vs. $\Delta_{X\Gamma}$ for the field of 2 kV/cm.

points. If there are no intersection points ($\Delta_{X\Gamma} < 0$), then D_0 is a steadily decreasing function of $|\Delta_{X,\Gamma}|$.

If the intersection points are sufficiently far apart, so that the particle is scattered when moving between them, then the probability of a transition in passing a single intersection point should be considered separately. In this case, the integral in (8) can be calculated by the stationary-phase method;[1] i.e.,

$$D(k_2) = \frac{2\pi V^2 m}{\hbar^2 F k_c(k_2)}, \qquad (10)$$

where $k_c(k_2)$ is the component of the wave vector k_1 corresponding to the subband intersection. We note that expression (10) is valid when $D \ll 1$, i.e., it is inapplicable for small k_c.

Let us find by way of example the probabilities of the zero-phonon transitions between the second Γ and the first X_z subbands in a heterostructure consisting of alternating GaAs (85 Å) and AlAs (17 Å) layers (the possibility of designing a laser operating by intersubband transitions in a structure with similar parameters was considered in [4]). Figure 1 shows the layout of the size-quantization subband edges for this structure and the wave-vector dependences of the energies in the Γ1, Γ2, and X_z1 subbands. The effective interaction energy of the Γ1 and X_z1 subbands is 0.9 meV.

Figure 2 shows the probability of a zero-phonon transition between the Γ2 and X_z1 subbands calculated as a function of the final wave-vector component aligned with the electric field for the heterostructure under consideration. The wave-vector component perpendicular to the electric field was assumed to be zero. The subband intersection point corresponds to $k_1 \approx \pm 2.9 \times 10^6$ cm^{-1}. The initial wave vector was assumed to be $-\infty$. The insert in Fig. 2 shows similar dependences for the case where the initial wave vector is zero. It is seen from Fig. 2 that, in agreement with the above consideration, the region in which the zero-phonon transitions are effective grows in size with increasing electric field.

Figure 3 shows the probabilities of the zero-phonon transitions in relation to the electric field strength for electron motion from $k_0 = -\infty$, 0 to $k_1 = +\infty$ ($k_2 = 0$) obtained by solving (7) (curves *1, 2*) and from (9) and (10) (curves *3, 4*). It can be seen from Fig. 3 that equations (9) and (10) describe the probability of the zero-phonon transitions adequately at field strengths higher than 2 kV/cm. In the insert, the probabilities of the zero-phonon transitions are plotted against $\Delta_{X\Gamma} = \Delta_{X\Gamma}(k_2 = 0) - \hbar^2 k_2^2/2m$ for the electric field strength of

[1] There is a misprint in [8] in an expression similar to (10).

2 kV/cm. The probability decreases abruptly in the range $\Delta_{X\Gamma} < 0$ where there is no subband intersection.

DIPOLE Γ–*X* TRANSITIONS

Let us now find the probability of the dipole transition of an electron from the X_z1 subband to the Γ1 subband under the action of a weak electromagnetic field $E_1\exp(i\omega t)$ directed along the *z*-axis in the presence of a strong in-plane dc electric field aligned with the x_1 axis for the heterostructure discussed above. To find the probability of the dipole transition, we solve the time-dependent Schrödinger equation. Let an electron with the wave vector component along the dc electric field k_0 reside at the initial instant of time $t = 0$ in the X_z1 subband. We seek a solution of the Schrödinger equation in the form

$$\Psi(k, t) = a_{\Gamma1}(k_2, t)\Psi_{\Gamma1} + a_{\Gamma2}(k_2, t)\Psi_{\Gamma2} + a_X(k_2, t)\Psi_X, \tag{11}$$

where

$$\Psi_X(r, t) = \Psi_X(z)\delta\left(k_1 - k_0 - \frac{Ft}{\hbar}\right) \times \exp\left\{\frac{-i}{F}\left[\int_0^{k_0 + \frac{Ft}{\hbar}} \varepsilon_X(\hat{k}_1, k_2)d\hat{k}_1\right] + ik_1x + ik_2y\right\}, \tag{12}$$

$$\Psi_{\Gamma1,2}(r, t) = \Psi_{\Gamma1,2}(z)\delta\left(k_1 - k_0 - \frac{Ft}{\hbar}\right) \times \exp\left\{\frac{-i}{F}\left[\int_0^{k_0 + \frac{Ft}{\hbar}} \varepsilon_{\Gamma1,2}(\hat{k}_1, k_2)d\hat{k}_1\right] + ik_1x + ik_2y\right\},$$

and $\Phi_J(z)$ is the wave function component in the *J* subband which governs the electron motion transverse to the QW. We neglect the interaction between the X_z1 and Γ1 subbands, since it is much weaker than that between the X_z1 and Γ2 subbands. Then, multiplying the Schrödinger equation by $\Phi_{\Gamma1}(z)$ and integrating over *z*, we obtain the following equation for $a_{\Gamma1}(t)$:

$$i\hbar\frac{d}{dt}a_{\Gamma1}(k_2, t) = -eE_1\exp(i\omega t)z_{12}a_{\Gamma2}(k_2, t) \times \exp\left\{\frac{i}{F}\left[\int_0^{k_0 + \frac{Ft}{\hbar}} (\varepsilon_{\Gamma1}(\hat{k}_1, k_2) - \varepsilon_{\Gamma2}(\hat{k}_1, k_2))d\hat{k}_1\right]\right\}. \tag{13}$$

Here, $z_{12} = \int_{-\infty}^{\infty} \Phi^*_{\Gamma1}(z)z\Phi_{\Gamma2}(z)dz$ is the matrix element of *z* between the Γ1 and Γ2 subbands. Taking into account the interaction between the X_z1 and Γ2 subbands in the context of the perturbation theory, we find

$$a_{\Gamma2}(k_2, t) = \frac{V}{iF}\int_{k_0}^{k_0 + \frac{Ft}{\hbar}} \exp\left(\frac{ig(k, k_2)}{F}\right)dk,$$
$$g(k, k_2) = \int_0^k (\varepsilon_{\Gamma2}(\tilde{k}_1, k_2) - \varepsilon_{X1}(\tilde{k}_1, k_2))d\tilde{k}_1. \tag{14}$$

Integrating (13) with the use of (14) and taking into account that $\varepsilon_{\Gamma1}(k_1, k_2) - \varepsilon_{\Gamma2}(k_1, k_2) = \Delta$ is constant, we have

$$a_{\Gamma1}(k_2, t) = \frac{eE_1z_{12}}{\hbar}\frac{V}{F}\int_0^t dx \times \exp(i\bar{\omega}x)\int_{k_0}^{k_0 + \frac{Fx}{\hbar}} \exp\left(\frac{ig(k, k_2)}{F}\right)dk, \tag{15}$$

$$\bar{\omega} = \omega - \frac{\Delta}{\hbar}.$$

Integrating (15) by parts, we arrive at the following expression for $a_{\Gamma1}(k_2, t)$:

$$a_{\Gamma1}(k_2, t) = \frac{eE_1Vz_{12}\exp\left(-i\frac{\hbar\bar{\omega}k_0}{F}\right)}{iF\hbar\bar{\omega}} \times \left[\exp\left(\frac{i}{F}[\bar{\omega}(\hbar k_0 + Ft)]\right)\int_{k_0}^{k_0 + \frac{Fx}{\hbar}} \exp\left(\frac{ig(k, k_2)}{F}\right)dk - \int_{k_0}^{k_0 + \frac{Fx}{\hbar}} \exp\left(\frac{i}{F}[\hbar\bar{\omega}k + g(k, k_2)]\right)dk\right]. \tag{16}$$

Using (16), the squared absolute value of $a_{\Gamma1}(k_2, t)$ can be written as a sum of three terms

$$|a_{\Gamma1}(k_2, t)|^2 = A(k_2, t) + B(k_2, t) + C(k_2, t), \tag{17}$$

where

$$A(k_2, t) = \frac{|eE_1z_{12}V|^2}{F^2(\hbar\bar{\omega})^2}[(R_1(k_2, t) - R_2(k_2, t, \omega))^2 + (I_1(k_2, t) - I_2(k_2, t, \omega))^2], \tag{18}$$

$$B(k_2, t) = \frac{4|eE_1 z_{12} V|^2}{F^2(\hbar\bar{\omega})^2}(R_1(k_2, t)R_2(k_2, t) + I_1(k_2, t)I_2(k_2, t))\sin^2\left(\frac{\hbar\bar{\omega}\left(k_0 + \frac{Ft}{\hbar}\right)}{2F}\right), \quad (19)$$

$$C(k_2, t) = \frac{2|eE_1 z_{12} V|^2}{F^2(\hbar\bar{\omega})^2}(I_1(k_2, t)R_2(k_2, t) - I_2(k_2, t)R_1(k_2, t))\sin\left(\frac{\hbar\bar{\omega}\left(k_0 + \frac{Ft}{\hbar}\right)}{2F}\right), \quad (20)$$

$$R_1(k_2, t) = \mathrm{Re}\left(\int_{k_0}^{k_0 + \frac{Ft}{\hbar}} \exp\left(\frac{ig(k, k_2)}{F}\right)dk\right),$$

$$I_1(k_2, t) = \mathrm{Im}\left(\int_{k_0}^{k_0 + \frac{Ft}{\hbar}} \exp\left(\frac{ig(k, k_2)}{F}\right)dk\right), \quad (21a)$$

$$R_2(k_2, t) = \mathrm{Re}\left(\int_{k_0}^{k_0 + \frac{Ft}{\hbar}} \exp\left(\frac{i}{F}[\hbar\bar{\omega}k + g(k, k_2)]\right)dk\right), \quad (21b)$$

$$I_2(k_2, t) = \mathrm{Im}\left(\int_{k_0}^{k_0 + \frac{Ft}{\hbar}} \exp\left(\frac{i}{F}[\hbar\bar{\omega}k + g(k, k_2)]\right)dk\right). \quad (21c)$$

As t tends to infinity, $B(k_2, t)$ is proportional to $t\delta(\hbar\omega - \Delta)$. Indeed, using the equality [8]

$$\lim_{t\to\infty}\frac{\sin^2\alpha t}{\pi t\alpha^2} = \delta(\alpha), \quad (22)$$

$B(k_2 t)$ can be rewritten as

$$B(k_2, t) \approx \frac{2\pi(eE_1 z_{12})^2 D(k_0, \infty, k_2)}{\hbar}t\delta(\hbar\omega - \Delta), \quad (23)$$

where $D(k_0, \infty, k_2)$ is the probability of the zero-phonon transition with the electron moving from $k_1 = k_0$ to $k_1 = \infty$, as determined from (8). It is apparent that this term describes the dipole transitions of the electrons brought into the Γ2 subband via the zero-phonon transitions.

It can be readily shown that, as t tends to infinity, $C(k_2, t)$ is also proportional to $\delta(\hbar\omega - \Delta)$. To this end, we use the equality

$$\lim_{t\to\infty}\frac{\sin\alpha t}{\pi\alpha} = \delta(\alpha). \quad (24)$$

Then, $C(k_2, t)$ can be expressed as

$$C(k_2, t) = \frac{2\pi(eE_1 z_{12} V)^2}{F^2}G(k_2)\delta(\hbar\omega - \Delta), \quad (25)$$

$$G(k_2) = \int_{k_0}^{\infty}\int_{k_0}^{\infty} x\cos\left(\frac{g(x, k_2) + g(y, k_2)}{F}\right)dxdy. \quad (26)$$

The probability of the dipole transition is the easiest to find when k_0 is negative and its absolute value is large. In this case, the main contribution to the integrals (21) comes from the regions where $\delta\varepsilon(k_1, k_2)$ is the smallest (i.e., the regions of the closest approach of the Γ2 and X_z1 subbands), and, therefore, $-\infty$ can be taken as the lower limit of integration. The integral (26) vanishes at such k_0. Hence, $C = 0$, and only two terms remain in the expression for the transition probability: A and B. The expression for $A(k_2, \infty)$ can thus be written as follows:

$$A(k_2, \infty) = \left(\frac{2\pi eE_1|z_{12}|V}{\hbar\bar{\omega}V_{FK}}\right)^2\left\{\mathrm{Ai}\left(\frac{\hbar^2 k_2^2}{2mV_{FK}} - \frac{\Delta_{X1\Gamma 2}}{V_{FK}}\right) - \mathrm{Ai}\left(\frac{\hbar^2 k_2^2}{2mV_{FK}} + \frac{\hbar\bar{\omega} - \Delta_{X1\Gamma 2}}{V_{FK}}\right)\right\}^2. \quad (27)$$

We note that the dependence of A on ω has a maximum in the $V_{FK}/\hbar$-vicinity of the frequency $\omega = \Delta/\hbar$. The appearance of this nonresonance term is due to special features of the dynamics of an electron passing the regions where the Γ–X interaction is effective. It is these regions that mainly contribute to the integrals (21).

It is significant that the transition probability B is proportional to time. Therefore, the corresponding absorption coefficient can be calculated using the Fermi Golden Rule. The corresponding contribution is merely proportional to the probability of the Γ2–Γ1 optical transition for an electron that has experienced a direct X_z1–Γ2 transition. The contribution corresponding to A is time-independent. This is the probability of the optical transition of an electron passing through the region of the effective Γ–X interaction. The power absorbed in such transitions is proportional to the product of the transition probability (A) and the flux of electrons in the momentum space. Thus, we arrive at the following expression for the power absorbed at $\hbar\omega \neq \Delta$

in a system of *N* QWs, with the level broadening due to collisions neglected,

$$P(\omega) = \frac{L_1 L_2 F N \omega}{(2\pi)^2} \int_{-\infty}^{\infty} f(k_2) A(k_2, \infty) dk_2, \qquad (28)$$

where L_1 and L_2 are the in-plane dimensions of the system along the x_1 and x_2 axes, respectively; $f(k_2)$ is the difference in the probabilities of the Γ1- and X_z1-state occupation. Let the radiation propagate along the x_2 axis. Then, the power of the wave incident on the structure can be written as

$$I(\omega) = \frac{L_1 L_3 n c E_1^2}{2\pi}, \qquad (29)$$

where L_3 is the system dimension along *z*, *n* is the refractive index, and *c* is the speed of light. Using (28) and (29), we can find the absorption coefficient

$$\alpha(\omega) = \frac{4P(\omega)}{I(\omega)L_2}$$

$$= \frac{32\pi e^2 |z_{12}|^2 V^2 \omega m}{dnc(\hbar\omega - \Delta)^2 \hbar^2} \int_0^{\infty} \left\{ \mathrm{Ai}\left(x^2 - \frac{\Delta_{X1\Gamma2}}{V_{FK}}\right) \right. \qquad (30)$$

$$\left. - \mathrm{Ai}\left(x^2 - \frac{\Delta_{X1\Gamma2} - \hbar\omega + \Delta}{V_{FK}}\right) \right\}^2 f(k_2) dx,$$

where $d = L_3/N$ is the structure period along the *z* direction. In deriving (30), account was taken of the spin degeneracy of the electron states and the probability of the transition from an AlAs layer into the two neighboring GaAs layers.

Figure 4 shows the α(ω) dependence for a periodic heterostructure comprising 87-Å-thick GaAs layers and 17-Å-thick AlAs layers for different electric field strengths. In our calculations, we took $f(k_2) = 1$. It can be seen from Fig. 4 that, as the electric field increases, the α(ω) spectrum broadens near $\omega = \Delta/\hbar$, with its intensity decreasing simultaneously. The reason for the spectrum broadening is that the energy range of the Γ–*X* interaction (V_{FK}) becomes wider with increasing electric field strength. The intensity decrease is due to a simultaneous weakening of this interaction. Since nonresonance transitions mainly occur in those regions in *k* space where the Γ–*X* interaction is effective, $f(k_2)$ should be taken for these regions.

In the absence of a dc electric field, the probability of the dipole transition from the Γ1 states into the states with energies $E_{\pm}(k)$ can be calculated in the conventional way. We now write out the expressions for the transition matrix elements

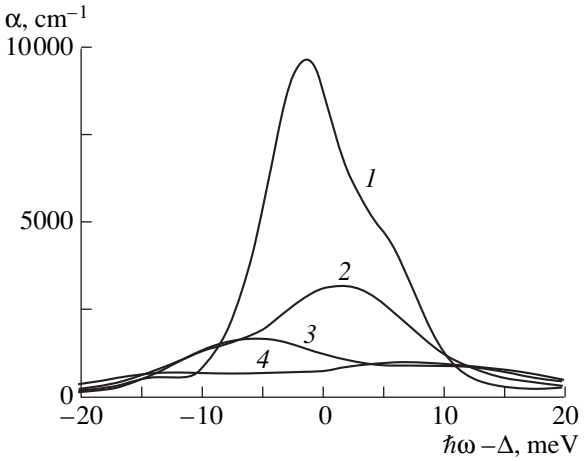

Fig. 4. Frequency dependence of the absorption coefficient for different electric field strengths, calculated by (31) with $f = 1$ for the GaAs/AlAs periodic heterostructure having the electronic structure shown in Fig. 1. Curves *1–4* correspond to the electric field strengths of 5, 9, 12, and 15 kV/cm.

$$|z_{\Gamma1,\pm}(k)|^2 = \frac{|z_{12}|^2}{1 + \frac{(E_{\pm}(k) - \varepsilon_{\Gamma2}(k))^2}{V^2}}. \qquad (31)$$

It follows from (31) that the characteristic scale of the $|z_{\Gamma1,\pm}|^2$ decrease with the transition energy deviating from Δ (i.e., $E_{\pm}$ deviating from $\varepsilon_{\Gamma2}$) equals *V*. For the structure in question, this value is much less than the energy of level broadening lying in the range of 1–10 meV. Therefore, the broadening of the transition spectral line due to the Γ–*X* interaction in the absence of an electric field will modify the line shape only slightly. By contrast, in sufficiently strong electric fields, the energy V_{FK} may be comparable to or even exceed the energy of levels broadening, and, therefore, the shape of the absorption line depends on the electric field strength. We note that a similar dependence is observed for the Franz–Keldysh effect in interband light absorption [10].

ACKNOWLEDGMENTS

This work was supported in part by the Russian Foundation for Basic Research (project no. 99-02-17873), the Program "Physics of Solid State Nanostructures" (grant no. 98-02-1098), and the International Center–Foundation for Advanced Research in Nizhni Novgorod (grant no. 99-2-11).

REFERENCES

1. J. Faist, F. Capasso, D. L. Sivco, *et al.*, Science **264**, 553 (1994).

2. O. Gauthier-Lafaye, F. H. Julien, S. Cabaret, *et al*., Appl. Phys. Lett. **74**, 1537 (1999).
3. V. Ya. Aleshkin and A. A. Andronov, Pis'ma Zh. Éksp. Teor. Fiz. **68**, 73 (1998) [JETP Lett. **68**, 78 (1998)].
4. V. Ya. Aleshkin, A. A. Andronov, and E. V. Demidov, Mater. Sci. Forum **297–298**, 221 (1999).
5. H. C. Liu, Appl. Phys. Lett. **51**, 1019 (1987).
6. Z. S. Gribnikov and O. É. Raĭchev, Fiz. Tekh. Poluprovodn. (Leningrad) **23**, 2171 (1989) [Sov. Phys. Semicond. **23**, 1344 (1989)].
7. V. Ya. Aleshkin and Yu. A. Romanov, Zh. Éksp. Teor. Fiz. **87**, 1857 (1984) [Sov. Phys. JETP **60**, 1068 (1984)].
8. L. D. Landau and E. M. Lifshitz, *Quantum Mechanics: Non-Relativistic Theory* (Nauka, Moscow, 1989; Pergamon, Oxford, 1977).
9. *Handbook of Mathematical Functions*, Ed. by M. Abramowitz and I. Stegun (Dover, New York, 1965; Nauka, Moscow, 1979).
10. A. I. Ansel'm, *Introduction to the Theory of Semiconductors* (Nauka, Moscow, 1978).

Translated by S. Goupalov

Semiconductors, Vol. 34, No. 5, 2000, pp. 583–588. Translated from Fizika i Tekhnika Poluprovodnikov, Vol. 34, No. 5, 2000, pp. 602–606.

LOW-DIMENSIONAL SYSTEMS

On the Spectra of Electrons and Holes in an Open Spherical Nanoheterostructure (through the Example of GaAs/$Al_xGa_{1-x}As$/GaAs)

N. V. Tkach, V. A. Holovatsky, and O. N. Voĭtsekhivska

Chernivtsi State University, Chernivtsi, 274012 Ukraine

Submitted June 17, 1999; accepted for publication November 25, 1999

Abstract—The spectra of the quasi-stationary electron and hole states in an open spherical nanoheterostructure are calculated in the effective mass approximation using the *S*-matrix theory. Numerical calculation is performed through the example of the GaAs/$Al_xGa_{1-x}As$/GaAs system. A complete system of electron and hole wave functions is obtained for nanoheterostructures consisting of an arbitrary number of layers. Quasiparticle lifetimes as a function of the GaAs/$Al_xGa_{1-x}As$/GaAs nanosystem geometrical parameters and Al content *x* are calculated. © *2000 MAIK "Nauka/Interperiodica".*

INTRODUCTION

Spectra of electrons, holes, excitons, and phonons and interactions between these quasiparticles in spherical semiconductor nanocrystals embedded in bulk semiconductor or dielectric matrices have been long investigated experimentally [1–5] and theoretically [6–12], and physical processes in simple quantum dots have been studied in detail.

With modern technological methods, multilayer spherical nanoheterostructures can be fabricated [13–15]. This possibility has stimulated interest in theoretical studies of the spectra and interactions of quasiparticles (electrons, holes, excitons, and phonons) in such systems.

The theory of discrete spectra, which describes the stationary states of electrons, holes, and excitons in multilayer spherical quantum wells, was developed in [13, 14, 16] in the effective mass approximation. The theory of phonon spectra of the multilayer spherical nanoheterostructures was developed in [16, 17] on the basis of the dielectric continuum model. Hamiltonians describing interaction of confined and interface phonons with electrons, holes, and excitons were also obtained in these works, and the energies of the ground electron and hole stationary states renormalized by the interaction with phonons were calculated.

In the theory developed in the above-mentioned papers [13, 14, 16], it was assumed either explicitly or implicitly that the outer medium, where the multilayer spherical nanoheterostructure is embedded, acts as a potential barrier with respect to the inner layers of the structure: stationary electron, hole, and exciton states can be formed only in such closed systems (Fig. 1a). The theory developed in the cited papers cannot be applied to open multilayer spherical nanoheterostructures, in which the outer medium does not present a potential barrier for electrons or holes, because, in such systems, the quasiparticles have a nonvanishing probability to appear at infinity. This changes the wave functions radically and results in the formation of quasi-stationary states with finite lifetime. To our knowledge, there is currently no theory that describes electron and hole spectra and interactions between them and the other quasiparticles in open semiconductor spherical nanoheterostructures.

It is the goal of this work to study the spectra and determine the wave functions of electron and hole quasi-stationary states in open multilayer spherical nanoheterostructures. In the context of the effective mass approximation, which has proven appropriate for closed-type nanostructures [13, 16, 17], one is able not only to calculate the dependence of the electron and hole spectral characteristics on the geometric parameters of the structure, but, using the complete system of wave functions obtained in this work, also to determine, if needed, the Hamiltonian of interaction with confined and interface phonons and to study this interaction.

1. GENERAL THEORY

We will study the electronic spectrum of an open spherical nanoheterostructure that consists of a core O and an arbitrary number N of layers and that is embedded in an infinite outer medium (layer number $N + 1$). The layout and electron potential energy profile of the structure is shown in Fig. 1b. The electron in the ith layer is characterized by effective mass m_i (equal to that in the corresponding crystal bulk) and potential energy U_i; the potential of the outer medium is set equal to zero: $U_{N+1} = 0$.

1063-7826/00/3405-0583$20.00 © 2000 MAIK "Nauka/Interperiodica"

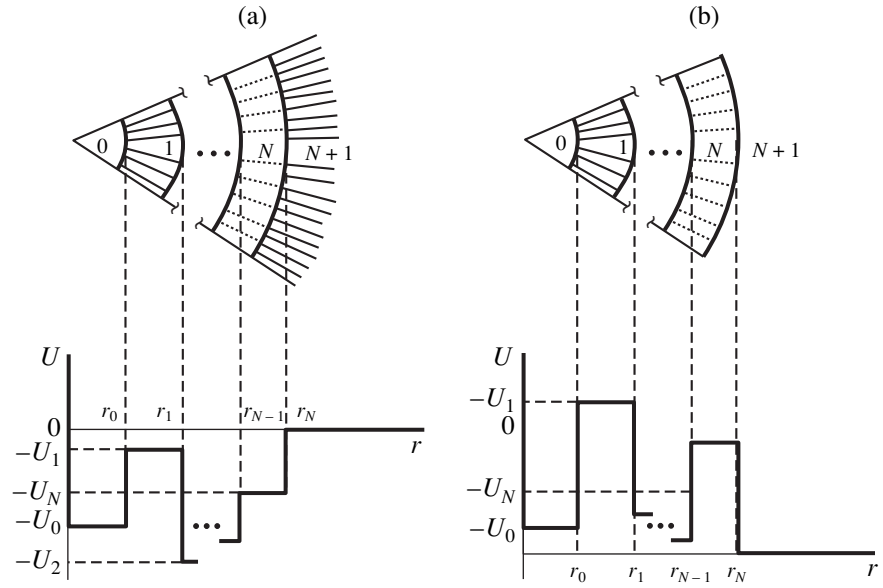

Fig. 1. Structure layout and electron potential energy diagram for (a) closed and (b) open nanoheterostructures.

Thus, using spherical coordinates with the origin at the center of the heterostructure, we can write

$$m(r) = \sum_{i=0}^{N+1} m_i \sigma(r - r_i),$$
$$U(r) = \sum_{i=0}^{N+1} U_i \sigma(r - r_i), \tag{1}$$

where

$$\sigma(r - r_i) = \begin{cases} 1, & r_{i-1} \le r \le r_i, \\ 0, & 0 \le r \le r_{i-1}, \quad r_i < r < \infty. \end{cases} \tag{2}$$

The solution to the Schrödinger equation

$$\left(-\frac{\hbar^2}{2}\nabla\frac{1}{m(r)}\nabla + U(\mathbf{r})\right)\Psi(\mathbf{r}) = E\Psi(\mathbf{r}) \tag{3}$$

can be sought in the following form:

$$\Psi(\mathbf{r}) = R_l(r)Y_{lm}(\theta, \varphi), \tag{4}$$

where

$$R_l(r) = \sum_{i=0}^{N+1} R_l^{(i)}(r)\sigma(r - r_i) \tag{5}$$

are the radial wave functions and $Y_{lm}(\theta, \varphi)$ are the spherical harmonics.

Substituting (4) into (3), we obtain a set of $N + 2$ equations for $R_l^{(i)}(r)$ of the form

$$\frac{1}{r^2}\frac{d}{dr}\left(r^2\frac{dR_l^{(i)}}{dr}\right) + \left[K_i^2 - \frac{l(l+1)}{r^2}\right]R_l^{(i)}(r) = 0, \tag{6}$$

where

$$K_i^2 = \frac{2m_i}{\hbar^2}(E - U_i)$$
$$= \begin{cases} k_i^2, & E > U_i, \quad i = 0, \ldots, N, \\ -\chi_i^2, & E \le U_i, \quad k_{N+1} \equiv k. \end{cases} \tag{7}$$

The solutions to (6) can be written as [18]

$$R_l^{(0)}(r) = K_0 A_l^{(0)}[h_l^-(K_0 r) + h_l^+(K_0 r)],$$
$$R_l^{(i)}(r) = K_i A_l^{(i)}[h_l^-(K_i r) - S_l^{(i)} h_l^+(K_i r)], \tag{8}$$
$$i = 1, \ldots, N,$$
$$R_l^{(N+1)}(r) = kA_l[h_l^-(kr) - S_l h_l^+(kr)],$$

where $h_l^{\pm}$ are the Hankel functions. Coefficient $A_l = 1/\sqrt{2\pi}$ is determined from the normalization condition for the radial wave function

$$\int_0^\infty R_{lk}^*(r)R_{lk'}(r)r^2 dr = \delta(k - k'); \tag{9}$$

S-matrix S_l and other unknown coefficients $A_l^{(i)}$ and $S_l^{(i)}$ are determined from the $2(N + 1)$ boundary conditions for the radial wave functions and their derivatives:

$$\left.\begin{aligned} R_l^{(i)}(K_i r_i) &= R_l^{(i+1)}(K_{i+1} r_i) \\ \frac{1}{m_i}\frac{dR_l^{(i)}(r)}{dr}\bigg|_{r=r_i} &= \frac{1}{m_{i+1}}\frac{dR_l^{(i+1)}(r)}{dr}\bigg|_{r=r_i} \end{aligned}\right\} \tag{10}$$
$$(i = 0, 1, \ldots, N).$$

Equation set (10) can be solved analytically in the general case. Designating

$$\Phi_l^{(0)}(K_0 r_0) = h_l^-(K_0 r_0) + h_l^+(K_0 r_0),$$
$$\Phi_l'^{(0)}(K_0 r_0) = \left.\frac{d\Phi_l^{(0)}(K_0 r)}{dr}\right|_{r = r_0}, \quad (11)$$

we determine the coefficient $S_l^{(1)}$ as

$$S_l^{(1)} = \frac{m_1 \Phi_l'^{(0)}(K_0 r_0) h_l^-(K_1 r_0) - m_0 \Phi_l^{(0)}(K_0 r_0) h_l'^-(K_1 r_0)}{m_1 \Phi_l'^{(0)}(K_0 r_0) h_l^+(K_1 r_0) - m_0 \Phi_l^{(0)}(K_0 r_0) h_l'^+(K_1 r_0)}. \quad (12)$$

The other coefficients $S_l^{(i)}$ are determined from the recursive relation

$$S_l^{(i)} = \frac{m_i \Phi_l'^{(i-1)}(K_{i-1} r_{i-1}) h_l^-(K_i r_{i-1}) - m_{i-1} \Phi_l^{(i-1)}(K_{i-1} r_{i-1}) h_l'^-(K_i r_{i-1})}{m_i \Phi_l'^{(i-1)}(K_{i-1} r_{i-1}) h_l^+(K_i r_{i-1}) - m_{i-1} \Phi_l^{(i-1)}(K_{i-1} r_{i-1}) h_l'^+(K_i r_{i-1})}, \quad (13)$$

where

$$\Phi_l^{(i-1)}(K_{i-1} r_{i-1}) = h_l^-(K_{i-1} r_{i-1}) - S_l^{(i-1)} h_l^+(K_{i-1} r_{i-1}), \quad (14)$$

$$\Phi_l'^{(i-1)}(K_{i-1} r_{i-1}) = \left.\frac{d\Phi_l^{(0)}(K_{i-1} r)}{dr}\right|_{r = r_{i-1}}.$$

Thus, the S-matrix, which determines the quasi-stationary state spectrum of the system, can be expressed as

$$S_l(k) = \frac{m_{N+1} \Phi_l'^{(N)}(K_N r_N) h_l^-(k r_N) - m_N \Phi_l^{(N)}(K_N r_N) h_l'^-(k r_N)}{m_{N+1} \Phi_l'^{(N)}(K_N r_N) h_l^+(k r_N) - m_N \Phi_l^{(N)}(K_N r_N) h_l'^+(k r_N)}. \quad (15)$$

Since the coefficients $A_l^{(i)}$ are defined unambiguously by

$$A_l^{(i)} = \frac{1}{\sqrt{2\pi}} \frac{k}{K_i} \prod_{p=i}^{N} \frac{\Phi_l^{(p)}(K_{p+1} r_p)}{\Phi_l^{(p)}(K_p r_p)}, \quad (16)$$

the radial wave functions $R_{nl}(r)$ and, consequently, the wave functions $\Psi_{nlm}(\mathbf{r})$ are also uniquely defined.

According to the general theory [18], one has to find the poles of the S matrix (15) that are numbered by $n = 1, 2, \ldots, n_{\max}$. The real part of a pole determines the energy E_{nl} of a quasi-stationary state, and its imaginary part determines the particle lifetime τ_{nl} in that state. The wave functions of the quasi-stationary states are given by

$$\Psi_{nlm}(\mathbf{r}) = R_{nl}(r) Y_{lm}(\theta, \varphi), \quad (17)$$

and the states of the continuous spectrum are represented as

$$\Psi_{klm}(\mathbf{r}) = R_{kl}(r) Y_{lm}(\theta, \varphi). \quad (18)$$

The set of wave functions $\Psi_{nlm}(\mathbf{r})$ and $\Psi_{klm}(\mathbf{r})$ is complete and orthonormalized. Thus, the secondary quantization representation can be used to study the interaction of electrons in an open spherical nanoheterostructure with the quantized fields (phonons and photons).

2. QUASI-STATIONARY STATES IN AN OPEN SPHERICAL NANOHETEROSTRUCTURE

Next, relying on the theory developed in the previous section, we study the quasi-stationary electron and hole states in a spherical GaAs/Al_xGa_{1-x}As/GaAs heterostructure.

Calculating the S-matrix according to (15) for $l = 0$, we have

$$S_0(k) = e^{-2ikR_1} \frac{g^- + \Delta m}{g^+ + \Delta m} \frac{e^{-2\chi\rho} + \dfrac{g^+ - \Delta m}{g^- + \Delta m} \xi_0(k)}{e^{-2\chi\rho} + \dfrac{g^- - \Delta m}{g^+ + \Delta m} \xi_0(k)}, \quad (19)$$

where

$$\xi_0(k) = \frac{m_1 k R_0 \cot(kR_0) + m_0 R_0 \chi + \Delta m}{m_1 k R_0 \cot(kR_0) - m_0 R_0 \chi + \Delta m}, \quad (20)$$

$\rho = R_1 - R_0$, $\Delta m = m_0 - m_1$, $g^\pm = (m_0\chi \pm ikm_1)R_1$; for $l = 1$, we have

$$S_1(k) = e^{-2ikR_1} G_+(k) \frac{e^{-2\chi\rho} - G_-^*(k)\xi_1(k)}{e^{-2\chi\rho} - G_-(k)\xi_1(k)}, \quad (21)$$

where

$$G_{\pm}(k) = \frac{2\Delta m(1 \pm ikR_1)(xR_1 \pm 1) + R_1^2[m_0\chi^2 + m_1k^2 \pm k\chi R_1(km_1 + i\chi m_0)]}{2\Delta m(1 - ikR_1)(xR_1 + 1) + R_1^2[m_0\chi_0^2 + k\chi R_1(km_1 - i\chi m_0)]},$$

$$\xi_1(k) = \frac{2\Delta m\eta_-(1 + xR_0) + R_0^2[m_0\chi^2\eta_- + m_1k^2(1 + \chi R_0)]}{2\Delta m\eta_-(1 - xR_0) + R_0^2[m_0\chi^2\eta_+ + m_1k^2(1 + \chi R_0)]}, \quad (22)$$

$$\eta_{\pm} = 1 \pm kR_0\cot(kR_0),$$

and $G_-^*(k)$ is a complex conjugate to $G_-(k)$ with k and χ as real quantities.

Equation $S_l^{-1}(k) = 0$ is transcendental, and one cannot find the poles of the S-matrices given by (19) and (21) analytically; thus, below they are calculated numerically. Only for the high barrier strength ($\chi\rho \gg 1$) are the expressions for S-matrix simplified, and the corresponding levels of the quasi-stationary spectrum are determined by

$$\xi_l(k) = 0, \quad l = 0, 1. \quad (23)$$

For the lifetimes of electrons and holes in the corresponding states, we obtain the following analytical expressions:

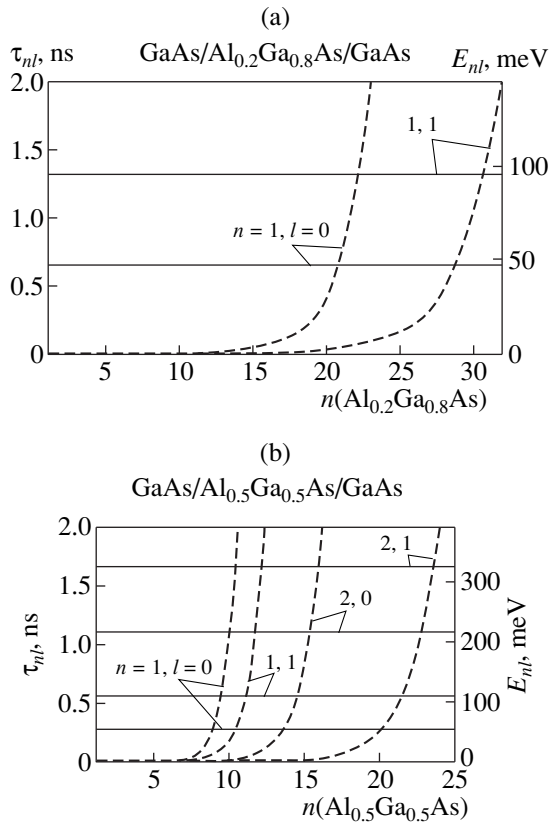

Fig. 2. Electron quasi-stationary state energies E_{nl} (full lines) and lifetimes τ_{nl} (broken lines) in a 15-monolayer GaAs quantum well in relation to the barrier width (the number of $Al_xGa_{1-x}As$ monolayers) for Al content x = (a) 0.2 and (b) 0.5.

$$\tau_{n0} = \frac{\hbar e^{2\chi_n\rho}}{16E_{n0}} \times \frac{\left[m_1^2k_n^2 + \left(m_0\chi_n + \frac{\Delta m}{R_1}\right)^2\right]\eta_n(\chi_nR_0 + 1)}{m_1^2\chi_n^3k_n}, \quad (24)$$

$$\tau_{n1} = \frac{\hbar e^{2\chi_n\rho}}{16E_{n1}}[\alpha_1^2(4 + \beta_1^2) + 2\mu\alpha_1\gamma_1(2 + \beta_1) + \mu^2\gamma_1^2(1 + \beta_1)]\frac{\mu^2\gamma_0^2 - \mu\alpha_0\gamma_0 - 2\alpha_0^2 + \delta}{\mu^2\chi_n^6k_n^3R_0^3R_1^6}, \quad (25)$$

where

$$\eta_n = \left(m_0^2\chi_n^2 + m_1^2k_n^2 + m_0\Delta m\frac{\chi_n}{R_1}\right),$$

$$\alpha_p = R_p\chi_n \pm 1, \ \beta_p = R_p^2k_n^2, \ \gamma_p = 1 + \alpha_p^2 \ (p = 0, 1),$$

$$\delta = 3\beta_0 + R_0\chi_0\beta_0(2 + \alpha_0), \quad \mu = \frac{m_0}{m_1}.$$

The characteristics of electron and hole spectra were calculated for the particular case of the GaAs/$Al_xGa_{1-x}As$/GaAs spherical nanoheterostructure in the context of the theory outlined above.

Electron and hole effective masses in bulk $Al_xGa_{1-x}As$ in relation to Al content x are determined by the following expressions [19, 20]: $m_1^e = (0.067 + 0.083x)m_0$ and $m_1^h = (0.35 + 0.05x)m_0$, where m_0 is the free electron mass. The height (in eV) of the electron and hole potential barriers introduced by $Al_xGa_{1-x}As$ layer equals, correspondingly,

$$V_e = 0.6(1.135x + 0.37x^2),$$
$$V_h = 0.43(1.55x + 0.37x^2). \quad (26)$$

The calculated electron and hole energies E_{nl} and lifetimes τ_{nl} in the states with orbital quantum number $l = 0$ and $l = 1$ in relation to the barrier width (represented by the number of $Al_xGa_{1-x}As$ layers n) for a given quantum well radius (represented by the number of GaAs layers n_{GaAs}) are shown in Figs. 2 and 3. One can see that the electron and hole energy levels virtually do not shift with varying barrier width, while the life-

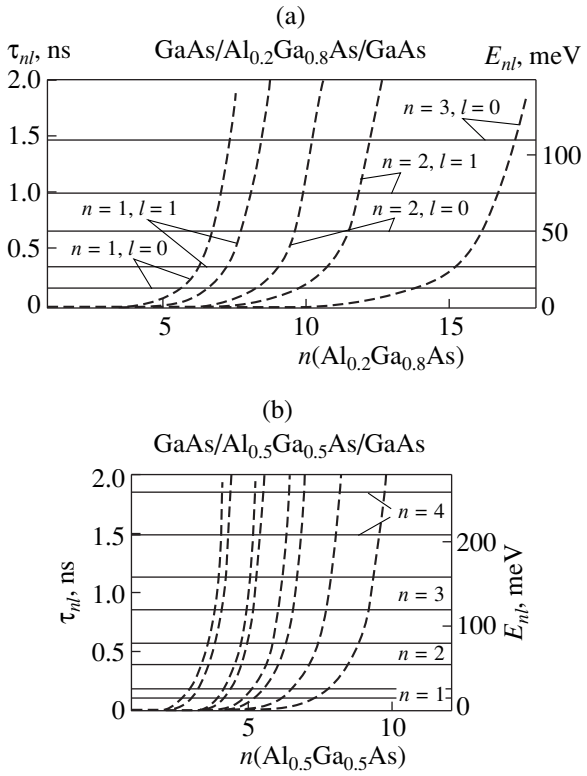

Fig. 3. Hole quasi-stationary state energies E_{nl} (full lines) and lifetimes τ_{nl} (broken lines) in a 15-monolayer GaAs quantum well in relation to the barrier width (the number of $Al_xGa_{1-x}As$ monolayers) for Al content x = (a) 0.2 and (b) 0.5.

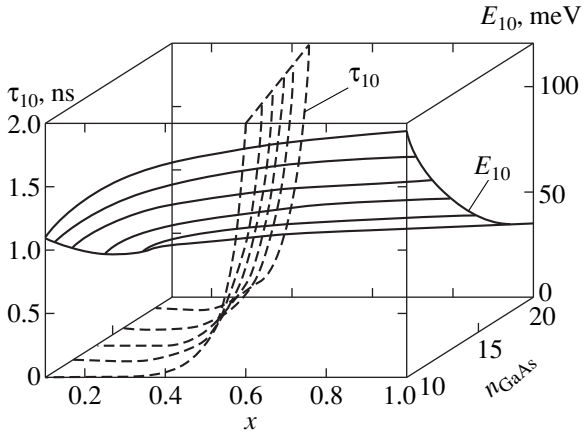

Fig. 4. The electron ground state energy (full lines) and lifetime (broken lines) in relation to Al content x in the barrier and the number of GaAs monolayers (the well width) for fixed barrier width (10 $Al_xGa_{1-x}As$ monolayers).

time τ_{nl} increases exponentially with increasing n for all states of both quasiparticles. For a given barrier width, the lifetime is higher for the states with lower energies. This is readily understood: lowering the energy is equivalent to an increase in "effective barrier strength" for a quasiparticle in the corresponding state, which hinders its penetration through the barrier and, consequently, increases its lifetime in the quantum well. Since $m_h > m_e$, the hole lifetime is always longer than the electron lifetime under similar conditions, because it is more difficult for a hole to penetrate through the barrier.

In Fig. 4, we show the calculated ground-state energy E_{01} and lifetime τ_{01} of electrons in relation to the well width n_{GaAs} and Al content x in the barrier layer for a given barrier width (n = 5). One can see that an increase in the quantum well width at fixed Al content results in the reduction of the absolute value of the ground state energy; the electron lifetime in this case increases, as has been mentioned above. Increasing x results, according to (26), in an increase in the potential barrier height, which leads to an increase in the ground state energy and lifetime.

The energy position of electron and hole levels is weakly sensitive to the variations in the barrier width but highly sensitive to the variations in the well width. The quasiparticle lifetimes in the quasi-stationary states are strongly influenced by variation both in the barrier and well widths.

Thus, the proposed theory enables us to obtain a complete set of wave functions and calculate the spectral characteristics of the complex spherical quantum wells (nanoheterostructures) with quasi-stationary states.

Finally, let us consider the following important issue. The general theory developed here is valid for the case where the electron and hole bulk band structure of the materials composing the nanoheterostructure under study can be described by the single-band model. The theory applicable to the nanoheterostructures composed of multiband materials has to start from the Schrödinger equation (3) in its matrix form. However, since the quasiparticle states in the quantum dots have no particular quasi-momentum, only effective masses and potential energies of all types of holes enter the theory in the models that neglect the mixing of the states [21]. Consequently, the matrix form of the Schrödinger equation for holes decomposes into a set of separate equations. Thus, in a model that neglects state mixing, the spectra and lifetimes for other types of holes can be calculated in terms similar to those described here.

REFERENCES

1. A. I. Ekimov and A. A. Onushchenko, Fiz. Tekh. Poluprovodn. (Leningrad) **16**, 1215 (1982) [Sov. Phys. Semicond. **16**, 775 (1982)].
2. H. Weller, H. M. Schmidt, U. Koch, *et al.*, Chem. Phys. Lett. **124**, 557 (1986).
3. A. Nakamura, H. Yamada, and T. Tokizaki, Phys. Rev. B: Condens. Matter **40**, 8585 (1989).
4. M. G. Bawendi, W. L. Wilson, L. Rothberg, *et al.*, Phys. Rev. Lett. **65**, 1623 (1990).

5. A. I. Ekimov, A. L. Éfros, and A. A. Onushenko, Solid State Commun. **56**, 921 (1985).
6. A. L. Éfros and A. L. Éfros, Fiz. Tekh. Poluprovodn. (Leningrad) **16**, 1209 (1982) [Sov. Phys. Semicond. **16**, 772 (1982)].
7. T. Takagahara, Phys. Rev. B: Condens. Matter **36**, 9293 (1987).
8. Y. Kayanuma, Phys. Rev. B: Condens. Matter **38**, 9797 (1988).
9. E. Hanamura, Phys. Rev. B: Condens. Matter **37**, 1273 (1988).
10. M. Klein, F. Hache, D. Ricard, *et al.*, Phys. Rev. B: Condens. Matter **42**, 11123 (1990).
11. P. A. Knipp and T. L. Reinecke, Phys. Rev. B: Condens. Matter **48**, 18037 (1993).
12. J. C. Marini, B. Stebe, and E. Kartheuser, Phys. Rev. B: Condens. Matter **50**, 14302 (1994).
13. D. Schooss, A. Mews, A. Eychmüller, *et al.*, Phys. Rev. B: Condens. Matter **49**, 17072 (1994).
14. J. W. Haus, H. S. Zhou, I. Honma, and H. Komiyama, Phys. Rev. B: Condens. Matter **47**, 1359 (1993).
15. A. Mews, A. V. Kadavanich, U. Banin, *et al.*, Phys. Rev. B: Condens. Matter **53**, R13242 (1996).
16. N. V. Tkach, Fiz. Tverd. Tela (Leningrad) **39**, 1109 (1997) [Phys. Solid State **39**, 995 (1997)].
17. M. Tkach, V. Holovatsky, O. Voitsekhivska, and M. Min'kova, Phys. Status Solidi **203**, 373 (1997).
18. A. I. Baz', Ya. B. Zel'dovich, and A. M. Perelomov, *Scattering, Reactions and Decays in Nonrelativistic Quantum Mechanics* (Nauka, Moscow, 1971, 2nd ed.; Israel Program for Scientific Translations, Jerusalem, 1966).
19. G. Q. Hai, F. M. Peters, and J. T. Devreese, Phys. Rev. B: Condens. Matter **48**, 4666 (1993).
20. S. Le Goff and B. Stebe, Phys. Rev. B: Condens. Matter **47**, 1383 (1993).
21. P. C. Sercel and K. J. Vahala, Phys. Rev. B: Condens. Matter **42**, 3690 (1990).

Translated by M. Skorikov

Semiconductors, Vol. 34, No. 5, 2000, pp. 589–593. Translated from Fizika i Tekhnika Poluprovodnikov, Vol. 34, No. 5, 2000, pp. 607–611.

LOW-DIMENSIONAL SYSTEMS

Study of Decay of Elastically Strained Germanium Film at the Silicon Surface

I. V. Zakurdaev*, M. V. Baĭzer*, S. Yu. Sadof'ev*, and M. M. Rzaev**

** Ryazan State Radio Engineering Academy, Ryazan, 390005 Russia*

e-mail: nich@rricnit.ryazan.su

*** Lebedev Institute of Physics, Russian Academy of Sciences, Leninskiĭ pr. 53, Moscow, 117924 Russia*

Submitted November 29, 1999; accepted for publication December 1, 1999

Abstract—The results of studying the initial stage of the surface self-organization in a Ge/Si(001) heteroepitaxial system are reported; this stage begins with step bunching and ends with origination of three-dimensional irregularities. The force inducing the directional drift of germanium adatoms is calculated, and the smallest attainable island sizes are estimated taking into account the kinetic features of directional mass transport.

1. INTRODUCTION

In recent years, interest has been attracted to the processes of decay of elastically strained germanium film at the silicon surface in connection with the problem of developing semiconductor structures that involve quantum dots and are made of materials conventional for microelectronics. The challenge consists in formation of islands that have ultimately small sizes (≤10 nm) and are structurally perfect. This problem is solved with good results for heterostructures based on III–V compounds; in particular, the formation of arrays of quantum dots in an InAs/GaAs(001) system was reported [1, 2]. However, attempts to obtain nanocluster ensembles with a good uniformity in sizes in a Ge/Si(001) system have failed; in any case, the sizes of the formed islands have exceeded those required for the formation of quantum dots [3].

In calculations of the finite size of islands, the following energy characteristics are primarily considered: minimization of the film free energy due to the formation of islands that have a shape close to the equilibrium one, with a change in the island shape being related to the anisotropy of elastic forces in the strained crystalline film [4]. However, directional mass transport can play an important role in the processes of self-organization [5]. In this case, in order to calculate the island size, one should know the magnitude of the force inducing the mass transport and the extent of anisotropy of the surface diffusion. It is expedient to calculate the force on the basis of experimental data on the formation the step bunches, because this process has been theoretically considered most thoroughly for various cases [5–7].

In [6], the force acting on the steps at the surface and resulting in the formation of the periodic structure ("natural roughness") due to lowering of the crystal's surface energy was calculated. As a rule, in the majority of metals and semiconductors, the formation of "natural roughness" is observed only at surfaces similar in orientation to those of close-packed structures. In [6], the following expression was obtained:

$$F_1 = \alpha_1 L^{-2}. \quad (1)$$

Here,

$$\alpha_1 = \frac{4(1-\sigma^2)}{\pi E}\gamma^2 a^2,$$

σ is the Poisson ratio, E is the Young modulus, γ is the surface energy, a is the interatomic distance, and L is the average distance between steps in the state of equilibrium.

In [7], the force acting on the steps at the surface of elastically strained film was represented as

$$F_2 = \alpha_2 \ln L, \quad (2)$$

where

$$\alpha_2 = \frac{\varepsilon^2 h^2}{M},$$

ε is the bulk stress, h is the step height, and M is the elastic modulus.

In [7], the step bunching at the surface of an elastically strained film in the case of simultaneous action of the forces given by (1) and (2) was considered and it was shown that intense development of steps (2D formations) was possible for $L_{av}/L_0 \geq 1$, where L_{av} is the average distance between the steps at the substrate (this distance is defined by orientation) and $L_0 = (\alpha_1/\alpha_2)^{1/2}$.

The objectives of this work were to verify experimentally the inferences made in [7], to calculate the force F_2, and to estimate the smallest attainable sizes of the islands in a system consisting of germanium film at

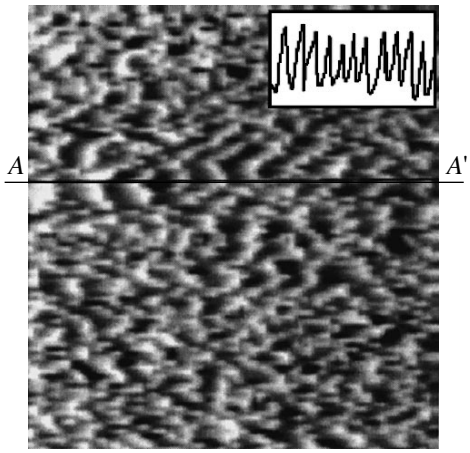

Fig. 1. An STM image of the surface topography; the insert shows the surface profilogram across the *AA*' section. The substrate temperature during epitaxy was 200°C, and the effective thickness of the germanium film was 5 ML. The scanned area was 740×740 Å^2.

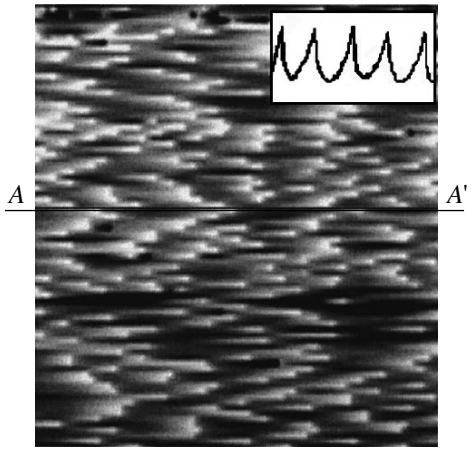

Fig. 2. An STM image of the surface topography; the insert shows the surface profilogram across the *AA*' section. The substrate temperature during epitaxy was 200°C, and the effective thickness of germanium film was 15 ML. The scanned area was 740×740 Å^2.

the silicon surface on the basis of the kinetic characteristics of directional mass transport.

Among the characteristic features of the system under consideration, we can single out very fast transition from the stage of pseudomorphic two-dimensional growth to that of three-dimensional (3D) growth if the thickness of the film exceeds a certain critical value, which is typically equal to 5–6 monolayers (ML). Taking into account the latter fact, we studied the formation of steplike surface irregularities at the lowest temperature (T_s = 200°C), making it possible to prolong the stage of formation of the island structure. We studied structural changes in the film surface using high energy electron diffraction (HEED), and also the air-ambient versions of scanning tunneling microscopy (STM) and atomic-force microscopy (AFM).

2. EXPERIMENT AND RESULTS

In accordance with the objectives of this work, we studied structural changes in the surface of a Ge/Si(001) heteroepitaxial system in relation to the effective thickness of deposited germanium layer (d_{eff}).

The samples used in the experiments were grown by molecular-beam epitaxy (MBE) on a KÉF-4.5 (Si:P with $\rho = 4.5\ \Omega$ cm) (001) substrate misoriented by 0.5° to the [001] direction; a Katun' MBE system was used. Following the conventional procedure for removal of the native-oxide layer from the substrate surface, a 200-nm-thick silicon buffer layer was grown at a temperature of 800°C. After that, the substrate was cooled to a given temperature and a germanium film with thicknesses of 6.4, 10, 15, and 20 ML was deposited, with the deposition rate equal to 0.22 Å/s.

A Skan-8 tunneling microscope and a Solver P4-SPM-MDT scanning probe microscope were used in the STM and AFM studies, respectively.

Examinations of HEED patterns showed that, at a temperature of epitaxy of T_s = 200°C, two-dimensional growth of germanium film persisted up to a film thickness equal to 15 ML; only in films 20 ML thick was the formation of 3D structures evident. The type of reconstruction of the germanium surface was (2×1). The difference between the diffraction patterns obtained from the buffer silicon layer and the germanium surfaces consisted in the fact that, in the latter case, the reflections spots were appreciably broadened and had lower intensity, which was indicative of the development of fine-structure roughness at the germanium surface.

2.1. STM Observations

As the probe tip, we used a gold wire that was 0.28 mm in diameter and was sharpened by a mechanical cut. In spite of the conventional difficulties related to the STM observation of the semiconductor surface under atmospheric-air conditions, we managed to obtain a large number of stable STM images with high reproducibility. The attempts to observe the morphology of the silicon substrate without a preliminary treatment (aimed at removing the native-oxide layer and passivating the surface) failed. The scanned area varied from 300×300 Å^2 to 1×1 μm^2.

Figures 1 and 2 show the STM images of the surface topography and the profiles of the surface sections of germanium films 5 and 15 ML thick, respectively; the films were deposited onto the silicon substrate at a temperature of T_s = 200°C. A similar image was obtained for the film with d_{eff} = 10 ML. In all structures, steplike formations, which, as a rule, are observed at the crystal

surface under external effect (for example, under electrothermal diffusion of atoms [5, 8]), are evident. The period of the steps varies from 65 to 140 Å as the germanium-film effective thickness increases from 5 to 15 ML.

The film thickness is proportional to the duration of deposition. The dependence of the step period d on the formation duration t was plotted on the basis of three points and yielded the dependence $d \propto t$.

Studying the characteristic sizes of structures in the films 10 ML thick, from the initial stage of the step formation at T_s = 200°C to the island growth at T_s = 350, 500, and 650°C, showed that these sizes apparently depend exponentially on temperature as $d \sim D_s^{1/2}$, where D_s is the surface-diffusion coefficient. If the formation time and the effective thickness of germanium film are fixed, the active process of formation of the island structure is observed at MBE temperatures exceeding 350°C, with the sizes, shape, and density of islands depending significantly on the MBE-growth temperature and possible conditions of the postgrowth annealing [9].

2.2. AFM Observations

The AFM observations were performed in a contact mode using a cantilever with a silicon probe that had a tip radius less than 10 nm. Characteristic scanned areas were varied from 1×1 μm^2 to 7×7 μm^2.

Structural roughness was not observed on the surface of films 5 and 10 ML thick (T_s = 200°C). In the films with d_{eff} = 15 ML, we observed undulatory extended irregularities (Fig. 3) pointing to the onset of the localized-island formation. Apparently, the steplike structure shown in Fig. 2 covers the undulatory surface irregularities shown in Fig. 3. On the other hand, the observed structure may be referred to as pitted, because it involves characteristic depressions with a diameter of about 450 nm and a depth of 40 Å. Such depressions, although with much smaller sizes (tens of angströms in diameter) were also observed in STM images.

3. DISCUSSION

Observation of the initial stage of development of irregularities at the silicon surface covered with an elastically strained germanium film made it possible to make the following conclusions:

(i) in the initial stage of self-organization (clusterization) of germanium film at a low temperature (T_s < 350°C), the development of steplike structure is observed, with characteristic sizes being $h \le 2$ nm and $d \approx 6.5$–14 nm;

(ii) the average step-growth rate is $v \sim 10^{-8}$ cm/s and exceeds the rate of development of natural roughness by a factor of 10^2 at the same relative temperature ($T \sim 0.2T_m$) [10]; and

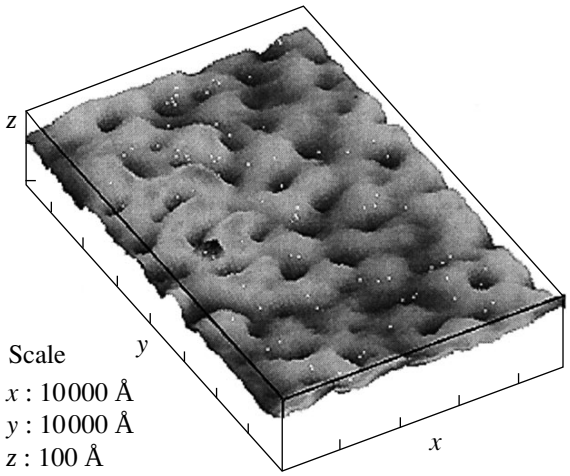

Fig. 3. An AFM 3D image of the surface topography. The substrate temperature during epitaxy was 200°C. The effective thickness of the germanium film was 15 ML. The scanned area was 5×7 μm^2.

(iii) the repetition period of the steps depends on the film thickness and the duration of the film growth as $d \sim h$ and $d \sim t$, respectively.

We now use formulas (1) and (2) to estimate the values of quantities α_1 and α_2. In calculations of α_1, we assumed that σ = 0.3, $E = 7 \times 10^{11}$ dyne/cm^2, $\gamma = 10^3$ dyne/cm [11], and $a = 2.5 \times 10^{-8}$ cm; we obtained $\alpha_1 = 10^{-2}$ dyne cm^2. In the second case, we assumed that h = 1 nm, $\varepsilon = 10^9$ dyne/cm^2 [12], and $M = 10^{12}$ dyne/cm^2 and obtained $\alpha_2 = 10^{-8}$ dyne. We can now evaluate the key parameter of the theory [6]: $L_0 = (\alpha_1/\alpha_2)^{1/2} = 3 \times 10^{-7}$ cm. The average distance between the steps on the vicinal face (001)Ge is $L_{av} = 1.5 \times 10^{-6}$ cm. Thus, we have $L_{av}/L_0 > 1$, which corresponds to active step-bunching [7].

The most important outcome of the above estimations and of the fact that they are consistent with experimental data is the possibility of calculating the force that induces the directional drift of germanium adatoms. Knowledge of this force makes it possible to estimate the smallest attainable sizes of islands in the system under consideration.

It is worth noting, first of all, that the force acting on an adatom in the course of directional mass transport, which induces the step formation, can be derived most precisely from the experiments with electrical transport. In the case of transition metals, $F = 10^{-12}$ dyne [8], whereas, for semiconductors (for example, silicon), we have $F = 5 \times 10^{-11}$ dyne [13]. Simultaneous observations of the development of natural roughness and the formation of structure under the effect of electric forces made it possible to find that the force, which is induced by the chemical-potential gradient and gives rise to natural roughness, is comparable to the force involved in the electrical transport [10]; i.e., this force may be esti-

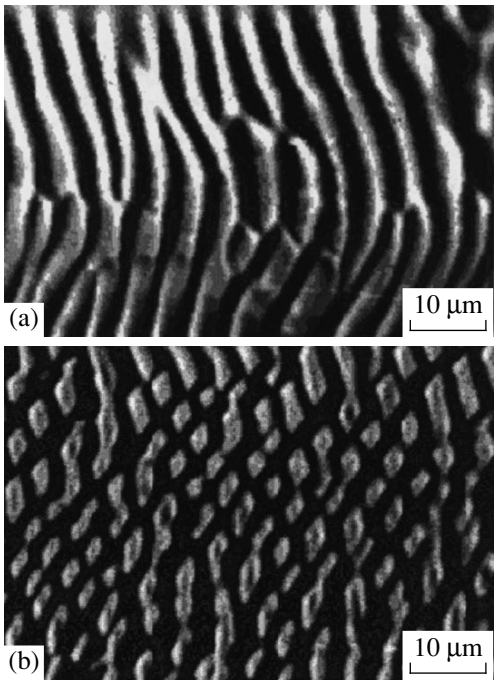

Fig. 4. An optical image of the surface topography of a (112)Mo vicinal face after annealing by direct current $j = 5 \times 10^3$ A/cm^2 in a temperature-gradient field of $\nabla T = 2000$ K/cm for 150 h at $T = 2100$ K: (a) the forces inducing the electrical transport and thermal transport coincide in direction and (b) the directions of these forces are opposite.

mated as $F \approx 10^{-11}$ dyne in the case of semiconductors. Self-organization of elastically strained films proceeds much more actively than in the cases considered. Taking into account that the rate of mass transport is proportional to the acting force for T = const, we infer that the formation of steps with the rate of $v \sim 10^{-8}$ cm/s at $T = 200$°C is possible for $F > 10^{-9}$ dyne. Calculation based on relationship (2) yields $F_2 = \alpha_2 \ln L = 2 \times 10^{-8}$ dyne for $L = 20$ (the ratio of the step period to the interatomic distance).

On the basis of general relationships of the thermodynamics of irreversible processes, the following identical formulas were derived in [5, 8] for the estimates of the period of self-organizing irregularities:

$$d = 2\pi\left[\frac{D_s\gamma\omega}{\left(\frac{\partial D_s}{\partial\theta}\right)F}\right]^{1/2}. \qquad (3)$$

Here, $\partial D_s/\partial\theta$ is the parameter accounting for a change in the surface diffusion coefficient at the curved surface ($\theta = \partial z/\partial x$ is the angle of deviation of the surface irregularity from the mean plane $z = 0$) and ω is the atom volume.

In deriving formula (3), it was shown [5, 10] that the development of self-organizing surface irregularities is possible if the direction of the gradient of the surface-diffusion coefficient is opposite to that of external force vector, i.e., if the quantity $(\partial D_s/\partial\theta)F$ is negative. Otherwise, the effects of external force and the force induced by the Laplace pressure combine, which results in a leveling-off of the surface. The development of a step-like structure on the surface of germanium film at the initial stage of island formation causes the structural anisotropy to increase (the atoms predominantly diffuse along the step edges, i.e., along the direction [110]). It is to this factor that the formation of extended undulatory islands of $Ge_{1-x}Si_x$ at the Si(100) surface (as observed in [14]) can be related. Confirmation of the determining role of anisotropy of the surface-diffusion coefficient in the self-organization can be recognized in experiments with structurization of the surface of a pure crystal (for example, molybdenum) in the case where two forces inducing electrical transport and thermal transport are simultaneously in effect. Figure 4 shows various structures at the surface of the Mo(112) vicinal face misoriented by 3° in the $[1\bar{1}0]$ direction from the direction of the forces. In the case of opposite direction of the forces, decay of the steps into individual islands is observed in the zone where the equivalence of forces should be expected (Fig. 4b). In our opinion, such a situation can arise if structural anisotropy, which ensures the motion of atoms at large angles to the direction of forces, is pronounced [5]. In any case, it is unjustified here to take elastic forces into consideration; in fact, the observed variation in the surface structure is related only to special features of anisotropy in the surface diffusion in the field of external forces.

We now return to relationship (3) and estimate the value d of the smallest attainable size of germanium islands taking into account the diffusion kinetics. Assuming that $D_s/(\partial D_s/\partial\theta) \approx 1$, $\omega = 10^{-23}$ cm^3, and the force $F = 10^{-8}$ dyne, we obtain $d \approx 60$ nm, which is consistent with experimental data [9, 14, 15]. It follows from formula (3) that the island size can be decreased by increasing the force F or by properly selecting the crystallographic orientation of the substrate (with a resulting decrease in the surface diffusivity of atoms as its anisotropy increases). The effect of both factors was qualitatively observed in [14].

It is noteworthy that the dependence $d \sim F^{-1/2} \sim \varepsilon^{-1}$ of the island size on the force and, correspondingly, on the degree of the lattice mismatch, which we obtained in this work, agrees well with a similar dependence obtained in [16]. It was shown in [16] that, in an InAs/GaAs system, a variation in the arsenic flux affects significantly the conditions of the island growth; namely, an increase in pressure, i.e., an increase in surface diffusivity due to an increase in the arsenic-adatom concentration, causes the island size to increase, which also follows from formula (3).

CONCLUSION

Our STM, AFM, and HEED studies of decay of elastically strained germanium film at the silicon surface in a Ge/Si(001) heteroepitaxial system made it possible to evaluate, to the first approximation, the force inducing the directional drift of germanium adatoms; we also managed to estimate the smallest attainable island size on the basis of kinetic characteristics of directional mass transport. The smallest island size was shown to be 60 nm. The possibility of further decreasing the island size relies on an increase in the force acting on an adatom or, with allowance made for the determining role of the surface-diffusivity anisotropy in the surface self-organization, on the proper selection of the crystallographic orientation of the substrate.

ACKNOWLEDGMENTS

This work was supported in part by the Russian Foundation for Basic Research (project no. 99-02-17795) and by the Ministry of Education of Russian Federation under the Program "Electronics and Radio Engineering."

REFERENCES

1. Zh. I. Alferov, Fiz. Tekh. Poluprovodn. (St. Petersburg) **32**, 3 (1998) [Semicond. **32**, 1 (1998)].
2. N. N. Ledentsov, V. M. Ustinov, V. A. Shchukin, *et al.*, Fiz. Tekh. Poluprovodn. (St. Petersburg) **32**, 385 (1998) [Semicond. **32**, 343 (1998)].
3. O. P. Pchelyakov, Yu. B. Bolkhovityanov, L. V. Sokolov, *et al.*, in *Proceedings of Conference on Nanophotonics, Nizhni Novgorod, 1999*, p. 15.
4. J. Tersoff and R. M. Tromp, Phys. Rev. Lett. **70**, 2782 (1993).
5. Ya. E. Geguzin and Yu. S. Kaganovskiĭ, *Diffusion Processes at the Crystal Surface* (Énergoatomizdat, Moscow, 1984).
6. V. I. Marchenko and A. Yu. Parshin, Zh. Éksp. Teor. Fiz. **79** (1), 257 (1980) [Sov. Phys. JETP **52**, 129 (1980)].
7. J. Tersoff, Y. H. Phang, Z. Zhang, *et al.*, Phys. Rev. Lett. **75**, 2730 (1995).
8. I. V. Zakurdaev, Izv. Akad. Nauk SSSR, Ser. Fiz. **40** (8), 1554 (1976).
9. Yu. G. Sadof'ev, K. V. Malakhov, M. M. Rzaev, *et al.*, in *Proceedings of Conference on Nanophotonics, Nizhni Novgorod, 1999*, p. 90.
10. I. V. Zakurdaev and G. N. Shuppe, *Mass-Transport Processes and Changes in the Surface Structure of Crystals* (TsNII "Élektronika," Moscow, 1983), Chap. 2, No. 11 (965), p. 64.
11. *Reference Book for Chemists* (Goskhimizdat, Moscow, 1963), Vol. 1, p. 1071.
12. C. Kittel, *Introduction to Solid State Physics*, 5th ed. (Wiley, New York, 1976; Nauka, Moscow, 1978).
13. H. Tokumoto, K. Miki, Y. Morita, *et al.*, Ultramicroscopy **42**–**44**, 816 (1992).
14. C. Teichert, Y. H. Phang, L. J. Peticolas, *et al.*, in *Surface Diffusion: Atomistic and Collective Processes, NATO-ASI Series* (Plenum Press, New York, 1997), p. 297.
15. O. P. Pchelyakov, A. V. Dvurechenskiĭ, V. A. Markov, *et al.*, in *Proceedings of All-Russia Conference on Si- and Ge-based Nanostructures, Nizhni Novgorod, 1998*, p. 7.
16. V. A. Schukin, N. N. Ledentsov, P. S. Kop'ev, *et al.*, Phys. Rev. Lett. **75** (16), 2968 (1995).

Translated by A. Spitsyn

Semiconductors, Vol. 34, No. 5, 2000, pp. 594–597. Translated from Fizika i Tekhnika Poluprovodnikov, Vol. 34, No. 5, 2000, pp. 612–616.

LOW-DIMENSIONAL SYSTEMS

Stacked InAs/InGaAs Quantum Dot Heterostructures for Optical Sources Emitting in the 1.3 μm Wavelength Range

N. A. Maleev*, A. E. Zhukov*, A. R. Kovsh*, S. S. Mikhrin*, V. M. Ustinov*, D. A. Bedarev*, B. V. Volovik*, I. L. Krestnikov*, I. N. Kayander*, V. A. Odnoblyudov*, A. A. Suvorova*, A. F. Tsatsul'nikov*, Yu. M. Shernyakov*, N. N. Ledentsov*, P. S. Kop'ev*, Zh. I. Alferov*, and D. Bimberg**

** Ioffe Physicotechnical Institute, Russian Academy of Sciences, Politekhnicheskaya ul. 26, St. Petersburg, 194021 Russia*

*** Institut für Festkörperphysik, Technische Universität Berlin, D-10623 Berlin, Germany*

Submitted December 1, 1999; accepted for publication December 2, 1999

Abstract—A method is proposed for growing stacked InAs/InGaAs self-organized quantum dots on GaAs substrates. The technique allows fabrication of structures exhibiting intense and narrow-line photoluminescence in the 1.3 μm wavelength region. The influence of growth conditions on structural and optical characteristics was studied. The proposed structures show promise in developing vertical-cavity surface-emitting devices. *© 2000 MAIK "Nauka/Interperiodica".*

Further progress in developing high-speed optical-fiber data transmission systems demands that the semiconductor light emitters and detectors operating at 1.3 and 1.55 μm be improved. The shortcomings of the conventional InGaAsP/InP injection heterolasers are associated with the asymmetric directivity pattern of laser radiation, which hinders the introduction of the light beam into the optical waveguide; with low-temperature stability; and with a complicated fabrication technology that includes individual processing and measurement of any laser crystal [1]. Therefore, an active search is being conducted for new semiconducting materials for the spectral regions specified above. These include quantum well (QW) InGaAsN [2] and GaAsSb [3] structures and InGaAs structures with quantum dot (QD) arrays [4, 5] grown on GaAs substrates by molecular-beam epitaxy (MBE). The use of GaAs substrates makes possible the fabrication of the long-wavelength vertical-cavity surface-emitting lasers (VCSELs) by using high-quality quarter-wave AlGaAs/GaAs Bragg reflectors. Light sources of this kind have a potential for efficient introduction of light into a fiber, possess higher temperature stability, and allow the batch technology of fabrication and testing [6].

The longest lasing wavelength obtained for QW InGaAs/GaAs structures is 1.22 μm [7], which is due to the limitations imposed by the pseudomorphous growth technology on the QW width [8]. At the same time, the use of InGaAs and InAs/InGaAs QD arrays enabled the fabrication of vertical-cavity photodetectors [9] and low-threshold lasing, including that in the continuous-wave mode, for the 1.3 μm spectral region [4, 10]. However, the optical gain achieved in structures with QD arrays is not high enough to overcome the losses characteristic of the surface-emitting lasers operating in this spectral region. The observed gain saturation is due to the limited surface density of QDs combined with the inhomogeneous broadening of the density of states due to the variance in parameters of separate dots [11]. Therefore, developing the methods for fabrication of uniform QD arrays with high surface density and emitting in the 1.3 μm region is very important.

In this paper, we report the results of optimization of the design and the MBE conditions for the structures with stacked InAs/InGaAs QDs. The optimization enabled higher surface density of the QD array, with high intensity of the 1.3 μm photoluminescence (PL) line retained and with no line broadening as compared to single-layer QD structures. PL and electroluminescence (EL) in the 1.26–1.33 μm range is demonstrated for the epitaxial structures with vertical optical cavities.

The structures studied in this work were grown on semi-insulating GaAs(100) substrates in a Riber-32P MBE setup with a solid As_4 source. The substrate temperature was 485°C during the formation of QDs, QWs, and the entire thickness of the spacers (or some part of it) and was 600°C during the fabrication of the rest of the structure. A Philips EM 420 microscope with a 100–120-kV accelerating voltage was used for transmission electron microscopy (TEM). The PL was excited by an Ar^+ laser (514.5 nm) and was detected with a Ge photodiode. The excitation density was 100 W/cm^2.

Figure 1 shows a cross-sectional TEM image of a structure with InAs QDs in an external InGaAs QW.

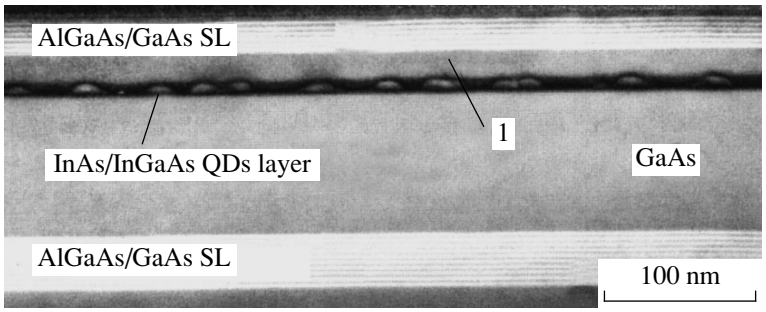

Fig. 1. Cross-sectional TEM image of a sample with a single InAs QD layer fabricated on a 4-nm-thick $In_{0.12}Ga_{0.88}As$ sublayer and covered with 6-nm $In_{0.12}Ga_{0.88}As$ and 10-nm GaAs layers.

Structures of this kind ensure a relatively high surface density of QDs [$(3.5–4.5) \times 10^{10}$ cm^{-2}] [5] as compared to $In_{0.5}Ga_{0.5}As$ QDs (1.0×10^{10} cm^{-2}) [4], also emitting in the 1.3 μm region. We study the possibility of increasing the surface density further by means of stacking, i.e., repeated deposition of several QD layers separated by GaAs spacers.

Previously, the stacking of QDs with relatively thin (1.5–10 nm) GaAs spacers has been successfully used to fabricate injection lasers involving the QD arrays and operating at shorter wavelengths [12]. However, an attempt to use this approach directly for InAs/InGaAs structures emitting in the 1.3 μm region resulted in a dramatic decrease in PL intensity both at liquid nitrogen and at room temperatures, and the respective PL spectra changed as well. As an example, Fig. 2 shows the PL spectra (at 77 and 300 K) for structures with one and three (three-stack) InAs QD layers grown on a 3-nm-thick InGaAs sublayer and coated with 5-nm-thick InGaAs and 10-nm-thick GaAs layers. All the spacers were grown at 480–490°C. A considerable decrease in PL intensity indicates the deterioration of the three-stack structure grown by this technique. A possible reason is that the lower QD layer affects the formation of further layers through stress fields generated above separate islands (see Fig. 1, region *1*).

We carried out studies aimed at optimizing the growth process for structures with stacked InAs/InGaAs QDs. It was found that the key point is to lower the total In content in separate layers to the maximum possible extent [13]. This was achieved by using InAs QDs deposited directly on GaAs and further overgrown with the next InGaAs layer with low In content (x_{InAs} = 0.1–0.15). Another fundamental point consists in using relatively thick (20–40 nm) GaAs spacers. In doing so, only the first, relatively thin (3–5 nm) part of the spacer, intended for conservation of the InAs/InGaAs QD shape, is grown at 480–490°C, and the remaining part is grown at 600°C, which is a temperature typical of the MBE GaAs growth. Figure 3 shows a cross-sectional TEM image of a sample with three stacked InAs QD layers coated with a 6-nm-thick $In_{0.12}Ga_{0.88}As$ layer and separated by GaAs spacers of 50-nm total thickness. Note that, in contrast to the conventional structures with stacked QD arrays in which vertical alignment is observed of QDs in neighboring layers, their positions are uncorrelated in our case. We suppose that this is due to the relatively large thickness of the spacers. A more detailed analysis demonstrated that the surface density of the QDs and their size distributions are the same in different layers. Figure 4 shows room temperature PL spectra of three samples with one or three InAs/InGaAs QD arrays with varied thickness of the GaAs spacers. The results presented confirm that the proposed growth technique allows preservation of the PL spectrum shape in the 1.3 μm region for the stacked InAs/InGaAs QD structures. In this case, the PL intensity for the samples with stacked QD layers does not decrease in comparison with the single-layer structures.

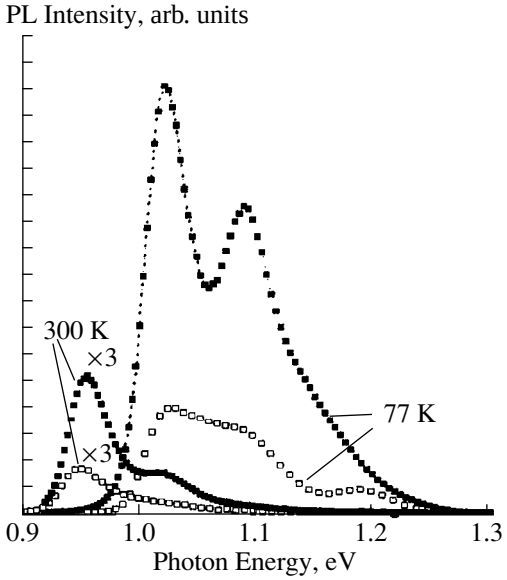

Fig. 2. PL spectra for structures with a single layer (full squares) and three (open squares) InAs QDs layers grown on the 3-nm-thick InGaAs sublayer and covered with 5-nm InGaAs and 10-nm GaAs layers.

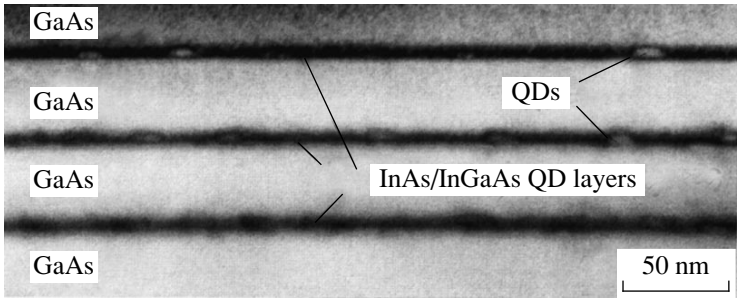

Fig. 3. Cross-sectional TEM image of a sample with three layers of InAs/InGaAs-QDs formed directly on GaAs and separated by GaAs spacers with a total thickness of 50 nm.

Previously, we demonstrated the possibility of using the structures with stacked InAs/InGaAs QD layers to fabricate laser diodes emitting in the 1.3 μm region [10]. Diodes with cleaved mirrors and a 100-μm-wide stripe have low threshold currents (90–105 A/cm^2) and high output power (2.7 W) at 1.26–1.28 μm. Below, we present results demonstrating the potential of the proposed technology for fabrication of vertical-cavity surface-emitting structures. The structures studied were grown in two stages. First, a bottom mirror based on an undoped AlAs/GaAs structure with layer thicknesses $\lambda/4n_i$ was grown by MBE [here, λ is the operating wavelength and n_i is the refractive index at this wavelength for AlAs ($i = 1$) or GaAs ($i = 2$)]. Then, a piece of semi-insulating GaAs substrate was placed onto the same holder and the second part of the structure was grown in the form of a GaAs layer with stacked InAs/InGaAs QD layers. The active region with QDs was sandwiched between short-period AlGaAs/GaAs superlattices. To avoid problems associated with possible AlAs oxidation, all the mirror structures were completed with a $\lambda/8n_2$ GaAs layer and coated with a ~0.1-μm layer of amorphous arsenic [14]. The design optical cavity length (the distance between the last quarter-wave AlAs layer and the structure surface) was $m\lambda_c/2n_2$, where m is an integer. Finally, the samples were removed from the growth chamber and spectra of reflectivity and PL were measured.

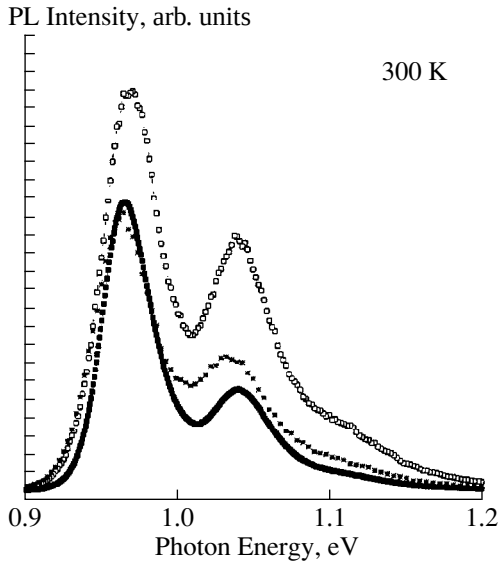

Fig. 4. PL spectra for three samples with a single layer (full squares) or three InAs/InGaAs-QD layers, with 18-nm (asterisks) or 30-nm (open squares) GaAs spacers.

Figure 5 shows the room temperature spectra of reflectivity and PL for a sample with a bottom Bragg reflector and also a PL spectrum for a sample without a reflector. The active region of the structure grown by the above-described technique contained three stacked InAs/InGaAs QD layers separated by GaAs spacers with a total thickness of 25 nm. The narrowing of the PL spectrum and a considerable (by an order of magnitude) increase in intensity is observed for the sample with the bottom mirror, confirming that the optical cavity has a substantial influence on the emission characteristics of the QD arrays [15, 16]. Depending on the specific features of the active region and on the optical cavity parameters, the PL spectra peaked in the region between 1.26 and 1.33 μm.

For EL studies, a structure was grown with a bottom Bragg mirror comprising 25 *n*-AlAs/*n*-GaAs pairs, an active region (cavity) of three stacked InAs/InGaAs QD layers, and an upper *p*-GaAs contact layer. The surface-emitting diode design with complete back-side metallization and upper annular contact was used. The nonrectifying contact to the *n*-type layers was fabricated by metallization with AuGa/Ni/Au, and the contact to *p*-type GaAs, with Cr/Au. The cylindrical current-flow region was confined by means of proton implantation. Figure 6 shows EL spectra of a surface-emitting diode with an active region 30 μm in diameter. The spectra were taken at room temperature in the pulsed mode for emission perpendicular to the sample surface. The current density was evaluated under the assumption of its uniform distribution over the device area. With increasing current density, the shape and the full width at half-maximum (FWHM) of the EL spectra change only slightly in comparison with the spontaneous emission spectra of the InAs/InGaAs QD laser structures [10, 13] and surface-emitting QD structures

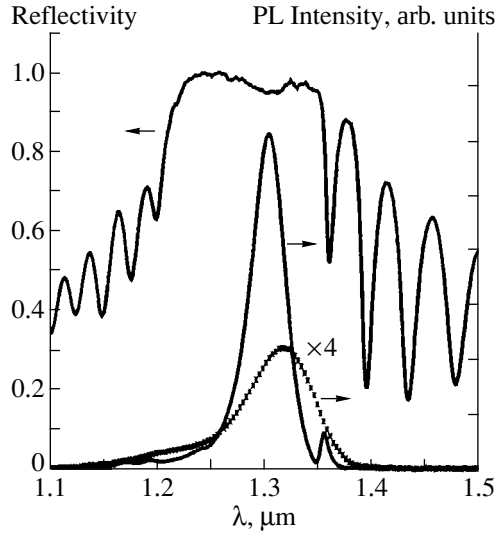

Fig. 5. Reflectivity and PL spectra for a structure with three InAs/InGaAs QD layers grown on the Bragg reflector (solid line), and the PL spectrum for a similar structure grown on the semi-insulating GaAs substrate (asterisks).

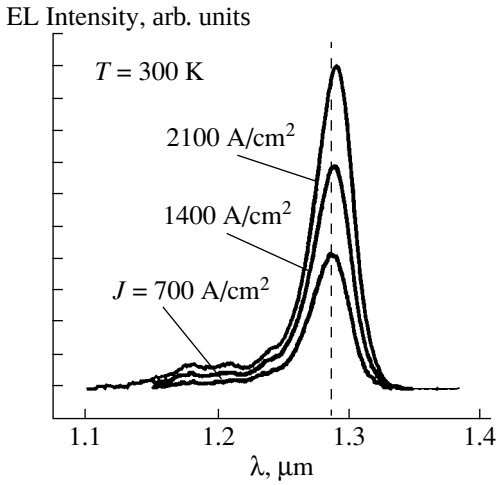

Fig. 6. EL spectra for a surface-emitting diode with an active region of three InAs/InGaAs-QD layers and a bottom Bragg reflector.

without optical cavity [17] characterized by increasing intensity of emission via excited states. This is due to the influence of the optical cavity. The relatively large FWHM of the EL spectra is caused by the use of a low-Q resonator, with the reflectivity of the upper mirror formed by the GaAs–air interface as low as about 30%.

In conclusion, a new technique is proposed in this work for fabrication of structures with stacked InAs/InGaAs QDs, providing small FWHM and high intensity of the PL line in the 1.3 μm spectral region. The obtained semiconductor heterostructures with vertical optical cavities and with an active region based on stacked arrays of InAs/InGaAs QDs show promise in fabrication of vertical structures that emit in the 1.3 μm region and are grown on the GaAs substrates.

ACKNOWLEDGMENTS

The work was supported by the RF Ministry of Science and Technology under the "Physics of Solid-State Nanostructures" Program (grant no. 99-2014), the Russian Foundation for Basic Research, NanoOp, and INTAS (grant no. 96-0467).

REFERENCES

1. G. P. Agrawal and N. K. Dutta, *Long Wavelength Semiconductor Lasers* (Van Nostrand Reinhold, New York, 1986).
2. K. Nakahara, M. Kondow, T. Kitatani, *et al.*, IEEE Photonics Technol. Lett. **10**, 487 (1998).
3. K. Nishi, T. Anan, and S. Sugou, in *Proceedings of IEEE/LEOS Summer Topical Meeting San Diego, USA, 1999*, IEEE Catalog Number 99 TH8455, 39.
4. D. Huffaker, G. Park, Z. Zou, *et al.*, Appl. Phys. Lett. **73**, 2564 (1998).
5. V. M. Ustinov, N. A. Maleev, A. E. Zhukov, *et al.*, Appl. Phys. Lett. **74**, 2815 (1999).
6. T.E. Sale, *Vertical Cavity Surface Emitting Lasers* (Wiley, New York, 1995).
7. F. Koyama, D. Schlenker, T. Miyamoto, *et al.*, Electron. Lett. **35**, 1079 (1999).
8. J. W. Matthews and A. E. Blakeslee, J. Cryst. Growth **27**, 118 (1974).
9. J. C. Campbell, D. L. Huffaker, H. Deng, *et al.*, Electron. Lett. **33**, 1337 (1997).
10. A. E. Zhukov, A. R. Kovsh, V. M. Ustinov, *et al.*, IEEE Photonics Technol. Lett. **11**, 1345 (1999).
11. A. E. Zhukov, A. R. Kovsh, and V. M. Ustinov, Fiz. Tekh. Poluprovodn. (St. Petersburg) **33**, 1395 (1999) [Semicond. **33**, 1260 (1999)].
12. D. Bimberg, N. Kirstaeder, N. N. Ledentsov, *et al.*, J. Sel. Top. Quantum Electron. **3**, 196 (1997).
13. N. A. Maleev, A. E. Zhukov, A. R. Kovsh, *et al.*, in *Proceedings of X European Workshop on MBE, Les Arcs, France, 1999* (Nanostructures, p. 2).
14. N. A. Maleev, A. E. Zhukov, A. R. Kovsh, *et al.*, Fiz. Tekh. Poluprovodn. (St. Petersburg) **33**, 629 (1999) [Semicond. **33**, 586 (1999)].
15. N. N. Ledentsov, D. Bimberg, V. M. Ustinov, *et al.*, Semicond. Sci. Technol. **14**, 99 (1999).
16. L. A. Graham, D. L. Huffaker, and D. G. Deppe, Appl. Phys. Lett. **74**, 2408 (1999).
17. D. L. Huffaker and D. G. Deppe, Appl. Phys. Lett. **73**, 520 (1998).

Translated by D. Mashovets

Semiconductors, Vol. 34, No. 5, 2000, pp. 598–602. Translated from Fizika i Tekhnika Poluprovodnikov, Vol. 34, No. 5, 2000, pp. 617–621.

AMORPHOUS, VITREOUS, AND POROUS SEMICONDUCTORS

Current–Voltage Characteristics of Electroluminescent Me/(*a*-Si:H):Er/*c*-Si Structures Prepared by Magnetron Sputtering

P. A. Ivanov, O. I. Kon'kov, and E. I. Terukov

Ioffe Physicotechnical Institute, Russian Academy of Sciences, Politekhnicheskaya ul. 26, St. Petersburg, 194021 Russia

Submitted October 29, 1999; accepted for publication November 2, 1999

Abstract—Current–voltage characteristics of electroluminescent structures composed of metal, erbium-doped amorphous silicon, and crystalline silicon and prepared by magnetron sputtering were measured and analyzed. It is shown that the carrier transport in a high-resistivity (*a*-Si:H):Er film (resistivity ~10^9 Ω cm) proceeds by the mechanism of unipolar-injection space-charge-limited currents controlled by two types of traps. Trap parameters, namely, the densities and ionization energies of acceptor and donor centers (~10^{19} cm^{-3} for both types of traps; 0.85–0.95 eV and 0.4 eV, respectively) are estimated by analyzing the current–voltage characteristics. In the light of the results obtained, the published excitation mechanism of erbium-related electroluminescence in such a material is discussed. © *2000 MAIK "Nauka/Interperiodica".*

1. INTRODUCTION

The encouraging results obtained in studying erbium-doped crystalline silicon as a material for 1.54 μm light-emitting diodes stimulated recent investigations of erbium-doped amorphous hydrogenated silicon (*a*-Si:H):Er). In particular, the efficient photoluminescence from Er ions has been observed in this material [1], and, recently, room-temperature electroluminescence (EL) was also observed in Me/(*a*-Si:H):Er/*c*-Si structures prepared by magnetron sputtering [2]. According to [3], the EL excitation mechanism in these structures is associated with the Auger process, with electrons from the *a*-Si conduction band captured by dangling bonds of silicon with energy transferred to the *f*-shell of erbium ions. It is supposed that the field-stimulated multiphonon tunneling emission of electrons trapped by the dangling bonds is the process responsible for steady-state EL. These processes describe fairly well the current and temperature dependences of the erbium EL in Me/(*a*-Si:H):Er/*c*-Si structures [3].

The mechanisms of charge-carrier transport in (*a*-Si:H):Er films and the influence of the Me/(*a*-Si:H):Er contacts and (*a*-Si:H):Er/*c*-Si heterocontacts on the current flow have not been adequately investigated. In this work, we present and analyze, for the first time, experimental *I–V* characteristics of Al/(*a*-Si:H):Er/*c*-Si structures obtained by magnetron sputtering in a wide range of current densities from 10^{-7} to 1 A/cm^2. The main goal of the study was to clarify the electron transport mechanisms in the (*a*-Si:H):Er films.

2. EXPERIMENTAL PROCEDURE

Figure 1 shows schematically a structure under study. An (*a*-Si:H):Er layer about 1 μm thick was deposited onto an *n*-type *c*-Si substrate by magnetron-assisted silane decomposition (MASD) [4]. Erbium was introduced in the course of decomposition from a metallic source. Thermally evaporated aluminum was used to fabricate metal contacts to (*a*-Si:H):Er and *c*-Si (deposition onto the (*a*-Si:H):Er film was carried out using a mask 1 mm in diameter).

The dc current–voltage characteristics (*I–V* curves) were measured in the dark. The polarity of the applied voltage corresponded to that exciting the erbium-related EL in these structures, with the metallic contact to the (*a*-Si:H):Er film being negative. The *I–V* curves presented below were taken by measuring the stationary current for given voltages across the structure.

3. EXPERIMENTAL RESULTS AND ANALYSIS

Figure 2 shows an *I–V* curve of an EL structure at room temperature. As can be seen, in the log–log scale, the *I–V* curve comprises several clearly defined straight portions with different slopes, which can be approximated by the power-law dependences of current *I* on voltage *V*. In portion I, the *I–V* curve is ohmic, i.e., $I \propto V$. In portion II, the slope of the curve increases, so that $I \propto V^4$. Further on comes the relatively gently sloping and short (in the log scale) portion III characterized by a quadratic dependence, $I \propto V^2$. Finally, the *I–V* curve becomes steeper again in portion IV.

1063-7826/00/3405-0598$20.00

I–V curves of this kind are typical of the space-charge-limited currents (SCLC) in insulators with traps for carriers [5]. The specific features of the *I–V* curves for the Me/(*a*-Si:H):Er/*c*-Si structure studied suggest that (*a*-Si:H):Er is a high-resistivity *n*-type material with two groups of trap centers located in the upper half of the forbidden band. A scheme of energy levels in the gap of amorphous silicon at thermodynamic equilibrium is shown in Fig. 3. It is assumed that the Fermi level lies between the levels E_{t1} and E_{t2}, so that the lower level is nearly filled with electrons and the upper level is nearly empty. In terms of the SCLC model, the specific features of the obtained *I–V* curves for Me/(*a*-Si:H):Er/*c*-Si can be qualitatively interpreted as follows.

At equilibrium, a certain number of conduction electrons are present in the (*a*-Si:H):Er film, their density being determined by the Fermi level position in the gap. In its turn, the Fermi level position is determined by the concentrations and ionization energies of the E_{t1} and E_{t2} centers.

If a small voltage is applied to the structure, the electrons injected into amorphous silicon from the nonrectifying Al contact are captured by the E_{t2} traps. The film conductivity remains purely ohmic owing to the presence of equilibrium electrons (portion I in the *I–V* curve). With increasing voltage, the occupancy of the E_{t2} centers increases (the quasi-Fermi level for electrons moves progressively away from the E_{t2} level and approaches the conduction band), and the concentration of the injected free electrons in the conduction band increases as well. When the latter exceeds the concentration of equilibrium electrons, the current starts to grow abruptly with increasing applied voltage (portion II named in terms of the SCLC theory the "completely filled traps" (CFT) portion). The current rises by the $I \propto V^4$ law until it starts to be limited by carrier capture by the E_{t1} centers (as the quasi-Fermi level for electrons approaches the E_{t1} level). Further on, the *I–V* curve must follow the square law as long as the quasi-Fermi level remains below the E_{t1} level (portion III, "trap-controlled square law," TCSL). Finally, we ascribe the increase in the *I–V* curve slope for voltages higher than 10 V (with electric field strength in the film exceeding 10^5 V/cm) to the thermally assisted field emission of electrons from the trap levels.

Some additional evidence supporting the scheme of levels proposed for the SCLC interpretation were obtained by studying the *I–V* curves at temperatures above room temperature. Raising the temperature must lead to the following variations of the *I–V* curves. First, the resistivity of the amorphous film is bound to decrease with increasing temperature. Second, the voltage corresponding to the kink in the *I–V* curve between the ohmic and CFT sections must become higher owing to the shift of the Fermi level toward the gap center with increasing temperature. Third, the CFT law $I \propto V^4$ must evidently remain unchanged. Fourth, the thermally assisted field emission must be activated, so that the preceding TCSL portion may become less pronounced. Figure 4 shows the *I–V* curves taken between room temperature and 120°C. It can be seen that all the expected variations of the *I–V* curves are experimentally verified.

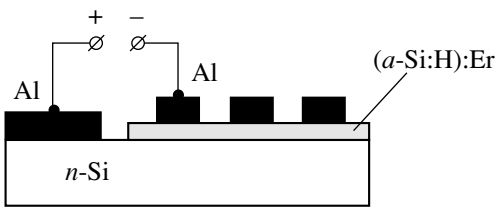

Fig. 1. Schematic of the Al/(*a*-Si:H):Er/*c*-Si structures studied.

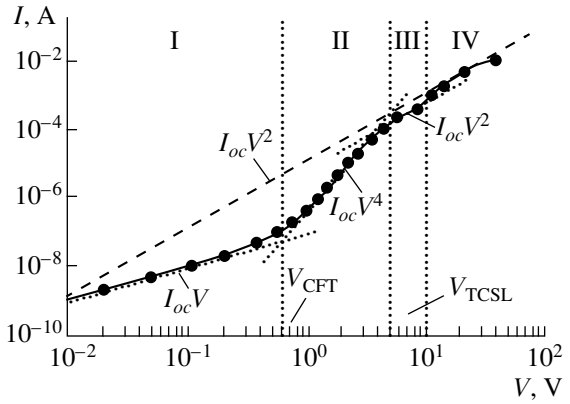

Fig. 2. Typical room-temperature *I–V* curve for Al/(*a*-Si:H):Er/*c*-Si structures exhibiting erbium-related EL. Portions of the curve: I, ohmic; II, completely filled traps (CFT); III, trap-controlled square law (TCSL); and IV, thermally stimulated field emission from trap levels.

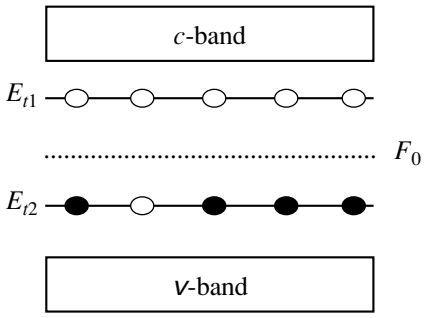

Fig. 3. Scheme of energy levels in the forbidden band of amorphous silicon (at thermodynamic equilibrium) used in the space-charge-limited current model. F_0 is the Fermi level.

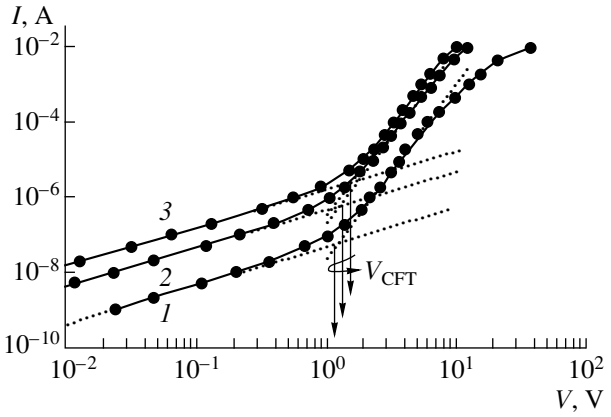

Fig. 4. *I–V* curves taken for an Al/(*a*-Si:H):Er/*c*-Si structure at temperatures of (*1*) 293, (*2*) 343, and (*3*) 393 K.

Now, based on the SCLC theory [5], we perform a semi-quantitative analysis of the *I–V* curves to evaluate some parameters of amorphous silicon and the electron traps.

3.1. Resistivity, Concentration, and Mobility of Equilibrium Carriers in (a-Si:H):Er

The film resistivity calculated from the ohmic portion of the *I–V* curve at room temperature is $\rho = 8 \times 10^8\ \Omega$ cm.

According to the SCLC theory, the electron mobility in an ideal insulator (without traps and free carriers) can be determined from the "trap-free square law" (TFSL) describing the *I–V* curve of an ideal insulator

$$J \approx \varepsilon\mu\frac{V^2}{L^3}, \tag{1}$$

where ε is the static dielectric constant of the insulator, μ is the electron mobility, and L is the insulator film thickness [note that the carrier concentration does not appear in relation (1)]. The same law represents the limiting *I–V* curve for a nonperfect insulator at a rather high applied voltage, when the number of injected electrons significantly exceeds the number of initially empty electron traps. Thus, in our case, the lower limit to the electron mobility can be evaluated by plotting a $I \propto V^2$ line tangent to the experimental *I–V* curve at the maximal currents through the structure (see Fig. 2). Assuming for evaluation that $\varepsilon = 8.85 \times 10^{-14}$ F/cm and $L = 10^{-4}$ cm, we obtain $\mu > 0.02$ cm^2/(V s). Note that the most straightforward method for determining the mobility in high-resistivity materials is the pulsed measurement of transient SCLC. However, in the case in question, the use of this method is somewhat complicated by the small film thickness and, consequently, the short time of electron transit through the sample from the cathode to the anode. As the upper limit to the mobility in amorphous silicon, we can take a value on the order of 1 cm^2/(V s). Thus, the electron mobility in the films studied is within 0.02–1 cm^2/(V s). Using these parameters, we evaluate the equilibrium concentration of free electrons (n_0) from the relation $\rho = (qn_0\mu)^{-1}$, where q is the elementary charge. At room temperature, we have $n_0 = 10^{10}$–4×10^{11} cm^{-3}.

3.2 Fermi Level Position in the Forbidden Band of Amorphous Silicon under Equilibrium Conditions

With the free electron concentration in the conduction band known, the position of the Fermi level in the gap ($E_C - F_0$) can be determined from

$$n_0 = N_C\exp\left(-\frac{E_C - F_0}{kT}\right), \tag{2}$$

where N_C is the effective density of states in the conduction band and kT is the thermal energy. Assuming for evaluation that $N_C = 5 \times 10^{20}$ cm^{-3}, we obtain $E_C - F_0 = 0.54$–0.64 eV.

3.3. Ionization Energies and Concentrations of Traps

According to the SCLC theory, the voltage V_{CFT} at which the portion of completely filled traps with energy E_{t2} begins is related to the concentration of initially empty traps (p_{t02}) by

$$V_{CFT} = \frac{qp_{t02}L^2}{\varepsilon}. \tag{3}$$

For $V_{CFT} = 0.6$ V (see Fig. 2), we have $p_{t02} = 3 \times 10^{13}$ cm^{-3}. Note that in the films under study $p_{t02} \gg n_0$.

Based on previous investigations of (*a*-Si:H):Er, it is reasonable to suppose that the E_{t2} traps are deep acceptors, e.g., dangling silicon bonds or *D*-centers [3]. It is generally assumed that the *D*-center concentration (N_{t2}) in amorphous hydrogenated silicon is on the order of 10^{19} cm^{-3}. Thus, as follows from the p_{t02} calculation, the equilibrium occupancy of *D*-centers is nearly unity (the Fermi level lies above the *D*-center level). With known N_{t2} and F_0 values, the energy position of the E_{t2} level can be determined from

$$p_{t02} = \frac{N_{t2}}{1 + g_A\exp\left(\dfrac{F_0 - E_{t2}}{kT}\right)} \approx \frac{N_{t2}}{g_A}\exp\left(\frac{E_{t2} - F_0}{kT}\right), \tag{4}$$

where g_A is the spin degeneracy of the E_{t2} level. Assuming that $N_{t2} = 10^{19}$ cm^{-3} and $g_A = 2$, we obtain $E_C - E_{t2} = 0.85$–0.95 eV.

Further, the energy position of the E_{t1} level can be determined assuming that, at the point where TCSL

sets in, the quasi-Fermi level for electrons (F_{CFT}) coincides with the E_{t1} level to within kT, i.e.,

$$E_C - E_{t1} \approx E_C - F_{CFT} = kT \ln \frac{N_C}{n_{CFT}}, \quad (5)$$

where n_{CFT} is the concentration of free electrons injected into the film at the voltage of TCSL onset (V_{CFT}). This voltage is related to the n_{CFT} by an expression similar to (3):

$$V_{CFT} = \frac{q n_{CFT} L^2}{\varepsilon}. \quad (6)$$

For V_{CFT} = 4 V (see Fig. 2), we obtain $n_{CFT} = 2 \times 10^{14}$ cm^{-3} and $E_C - E_{t1}$ = 0.38 eV. The concentration of the E_{t1} centers, N_{t1}, can be determined from the equation of bulk electroneutrality for the equilibrium conditions (there is good reason to believe that the E_{t1} traps are donors of the type of erbium–oxygen complexes [6]). If both donor (E_{t1}) and acceptor (E_{t2}) states are present, the electroneutrality equation can be written as

$$n_0 + N_{t2}^- = N_{t1}^+, \quad (7)$$

where N_{t2}^- and N_{t1}^+ are the concentrations of ionized acceptors and donors, respectively. Note that in our case $N_{t2}^- \approx N_{t2}$ and $n_0 \ll N_{t2}$, so that relation (7) can be rewritten as

$$N_{t2} = \frac{N_{t1}}{1 + g_D \exp\left(\frac{F_0 - E_{t1}}{kT}\right)}, \quad (8)$$

wherefrom the donor concentration (N_{t1}) can be calculated directly, since the values of F_0, N_{t2}, and E_{t1} are already determined. Since $E_{t1} - F_0 \gg kT$, we obtain $N_{t1} - N_{t2} \approx 10^{19}$ cm^{-3}. This result stems from the fact that the position of F_0 is between the donor and acceptor levels, so that we have nearly complete mutual compensation of the donors and acceptors, with the free electron concentration in the conduction band negligible as compared to the concentration of the traps.

4. DISCUSSION

According to the model from [3] the main process responsible for light emission in the (*a*-Si:H):Er film is the capture of an electron from the conduction band to an empty *D*-center level. In this model, the radiative recombination rate must be proportional to the product np_{t2}, where n is the electron concentration in the conduction band and p_{t2} is the concentration of empty *D*-centers (traps with energy E_{t2}). However, when the current flow is governed by the SCLC mechanism, injected free electrons *accumulate* in the (*a*-Si:H):Er film just as the D-centers *are filled*; that is, an increase in the electron concentration n is accompanied by the corresponding decrease in p_{t2}. Thus, rather conflicting conditions are to be fulfilled to obtain an efficient luminescence. In this situation, the important role of thermally assisted field emission becomes apparent: it makes the *D*-centers free for the further capture of carriers.

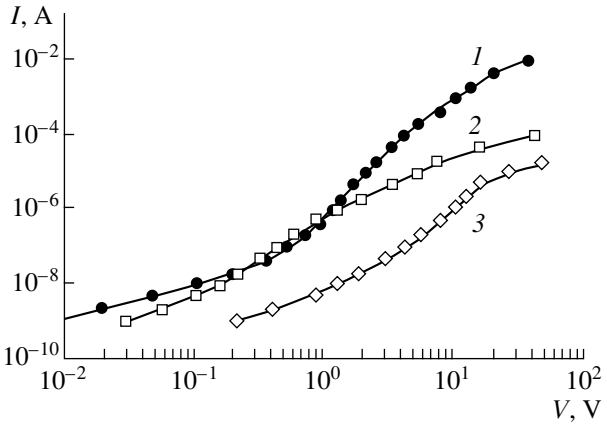

Fig. 5. Room-temperature *I–V* curves for (*1*) emitting and (*2*, *3*) nonemitting Al/(*a*-Si:H):Er/*c*-Si structures.

In the framework of this model, it may be assumed that the EL efficiency can be improved by (i) adjusting the *D*-center concentration; (ii) adjusting the Fermi level position in amorphous silicon (by appropriate doping), so that the *D*-centers are filled with electrons even under equilibrium conditions; (iii) making the film thinner, which must lower the onset voltage of the field emission of electrons; and (iv) adjusting the trap distribution across the film thickness, since, generally speaking, the electric field is rather nonuniformly distributed across the film under the SCLC conditions.

To somewhat clarify the problem of the poorly reproducible properties of the Me/(*a*-Si:H):Er/*c*-Si structures, it seemed of interest to compare the *I–V* curves of luminescent and nonluminescent structures. Figure 5 shows the corresponding *I–V* curves for several samples. As can be seen, the *I–V* curves for nonluminescent structures differ from those for luminescent ones mainly in low currents up to fields on the order of 10^5 V/cm. This means that, up to high fields, carriers injected into the film are mostly captured by the traps, with the free electron concentration evidently remaining low. An additional argument in favor of this statement is that nonluminescent films apparently have higher resistivity, with the Fermi level lying deeper in the forbidden band and the initial occupancy of the *D*-centers being lower than that in the emitting films.

5. CONCLUSION

The results obtained in this work suggest that the electroluminescent (*a*-Si:H):Er films prepared by magnetron sputtering are composed of high-resistivity *n*-type material in which the carrier (electron) transport

occurs by the mechanism of space charge limited monopolar injection currents controlled by two types of traps (donor complexes and acceptor states which constitute silicon dangling bonds). To improve the EL efficiency of this material, optimization of the structural parameters is necessary, including the carrier mobility, concentrations of donor dopants and dangling bonds, film thickness, and distribution of impurities and dangling bonds across the films.

6. ACKNOWLEDGMENTS

The authors are especially grateful to M.S. Bresler, O.B. Gusev, K.D. Tsendin, and other colleagues from the Ioffe Physicotechnical Institute, Russian Academy of Sciences, for their helpful participation in discussions. This work was supported by COPERNICUS (grant no. 977048-SIER).

REFERENCES

1. M. S. Bresler, O. B. Gusev, V. Kh. Kudoyarova, *et al.*, Appl. Phys. Lett. **67**, 3599 (1995).
2. M. S. Bresler, O. B. Gusev, B.P. Zakharchenya, *et al.*, Fiz. Tverd. Tela **38**, 1189 (1996) [Phys. Solid State **38**, 658 (1996)]; O. B. Gusev, A. N. Kuznetsov, E. I. Terukov, *et al.*, Appl. Phys. Lett. **70**, 240 (1997).
3. O. B. Gusev, M. S. Bresler, B. P. Zakharchenya, *et al.*, Fiz. Tverd. Tela **41**, 210 (1999) [Phys. Solid State **41**, 185 (1999)].
4. V. Marakhonov, N. Rogachev, J. Ishkalov, *et al.*, J. Non-Cryst. Solids **137–138**, 817 (1991).
5. M. A. Lampert and P. Mark, *Current Injection in Solids* (Academic, New York, 1970; Mir, Moscow, 1973).
6. V. F. Masterov, F. S. Nasredinov, P. P. Seregin, *et al.*, Pis'ma Zh. Tekh. Fiz. **22**, 25 (1996) [Tech. Phys. Lett. **22**, 960 (1996)].

Translated by D. Mashovets

Semiconductors, Vol. 34, No. 5, 2000, pp. 603–605. Translated from Fizika i Tekhnika Poluprovodnikov, Vol. 34, No. 5, 2000, pp. 622–624.

AMORPHOUS, VITREOUS, AND POROUS SEMICONDUCTORS

Charge-Carrier Transport in a Double-Collector Magnetotransistor

M. A. Glauberman, V. V. Kozel, and A. V. Nakhabin

Educational–Research and Production Center, Mechnikov State University, Odessa, 270063 Ukraine

Submitted October 27, 1999; accepted for publication November 25, 1999

Abstract—The numerical analysis of the charge-carrier transport in lateral double-collector magnetotransistors is presented. The final concentration distribution of the carriers injected in the base of the magnetotransistor under the influence of the magnetic field as well as the emitter-size dependence of the device sensitivity were calculated. © *2000 MAIK "Nauka/Interperiodica".*

Double-collector magnetotransistors stand out among semiconductor magnetosensitive structures because of their high magnetosensitivity in normal conditions (≈100 μA/T and more). This substantially extends the functional capabilities of galvanomagnetic transducers.

This work is devoted to the numerical analysis of the magnetosensitivity of lateral planar magnetotransistors, namely, the investigation of the distribution of injected minority charge carriers for the structure of the double-collector magnetotransistor, whose schematic diagram is shown in Fig. 1. Until now, this problem was solved using the Green function method [1]. However, this method of solving is imprecise because of a number of flaws. In this method, a finite series is substituted for the double sums of the infinite series, while their convergence is far from being rapid, and the use of an arbitrarily shaped emitter complicates the calculations. In addition, the mechanisms of magnetosensitivity of a double-collector magnetotransistor were related only to the deviation of trajectories of the injected carriers under the influence of Lorentz forces and the Hall field. However, the effect of the spatial modulation of the emitter injection under the influence of the Hall field [2] was not taken into account, although we deal with the extended emitter. It is clear from the aforesaid that a numerical simulation should be used for an adequate consideration of the major physical factors that are characteristic of a double-collector magnetotransistor. Additionally, corresponding boundary conditions should be taken into account as well as the necessity to improve the structure of the transistor.

The equation that describes the distribution of injected charge carriers in the presence of a transverse magnetic field is written as [1]

$$B\left(\frac{\partial^2 p}{\partial x^2}+\frac{\partial^2 p}{\partial y^2}\right)-A\frac{\partial p}{\partial x}+M\frac{\partial p}{\partial y}-p=-\rho(x,y)\delta_{xx'}\delta_{yy'}, \quad (1)$$

$$\rho=\rho_0\exp\left(\frac{qU_{e0}}{kT}\right), \quad (2)$$

where U_{e0} is the emitter voltage, p is the hole concentration, and the coefficients B, A, and M are given by

$$B=\frac{kT}{q}\mu_p\tau_p, \quad A=\frac{\mu_p J_n}{\mu_n q n_0}\tau_p,$$

$$M=\frac{3\pi}{8}\frac{\mu_p J_n}{\mu_n q n_0}(\mu_n B_z+\mu_p B_z)\tau_p.$$

Here, n_0 and p_0 are the thermal-equilibrium concentrations of electrons and holes, J_n is the electric-current density of the majority carriers in the base, and μ_n, τ_n, μ_p, and τ_p are the mobility and lifetime for electrons and holes, respectively. The $\rho(x, y)$ quantity is considered to mean the emitter capability. It follows from [2] that the

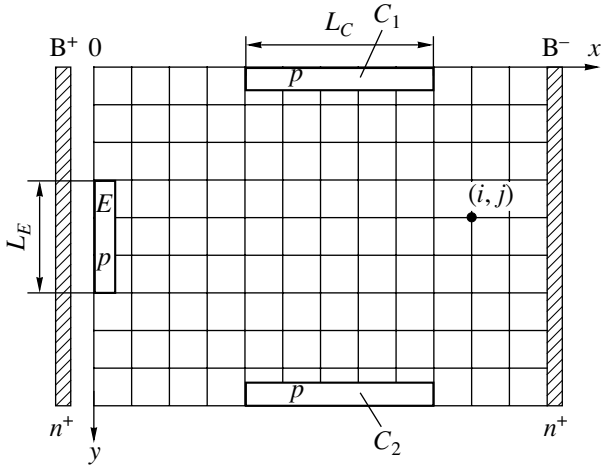

Fig. 1. Schematic diagram for simulation of the planar double-collector magnetotransistor. E is the emitter, C_1 and C_2 are the collectors, and B^+ and B^- are the base regions.

1063-7826/00/3405-0603$20.00

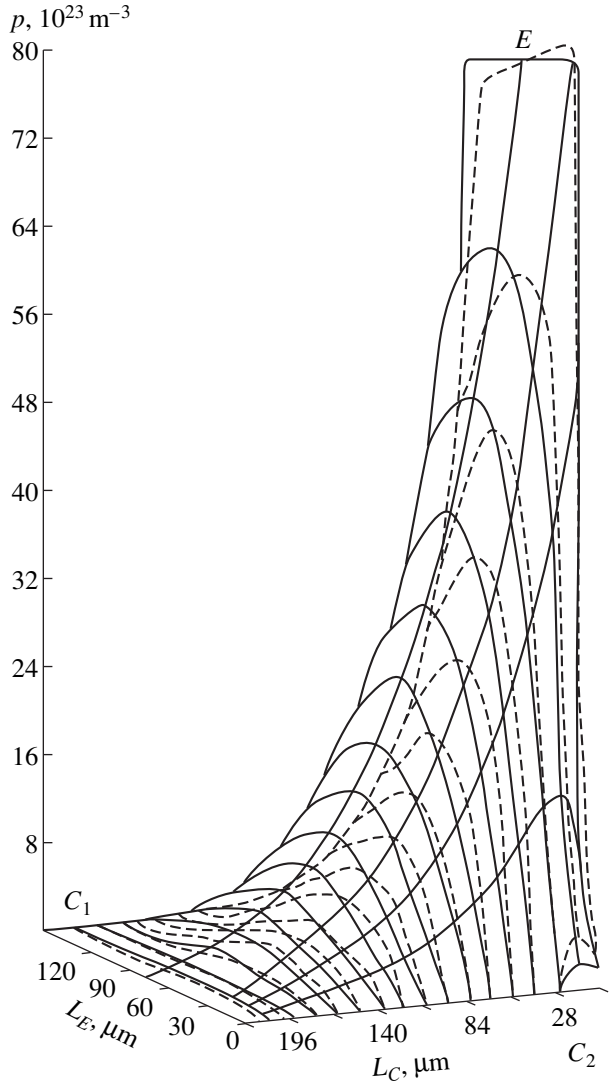

Fig. 2. Concentration distribution of the injected carriers in the base of a double-collector magnetotransistor in the absence of a magnetic field (solid lines) and under the influence of the magnetic field of 0.6 T (dashed lines). L_C = 224 μm, and L_E = 87 μm.

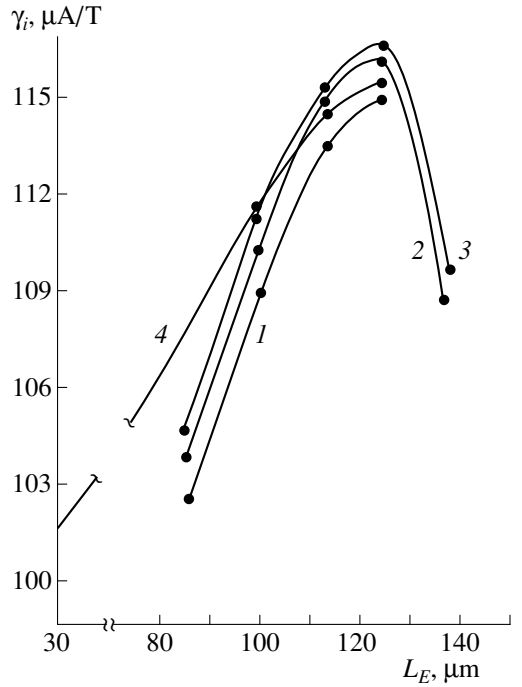

Fig. 3. Dependences of the current magnetosensitivity of a double-collector magnetotransistor γ_i on the emitter length L_E at the collector length L_C (*1*) 147, (*2*) 182, (*3*) 223, and (*4*) 180 μm. Curves (*1*)–(*3*) correspond to calculations, and curve (*4*) is experimental.

presence of the Hall field E_H, which appeared because of the current flow of the majority carriers between the bases B^+ and B^-, induces the potential distribution $\varphi_H = |\mathbf{E}_H \times \mathbf{y}|$ in the base. For this reason, the spatial modulation of injection along the emitter appears, and the quantity ρ becomes redistributed along the *y* axis according to the law

$$\rho = \rho_0 \exp\left[\frac{q}{kT}(U_{e0} + |\mathbf{E}_H \times \mathbf{y}|)\right]. \quad (3)$$

Equation (1) is a linear elliptic differential equation of the second order with two independent variables. In order to solve it numerically, we used the finite difference method [3]. Let us partition the base by the rectangular mesh with the step STX = 3 μm along the 0*x* axis and STY = 7 μm along the 0*y* axis (Fig. 1). The procedure for solving equation (1) comprises the substitution of the set of difference equations for the differential equation. The concentration of the carriers injected into the base is determined for each mesh point. In practice, the problem was solved with introducing the accelerating Liebmann multiplier using the method of alternating directions [3]. Boundary conditions are chosen on the assumption that condition (3) is fulfilled for the emitter, and no carrier flow through the surfaces and boundaries of the structure under investigation is observed. The uniform current of the majority carriers flows between the bases B^+ and B^-, and its density $J_n = 6 \times 10^3$ A/m^2. The base size is 150 × 350 μm. The sizes of the emitter and collectors varied within the mentioned limits. The self-consistent difference iterative process terminated at the maximum discrepancy between two successive iterations for a single mesh point was less that 0.01%. The result of the numerical solution is shown in Fig. 2. As can be seen, the shift of the concentration peak towards one of the collectors as well as a more abrupt fall in the concentration along the base is observed on switching the magnetic field. The reason for this is that the injected charge carriers passed a longer path before arrival at the collector in the absence of the magnetic field. The diffusion length of

these carriers decreases under the influence of the magnetic field, i.e., most of the injected carriers deviate and arrive at the collector from the base region closest to the emitter. These carriers take no part in the subsequent redistribution, and there is no necessity to fabricate excessively extended collectors. As for the choice of the optimum collector size, this problem is considered in detail in [4]. Here, we restrict ourselves to the data on the dependence of the magnetosensitivity γ_i on the emitter length for given distances between the collectors and bases (Fig. 3); these data were obtained from the numerical simulation. The spatial modulation of injection along the emitter affects the magnetosensitivity. On the one hand, an increase in the emitter length enhances the difference signal taken from the collectors. On the other hand, as the emitter edges become closer to the collectors, the contribution from the redistribution of the carriers in the bulk of the base under the influence of the magnetic field decreases. The influence of the mentioned factors as well as the carrier recombination in the base of the double-collector magnetotransistor defines the optimum collector size. As can be seen in Fig. 3, the magnetosensitivity behavior experiences no variations, and the optimum magnetosensitivity corresponds to the structure with the emitter length, which is equal to approximately 4/5 of the distance between collectors. The influence of the collector lengths is insignificant. The experimental dependence of γ_i on the emitter length is also shown in Fig. 3. The experimental and calculated dependences coincide for the emitter current I_E = 0.6 mA, the base current I_{BB} = 3 mA, and a magnetic field of 0.3 T. Thus, the considered method of simulation constitutes an efficient tool for selection of the optimum topology (for example, from magnetosensitivity) of the double-collector magnetotransistors.

REFERENCES

1. I. M. Vikulin, M. A. Glauberman, and N. A. Kanishcheva, Fiz. Tekh. Poluprovodn. (Leningrad) **11**, 645 (1977) [Sov. Phys. Semicond. **11**, 377 (1977)].
2. A. W. Vinal and N. A. Masnari, Tech. Dig. Int. Electron Devices Meet. **12**, 308 (1982).
3. D. D. McCracken and W. S. Dorn, *Numerical Methods and FORTRAN Programming* (Wiley, New York, 1964; Mir, Moscow, 1977, 2nd ed.).
4. I. M. Vikulin, M. A. Glauberman, N. A. Kanishcheva, *et al.*, Fiz. Tekh. Poluprovodn. (Leningrad) **15**, 399 (1981) [Sov. Phys. Semicond. **15**, 229 (1981)].

Translated by N. Korovin

Semiconductors, Vol. 34, No. 5, 2000, pp. 606–608. Translated from Fizika i Tekhnika Poluprovodnikov, Vol. 34, No. 5, 2000, pp. 625–627.

PHYSICS OF SEMICONDUCTOR DEVICES

A Method for Modulation of the Charge-Carrier Mobility in a Semiconductor

V. V. Novikov, R. R. Vardanyan, and É. E. Pakhomov

ZAO Avangard-Élektronika, St. Petersburg, 195271 Russia

Submitted September 2, 1999; accepted for publication November 23, 1999

Abstract—A new method for modulating the mobility of the majority and minority charge carriers in silicon was studied. It is shown that, under the effect of local avalanche breakdown of a *p–n* junction, the charge-carrier mobility in the bulk of the semiconductor increases or decreases, depending on the orientation of the *p–n* junction subjected to breakdown in relation to the direction of motion of the charge carriers. © *2000 MAIK "Nauka/Interperiodica".*

The modulation of the electrical conductivity of silicon under the effect of local avalanche breakdown was studied in [1]. The structure considered in [1] consisted of a *p–n* junction operating in the avalanche-breakdown mode and a resistor located at a distance well away from the breakdown region (20–100 μm). It was shown that the conductance of the resistor increased by a factor of 1.5 when the breakdown of the *p–n* junction was initiated by a current of up to 5 mA. In [1], such a modulation of electrical conductivity was accounted for by the acoustic transport of the majority charge carriers generated by the avalanche breakdown into the resistor region.

In this work, we will study the modulation of mobility of the majority and minority charge carriers in the bulk of a semiconductor under the effect of local avalanche breakdown of the *p–n* junction. We consider a silicon structure consisting of a central *p–n* junction *1* and an annular field-effect transistor (FET) with an *n*-channel that encloses the *p–n* junction (Fig. 1). We studied the influence of avalanche breakdown of junction *1* on the mobility of majority charge carriers in the channel of the FET and also on the channel resistance. The mobility of majority charge carriers was determined from the measurements of the magnetoresistance. A magnetic field was directed perpendicularly to the sample surface. The channel resistance was measured both in the absence and in the presence of the magnetic field. The structure studied had a configuration similar to that of the Corbino disk, which precluded the generation of the Hall emf.

The obtained dependences of the electron mobility and the ohmic resistance of the FET channel on the breakdown current for one of the samples are shown in Fig. 2. It is noteworthy that the electron flow is directed from the source *S* to the drain *D* (Fig. 1) in accordance with the polarity of the current source included in the measurement circuit involving the load resistance R_l. It follows from Fig. 2 that, as the current initiating the breakdown of *p–n* junction *1* increases, the electron mobility increases and the FET channel resistance decreases. This can be explained in the following way. In the case of avalanche breakdown of the *p–n* junction, acoustic phonons are generated and propagate through the crystal. In the course of the motion of acoustic phonons, they drag electrons and, thus, increase their velocity and, consequently, their mobility (the direction of motion of phonons coincides with that of electrons). This fact also explains a decrease in the FET channel resistance. It is worth noting that, in the case of avalanche breakdown, optical phonons are also generated in addition to the generation of acoustic phonons. The absorption of photons in the bulk of the semiconductor and the generation of nonequilibrium charge carriers in turn contribute to a decrease in the channel resistance.

The results of measurements of the electron mobility and the FET channel resistance on the current initiating the breakdown of *p–n* junction *1* for reverse direction of the electron flow (from the drain to the source) are shown in Fig. 3. It can be seen that, as the breakdown current increases, the electron mobility decreases, and the channel resistance initially decreases and then begins to increase. A decrease in mobility is caused by the deceleration of electrons by acoustic phonons that propagate in the direction opposite to that of electron motion. A decrease in the channel resistance at the initial stage may be accounted for by the absorption of photons and by the generation of nonequilibrium charge carriers in the bulk of the semiconductor. Later on, as the breakdown-initiating current increases, an increase in the channel resistance sets in owing to the fact that a decrease in mobility now becomes most important. We note that we did not observe any significant influence of the bias voltage applied to the gate *G* (Fig. 1) on the mobility modulation in the structures studied.

We now consider the influence of the local avalanche breakdown of the *p–n* junction on the mobility

1063-7826/00/3405-0606$20.00 © 2000 MAIK "Nauka/Interperiodica"

of charge carriers in the bulk of the semiconductor. As is known, the generation of photons in the course of the avalanche breakdown of *p–n* junction *1* (Fig. 1) and their absorption in the bulk of the semiconductor leads to the generation of minority charge carriers that are separated by *p–n* junction *2*; i.e., the so-called avalanche-generation current is observed [2]. We first consider the influence of acoustic phonons on the avalanche-generation current of *p–n* junction *2*. To this end, we represent the structure under consideration in a simplified one-dimensional form in the case where this structure is subjected to a magnetic field *B* (Fig. 4). Under the effect of a magnetic field whose induction vector is perpendicular to the direction of flow of the minority charge carriers, the trajectory of the flow becomes bended, the effective diffusion length decreases, and, consequently, the avalanche-generation current also decreases [3]. We assume that the photons generated as a result of the breakdown of *p–n* junction *1* are completely absorbed in the *n*-layer. The continuity equation for holes, with allowance made for the effect of the magnetic field, may be written as [3]

$$\frac{d^2\Delta P}{dx^2} - \frac{\Delta P}{D^B\tau_p} = -\frac{GK}{D^B}e^{-i\alpha}, \qquad (1)$$

where *G* in the intensity of photon emission, i.e., the number of quanta of light penetrating through the unit surface area into the *n*-region from the space-charge region of *p–n* junction *1* per unit time, and *K* is the absorption coefficient for light.

In expression (1), the diffusion coefficient D^B is given by

$$D^B = \frac{D}{1 + (\mu_p^* B)^2},$$

where μ_p^* is the hole mobility and *B* is the magnetic field induction.

Solving equation (1) supplemented with the boundary conditions

$$\Delta P|_{x=0} = 0, \quad \Delta P|_{x=w} = 0$$

and substituting the solution to the expression for the hole-current density

$$J_p^B = -qD^B(\Delta P/dx),$$

we obtain the following expression in the case of $Kw > 1$ and $K^2L^2 > 1$:

$$J_p^B = \frac{qG}{KL_p^B \sinh(w/L_p^B)}. \qquad (2)$$

Here,

$$L_p^B = \frac{L_p}{[1 + (\mu_p^* B)^2]^{1/2}}. \qquad (3)$$

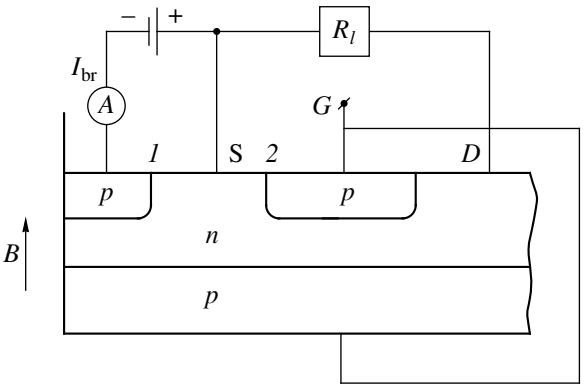

Fig. 1. The structure of the field-effect transistor and *p–n* junction *1*. The arrow indicates the direction of the magnetic field *B*.

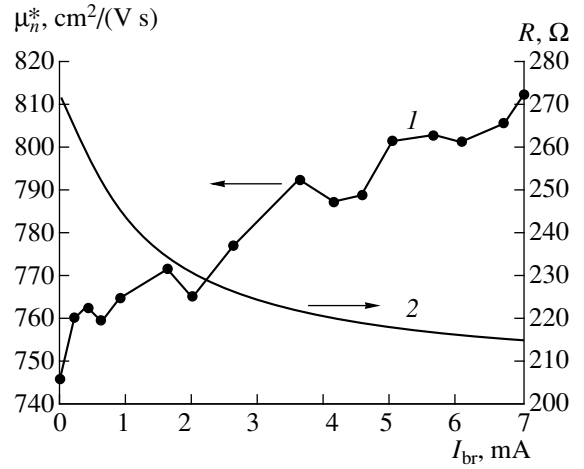

Fig. 2. Dependences of (*1*) the electron mobility μ_n^* in the channel and (*2*) the channel resistance on the current I_{br} initiating the breakdown of *p–n* junction *1*. The direction of propagation of acoustic phonons coincides with that of the motion of electrons.

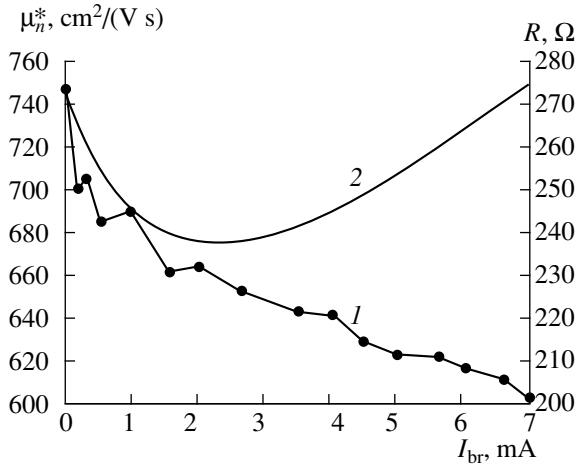

Fig. 3. The dependences similar to those shown in Fig. 2 but for the case where the direction of propagation of acoustic phonons is opposite to that of the motion of electrons.

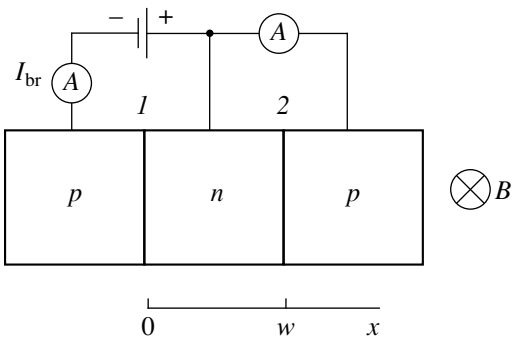

Fig. 4. One-dimensional model of the structure under investigation.

It follows from expression (2) that the ratio of the currents J_p^B (for $B \neq 0$) and J_p (for $B = 0$) is independent of the photon-emission intensity G. Therefore, the ratio J_p^B/J_p is bound to be independent of the current initiating the breakdown of p–n junction *1*; i.e., it is expected to be independent of the emission intensity G. However, as experimental studies showed, the ratio J_p^B/J_p decreased as the current initiating the breakdown of p–n junction *1* increased. Thus, the ratio $J_p^B/J_p = 0.991$ for the breakdown-initiating current of $I_{br} = 1$ mA, whereas $J_p^B/J_p = 0.962$ for $I_{br} = 5$ mA (the measurements were performed for $B = 1.5$ T). This means that the sensitivity of the structure to the magnetic field increases as the current initiating the breakdown of p–n junction *1* increases. This is related to an increase in the mobility of minority charge carriers μ_p^* in accordance with formula (3). Such an increase in the mobility of minority charge carriers can also be explained by the drag of the carriers by acoustic phonons.

ACKNOWLEDGMENTS

We thank R.P. Seisyan for his helpful participation in discussion of the results.

REFERENCES

1. Yu. P. Kuznetsov, V. V. Novikov, É. E. Pakhomov, and V. A. Chetskiĭ, Pis'ma Zh. Tekh. Fiz. **15** (5), 88 (1989) [Sov. Tech. Phys. Lett. **15**, 202 (1989)].
2. P. A. Childs, J. Appl. Phys. **55** (12), 4304 (1984).
3. R. R. Vardanyan, Izv. Akad. Nauk Arm. SSR, Fiz. **22** (3), 149 (1987).

Translated by A. Spitsyn

Semiconductors, Vol. 34, No. 5, 2000, pp. 609–613. Translated from Fizika i Tekhnika Poluprovodnikov, Vol. 34, No. 5, 2000, pp. 628–632.

PHYSICS OF SEMICONDUCTOR DEVICES

Power Conversion Efficiency of Quantum Dot Laser Diodes

A. E. Zhukov*, A. R. Kovsh*, S. S. Mikhrin*, N. A. Maleev*, V. A. Odnoblyudov*, V. M. Ustinov*, Yu. M. Shernyakov*, E. Yu. Kondrat'eva*, D. A. Livshits*, I. S. Tarasov*, N. N. Ledentsov*, P. S. Kop'ev*, Zh. I. Alferov*, and D. Bimberg**

** Ioffe Physicotechnical Institute, Russian Academy of Sciences, Politekhnicheskaya ul. 26, St. Petersburg, 194021 Russia*

e-mail: zhukov@beam.ioffe.rssi.ru

*** Institut für Festkörperphysik, Technische Universität Berlin, D-10623 Berlin, Germany*

Submitted December 6, 1999; accepted for publication December 7, 1999

Abstract—The power conversion efficiency of laser diodes with an array of quantum dots in the active region is analyzed. A model is proposed which allows analytical determination of the optimal cavity length corresponding to the highest conversion efficiency for a given output power. A comparison is made with experimental data for high-power lasers based on submonolayer quantum dots emitting at 0.94 μm. © *2000 MAIK "Nauka/Interperiodica".*

One of the most important device characteristics of a laser diode is the efficiency of conversion η_C of the input electric power into output optical power P. Apparently, the conversion efficiency depends both on the power and on the cavity length. The same output power can be obtained in laser diodes with different cavity lengths, but the conversion efficiencies will be different.

In this work, the problem of diode design optimization is set as associated with finding the optimal cavity length L_{opt} corresponding to the highest conversion efficiency attainable for a given output power and to the maximum conversion efficiency. A simple analytical model is developed that can be used to determine these characteristics for a laser with an active region based on an array of quantum dots and to establish a relationship between the characteristics and such intrinsic parameters of the laser as resistivity, internal loss, differential gain, transparency current, etc. As objects of the study, we chose 0.94-μm high-power lasers with an active region based on an array of submonolayer quantum dots (SML QDs).

The conversion efficiency of a laser diode is defined as a ratio of the total output optical power to the input electric power and can be approximately written as

$$\eta_C(P, L) = \frac{P}{IV_0 + I^2R_S}, \tag{1a}$$

where

$$I = P/\eta + I_{th} \tag{1b}$$

is the drive current necessary for the required power to be attained; η and I_{th} are the differential efficiency and threshold current, both depending on the cavity length L; V_0 is the diode cutoff voltage; and R_S is the series resistance of the diode and is also cavity-length dependent.

It was shown [1] that, for a diode with cavity length L, the efficiency η_C reaches its maximum value

$$\eta_C^{peak} = \frac{\eta(L)}{V_0}[x/(1 + \sqrt{1 + x})^2] \tag{2a}$$

at output power

$$P_0 = \eta(L)I_{th}(L)\sqrt{1 + x}. \tag{2b}$$

Here, $x = V_0/I_{th}(L)R_S(L)$ is a length-dependent dimensionless parameter. A decrease in the conversion efficiency, occurring when the output power becomes higher than P_0, is due to a higher voltage drop across the series resistance of the diode.

Figure 1 shows the output power, diode voltage, and conversion efficiency as functions of the drive current for a laser diode that has uncoated faces, a cavity length of 1.76 mm, and a stripe width of 100 μm and that emits in the 0.94-μm region. The active region of the laser is an array of QDs formed by submonolayer deposition of InAs/GaAs [2]. The epitaxial growth technique and the procedure used to measure the device characteristics were described in detail in [3]. As can be seen from Fig. 1, the maximum conversion efficiency η_C^{peak} = 50.5% is achieved in the diode with the given cavity length at a current of 2.4 A, with an output power of

1063-7826/00/3405-0609$20.00

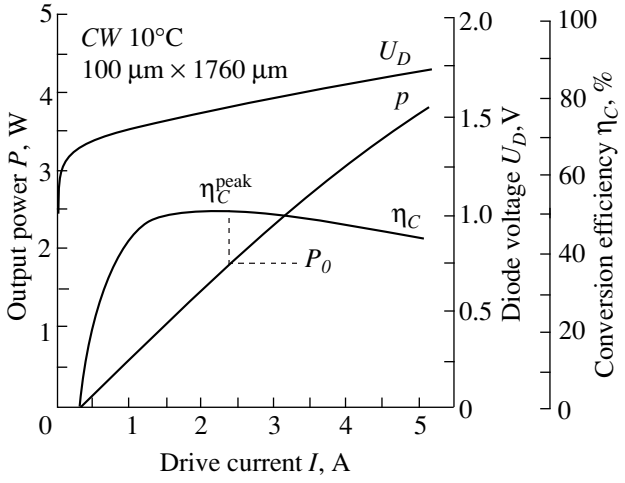

Fig. 1. Optical output power P, diode voltage U_D, and conversion efficiency η_C vs. drive current in the continuous-wave mode, determined experimentally at 10°C for a stripe laser diode (stripe width 100 μm and cavity length 1.76 mm) with an active region based on SML InAs QDs. The highest conversion efficiency $\eta_C^{peak} = 50.5\%$ is achieved for the given diode at $P_0 = 1.9$ W.

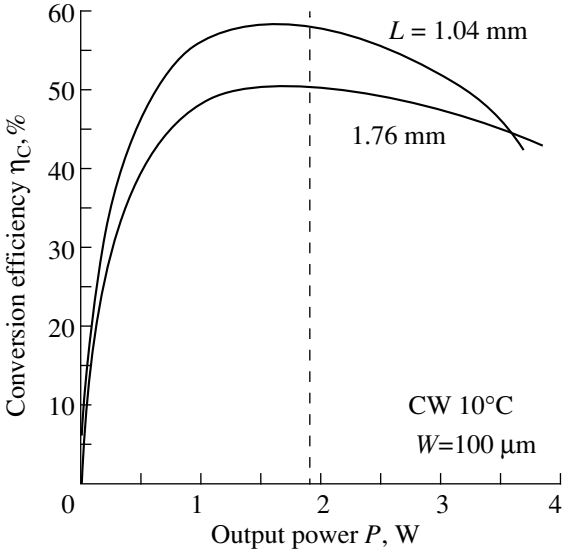

Fig. 2. Conversion efficiency vs. the output optical power for diodes with cavity lengths of 1.04 and 1.76 mm (see also the caption to Fig. 1). The vertical dashed line corresponds to the power at which the highest conversion efficiency is achieved for the diode with a cavity length of 1.76 mm.

$P_0 = 1.9$ W. Note that the achieved maximum power (3.9 W) is the highest among all types of QD lasers [4]. Taking into account the experimental values of the threshold current ($I_{th} = 330$ mA), differential efficiency ($\eta = 0.92$ W/A), series resistance ($R_S = 70.7$ mΩ), and diode cutoff voltage ($V_0 = 1.37$ V), the η_C^{peak} value calculated by (2a) is 51.5%, which is in good agreement with the experimental value.

It may appear that, for a power of $P = P_0$, the conversion efficiency calculated by (2a) is the highest possible for any cavity length. The conversion efficiency of diodes with different cavity lengths is shown in Fig. 2 as a function of output power. It can be seen that, although $P = 1.9$ W constitutes the condition for attaining the maximum conversion efficiency in a diode with cavity length $L = 1.76$ mm, there exist cavities, in particular, with $L = 1.04$ mm, for which even higher conversion efficiency is achieved at the given output power.

Thus, the analysis performed in [1] and described by expressions (2) fails to attain the solution to the problem of diode design optimization as it was formulated above. The approach developed in this work is based on satisfying the condition

$$\left.\frac{\partial \eta_C(P, L)}{\partial L}\right|_{P = \text{const}} = 0, \qquad (3a)$$

that determines the cavity length L_{opt} for which the highest conversion efficiency $\eta_C^{max}(P)$ is achieved for a given output power P. Expression (3a) can be transformed into

$$V_0 C + 2R_S I C = -I^2 dR_S/dL, \qquad (3b)$$

where $C = \partial I/\partial L|_{P = \text{const}}$ is the partial derivative with respect to L of the current necessary to achieve the prescribed power P [expression (1b)]. Evidently, the value of C depends on both the power P and the cavity length L. Moreover, the dependence on L is rather complicated in the general case, since it reflects changes in both the threshold current and differential efficiency.

However, consideration of lasers with an active region based on a QD array makes it possible to simplify the expressions significantly and obtain elementary analytical relations for sought-for L_{opt} and $\eta_C^{max}(P)$. A characteristic feature of a QD laser is the linear relationship between the threshold current density J_{th} and the optical-mode gain g

$$g = \beta(J_{th} - J_0) \qquad (4)$$

for gains not exceeding the saturation gain g^{sat}. Here, β is the current-independent differential gain and J_0 is the transparency current.

As shown in [5], expression (4) is approximately valid at rather high temperatures determined by the condition $k_B T > 2\sigma$, where k_B is the Boltzmann constant and 2σ is the inhomogeneous broadening of the density of states associated with the QD array. In the considered case of SML QDs, the inhomogeneous broadening found from photoluminescence spectra is approxi-

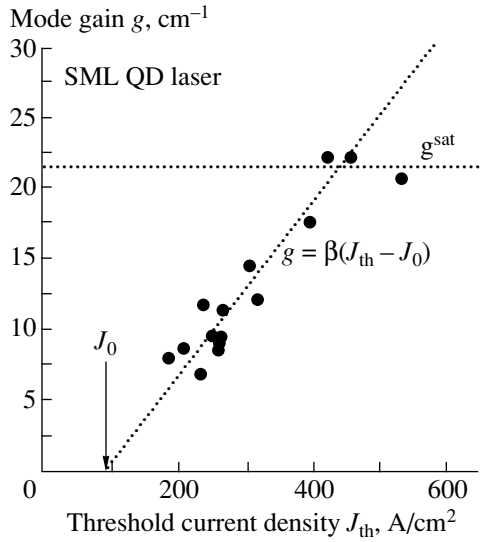

Fig. 3. Mode gain as a function of the threshold current density (full circles), measured for laser diodes with different cavity lengths. The inclined dotted line is a linear fit to the experimental data by expression (4) for a transparency current of J_0 = 90 A/cm^2 and a differential gain of β = 0.06 cm/A. The horizontal dotted line corresponds to a saturated gain of g^{sat} = 21.5 cm^{-1}.

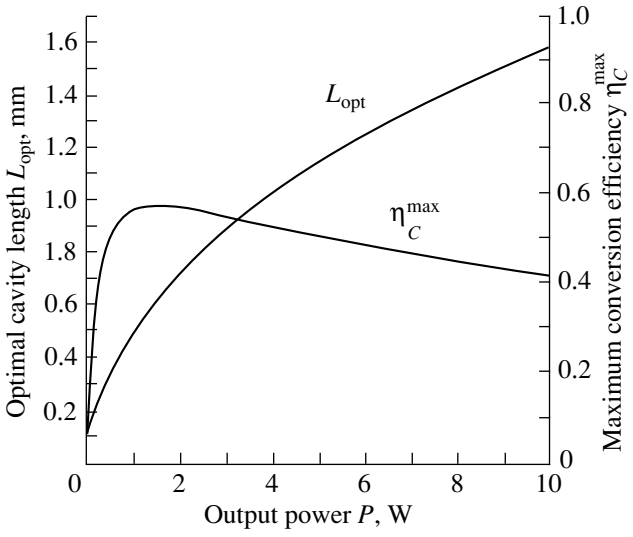

Fig. 4. Maximum conversion efficiency η_C^{max} and the corresponding optimal cavity length L_{opt} in relation to the output optical power P, as calculated with expressions (6a)–(6c). The structure's parameters are taken to be β = 0.06 A/cm, J_0 = 90 A/cm^2, $\rho_S = 1.244 \times 10^{-4}$ Ω cm^2, V_0 = 1.37 V, W = 100 μm, α_i = 2.3 cm^{-1}, and η_0 = 1.31 W/A.

mately 25 meV. Thus, at temperatures close to room temperature, expression (4) must well describe experimental data.

The relationship between the gain and threshold current density is found experimentally for the laser under study with different cavity lengths and is illustrated in Fig. 3. The optical gain was calculated as a sum of the mirror loss α_m and internal loss α_i. The latter was evaluated from the dependence of the differential efficiency on L and was taken to be 2.3 cm^{-1}. As can be seen from Fig. 3, at a transparency current J_0 = 90 A/cm^2 and differential gain β = 0.06 cm/A, expression (4) well describes experimental data for J_{th} = 500 A/cm^2, which corresponds to $L > 0.5$ mm. With the cavity length decreasing (threshold current density increasing) further, the gain saturates at g^{sat} = 21.5 cm^{-1}, which, to our knowledge, is the highest ever obtained saturated gain for injection lasers with a single layer of QDs in the active region.

The fact that the relation between the threshold current density and the gain is linear for not-too-short cavities allows expression (1b) to be transformed into

$$I = CL + I_P^0, \tag{5a}$$

$$C = \frac{P\alpha_i}{\eta_0 r} + W\left(\frac{\alpha_i}{r} + J_0\right), \tag{5b}$$

$$I_P^0 = \frac{P}{\eta_0} + W\frac{r}{\beta}. \tag{5c}$$

Here, W is the stripe width, η_0 is the internal differential efficiency, $r = 1/2\ln(1/R_1R_2)$, and $R_{1,2}$ are the power reflectivities of the cavity faces. We took into account the fact that $\alpha_m = r/L$ and $\eta = \eta_0\alpha_m/(\alpha_m + \alpha_i)$.

Thus, we found that the partial derivative with respect to L of the current required for attaining the prescribed power P is independent of L. This makes it possible to solve analytically equation (3b) and find the cavity length L_{opt} at which the maximum conversion efficiency $\eta_C^{max}(P)$ is attained at a given output power P:

$$L_{opt} = \frac{I_P^0}{C\sqrt{1 + B}}, \tag{6a}$$

$$\eta_C^{max}(P) = \frac{P}{V_0 I_P^0}\frac{B}{(1 + \sqrt{1 + B})^2}, \tag{6b}$$

$$B = \frac{WV_0}{\rho_S C}. \tag{6c}$$

Here, we took into account that the series resistance is inversely proportional to the diode area $R_S = \rho_S/WL$. For the lasers under study, the series resistivity $\rho_S = 1.24 \times 10^{-4}$ Ω cm^2.

Figure 4 shows the dependence of η_C^{max} on L for different output powers P, as calculated by expressions (6a)–(6c). The intrinsic parameters of the laser are given in the figure's caption. It can be seen that, with increasing output power, the optimal cavity length nec-

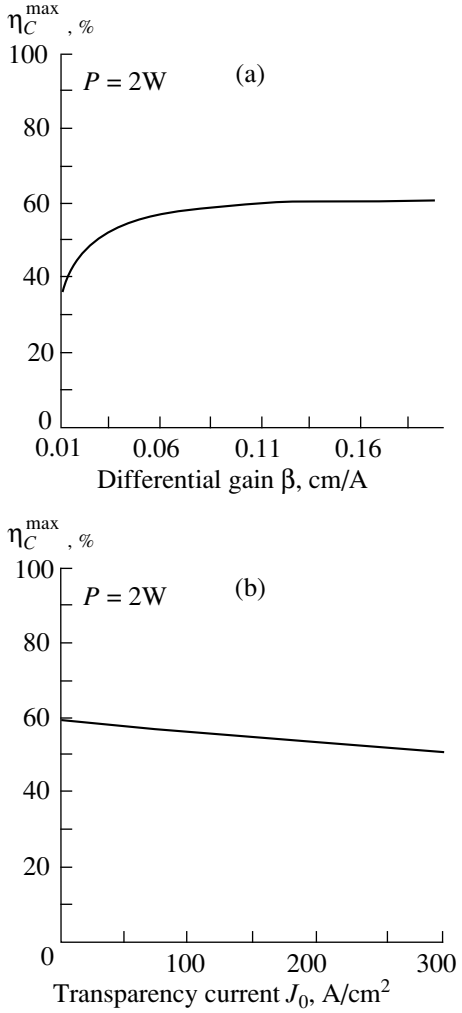

Fig. 5. Maximum conversion efficiency η_C^{max} as a function of (a) the differential gain β and (b) the transparency current J_0, as calculated with (6a)–(6c). Other structure parameters are the same as in Fig. 4.

essary to attain the maximum conversion efficiency increases. In particular, it follows from expression (6a) that, in the limit of an infinitely high output power, L_{opt} asymptotically approaches the r/α_i value.

Generally speaking, the output power of a laser diode cannot increase infinitely, being limited by catastrophic optical mirror damage or by a decrease in the differential efficiency because of the heating of the active region. It follows from Fig. 4 that, for the range of 2–4 W, which is achievable in practice in lasers with uncoated mirrors, the maximum conversion efficiency of the laser under study is attained for a cavity length of about 1 mm. The experimental data in Fig. 2 are in good agreement with the results of calculations: a conversion efficiency exceeding 55% in a wide range of output powers of 1–2.5 W is achieved in a laser with a cavity length of 1.04 mm. The largest value of η_C attained is 59%, which, as far as we know, is a record-breaking result for injection lasers based on QDs. Note that the highest reported conversion efficiency for quantum well lasers is 66% [6, 7].

Expressions (6a)–(6c) make it possible to analyze the dependence of maximum conversion efficiency on the laser-diode intrinsic parameters directly associated with the active region. As an example, Fig. 5 shows η_C^{max} values calculated for an output power of 2 W as functions of the differential gain β (Fig. 5a) and transparency current density J_0 (Fig. 5b).

As can be seen from Fig. 5a, the maximum conversion efficiency decreases rapidly when the differential gain becomes lower than $\beta \approx 0.05$–0.06 cm/A. The differential gain of a laser with a QD active region is mainly determined by the inhomogeneous broadening of the density of states associated with the QD array. For the laser structure under study, the inhomogeneous broadening was estimated to be 25 meV. The differential gain was 0.06 cm/A, which is close to the critical value below which the conversion efficiency falls dramatically. According to the data obtained, a less uniform array of QDs will hardly yield higher conversion efficiency. On the other hand, for β exceeding ~0.09 cm/A, the maximum conversion efficiency already depends on the differential gain only slightly. Thus, formation of an even more ordered array of QDs, although desirable, would hardly improve the device characteristics significantly.

According to the data presented in Fig. 5b, η_C^{max} depends only slightly on the transparency current density, in its turn proportional to the surface density of the QD array. This means that the QD array density can be changed without noticeably impairing the conversion efficiency of a laser diode. On the other hand, it is very desirable to increase the QD array density, because it would result in a higher saturated gain and a lower internal loss of a QD laser.

Thus, we studied the conversion efficiency of laser diodes with an active region based on a QD array. We developed a simple model that can be used to determine analytically the optimal cavity length for which the highest conversion efficiency is attained for a given output power and to determine the conversion efficiency itself and its dependence on such intrinsic parameters of a laser as material resistivity, internal loss, transparency current, etc. The results obtained with the model are in good agreement with experimental data for high power SML QD lasers emitting at 0.94 μm.

ACKNOWLEDGMENTS

The work was supported by the Russian Foundation for Basic Research and BMBF.

REFERENCES

1. D. P. Bour and A. Rosen, J. Appl. Phys. **66**, 2813 (1989).
2. A. Yu. Egorov, A. E. Zhukov, P. S. Kop'ev, *et al.*, Fiz. Tekh. Poluprovodn. (St. Petersburg) **28**, 604 (1994) [Semicond. **28**, 363 (1994)].
3. A. E. Zhukov, A. R. Kovsh, S. S. Mihkrin, *et al.*, Electron. Lett. **35**, 1845 (1999).
4. A. R. Kovsh, A. E. Zhukov, D. A. Livshits, *et al.*, Electron. Lett. **35**, 1161 (1999).
5. A. E. Zhukov, A. R. Kovsh, and V. M. Ustinov, Fiz. Tekh. Poluprovodn. (St. Petersburg) **33**, 1395 (1999) [Semicond. **33**, 1260 (1999)].
6. D. Botez, L. J. Mawst, A. Bhattacharya, *et al.*, Electron. Lett. **32**, 2012 (1996).
7. J. Wang, B. Smith, X. Xie, *et al.*, Appl. Phys. Lett. **74**, 1525 (1999).

Translated by M. Tagirdzhanov